



HAL
open science

Acoustic waves in porous media : numerical study of wave propagation in porous media with one or many mineral components : applications to real Fontainebleau and STATOIL samples

The Anh Nguyen

► **To cite this version:**

The Anh Nguyen. Acoustic waves in porous media : numerical study of wave propagation in porous media with one or many mineral components : applications to real Fontainebleau and STATOIL samples. Earth Sciences. Université Pierre et Marie Curie - Paris VI, 2015. English. NNT : 2015PA066205 . tel-01292919

HAL Id: tel-01292919

<https://theses.hal.science/tel-01292919>

Submitted on 24 Mar 2016

HAL is a multi-disciplinary open access archive for the deposit and dissemination of scientific research documents, whether they are published or not. The documents may come from teaching and research institutions in France or abroad, or from public or private research centers.

L'archive ouverte pluridisciplinaire **HAL**, est destinée au dépôt et à la diffusion de documents scientifiques de niveau recherche, publiés ou non, émanant des établissements d'enseignement et de recherche français ou étrangers, des laboratoires publics ou privés.

Université Pierre et Marie Curie

ED 398 : Géosciences, ressources naturelles et environnement

Laboratoire METIS – UMR 7619

ACOUSTIC WAVES IN POROUS MEDIA

*Numerical study of wave propagation in porous media with
one or many mineral components. Applications to real
Fontainebleau and STATOIL samples.*

Par

NGUYEN The Anh

Thèse de doctorat de

Géosciences, Géophysique, Géocomputations

Dirigée par

Pierre M. ADLER

Présentée et soutenue publiquement le 22 – 09 - 2015

Devant un jury composé de :

Claude BOUTIN	Professeur, ENTPE, France	Rapporteur
David M.J. SMEULDERS	Professeur, Delft University of Technology	Rapporteur
Olivier LOPEZ	Docteur, STATOIL, Norvège	Examineur
Christian MOYNE	Directeur recherche CNRS	Examineur
Alf Birger RUSTAD	Docteur, STATOIL, Norvège	Examineur
Alain TABBAGH	Professeur, UPMC, France	Examineur
Pierre M. ADLER	Directeur recherche CNRS	Examineur



NGUYEN, The Anh (Ph.D.)

Thesis directed by Prof. Pierre M. ADLER

ACOUSTIC WAVE IN POROUS MEDIA

Numerical study of wave propagation in porous media with one or many mineral components. Applications to real Fontainebleau and STATOIL samples.

The purpose of this Ph.D. thesis is to study acoustic waves in porous media. The homogenization theory (Boutin and Auriault, 1990; Malinetskaya, 2007; Li, 2010) is used together with the lattice models such as LBM, LSM, LSM2S, LBM-LSM, LBM-LSM2S in order to determine the macroscopic properties, the acoustic velocities, the attenuation effects in Fontainebleau samples with two components (pore and quartz) and in STATOIL samples with three components (pore, quartz and clay).

Three problems are studied numerically in this work. The first problem is devoted to characterizations of samples; this is done with the determination of the porosity and of the correlation functions with the corresponding Fourier components (Adler, 1992; Nguyen, 2013). The second one addresses wave propagation in dry samples; the velocities are derived from the effective stiffness tensor $C^{(eff)}$ which can be calculated by LSM (Pazdaniakou, 2012) or LSM2S. The third one corresponds to samples saturated by incompressible or compressible fluids; the velocities can be obtained from the Christoffel equation after determining $C^{(eff)}$, the dynamic permeability K and the reactions to fluid pressure α and β .

For Fontainebleau samples, the calculations are performed with basic existing models such as LSM, LBM, LBM-LSM. These basic models are extended to solids with multiple components; they are validated by comparisons with others (Nemat-Nasser and Iwakuma, 1982; Torquato, 1998, 2000; Cohen, 2004).

The velocities, the effective bulk and shear modulus of all the dry samples as well as the velocities and the attenuation effected in saturated samples are determined. These results are in good agreement compared with existing models and results, such as the IOS model of Arns (1996), the empirical models of Nur *et al.* (1991), Krief (1990) and with Gassmann's model.

The numerical results are slightly larger than the experimental data of Han (1986) and Gomez *et al.* (2010); the origin of this small discrepancy has been tentatively analysed, but its cause has not been unambiguously identified.

Keywords: porous media, lattice models, compressible fluids, lattice Boltzmann model, parallel programs.

Contents

Chapter

1	Introduction	1
2	General theory	3
2.1	Introduction	3
2.2	Reviews, methodologies	4
2.2.1	Acoustic waves in porous media	4
2.2.2	Methodologies	7
2.3	Characterization of geometry	8
2.3.1	Porosity	8
2.3.2	Correlation function	9
2.4	Conduction in porous media and determination of the length Λ	10
2.5	Flows in porous media	11
2.5.1	Local governing equations	11
2.5.2	Lattice Boltzmann Model (LBM)	13
2.5.3	Absolute permeability	19
2.5.4	Dynamic permeability	20
2.5.5	The dynamic permeability and the length Λ	23
2.6	Propagation of acoustic waves in dry porous media	24
2.6.1	Elastic waves in elastic media	25
2.6.2	Elastic waves in porous media	26

2.7	Propagation of acoustic waves in saturated porous media	27
2.7.1	Homogenization method	27
2.7.2	Multiple pores and compressible fluids	33
2.7.3	Determination of $\overline{\mathbf{K}}$, $\overline{\alpha}$, \mathbf{B} and \mathbf{C}^{eff}	34
2.7.4	Gassmann's model	36
2.8	Summary	38
3	Lattice models in calculations of porous media	39
3.1	Introduction	39
3.2	Lattice Spring Model	40
3.2.1	3D LSM	41
3.2.2	Linear springs	43
3.2.3	Angular springs	43
3.2.4	Combination of linear and angular springs	45
3.2.5	The problems of the original LSM	46
3.2.6	Geometry	49
3.2.7	Application of LSM to calculate effective stiffness tensors	50
3.3	The Lattice Spring Model for 2 solid components (LSM2S)	51
3.3.1	Geometry	52
3.3.2	Spring constants with two solids	53
3.3.3	The spatially periodic boundary conditions	53
3.3.4	Calculation of effective properties of porous media with two solids.	57
3.3.5	The algorithm	58
3.3.6	Validation	59
3.4	The coupled models: LBM-LSM and LBM-LSM2S	67
3.4.1	Geometry	68
3.4.2	Boundary conditions	69
3.4.3	LBM-LSM coupling	70
3.4.4	Implementation aspects	72

3.4.5	Development of the coupled LBM-LSM2S model	72
3.5	Summary	74
4	Acoustic wave velocities in Fontainebleau samples	75
4.1	Introduction	75
4.2	Characterizations of Fontainebleau samples	76
4.2.1	Sample FB8	78
4.2.2	Samples FB13, FB18 and FB22	80
4.2.3	The influence of porosity on the correlation function in Fontainebleau sandstones.	83
4.3	Acoustic wave velocities in the dry Fontainebleau sandstones	84
4.3.1	Effective stiffness tensor	84
4.3.2	Acoustic velocities	86
4.4	Additional comparisons	89
4.5	The formation factor F and the characteristic length Λ	92
4.6	Acoustic wave velocities in saturated Fontainebleau samples	94
4.6.1	Permeabilities	94
4.6.2	The coefficients α , β and the velocities in the saturated samples	108
4.7	Conclusions	126
5	Acoustic wave velocities in STATOIL samples with two solid components	127
5.1	Introduction	127
5.2	Characterizations of samples	128
5.2.1	Porosities and component proportions	130
5.2.2	Correlation functions	131
5.3	Acoustic velocities in the dry samples	133
5.3.1	Samples X2	135
5.3.2	Sample X7	145
5.3.3	Sample Y5 and Y13	147

5.4	Additional comparisons	150
5.5	The formation factor F and the characteristic length Λ	153
5.6	Acoustic velocities in saturated STATOIL samples	153
5.6.1	Permeabilities	155
5.6.2	Coefficients α, β and acoustic velocities in saturated samples	161
5.7	Conclusion	180
6	Conclusions	182
	Bibliography	185
	Appendix	
A	APPENDIX	190
A.1	Spring constants in the LSM2S model	190
A.2	The coarsening method	194
A.2.1	Coarsening of samples	194
A.2.2	Numerical results	195
A.2.3	Correction of the solid properties	198
A.3	Acoustic velocities in saturated Fontainebleau samples.	201
A.4	Acoustic waves in saturated STATOIL samples	222

Chapter 1

Introduction

The purpose of this thesis is to study acoustic wave propagation in dry or in saturated porous media on the pore scale. This phenomenon depends on the mechanic and hydraulic properties of media (*Boutin and Auriault, 1990; Malinouskaya, 2007; Li, 2010*).

The characteristics of wave propagation in homogeneous solid materials without pores are determined by the elastic constants (*Achenbach, 1973*). This result can be also extended in a first approximation to porous or heterogeneous media by reference to an equivalent homogeneous medium with adequate effective properties (*Boutin and Auriault, 1990; Malinouskaya, 2007*). However, heterogeneities or pores induce additional phenomena such as reflections and refractions (*Christensen, 1979*). They are quite complex, especially when the characteristic pore (or heterogeneity) scale l is not negligible compared to the wave length λ .

Wave propagation in saturated porous media is more challenging since there are two phases whose mechanical behaviours obey different laws. In the solid, propagation depends on the elastic properties, while in the fluid it is governed by the Navier-Stokes equations (*Boutin and Auriault, 1990; Li, 2010*).

In this thesis, we are interested in acoustic and dynamic properties of Fontainebleau and STATOIL samples. They are reconstructed samples obtained from real rocks by micro-CT. There are 4 Fontainebleau samples with porosities ranging from 8 to 22% of the same form, namely cubes of size $2736 \mu m$. The Fontainebleau samples include pore and quartz while the STATOIL samples include pore, clay and quartz and are parallelepipeds of various sizes. The porosities and the correlation functions (*Nguyen, 2013*) of these samples are calculated.

Attention is focused on the situation where $\lambda \gg l$. For dry samples, the wave velocities are derived from the effective elastic properties of samples such as the effective stiffness tensor C^{eff} . C^{eff} of Fontainebleau samples can be directly determined by the Lattice Spring Model (LSM) developed by *Pazdniakou* (2012) while the ones of STATOIL samples are simulated by the Lattice Spring Model for two solid (LSM2S) which is extended for porous media with many solid components. Six simulations are needed for each sample to obtain nine components of C^{eff} . Then, the velocities of the compressional and the shear waves can be derived along the three spatial axes.

Wave propagation in saturated samples is calculated by homogenization method where the interaction between the solid and the fluid phases is taken into account. The acoustic velocities are derived from the generalized Christoffel equation for a single pore filled by an incompressible fluid (*Boutin and Auriault*, 1990; *Malinouskaya*, 2007) or for many pores by a compressible fluid (*Pazdniakou*, 2012; *Li*, 2010)). The four needed coefficients to solve this equation can be fully determined by lattice models such as LSM, LSM2S (C^{eff}), LBM (dynamic permeability K) and coupled models LBM-LSM, LBM-LSM2S (fluid reactions α and β) (*Pazdniakou*, 2012). The Christoffel equation has three eigenvalues which correspond to the fast compressional, the slow compressional and the shear waves (*Biot*, 1956a,b). The influence of the compressibility coefficient on acoustic velocities is also taken into account.

The organization of this thesis is as follows. Chapter 2 "General theory" provides some general review and the methodologies for all samples. Chapter 3 "Lattice models in calculations of porous media" describes the used lattice models such as LSM, LBM-LSM, together with the extensions of LSM2S, LBM-LSM2S from the basic models. The calculations of dry and of saturated Fontainebleau samples are given in Chapter 4. The STATOIL samples with two solids are presented in Chapter 5. Finally, some conclusions are given in Chapter 6.

Chapter 2

General theory

2.1 Introduction

Propagation of waves in porous media is an important topic in many areas of Physics and it has various engineering applications. This phenomenon has been studied in soil mechanics, seismology, earthquake engineering, ocean engineering... and other domains.

The main purpose of this thesis is the study of acoustic wave propagation in porous media on the pore scale. It can be divided into three parts: characterization of samples, determination of acoustic velocities in dry samples and in saturated samples. The characterization includes the determination of porosity and of the correlation functions. The determination of the macroscopic conductivity tensor and the characteristic length Λ is also introduced.

The acoustic velocities in dry samples are derived from their macroscopic properties such as the effective stiffness tensor C^{eff} . These properties can be deduced by homogenization methods combined with numerical models (*Malinouskaya, 2007; Li, 2010; Pazdniakou, 2012*).

The propagation of acoustic waves in saturated samples is a more complex problem. The homogenization method for a single pore saturated by an incompressible fluid was developed by *Boutin and Auriault (1990)* and *Malinouskaya (2007)*. Then, it is extended to media with multiple disconnected pores and to compressible fluids (*Li, 2010; Pazdniakou, 2012*). Based on this method, the acoustic velocities can be determined by solving an eigenvalue problem (the Christoffel equation) after the determination of the necessary macroscopic properties. On the other hand, Gassmann's model is an approximate model which predicts the wave velocities in

saturated media and it is used for a comparison with the simulation results.

This chapter is organized as follows. First, Section 2.2 reviews some methods and methodologies. Then, the characterization of geometry is presented in Section 2.3. The conduction and the length scale Λ are described in Section 2.4. The Lattice Boltzmann model and permeabilities are introduced in Section 2.5. Sections 2.6 and 2.7 present acoustic wave propagation in dry and in saturated porous media. Finally, a summary is given in Section 2.8.

2.2 Reviews, methodologies

2.2.1 Acoustic waves in porous media

This problem has been studied for several decades theoretically and also experimentally; *Biot* (1941, 1956a,b), *Gassmann* (1951)... pioneered the field. For instance, Biot's work on wave propagation is considered as the first one employing fundamentals of porous media mechanics.

The acoustic wave velocities in dry porous media can be determined by solving an eigenvalue problem which is the so-called Christoffel equation (*Landau and Lifshitz*, 1986). The coefficients of this equation involve the macroscopic mechanical properties of the medium which depend on the structure and on the solid properties. Various methods have been proposed to derive the macroscopic elastic properties of the materials such as the variational method of *Hashin and Shtrikman* (1962a,b), the self-consistent approximations of *Clearly et al.* (1980), the multiple scale expansion of *Poutet et al.* (1996)... *Boutin and Auriault* (1990), *Arns* (1996), *Malinetskaya* (2007), *Li* (2010), *Pazdaniakou* (2012) have proposed other techniques.

Two types of waves can propagate through an isotropic and homogeneous material, namely the longitudinal and transversal waves with respect to the propagation direction; in this thesis, they are called compressional and shear waves. For anisotropic media, plane waves only propagate along the principal directions of the Christoffel equation with various velocities (*Li*, 2010). In heterogeneous media, two situations occur depending on the relative orders of magnitude of the wave length λ and of the characteristic size l of the heterogeneities. When $\lambda \sim l$, the problem is very complex with reflections and refractions due to local heterogeneities such as obstacles, different material properties... An analysis of the solutions of three-dimensional media with spatially

periodic discontinuities is presented by *Christensen* (1979).

When $\lambda \gg l$, the medium can be considered as an equivalent homogeneous material (*Li*, 2010); this assumption provides the general framework for study of acoustic waves in geological media. For a statistically isotropic medium, the classical formula still applies. There are only a few analysis for simple geometries. For instance, the dispersion of compressional and shear waves by an ellipsoid was analysed by a matched asymptotic development by *Datta* (1977). The finite difference or the finite element techniques are used by *Saenger et al.* (1977), *Roberts* (2002) and *Arns* (1996) in order to determine the macroscopic elastic properties of complex realistic structures.

When $\lambda \gg l$ and for a spatially periodic medium, the homogenization techniques can be used to determine the macroscopic properties by solving equations on the pore scale (*Sanchez*, 1980). *Boutin and Auriault* (1990) derived the equations of successive orders in a systematic way. The first order equations provide the polarization correction, the second ones give the velocity dispersion and the third ones the attenuation. *Malinouskaya* (2007) applied this theoretical framework to porous media. Moreover, they successfully developed a numerical tool (FMD) in order to calculate the macroscopic properties by solving first order local problems numerically. This was extended to higher orders by *Li* (2010).

Furthermore, *Pazdniakou* (2012) developed another numerical method, which can determine macroscopic properties of real materials, namely the Lattice Spring Model (LSM). In this model, the solids are modeled by a collection of springs connected at nodes (linear and angular springs). The macroscopic elastic constants can be derived by the elastic energy stored in an elastic element which is included in order to improve the accuracy of LSM. The power of this model was demonstrated, but it was limited to media with only one solid. In this thesis, this model is extended in order to address porous media with two (LSM2S) or more solids.

The description of wave propagation in saturated porous media is more complex than in dry ones, because two phases (solid and fluid) influence the macroscopic behaviour. The propagation of low- and high-frequency waves in porous media saturated by a viscous compressible fluid was first studied by *Biot* (1956a,b). Wave propagation can be described with the effective elastic

moduli, the permeability and the compressibility of the solid matrix. *Biot* (1941, 1956a,b) showed that there are three types of waves which are predicted by this theory at the macroscopic level; they are the fast compressional and shear waves and the slow compressional wave with a strong attenuation.

As for dry porous media, homogenization is a useful technique in order to describe wave propagations in saturated media. They are widely used by *Sanchez* (1980), *Boutin and Auriault* (1990)... In a medium saturated by a fluid, the wave propagation in the solid is governed by the elastodynamic equation and by the Navier-Stokes equation in the fluid. In the framework of homogenization theory, the medium is supposed to be homogeneous, spatially periodic and composed by identical unit cells; therefore, these local problems are solved on the unit cell. Then, the corresponding solutions are averaged over the unit cell in order to obtain the macroscopic properties of the medium. These averages are introduced into the generalized Christoffel equation whose eigenvalues are the acoustic velocities in the saturated medium.

Malinouskaya (2007) developed this homogenization method for porous media with a single pore saturated by an incompressible fluid. Then, *Li* (2010) extended it to multiple disconnected pores and compressible fluids characterized by a compressibility coefficient. In order to derive the wave velocities and also the macroscopic solid and relative fluid displacements, the effective stiffness tensor C^{eff} , the dynamic permeability K , the reaction of the solid matrix on the fluid pressure α and β are four necessary macroscopic properties. *Pazdniakou* (2012) used this homogenization method and developed numerical tools. These averaged quantities are calculated by combined models such as LBM, LSM, LBM-LSM... Then, the acoustic velocities in the medium can be derived by solving the generalized Christoffel equation. Thanks to that, the dependencies of the velocity and of the attenuation on the frequency are also studied. This method was shown to be efficient by *Pazdniakou* (2012); therefore, this methodology is followed in this thesis.

Gassmann's model is another possible approach to describe waves in saturated media (*Gassmann*, 1951; *Artola and Alvaradob*, 2006); for instance, it is widely used to calculate seismic velocity changes resulting from various fluid saturations in reservoirs. *Han and Batzle* (2004) presented Gassmann's equations in fields of seismic velocities. The shear and compressional wave velocities

can be predicted from the properties of the dry medium and of the saturating fluid. In fact, this approximate model has some limitations, such as the porous material is isotropic, elastic, homogeneous and composed of a single mineral; it does not apply to multiple minerals with different properties. Anyway, it is a simple method and it can be considered as suitable here. A short description of this approach is presented in Section 2.6.

2.2.2 Methodologies

Since the samples are composed by many elementary cubes which can be either solid or pore, the porosity is calculated by the counting method. Then, the number of solid and pore voxels can be determined and the sample porosity ε is obtained. The two point correlation function is determined along three directions and they are compared in order to characterize the samples.

The acoustic wave velocities in dry samples can be determined from the macroscopic properties of samples. The effective stiffness tensor is necessary and it can be directly calculated by using the program based on LSM (*Pazdniakou, 2012*) if the sample size is not very large and there is only one solid. For large samples, two methods are proposed which are the sub-sampling method and the coarsening method; it will be shown that the second one is adequate. Then, LSM is extended to LSM2S and LSMNS in order to determine the macroscopic properties of porous media with many solid components.

The calculation of acoustic waves in saturated porous media is based on the generalised Christoffel equation obtained from homogenization methods by *Malinouskaya (2007)* for a single pore and by *Li (2010)* for multi-pores and compressible fluids. Four macroscopic properties which are noted by C^{eff} , \mathbf{K} , α and β (or $\bar{\alpha}$ and \mathbf{B}) must be determined. They are calculated as follows. The effective stiffness tensor C^{eff} is determined by LSM or LSM2S. The absolute and dynamic permeabilities \mathbf{K} are calculated by the Lattice Boltzmann Model (LBM) for the original and the mirror configurations. The coefficients α and β which characterize the reaction of the solid matrix to the fluid pressure, are determined by simulations with the coupled models LBM-LSM for one solid component and with LBM-LSM2S for two solid components. Then, the acoustic velocities are derived for various frequencies and various compressibility coefficients. The influence of

frequency and of the Reynold number on the velocities and on the attenuation of three types of waves (fast, slow compressional and shear waves) are studied.

2.3 Characterization of geometry

The geometry is characterized before studying propagation in porous media. Porosity and correlation functions are calculated.

2.3.1 Porosity

The porosity of a sample has a significant influence on the mechanical properties and also on the flow characteristics through the samples. It is defined by

$$\varepsilon = \frac{V_p}{V_0} \quad (2.1)$$

where V_p is the void volume, V_0 the total volume. V_p can be derived from the number of void cubes in the samples.

The samples are composed of elementary cubes of size a which are solid or void. Along each axis, a sample is composed by many slices. For instance, along the z -direction, a sample has N_{cz} slices of the same size $N_{cx} \times N_{cy}$; in other words, each slice has $N_{cx} \times N_{cy}$ elementary cubes. The porosity is first calculated for each slice along one direction; it is denoted by $\varepsilon(z_i)$ for the slice i along the z -direction. The total number of cubes in this slice is

$$N_{total} = N_{cx} \times N_{cy} \quad (2.2)$$

The number of void $N_{pore}(z_i)$ in one slice is determined by the counting method for all the cubes present in this slice. The porosity of this slice is given by

$$\varepsilon(z_i) = \frac{N_{pore}(z_i)}{N_{total}} \quad (2.3)$$

where $z = \frac{z'}{a}$ with z' is the distance from the calculation slice to the boundary along the z -axis. The calculations are done for all the slices along the z -direction and the variations of slice porosity are presented in Fig. 2.1.a.

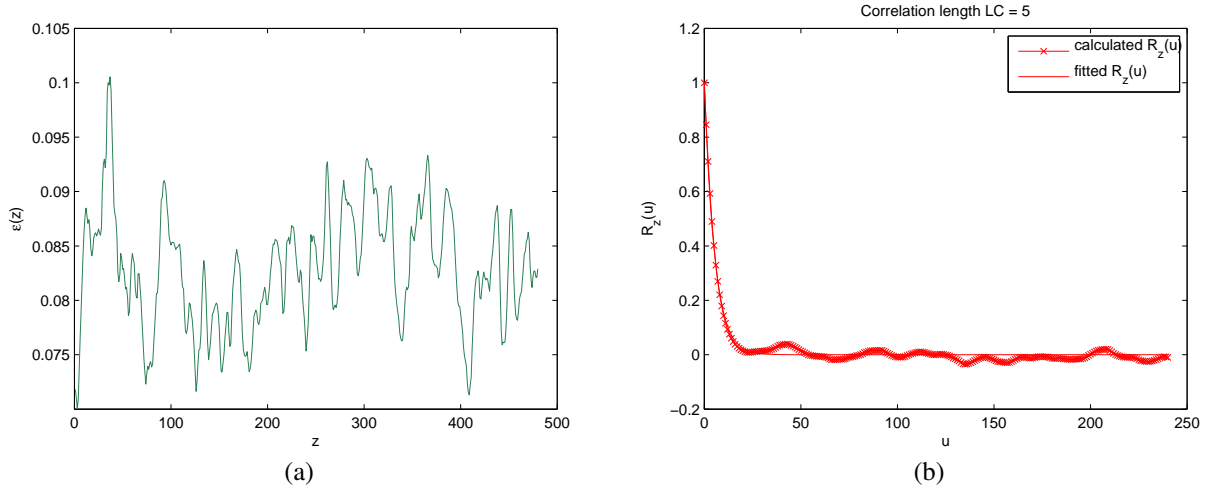


Figure 2.1: a. Porosity of slices along the z -direction of one sample. b. Correlation function of one slice along the z -direction.

Obviously, the average porosity along the z -direction $\varepsilon(z)$ can now be determined. The calculation is similar for the two other directions and $\varepsilon(x)$ and $\varepsilon(y)$ are obtained as well as the sample porosity ε .

2.3.2 Correlation function

For practical purposes, the porous media are constructed in a discrete manner; they are composed of $N_{cx} \times N_{cy} \times N_{cz}$ elementary cubes of the same size a . Each elementary cube, filled either with solid or void, can be characterized by the phase function $Z(\mathbf{r})$ as follows

$$Z(\mathbf{r}) = \begin{cases} 1 & \text{if } \mathbf{r} \text{ belongs to the pore space} \\ 0 & \text{otherwise} \end{cases} \quad (2.4)$$

where \mathbf{r} denotes the position with respect to an arbitrary origin. Consequently, the spatial variables \mathbf{r} and \mathbf{u} take only discrete values, identified with the location of the elementary cubes; the corresponding trios of integers are denoted by

$$\mathbf{r}' = \frac{\mathbf{r}}{a} = (i, j, k) \quad ; \quad \mathbf{u}' = \frac{\mathbf{u}}{a} = (r, s, t) \quad (2.5)$$

The correlation function $R_z(\mathbf{u})$ can be defined by

$$R_z(\mathbf{u}) = \frac{\overline{[Z(\mathbf{r}) - \varepsilon][Z(\mathbf{r} + \mathbf{u}) - \varepsilon]}}{(\varepsilon - \varepsilon^2)} \quad (2.6)$$

where the overbar denotes a statistical or a spatial average. *Adler* (1981) pointed out that the correlation function of isotropic media depends only on the norm u of the vector \mathbf{u} , in which case it is denoted by $R_Z(u)$.

The calculation of two point correlation functions and the least mean square filter will be done for each slice along the three different directions of a three-dimensional porous medium (as in Figure 2.1.b). Then, the Fourier components corresponding to R_Z can be calculated. *Adler* (1981) showed that if these Fourier components are always positive (or the negative values are negligible), the media can be considered as statistically homogeneous. In addition, by comparisons between the slices and between the three directions, we can appreciate geometrical properties of samples such as isotropy.

2.4 Conduction in porous media and determination of the length Λ

One of the macroscopic properties which characterize a porous medium is the macroscopic conductivity tensor $\overline{\Sigma}$. According to *Valfouskaya et al.* (2005), it can be derived from the resolution of the time-independent Laplace equation for the electric field ψ ,

$$\nabla^2 \psi = 0, \quad \mathbf{n} \cdot \nabla \psi = 0 \quad \text{on } S, \quad (2.7)$$

with adequate overall boundary conditions. S is the pore solid surface. When the porous medium is isotropic, the tensor is isotropic

$$\overline{\Sigma} = \overline{\Sigma} \mathbf{I} \quad (2.8)$$

A length scale Λ which can be used to characterize porous media was introduced by *Johnson et al.* (1986). It is an intrinsic measure of the interconnected pore size and is defined as

$$\Lambda = 2 \frac{\int_{\Omega} |\nabla \psi(\mathbf{r})|^2 d^3 r}{\int_S |\nabla \psi(\mathbf{r})|^2 d^2 s} \quad (2.9)$$

where $\psi(\mathbf{r})$ is the solution of the Laplace equation (*Pazdniakou and Adler, 2013*).

In this thesis, the macroscopic conductivity $\bar{\Sigma}$ as well as the length Λ of a porous medium can be determined by solving the Laplace equation (2.7) by a second order finite difference formulation of *Thovert et al.* (1990). They are related to the permeability K by the approximate formula

$$\Lambda^2 = 8KF \quad (2.10)$$

where F is the formation factor. F is defined by

$$F = \frac{\Sigma_0}{\bar{\Sigma}} \quad (2.11)$$

where Σ_0 is the fluid conductivity.

2.5 Flows in porous media

In this section, the Lattice Boltzmann Model (LBM) is described. It is useful to calculate permeability in reconstructed porous media. *Nguyen* (2013) and *Pazdniakou* (2012) used and developed LBM to simulate single and multiphase fluids through porous media.

LBM originated from the lattice gas automata (LGA) method (*Frisch et al.*, 1986; *d'Humières et al.*, 1986) in which space, time, and particle velocities are discrete. It was developed in order to overcome some deficiencies of LGA (*Zanetti*, 1989). Compared to the classical CFD methods, the fluid state in LBM is described by a particle distribution function where a particle is characterized by a given velocity at a given space point at a given time. The fluid flow is described by the evolution of the distribution function in time and space. The basic Navier-Stokes equation can be derived from the lattice Boltzmann equations (LBE) by using the Chapman-Enskog procedure (*Pazdniakou*, 2012; *Li*, 2010). Up to now, with its relative simplicity, LBM is a powerful numerical tool in large domains of physics and of fluid mechanics.

2.5.1 Local governing equations

As reminded above, the classical methods describe fluid motion by partial differential equations for the fluid density ρ , the pressure p , and the velocity \mathbf{u} . At each point of the fluid domain, if these values are determined, the fluid state is completely described. The real molecular structure

of the fluid is neglected and the fluid is considered as a continuous substance; hence, the fluid is described at the continuum level.

The Navier-Stokes equation is given by

$$\rho \left(\frac{\partial \mathbf{u}}{\partial t} + \mathbf{u} \cdot \nabla \mathbf{u} \right) = -\nabla p + \mu \nabla^2 \mathbf{u} + (\mu + \zeta) \nabla (\nabla \cdot \mathbf{u}) + \rho \mathbf{F} \quad (2.12)$$

where μ is the dynamic viscosity, ζ the volume viscosity and \mathbf{F} the body force. The viscosity is a measure of fluid resistance to flow. The kinematic viscosity ν is equal to $\frac{\mu}{\rho}$.

Usually, the incompressible form of the Navier-Stokes equations is used

$$\rho \left(\frac{\partial \mathbf{u}}{\partial t} + \mathbf{u} \cdot \nabla \mathbf{u} \right) = -\nabla p + \mu \nabla^2 \mathbf{u} + \rho \mathbf{F} \quad (2.13)$$

$$\nabla \cdot \mathbf{u} = 0. \quad (2.14)$$

The no-slip boundary condition is applied at the solid boundary

$$\mathbf{u} = \mathbf{0} \quad (2.15)$$

Equations (2.14), (2.15) form the basis for flow studies. The Navier-Stokes equation has no analytical solution except for some simple cases; therefore, numerical methods are necessary to solve it.

In hydrodynamics, dimensionless quantities are usually used and the Reynold number is one of the most important; it represents the ratio between inertial and viscous forces and characterizes the relative importance of these forces. It is given by

$$Re = \frac{UL}{\nu} \quad (2.16)$$

where L is a characteristic linear size, and U a characteristic fluid velocity. Obviously, a low Re is the result of high viscosity, low velocity and small pores. Therefore, for stationary flows, the Navier-Stokes equation (2.14) is simplified into the Stokes equations

$$0 = -\frac{\nabla p}{\rho} + \nu \nabla^2 \mathbf{u} + \mathbf{F} \quad (2.17a)$$

$$\nabla \cdot \mathbf{u} = 0. \quad (2.17b)$$

As the Navier-Stokes equation (2.14), the Stokes equation (2.17) has a small number of analytical solutions and the geometry of porous media is very complicated; therefore, numerical methods are necessary to solve them.

2.5.2 Lattice Boltzmann Model (LBM)

The basic concept of Boltzmann methods is that the fluid is composed of interacting particles that can be described by classical mechanics. In this description, a statistical treatment is necessary and suitable due to the large number of particles. Then, the fluid state is given by a distribution function in which each particle is characterized by a given velocity at a given space point at a given time.

2.5.2.1 Continuous Boltzmann equation

The continuous Boltzmann equation describes the fluid in terms of a particle distribution function $f(\mathbf{c}, \mathbf{r}, t)$ which is the probability of presence of the particle with velocity \mathbf{c} at point \mathbf{r} at time t . Then, the number of particles present in an elementary volume $d^3\mathbf{r}$ with velocities lying in the range $d^3\mathbf{c}$ at time t is given by $f(\mathbf{c}, \mathbf{r}, t)d^3\mathbf{r}d^3\mathbf{c}$. The particles are submitted to an external force \mathbf{F} per particle mass. The equation for no collision between the particles is given by

$$f(\mathbf{r} + \mathbf{c}dt, \mathbf{c} + \mathbf{F}dt, t + dt)d^3\mathbf{r}d^3\mathbf{c} = f(\mathbf{c}, \mathbf{r}, t)d^3\mathbf{r}d^3\mathbf{c} \quad (2.18)$$

Since the particles undergo collisions, this equation becomes

$$f(\mathbf{r} + \mathbf{c}dt, \mathbf{c} + \mathbf{F}dt, t + dt)d^3\mathbf{r}d^3\mathbf{c} - f(\mathbf{c}, \mathbf{r}, t)d^3\mathbf{r}d^3\mathbf{c} = Q(f, f)d^3\mathbf{r}d^3\mathbf{c}dt \quad (2.19)$$

where $Q(f, f)$ is the collision operator responsible for the changes in the distribution function due to collisions between particles. The Boltzmann equation is derived by expanding the left side ($dt \rightarrow 0$) and dividing (2.14) by $d^3\mathbf{r}d^3\mathbf{c}dt$

$$\frac{\partial f}{\partial t} + \mathbf{c} \cdot \nabla_{\mathbf{r}} f + \mathbf{F} \cdot \nabla_{\mathbf{c}} f = Q(f, f) \quad (2.20)$$

Bhartnagar, Groos and Krook (BGK) devised a simple collision operator $\Omega(f)$ (Bhartnagar

et al., 1954; Pazdaniakou, 2012)

$$\Omega(f) = \frac{1}{\tau}[f(\mathbf{c}, \mathbf{r}, t) - f^{eq}(\mathbf{c}, \mathbf{r}, t)] \quad (2.21)$$

where τ is the relaxation time and $f^{eq}(\mathbf{c}, \mathbf{r}, t)$ the equilibrium distribution. This operator is imprecise. Here, the two-relaxation-time (TRT) collision operator is used. It is expressed as

$$\Omega = \mathbf{A}(f^{eq} - f) \quad (2.22)$$

where \mathbf{A} is the collision matrix with the following form

$$\mathbf{A} = \mathbf{M}^{-1} \cdot \mathbf{S} \cdot \mathbf{M} \quad (2.23)$$

The diagonal matrix \mathbf{S} defines the relaxation rates for different fluid moments and given by

$$\begin{aligned} \mathbf{S} &= \text{diag}(0, s_e, s_\varepsilon, 0, s_q, 0, s_q, 0, s_q, s_\nu, s_\pi, s_\nu, s_\pi, s_\nu, s_\nu, s_\nu, s_m, s_m, s_m), \\ s_e &= s_\varepsilon = s_\pi = s_\nu, \quad s_m = s_q = 8 \frac{2 - s_\nu}{8 - s_\nu} \end{aligned} \quad (2.24)$$

A detailed description of matrix \mathbf{M} and \mathbf{S} is presented by *d'Humières et al.* (2002) and *Ginzburg and d'Humières* (2003). The LBM with relaxation parameters defined by (2.24) is named the two-relaxation-time (TRT) model. According to *Pazdaniakou* (2012), s_ν is generally chosen equal to $\frac{1}{\nu/c_s^2 + 1/2}$.

2.5.2.2 Lattice Boltzmann equation

LBM can be implemented on various types of lattices in 1D, 2D, 3D and 4D spaces with various discrete velocity sets which makes it a versatile instrument for numerical simulations of fluid flows. Here, the D3Q19 configuration in three dimensions is used, as displayed in Fig.2.2.

The corresponding discrete velocity set is composed by 19 vectors

$$\mathbf{c}_i = \begin{cases} (\pm 1, 0, 0)c, (0, \pm 1, 0)c, (0, 0, \pm 1)c, & i = 1, \dots, 6; \\ (\pm 1, \pm 1, 0)c, (\pm 1, 0, \pm 1)c, (0, \pm 1, \pm 1)c, & i = 7, \dots, 18; \\ (0, 0, 0), & i = 19; \end{cases} \quad (2.25)$$

For D3Q19, the following lattice weights are used

$$\omega_i = \begin{cases} \frac{1}{18}, & i = 1, \dots, 6; \\ \frac{1}{36}, & i = 7, \dots, 18; \\ \frac{1}{3}, & i = 19; \end{cases} \quad (2.26)$$

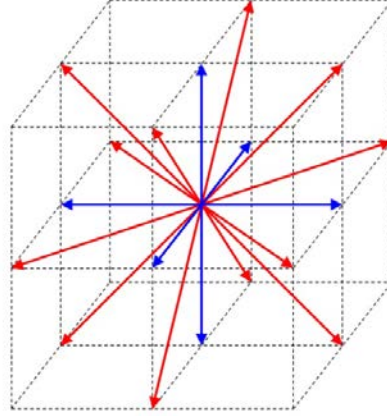


Figure 2.2: Three-dimensional lattices and discrete velocities D3Q19. The lengths of the blue, red discrete velocities vectors are $1c$, $\sqrt{2}c$ and $\sqrt{3}c$, respectively.

with $c_s^2 = \frac{1}{3}c^2$ (Pazdniakou, 2012). The sound speed c_s can be identified with θ

$$c_s = \sqrt{\theta} = \frac{c}{\sqrt{3}} \quad (2.27)$$

where $\theta = \frac{k_B T}{m}$ is the normalized temperature. Sometimes, c_s^2 needs to be an independent parameter (Ginzbourg and Adler, 1991) (for example when working with a multiphase LBM). Then, a new set of lattice weights ω_i^* can be obtained for D3Q19

$$\omega_i^* = \begin{cases} \frac{c_{s^*}^2}{6}, & i = 1, \dots, 6; \\ \frac{c_{s^*}^2}{12}, & i = 7, \dots, 18; \\ 1 - 2c_{s^*}^2, & i = 19; \end{cases} \quad (2.28)$$

where the sound speed c_{s^*} is an independent parameter. Obviously, the classical lattice weights correspond to $c_{s^*} = \frac{1}{\sqrt{3}}$.

2.5.2.3 Equilibrium distribution function

The equilibrium distribution function is an important component of any LBM. (2.15) and (2.21) imply

$$\frac{\partial f}{\partial t} + \mathbf{c} \cdot \nabla_{\mathbf{r}} f + \mathbf{F} \cdot \nabla_{\mathbf{c}} f = \frac{1}{\tau} [f - f^{eq}] \quad (2.29)$$

where \mathbf{F} is the body force and τ the relaxation time. The equilibrium function f^{eq} is given by

$$f^{eq}(\rho, \mathbf{v}) = \frac{\rho}{(2\pi\theta)^{D/2}} \exp\left[-\frac{(\mathbf{c} - \mathbf{v})^2}{2\theta}\right] \quad (2.30)$$

It was found that LBM can be obtained by a proper discretization of the continuous Boltzmann equation (Luo, 2000), a method which is more convenient for theoretical studies of LBM. Usually, the low Mach number expansion of the Maxwellian distribution is used in LBM as an equilibrium particle distribution function

$$f_i^{eq}(\rho, \mathbf{v}) = \rho \omega_i \left[1 + \frac{1}{c_s^2} (\mathbf{c}_i \cdot \mathbf{v}) + \frac{1}{2c_s^4} (\mathbf{c}_i \cdot \mathbf{v})^2 - \frac{1}{2c_s^2} |\mathbf{v}|^2 \right] \quad (2.31)$$

Using this equilibrium distribution function, the Navier-Stokes equation can be derived by the Chapman-Enskog decomposition at the macroscopic level. For the incompressible fluid simulation, the following equilibrium distribution function is used (Pan *et al.*, 2006)

$$f_i^{eq}(\rho, \mathbf{v}) = \omega_i \left[\rho + \rho_0 \left(\frac{1}{c_s^2} (\mathbf{c}_i \cdot \mathbf{v}) + \frac{1}{2c_s^4} (\mathbf{c}_i \cdot \mathbf{v})^2 - \frac{1}{2c_s^2} |\mathbf{v}|^2 \right) \right] \quad (2.32)$$

Since in porous media, the fluid flow is usually characterized by low Re , the Navier-Stokes equation can be replaced by the Stokes equation. In order to simulate Stokes flow by LBM, the nonlinear terms of the equilibrium distribution function are discarded

$$f_i^{eq}(\rho, \mathbf{v}) = \omega_i \rho \left[1 + \frac{1}{c_s^2} (\mathbf{c}_i \cdot \mathbf{v}) \right] \quad (2.33)$$

When the sound speed c_{s*} is an independent parameter, the equilibrium distribution is given by Nie *et al.* (1998)

$$f_i^{eq}(\rho, \mathbf{v}) = \rho \omega_i^* + \rho \omega_i \left[\frac{1}{c_s^2} (\mathbf{c}_i \cdot \mathbf{v}) + \frac{1}{2c_s^4} (\mathbf{c}_i \cdot \mathbf{v})^2 - \frac{1}{2c_s^2} |\mathbf{v}|^2 \right] \quad (2.34)$$

where c_s is the classical sound speed.

2.5.2.4 External force modeling

Various forces can be incorporated in LBM in order to simulate various situations (pressure gradients, gravity forces or force fields of complex structure...). The most usual way is to incorporate a body force in LBM (Luo, 2000)

$$F_i = -\omega_i \rho \left[\frac{\mathbf{c}_i - \mathbf{v}}{c_s^2} + \frac{\mathbf{c}_i \cdot \mathbf{v}}{c_s^4} \mathbf{c}_i \right] \cdot \mathbf{F} \quad (2.35)$$

which obeys the conditions

$$\sum_{i=1}^q F_i = 0 \quad (2.36a)$$

$$\sum_{i=1}^q \mathbf{c}_i F_i = -\rho \mathbf{F} \quad (2.36b)$$

$$\sum_{i=1}^q c_{i,\alpha} c_{i,\beta} F_i = -\rho [u_\alpha F_\beta + u_\beta F_\alpha], \quad (2.36c)$$

where the indices α, β denote the space coordinates. This term is used when the body force \mathbf{F} is not constant in space in order to preserve the Galilean invariance. *Luo* (2000) replaced (2.36c) by

$$\sum_{i=1}^q c_{i,\alpha} c_{i,\beta} F_i = 0, \quad (2.37)$$

The usual body force term is obtained for constant body force fields (like gravity)

$$F_i = -\omega_i \rho \frac{\mathbf{c}_i \cdot \mathbf{F}}{c_s^2} \quad (2.38)$$

When the redefined lattice weights ω_i^* are used, the body force term becomes

$$F_i = -\omega_i^* \rho \mathbf{c}_i \cdot \mathbf{F} \quad (2.39)$$

2.5.2.5 Chapman-Enskog analysis

The Chapman-Enskog analysis is applied to LBM in order to derive the macroscopic equation governing fluid flow. In most cases, we wish to obtain the continuity and the Navier-Stokes equations at the macroscopic level. It must be also noted that when working with LBM, some additional terms can be included in the traditional LBM in order to obtain a model with some special physical characteristics. These operations performed with Lattice Boltzmann equations necessitate a Chapman-Enskog procedure which can be applied to the BGK model and is presented by *Pazdaniakou* (2012). This analysis starts from the expansion of LBM components in terms of a small parameter η which is equal to δ_t (*Luo*, 2000) in the following. In terms of this small parameter, the particle distribution function and the time derivative operator are expanded as

$$f_i(\mathbf{r}, t) = \sum_{n=0}^{\infty} \eta^n f_i^{(n)}(\mathbf{r}, t) \quad (2.40a)$$

$$\partial_t = \sum_{n=0}^{\infty} \eta^n \partial_{t_n} \quad (2.40b)$$

For the Chapman-Enskog analysis, only the truncated parts of these expansions are necessary. The particle distribution function at point $(\mathbf{r} + \mathbf{c}_i \delta t, t + \delta t)$ is expanded into a Taylor series

$$f_i(\mathbf{r} + \mathbf{c}_i \delta t, t + \delta t) = \sum_{n=0}^{\infty} \delta t^n (\partial_t + \mathbf{c}_i \cdot \nabla)^{(n)} f_i(\mathbf{r}, t) \quad (2.41)$$

and the second order truncation of this expansion is used.

2.5.2.6 Bounce-back boundary conditions

The computational domain is usually represented by a unit cell which is often a cube of side $N_c a$. The behaviour of the distribution function on the solid-fluid interface must be properly defined. The bounce-back boundary condition is the oldest and most popular solid-fluid boundary condition used in LBM (*Ginzbourg and Adler, 1991*) and it was already used in LGA.

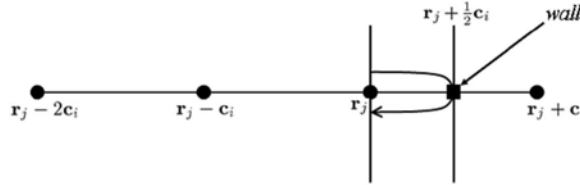


Figure 2.3: Bounce-back boundary conditions (*Pazdniakou, 2012*).

It is based on the principle that the post-collision particle distribution $f'_i(\mathbf{r}_j, t)$ leaving the boundary fluid point \mathbf{r}_j in the direction \mathbf{c}_i of the solid point $\mathbf{r}_i + \mathbf{c}_i$ at time t is returned back at time $t + 1$ with the opposite velocity $\mathbf{c}_i = \mathbf{c}_i'$ (see Fig. 2.3). This corresponds to a solid wall located at the middle of the two lattice points

$$f'_i(\mathbf{r}_j, t + 1) = f'_i(\mathbf{r}_j, t) \quad (2.42)$$

The bounce back condition conserves the local fluid mass and needs no additional information to calculate the unknown distribution function; it can be easily programmed and does not consume a lot of computer resources. Generally, if no additional effort is made, the bounce back

rule is first order accurate in space. The drawback of this condition is that the real position of the solid wall depends on the fluid viscosity (for the LBM with a BGK collision operator).

2.5.2.7 Implementation of the calculation

The bounce back boundary conditions are applied in the LBM program. The algorithm is divided into the collision and propagation steps which must be repeated at each lattice point during the simulation (Fig.2.4). The simulation is stopped when the steady state is reached. The convergence of LBM for Stokes and Navier-Stokes flows in periodic domains is proved theoretically by *Junk and Yang* (2009). In fact, the calculation program can be parallelized in order to speed up the calculation time. This has an important influence on the scalability since the fractional time spent in non-parallelized regions increased when increasing the number of processors (Amdahl's law). For the LBM code, an average speedup $S(8) \approx 6.5$ is obtained for 8 processors and it is considered as a good result.

2.5.3 Absolute permeability

Permeability is one of the most important properties of porous media. It describes the easiness of fluid flow through the porous medium. Darcy's law can be written as

$$\bar{\mathbf{v}} = -\frac{K}{\mu} \Delta p \quad (2.43)$$

where K is the permeability, μ the dynamic viscosity and $\bar{\mathbf{v}}$ the seepage velocity.

The permeability is necessary to study flows through saturated porous media (*Malinouskaya*, 2007). It can be calculated by various numerical methods. The Lattice Boltzmann Model was implemented by *Pazdniakou* (2012). The validation was done for the Poiseuille flow and presented by *Adler* (1992) and *Pazdniakou* (2012).

Since calculations are done for spatially periodic conditions, it is critical to ensure connection between two opposite faces. It guarantees the continuation of flows and there is no artificial loss of permeability due to the mismatch between the inlet and outlet as shown in Figure 2.5a. Therefore, depending on the sample geometry, the sample and its mirror image along the corre-

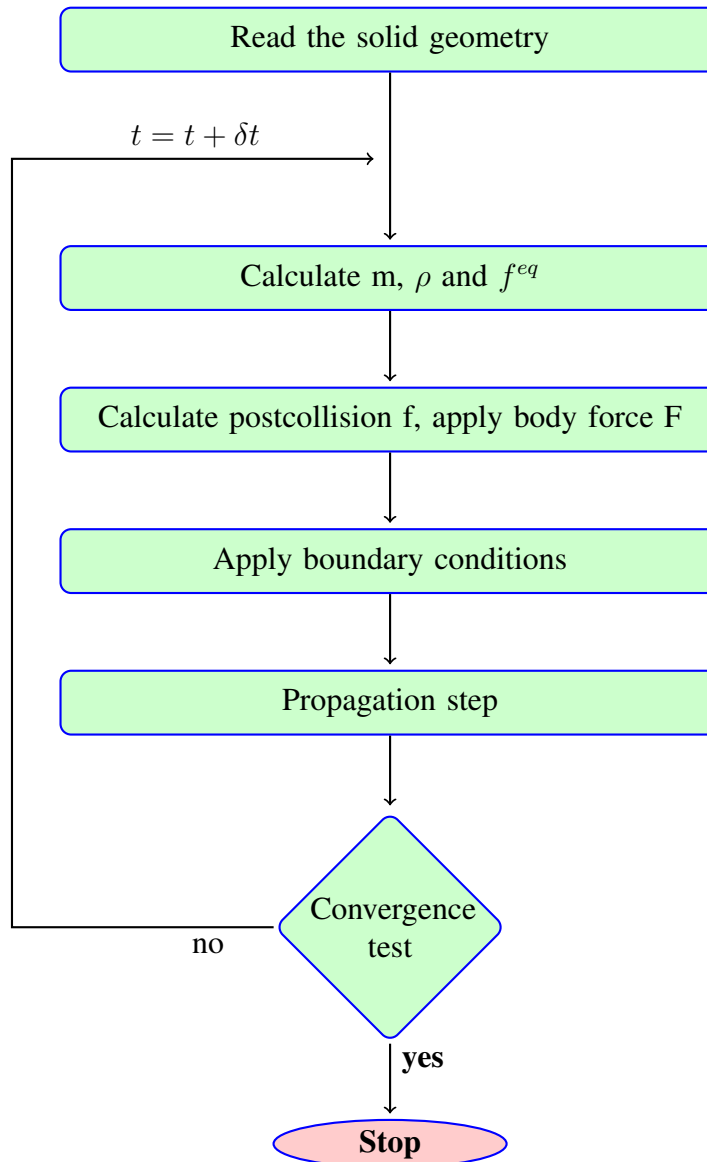


Figure 2.4: The LBM program flowchart.

sponding axis are used for simulation. If the medium is spatially periodic, we use it; otherwise, the mirror image is used (Figure 2.5b-c).

2.5.4 Dynamic permeability

Oscillating flows in porous media are of interest in various areas of Physics and industries and they are necessary in order to determine the acoustic velocities in saturated samples (*Malinouskaya*, 2007; *Li*, 2010; *Pazdniakou*, 2012).

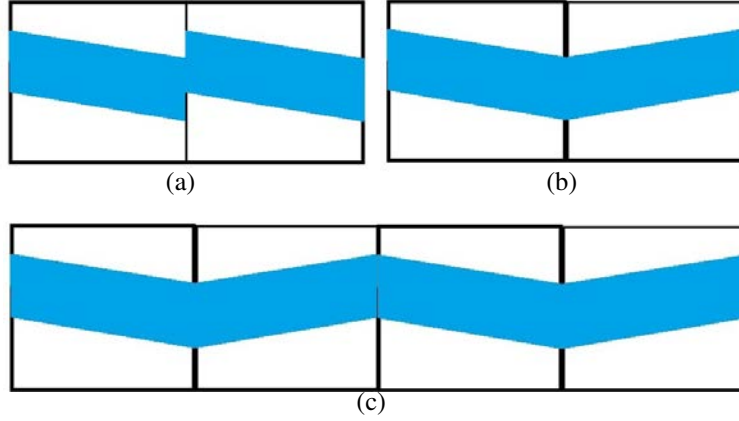


Figure 2.5: The mirror configurations. a. Calculation with the original configuration. b. The corresponding mirror configuration. c. The continuation of flows.

Biot (1956a) defined the dynamic permeability tensor $\mathbf{K}(\omega)$ as a complex valued tensor which depends on the frequency ω . The dynamic Darcy's law characterizing the oscillating flows is given by

$$\bar{\mathbf{v}} = -\frac{\rho}{\mu} \mathbf{K}(\omega) \cdot \mathbf{F} \quad (2.44)$$

where $\rho \mathbf{F}$ is equivalent to a macroscopic pressure gradient $\overline{\Delta P}$. For isotropic media, it becomes $K(\omega) \mathbf{I}$ where \mathbf{I} is the unit tensor and $K(\omega)$ a complex number which can be expressed as

$$K(\omega) = K_r(\omega) + iK_i(\omega) \quad (2.45)$$

Similarly to the absolute permeability, the dynamic permeability can be calculated by LBM. The calculation for a spatially periodic porous medium is as follows. An oscillating flow inside the unit cell is induced by an oscillating body force which is given by

$$\mathbf{F} = \mathbf{e} F \cos(\omega t) \quad (2.46)$$

where \mathbf{e} is one of the three unit basis vectors (x, y, z), and F the force amplitude. To calculate the dynamic permeability along the x -direction, \mathbf{e} is set equal to $(1, 0, 0)$. Then, with LBM, we can obtain the time dependent seepage fluid velocity \bar{v}_x which can be expressed as

$$\bar{v}_x = A \cos(\omega t + B) \quad (2.47)$$

where A is the seepage fluid velocity amplitude and B the phase shift. The simulation is automatically stopped when the relative difference between two successive amplitudes A measured when

\bar{v}_x is maximum, is less than a chosen value. Then, A and B can be found by using the least square fit method applied to the last period as in Figure 2.6.

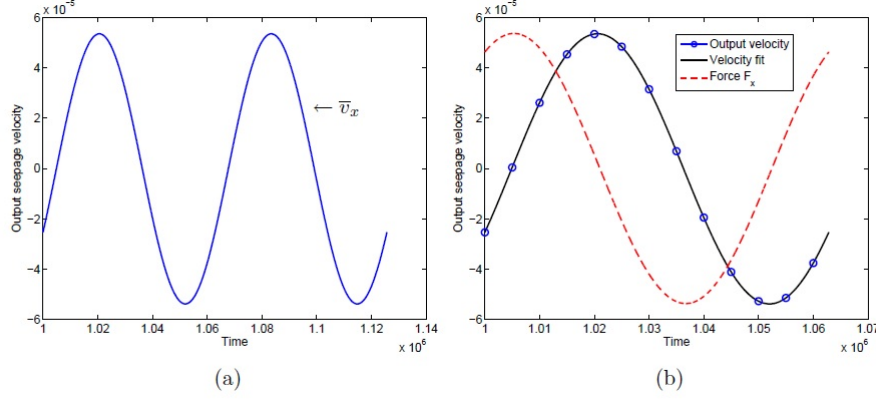


Figure 2.6: (a) The output seepage velocity \bar{v}_x as a function of time. When the difference between two successive amplitudes A measured is less than a specified value, the simulation is automatically stopped. (b) The least square fit method is applied to the last simulated period to approximate the seepage velocity (the blue solid line) by the function $A\cos(\omega t + B)$ (the black line). The red line is the body force F_x ; it shows the phase shift with \bar{v}_x .

Finally, the real and imaginary parts of the dynamic permeability are derived by solving the system (2.48).

$$K_r^2 + K_i^2 = \left(\frac{A\nu}{F}\right)^2 \quad ; \quad K_i = \tan(B)K_r \quad (2.48)$$

where ν is the kinematic viscosity. Hence, we have

$$K_r = \frac{A\nu}{F} \cos(B) \quad ; \quad K_i = \frac{A\nu}{F} \sin(B) \quad (2.49)$$

Since the parameters A and B are calculated numerically with LBM, the real and imaginary parts of the dynamic permeability can be derived from (2.49). The same procedure can be applied in order to calculate the other components of $\mathbf{K}(\omega)$ by choosing another value of ε_α .

The dynamic permeability is calculated by the program based on LBM and written in Fortran 90. The comparison between simulations by this program and analytical results of Poiseuille flow is used to validate the LBM (Pazdniakou, 2012). In the same way, the program is parallelized with OMP to decrease the simulation time. However, the calculation of dynamic permeability is much more cumbersome than of absolute permeability since it depends on the frequency ω . It is shown

in Section 4.4 that the memory requirements and the time depend on the frequency and are often larger than the ones for absolute permeability.

2.5.5 The dynamic permeability and the length Λ

The real part of dynamic permeability characterizes the flow due to the viscous forces and is a decreasing function of frequency; the imaginary part characterizes the phase shift due to fluid inertia and has a maximum. According to *Pazdaniakou and Adler (2013)*, this maximum corresponds to the transition from the viscous flow to the inertia flow regime and obtained for the frequency value ω_c . Then, the viscous penetration depth δ becomes the order of the pore size l_{pore}

$$l_{pore} = \frac{\Omega}{S} \sim \sqrt{\frac{2\mu}{\rho\omega_c}} \quad (2.50)$$

Zhou and Sheng (1989) pointed out that the dynamic permeability can be considered as a scaling function with only two parameters for various porous media and does not depend on their micro structure. It is expressed as

$$K(\omega) \simeq K_0 f\left(\frac{\omega}{\omega_c}\right) \quad (2.51)$$

where K_0 is the absolute permeability; ω_c is defined by

$$\omega_c = \frac{\mu\varepsilon}{\rho\tau K_0} \quad (2.52)$$

A more detailed form of (2.51) is also presented by *Zhou and Sheng (1989)*

$$K'(\omega'_c) = \begin{cases} 1 + iF_1^{-1}\omega'_c & \omega'_c \rightarrow 0, \\ \sqrt{2}F_2^{-1}(\omega'_c)^{-3/2} + i(\omega'_c)^{-1}, & \omega'_c \rightarrow \infty \end{cases} \quad (2.53)$$

The dimensionless dynamic permeability K' , frequency ω'_c and F_1, F_2 are defined as

$$K' = \frac{K}{K_0}, \quad \omega'_c = \frac{\omega}{\omega_c}, \quad F_1 = \frac{\tau K_0^2}{C_1 \varepsilon}, \quad F_2 = \left(\frac{\Lambda^2 \varepsilon}{\tau K_0}\right)^{1/2} \quad (2.54)$$

where τ is the tortuosity factor, Λ the length scale in Section 2.4, C_1 a coefficient homogeneous to the fourth power of a length (see (*Zhou and Sheng, 1989*)).

As indicated before, this scaling function is independent of the micro structure of porous media; therefore, it can be used in order to evaluate the dynamic permeability obtained by various

methods. For this purpose, the Poiseuille flow is used; the configuration is simple: a fluid oscillates in the channel limited by the solid planes $y = 0$ and h . The analytical solution of the dynamic permeability is deduced from the Darcy law

$$K = \frac{\nu}{\omega^2} \left[-i\omega + \frac{2\sqrt{i\omega\nu}}{h} \tanh\left(\sqrt{\frac{i\omega h}{\nu}}\right) \right] \quad (2.55)$$

Since the length scale Λ and the tortuosity of porous media are derived by solving the Laplace equation (2.7), the dimensionless dynamic permeability $K'(\omega'_c)$ can be also derived. *Pazdniakou* (2012) presented a comparison between the $K'(\omega'_c)$ of various porous media and the Poiseuille flow in order to verify the scaling behaviour. As it can be seen in Fig. 2.7, all the results do not depend on the structure of media and are close to the curve corresponding to the Poiseuille flow. Obviously, this is useful to evaluate the dynamic permeability which is obtained by simulation by LBM.

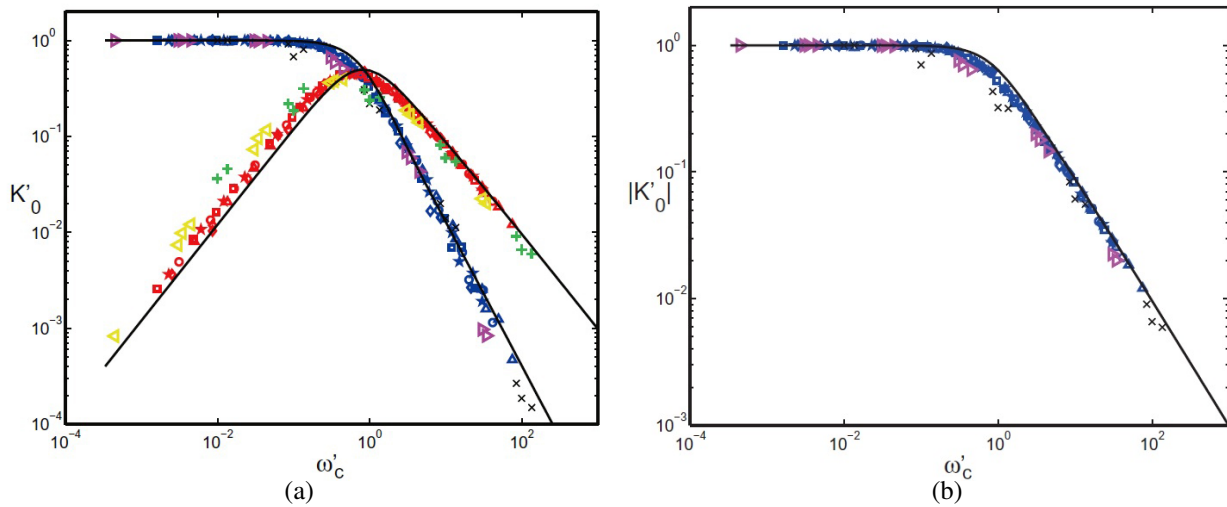


Figure 2.7: Universal scaling behaviour of the dynamic permeability. (a) The real and imaginary part of dimensionless dynamic permeability $K'(\omega'_c)$. (b) The absolute value $|K'(\omega'_c)|$. Data are for: numerical (points), Poiseuille (black solid line).

2.6 Propagation of acoustic waves in dry porous media

As indicated, propagation of acoustic waves in porous media is important in fundamental and in applied studies. This section presents the general determination of wave propagation in dry porous media by solving the fundamental dynamic equation at a microscopic level.

The velocity of plane acoustic waves can be determined by solving the so-called Christoffel equation (*Malinouskaya, 2007; Li, 2010*). Two types of waves can propagate through an isotropic and homogeneous material, namely the compressional and shear waves. In heterogeneous media such as porous media, two situations can be considered, $\lambda \sim l$ and $\lambda \gg l$. *Malinouskaya (2007)* considered the second situation where the medium is approximated by an equivalent homogeneous material. Therefore, it is possible to use the homogenisation method in order to determine the macroscopic properties by solving the equations at the microscopic level (*Sanchez, 1980*).

In this thesis, the acoustic waves velocity is derived by using the Lattice Spring Model (LSM) and the Lattice Spring Model for two solids (LSM2S) presented in Chapter 3.

2.6.1 Elastic waves in elastic media

The dynamical behaviour of an homogeneous elastic medium is governed by

$$\rho_s \frac{\partial^2 \mathbf{u}}{\partial t^2} = \nabla \cdot \boldsymbol{\sigma} \quad (2.56)$$

where ρ is the density, $\boldsymbol{\sigma}$ the stress tensor, \mathbf{u} the microscale displacement and t the time. The boundary condition is expressed as

$$\boldsymbol{\sigma} \cdot \mathbf{n} = 0 \quad \text{on} \quad \Gamma \quad (2.57)$$

where Γ is a free boundary, \mathbf{n} the unit normal to Γ . For elastic materials, the relation between the stress tensor and the strain tensor \mathbf{e} is expressed as

$$\boldsymbol{\sigma} = \mathbf{C}_{\{4\}} : \mathbf{e} \quad (2.58)$$

where $\mathbf{C}_{\{4\}}$ is the stiffness tensor. The strain tensor \mathbf{e} is given by

$$\mathbf{e} = \frac{\nabla \mathbf{u} + (\nabla \mathbf{u})^t}{2} \quad (2.59)$$

The subscript $\{4\}$ denotes the order of the tensor. At most, $\mathbf{C}_{\{4\}}$ has 21 independent components; this number can be decreased to 9 or 3 depending on the symmetries of the samples.

Plane harmonic waves are considered with a solid displacement \mathbf{u} of the form

$$\mathbf{u} = A \tilde{\mathbf{u}} e^{i(\omega t - \kappa \mathbf{p} \cdot \mathbf{x})} \quad (2.60)$$

where A is the wave amplitude, $\tilde{\mathbf{u}}$ the unit polarisation vector, ω the frequency, κ the wave number, \mathbf{p} the direction of propagation unit vector, and \mathbf{x} the position. The equations (2.56) and (2.60) yield the Christoffel equation (also called the dispersion equation) (Malinetskaya, 2007)

$$[\rho_s \omega^2 \mathbf{I} - \kappa^2 [\mathbf{p} \cdot \mathbf{C} \cdot \mathbf{p}]] \cdot \tilde{\mathbf{u}} = 0 \quad (2.61)$$

Since the Christoffel equation is homogeneous, the solution $\tilde{\mathbf{u}}$ is not trivial if and only if the determinant is zero

$$\det [\rho_s \omega^2 \mathbf{I} - \kappa^2 [\mathbf{p} \cdot \mathbf{C} \cdot \mathbf{p}]] = 0 \quad (2.62)$$

The wave celerities can be derived from equation (2.62)

$$c_{phase} = \frac{\omega}{\kappa} \quad (2.63)$$

2.6.2 Elastic waves in porous media

The considered porous media are supposed to be statistically homogeneous and they are represented by a unit cell which is periodically replicated in space. When $\lambda \gg l$, the elastic properties of porous media are given by the effective stiffness tensor $\mathbf{C}^{(eff)}$. Then, the elasticity equation and the Christoffel equation become

$$\rho_s \frac{\partial^2 \mathbf{u}}{\partial t^2} = \nabla \cdot \boldsymbol{\sigma} = \nabla \cdot \mathbf{C}^{(eff)} : \boldsymbol{\varepsilon} \quad (2.64a)$$

$$[\rho_s \omega^2 \mathbf{I} - \kappa^2 [\mathbf{p} \cdot \mathbf{C}^{(eff)} \cdot \mathbf{p}]] \cdot \tilde{\mathbf{u}} = 0 \quad (2.64b)$$

Condition (2.62) yields the wave celerities. If the homogeneous medium has a cubic symmetry, the P-wave (compressional wave) and S-wave (shear wave) velocities are

$$v_p = \sqrt{\frac{C_{xxxx}^{(eff)}}{\bar{\rho}}}; \quad v_s = \sqrt{\frac{C_{yzyz}^{(eff)}}{\bar{\rho}}} \quad (2.65)$$

where $\bar{\rho}$ is the average density of the unit cell

$$\bar{\rho} = \frac{1}{V} \int_V \rho dV = (1 - \varepsilon) \rho \quad (2.66)$$

2.7 Propagation of acoustic waves in saturated porous media

As presented in Section 2.2, the homogenization method developed by *Malinouskaya* (2007) and *Li* (2010) associated with lattice models of *Pazdniakou* (2012) is used in this thesis in order to derive acoustic velocities in porous media with a single pore or multi-pores saturated by incompressible or compressible fluids.

2.7.1 Homogenization method

In this section, the theoretical basis of the homogenization method is summarized. This method was used by *Malinouskaya* (2007) and *Li* (2010).

The porous medium contains heterogeneities whose size l is supposed to be much smaller than the overall size of the medium \mathbb{L} . The medium is assumed to be statistically homogeneous on some intermediate scale between l and \mathbb{L} ; therefore, it can be regarded as spatially periodic, i.e., it is composed of replicated unit cells Ω of size L . Since the pore space is filled by a Newtonian fluid, the unit cell Ω is given by

$$\Omega = \Omega_s \cup \Omega_f \quad (2.67)$$

where Ω_s is the solid phase and Ω_f the fluid phase. Ω_s is composed by an isotropic elastic material; Ω_f is composed of a single or some disconnected pores (*Pazdniakou*, 2012). The Newtonian fluid is compressible (*Li*, 2010) or incompressible (*Malinouskaya*, 2007). The calculation of a single pore is detailed in this section; then, the corresponding results of multiple pores are presented.

2.7.1.1 Basic equations

We consider the propagation of an harmonic wave of pulsation ω and wave length λ such that

$$l \ll \Upsilon = \frac{\lambda}{2\pi} \quad (2.68)$$

where Λ is the macroscopic scale.

The separation between microscale l and macroscale Υ allows us to use the homogenization

theory. The small parameter η is defined as

$$\eta = \frac{l}{\Upsilon} \ll 1 \quad (2.69)$$

Two spatial variables \mathbf{x} and \mathbf{y} are introduced; \mathbf{x} is macroscopic (of order Υ) while \mathbf{y} is microscopic (of order l). They are related to one another by

$$\mathbf{y} = \eta^{-1} \mathbf{x} \quad (2.70)$$

Therefore, the spatial gradient operator can be expressed as

$$\nabla = \nabla_x + \eta^{-1} \nabla_y \quad (2.71)$$

The wave propagation is governed on the microscopic level by the elastic equation

$$\nabla \cdot \boldsymbol{\sigma}_s = -\rho_s \omega^2 \mathbf{u}_s \quad \text{in} \quad \Omega_s \quad (2.72)$$

where ρ_s is the solid density, \mathbf{u}_s the solid displacement. For an harmonic wave, the displacement \mathbf{u}_s is of the form

$$\mathbf{u} = \hat{\mathbf{u}} e^{i\omega t} \quad (2.73)$$

The fluid is supposed to be Newtonian and incompressible. The Navier-Stokes equation can be rewritten as

$$\begin{aligned} i\omega \rho_f \mathbf{v}_f &= \nabla \cdot \boldsymbol{\sigma}_f \\ \nabla \cdot \mathbf{v}_f &= 0 \end{aligned} \quad (2.74)$$

where ρ_f is the fluid density, \mathbf{v}_f the fluid velocity.

At the solid-fluid interface, the no-slip boundary condition with the continuity of displacement and normal stress is given by

$$\begin{aligned} \mathbf{u}_s &= \mathbf{u}_f & \text{on} & \Gamma \\ \boldsymbol{\sigma}_s \cdot \mathbf{n} &= \boldsymbol{\sigma}_f \cdot \mathbf{n} & \text{on} & \Gamma \end{aligned} \quad (2.75)$$

where \mathbf{n} is the unit normal to the solid-fluid interface $\Gamma = \Omega_s \cap \Omega_f$.

Hereafter, all quantities related to solid and fluid are denoted by the indices s and f , respectively.

2.7.1.2 Double scale expansion

The medium is assumed to be spatially periodic as described above. *Malinouskaya* (2007) pointed out that any function of space can be represented as a function of two spatial variables $\mathbf{f}(\mathbf{x}, \mathbf{y})$. It can be expanded as a series in terms of the small parameter η as

$$\mathbf{f}(\mathbf{x}, \mathbf{y}) = \sum \eta^j \mathbf{f}^{(j)}(\mathbf{x}, \mathbf{y}) \quad (2.76)$$

Because of the spatial periodicity of the medium, $\mathbf{f}(\mathbf{x}, \mathbf{y})$ and also $\mathbf{f}^{(j)}(\mathbf{x}, \mathbf{y})$ are periodic functions of \mathbf{y} . Then, this expansion can be applied to the solid and fluid displacements \mathbf{u}_s and \mathbf{u}_p and to the fluid pressure p

$$\mathbf{u}_s(\mathbf{x}, \mathbf{y}, t) = \sum \eta^j \mathbf{u}_s^{(j)}(\mathbf{x}, \mathbf{y}, t) \quad (2.77a)$$

$$\mathbf{u}_f(\mathbf{x}, \mathbf{y}, t) = \sum \eta^j \mathbf{u}_f^{(j)}(\mathbf{x}, \mathbf{y}, t) \quad (2.77b)$$

$$p(\mathbf{x}, \mathbf{y}, t) = \sum \eta^j p^{(j)}(\mathbf{x}, \mathbf{y}, t) \quad (2.77c)$$

The strain tensor \mathbf{e} and the stress tensor $\boldsymbol{\sigma}_s$ can be expanded by substitution of (2.77.a) into equation (2.72). A series of equations for the solid phase for each order of the small parameter η is obtained

$$\begin{aligned} \eta^{-2} : \quad & \nabla_{\mathbf{y}} \cdot \boldsymbol{\sigma}_s^{(-1)} = 0 \\ \eta^{-1} : \quad & \nabla_{\mathbf{y}} \cdot \boldsymbol{\sigma}_s^{(0)} + \nabla_{\mathbf{x}} \cdot \boldsymbol{\sigma}_s^{(-1)} = 0 \\ \eta^0 : \quad & \nabla_{\mathbf{y}} \cdot \boldsymbol{\sigma}_s^{(1)} + \nabla_{\mathbf{x}} \cdot \boldsymbol{\sigma}_s^{(0)} = -\rho_s \omega^2 \mathbf{u}_s^{(0)} \\ \eta^j : \quad & \nabla_{\mathbf{y}} \cdot \boldsymbol{\sigma}_s^{(j+1)} + \nabla_{\mathbf{x}} \cdot \boldsymbol{\sigma}_s^{(j)} = -\rho_s \omega^2 \mathbf{u}_s^{(j)} \end{aligned} \quad (2.78)$$

The local description of the fluid velocity and stress tensor are expanded as

$$\mathbf{v}_f(\mathbf{x}, \mathbf{y}, t) = \sum \eta^j \mathbf{v}_f^{(j)}(\mathbf{x}, \mathbf{y}, t) \quad (2.79a)$$

$$\boldsymbol{\sigma}_f(\mathbf{x}, \mathbf{y}, t) = \sum \eta^j \boldsymbol{\sigma}_f^{(j)}(\mathbf{x}, \mathbf{y}, t) \quad (2.79b)$$

with $\mathbf{v}_f^{(j)} = i\omega \mathbf{u}_f^{(j)}$; $\mathbf{v}_f^{(j)}$ is periodic.

Substitution of the expansion (2.79) into equation (2.74) yields a series of equations for the fluid phase similar to that for the solid one for each order of the small parameter η

$$\begin{aligned} \eta^{-2} : \quad & \nabla_y \cdot \boldsymbol{\sigma}_f^{(-1)} = 0 \\ \eta^{-1} : \quad & \nabla_y \cdot \boldsymbol{\sigma}_f^{(0)} + \nabla_x \cdot \boldsymbol{\sigma}_f^{(-1)} = 0 \\ \eta^0 : \quad & \nabla_y \cdot \boldsymbol{\sigma}_f^{(1)} + \nabla_x \cdot \boldsymbol{\sigma}_f^{(0)} = -\rho_f i\omega \mathbf{v}_f^{(0)} \\ \eta^j : \quad & \nabla_y \cdot \boldsymbol{\sigma}_f^{(j+1)} + \nabla_x \cdot \boldsymbol{\sigma}_f^{(j)} = -\rho_f i\omega \mathbf{v}_f^{(j)} \end{aligned} \quad (2.80)$$

$$\begin{aligned} \nabla_y \cdot \mathbf{v}_f^{(0)} &= 0 \\ \nabla_y \cdot \mathbf{v}_f^{(j+1)} + \nabla_x \cdot \mathbf{v}_f^{(j)} &= 0, \quad j = 1, 2, 3, \dots \end{aligned} \quad (2.81)$$

Similarly, the boundary conditions for each order of η at the solid-fluid interfaces are

$$\begin{aligned} \mathbf{u}_s^{(j)} &= \mathbf{u}_f^{(j)} \quad \text{on } \Gamma \\ \boldsymbol{\sigma}_s^{(j)} \cdot \mathbf{n} &= \boldsymbol{\sigma}_f^{(j)} \cdot \mathbf{n} \quad \text{on } \Gamma \end{aligned} \quad (2.82)$$

According to *Malinetskaya* (2007), the precise local description of the wave propagation depends on its mode. *Boutin and Auriault* (1990) found out three macroscopical behaviours depending on the various orders ($O(\eta^{(0)})$, $O(\eta^{(1)})$, $O(\eta^{(2)})$) of the transient Reynolds number defined by

$$R_T = \frac{\rho_f \omega l^2}{\mu_f} \quad (2.83)$$

where μ_f is the dynamic viscosity of fluid and l the characteristic microscale length. These three kinds are associated with a biphasic macroscopic behaviour, an elastic macroscopic behaviour and a viscoelastic macroscopic behaviour, respectively. They are also related to the contrast between the mechanical properties \mathbf{C} of the solid and the ones of the fluid $\frac{\omega \mu}{|\mathbf{C}|}$.

The order $O(\eta^{(0)})$ of the Reynold number corresponds to the order $O(\eta^{(2)})$ of this contrast, this corresponds to the biphasic mode where the relative solid-fluid motion is not zero. In *Malinetskaya* (2007), the fluid stress tensor is of the form

$$\boldsymbol{\sigma}_f = -Ip + \eta^2 \mu_f (\nabla \mathbf{v}_f + (\nabla \mathbf{v}_f)^T) \quad (2.84)$$

Substitution of the expansions of $\boldsymbol{\sigma}_f$, p and \mathbf{v}_f into (2.84) yields the expansion of the fluid stress tensor as

$$\begin{aligned}\boldsymbol{\sigma}_f^{(-1)} &= 0 \\ \boldsymbol{\sigma}_f^{(0)} &= -\mathbf{I}p^{(0)} \\ \boldsymbol{\sigma}_f^{(1)} &= -\mathbf{I}p^{(1)} + \mu_f[\nabla_y \mathbf{v}_f^{(0)} + (\nabla_y \mathbf{v}_f^{(0)})^T] \\ \boldsymbol{\sigma}_f^{(j)} &= -\mathbf{I}p^{(j)} + \mu_f[\nabla_y \mathbf{v}_f^{(j-1)} + (\nabla_y \mathbf{v}_f^{(j-1)})^T] + \mu_f[\nabla_x \mathbf{v}_f^{(j-2)} + (\nabla_x \mathbf{v}_f^{(j-2)})^T]\end{aligned}\quad (2.85)$$

From equations (2.78), (2.81), (2.86), a series of microscopic equations for orders of η is obtained

$$\begin{aligned}\eta^{-2} : \quad & \nabla_y \cdot \mathbf{C} : \mathbf{e}(\mathbf{u}_s^{(0)}) = 0 \quad \text{in } \Omega_s \\ & \{\mathbf{C} : \mathbf{e}(\mathbf{u}_s^{(0)})\} \cdot \mathbf{n} = 0 \quad \text{in } \Gamma \\ \\ \eta^{-1} : \quad & \nabla_y \cdot \mathbf{C} : [\mathbf{e}(\mathbf{u}_s^{(1)}) + \mathbf{E}(\mathbf{u}_s^{(0)})] + \nabla_x \cdot \mathbf{C} : \mathbf{e}(\mathbf{u}_s^{(0)}) = 0 \quad \text{in } \Omega_s \\ & -\nabla_y p^{(0)} = 0 \quad \text{in } \Omega_f \\ & \{\mathbf{C} : [\mathbf{e}(\mathbf{u}_s^{(1)}) + \mathbf{E}(\mathbf{u}_s^{(0)})] + \mathbf{I}p^{(0)}\} \cdot \mathbf{n} = 0 \quad \text{on } \Gamma \\ \\ \eta^0 : \quad & \nabla_y \cdot \mathbf{C} : [\mathbf{e}(\mathbf{u}_s^{(2)}) + \mathbf{E}(\mathbf{u}_s^{(1)})] + \nabla_x \cdot \mathbf{C} : [\mathbf{e}(\mathbf{u}_s^{(1)}) + \mathbf{E}(\mathbf{u}_s^{(0)})] = -\rho_s \omega^2 \mathbf{u}_s^{(0)} \quad \text{in } \Omega_s \\ & -\nabla_y p^{(1)} + \nabla_y \cdot [\mu_f(\nabla_y \mathbf{v}_f^{(0)} + (\nabla_y \mathbf{v}_f^{(0)})^T)] - \nabla_x p^{(0)} = i p_f \omega \mathbf{v}_f^{(0)} \quad \text{in } \Omega_f \\ & \mathbf{u}_s^{(0)} = \mathbf{u}_f^{(0)} \quad \text{on } \Gamma \\ & \{\mathbf{C} : [\mathbf{e}(\mathbf{u}_s^{(2)}) + \mathbf{E}(\mathbf{u}_s^{(1)})] + \mathbf{I}p^{(1)} - [\mu_f(\nabla_y \mathbf{v}_f^{(0)} + (\nabla_y \mathbf{v}_f^{(0)})^T)]\} \cdot \mathbf{n} = 0 \quad \text{on } \Gamma\end{aligned}\quad (2.86)$$

Then, these microscopic equations are integrated over Ω_s and Ω_f for the solid and fluid phases as in *Malinouskaya (2007)*. Hence, the equations of acoustic wave propagation in a porous medium saturated at the macroscopic scale can be expressed as

$$\nabla_x \cdot \mathbf{C}^{eff} : \mathbf{E}(\mathbf{U}_s^{(0)}) + \nabla_x \cdot \boldsymbol{\alpha} p^{(0)} = -\langle \rho \rangle \omega^2 \mathbf{U}_s^{(0)} - \rho_f \omega^2 \langle \mathbf{W} \rangle \quad (2.87a)$$

$$i\omega \langle \mathbf{W} \rangle = \frac{1}{\mu} \mathbf{K} \cdot (-\nabla_x p^{(0)} + \rho_f \omega^2 \mathbf{U}_s^{(0)}) \quad (2.87b)$$

$$\nabla_x \langle \mathbf{W} \rangle = \beta p^{(0)} - \boldsymbol{\alpha} : \mathbf{E}(\mathbf{U}_s^{(0)}) \quad (2.87c)$$

where \mathbf{C}^{eff} is the effective stiffness tensor, $\mathbf{E}(\mathbf{U}_s^{(0)})$ the imposed macroscopic deformation, $\mathbf{U}_s^{(0)}$ the macroscopic solid displacement, α and β the coefficients describing the reaction of the solid matrix to the fluid pressure, $p^{(0)}$ the macroscopic fluid pressure and \mathbf{K} the dynamic permeability (Pazdaniakou, 2012). Since $\mathbf{U}_s^{(0)}$ is a constant over the unit cell, the relative fluid displacement is given by

$$\mathbf{W} = \mathbf{u}_f^{(0)} - \mathbf{U}_s^{(0)} \quad (2.88)$$

It is important to note that \mathbf{W} is an Ω periodic function and it is not zero since the fluid displacement $\mathbf{u}_f^{(0)}$ is different from $\mathbf{U}_s^{(0)}$.

2.7.1.3 Macroscopic descriptions

At the macroscopic level, the subscripts $x, s, {}^{(0)}$ and the symbol $\langle \rangle$ of \mathbf{W} can be skipped in equation (2.87). One has the equations

$$\nabla \cdot \mathbf{C}^{\text{eff}} : \mathbf{E}(\mathbf{U}) + \nabla \cdot \boldsymbol{\alpha} p = -\langle \rho \rangle \omega^2 \mathbf{U} - \rho_f \omega^2 \mathbf{W} \quad (2.89a)$$

$$i\omega \mathbf{W} = \frac{1}{\mu} \mathbf{K} \cdot (-\nabla p + \rho_f \omega^2 \mathbf{U}) \quad (2.89b)$$

$$\nabla \cdot \mathbf{W} = \beta p - \boldsymbol{\alpha} : \mathbf{E}(\mathbf{U}) \quad (2.89c)$$

As indicated above, in this method, a harmonic wave propagating along the direction \mathbf{p} is considered. Therefore, the displacement and the pressure can be given by

$$\mathbf{U} = \hat{\mathbf{U}} e^{-ikx\mathbf{p} + i\omega t} \quad (2.90a)$$

$$\mathbf{W} = \hat{\mathbf{W}} e^{-ikx\mathbf{p} + i\omega t} \quad (2.90b)$$

$$p = \hat{P} e^{-ikx\mathbf{p} + i\omega t} \quad (2.90c)$$

where k is the wave number.

According to *Pazdaniakou* (2012), the phase wave velocity is defined by

$$c = \frac{\omega}{k} \quad (2.91)$$

Using (2.90) and (2.91), equations (2.89) can be simplified and the velocity c with the vectors $\hat{\mathbf{U}}$ and $\hat{\mathbf{W}}$ can be found by solving the eigenvalue problem of the Christoffel equation

$$\begin{pmatrix} \mathbf{p} \cdot \mathbf{C}^{eff} \mathbf{p} - \beta^{-1} \mathbf{p} \cdot \boldsymbol{\alpha} \boldsymbol{\alpha} \cdot \mathbf{p} & \beta^{-1} \mathbf{p} \cdot \boldsymbol{\alpha} \mathbf{p} \\ -\frac{\omega}{\mu_f \beta} \mathbf{K} \cdot \mathbf{p} \boldsymbol{\alpha} \cdot \mathbf{p} & \frac{\omega}{\mu_f \beta} \mathbf{K} \cdot \mathbf{p} \mathbf{p} \end{pmatrix} \begin{pmatrix} \hat{\mathbf{U}} \\ \hat{\mathbf{W}} \end{pmatrix} = c^2 \begin{pmatrix} \langle \rho \rangle \mathbf{I} & \rho_f \mathbf{I} \\ -\frac{\omega \rho_f}{\mu_f} \mathbf{K} & i \mathbf{I} \end{pmatrix} \begin{pmatrix} \hat{\mathbf{U}} \\ \hat{\mathbf{W}} \end{pmatrix} \quad (2.92)$$

It is clear that the four macroscopic properties \mathbf{K} , $\boldsymbol{\alpha}$, β and \mathbf{C}^{eff} must be determined in order to solve (2.92).

2.7.2 Multiple pores and compressible fluids

The fluid compressibility has an obvious influence on the macroscopic properties of saturated porous media. It is related to the fluid pressure by

$$p(t) - p_0 = c_s^2 (\rho_f(t) - \rho_0) \quad (2.93)$$

where c_s is the sound speed, ρ_0 and p_0 the fluid density and fluid pressure in the equilibrium state. Then, the compressibility coefficient is defined by

$$c_f = \frac{1}{\rho_f c_s^2} \quad (2.94)$$

The influence of disconnected pores on the acoustic wave propagation in saturated media was considered by *Pazdaniakou* (2012) and *Li* (2010). *Li* (2010) pointed out that for a medium with n disconnected pores saturated by a compressible fluid, equations (2.89) which describe wave propagation through a saturated porous medium transform into

$$\nabla \cdot \mathbf{C}^{eff} : \mathbf{E}(\mathbf{U}) + \nabla \cdot \bar{\boldsymbol{\alpha}} \star \bar{p} = -\langle \rho \rangle \omega^2 \mathbf{U} - \rho_f \omega^2 \bar{\mathbf{I}} \star \bar{\mathbf{W}} \quad (2.95a)$$

$$i\omega \bar{\mathbf{W}} = \frac{1}{\mu} \bar{\mathbf{K}} \cdot (-\nabla \bar{p} + \rho_f \omega^2 \bar{\mathbf{I}} \mathbf{U}) \quad (2.95b)$$

$$\nabla \cdot \bar{\mathbf{W}} = (\mathbf{B} - c_f \bar{\boldsymbol{\epsilon}}) \star \bar{p} + \bar{\boldsymbol{\alpha}} : \mathbf{E}(\mathbf{U}) \quad (2.95c)$$

In this compact formulation, some special vector notations are used, such as \bar{I} , \bar{p} ... They can be explained as follows. \bar{I} is a column vector of size n whose components are all equal to 1. The variables relative to the pore are denoted by the superscripts i and j . Then, one has

$$\bar{p} = (p^i) \quad , \quad \bar{\mathbf{W}} = (\mathbf{W}^i) \quad , \quad \bar{\alpha} = (\alpha^i) \quad (2.96)$$

where p^i , \mathbf{W}^i and α^i are the pressure, the averaged fluid displacement and the coefficient relative to the pore i . \mathbf{B} is the pore interaction matrix B^{ij} . $\bar{\epsilon}$ and $\bar{\mathbf{K}}$ are expressed as

$$\bar{\epsilon} = \begin{pmatrix} \epsilon^1 & & \\ & \ddots & \\ & & \epsilon^n \end{pmatrix} \quad , \quad \bar{\mathbf{K}} = \begin{pmatrix} \mathbf{K}^1 & & \\ & \ddots & \\ & & \mathbf{K}^n \end{pmatrix} \quad (2.97)$$

where ϵ^i is the volume fraction, \mathbf{K}^i the permeability of Ω_f^i . The special symbol \star denotes an inner product over the pore indices (superscripts), equivalent to the scalar product (\cdot) over spatial indices (subscripts). The compressibility effects or the compressibility coefficient, from now on, are taken into account by \bar{G}

$$\bar{G} = (\mathbf{B} - c_f \bar{\epsilon})^{-1} \quad (2.98)$$

Then, thanks to equation (2.95), similarly to the case of a single pore, the wave velocity c , the solid displacement $\hat{\mathbf{U}}$, the averaged fluid displacement $\hat{\bar{\mathbf{W}}}$ can be found by solving the eigenvalue problem of the Christoffel equation for a saturated porous medium with multi-pores and compressibility fluids

$$\begin{pmatrix} [\mathbf{p} \cdot (\mathbf{C}^{eff} - \bar{\alpha} \star \bar{G} \star \bar{\alpha}) \cdot \mathbf{p}] & [\mathbf{p} \cdot \bar{\alpha} \star \bar{G} \mathbf{p}] \star \cdot \\ [-\frac{1}{\mu_f} \bar{\mathbf{K}} \cdot \mathbf{p} \bar{G} \star \bar{\alpha} \cdot \mathbf{p}] & [\frac{1}{\mu_f} \bar{\mathbf{K}} \cdot \mathbf{p} \bar{G} \mathbf{p}] \star \cdot \end{pmatrix} \begin{pmatrix} \hat{\mathbf{U}} \\ \hat{\bar{\mathbf{W}}} \end{pmatrix} = c^2 \begin{pmatrix} \langle \rho \rangle & \rho_f \bar{\mathbf{I}} \star \\ -\frac{\rho_f}{\mu_f} \bar{\mathbf{K}} & \frac{i}{\omega} \end{pmatrix} \begin{pmatrix} \hat{\mathbf{U}} \\ \hat{\bar{\mathbf{W}}} \end{pmatrix} \quad (2.99)$$

Similarly to a single pore, the four quantities $\bar{\mathbf{K}}$, $\bar{\alpha}$, \mathbf{B} and \mathbf{C}^{eff} are necessary. The determination of these properties was studied in *Malinouskaya* (2007), *Li* (2010) and *Pazdniakou* (2012).

2.7.3 Determination of $\bar{\mathbf{K}}$, $\bar{\alpha}$, \mathbf{B} and \mathbf{C}^{eff}

The four quantities $\bar{\mathbf{K}}$, $\bar{\alpha}$, \mathbf{B} and \mathbf{C}^{eff} characterize the hydrodynamical and mechanical properties of the porous medium. They must be determined in order to obtain the acoustic veloci-

ties in porous media with a single pore or multi-pores saturated by an incompressible or compressible fluid. This section presents their physical meanings and the methods of determination which are applied in this thesis.

- Effective stiffness tensor C^{eff} : this is the effective stiffness tensor of the dry medium. It characterizes the elastic properties of the porous medium at the macroscopic level. The average stress tensor $\langle \sigma \rangle$ is related to the mean strain tensor $\langle \varepsilon \rangle$ by C^{eff} as for an elastic material. It can be directly determined by the LSM and LSM2S as presented in the calculation of acoustic waves propagation in dry porous media.
- Dynamic permeability $\overline{\mathbf{K}}$: It is obtained by calculating the permeability tensors of all disconnected pores. In most cases, only one pore is percolating. The dynamic permeabilities \mathbf{K} are complex and frequency dependent (*Biot, 1941*). \mathbf{K} is used to characterize oscillating flows in porous media. The theoretical basis of the dynamic permeability calculation was presented; in order to determine \mathbf{K} , the numerical tool is LBM.
- The coefficients $\overline{\alpha}$, \mathbf{B} (α and β): they characterize the reaction of the solid matrix to the fluid pressure. $\overline{\alpha}$ characterizes the variation of the pore volume when the medium is submitted to the macroscopic strain \mathbf{E} . B^{ij} is the variation of the pore volume Ω_f^i when a unit pressure is imposed in the pore j . In fact, $\overline{\alpha}$ and \mathbf{B} are considered as a generalisation of α and β for one pore.

According to *Li (2010)*, \mathbf{q}^i is necessary in the calculation of $\overline{\alpha}$ and \mathbf{B} . This is the displacement field in the porous medium when the unit fluid $p^i = 1$ is exerted on the pore surface Γ^i while the other pores are at a zero fluid pressure. It can be found from the equations

$$\begin{cases} \nabla_y \cdot [\mathbf{C} : \mathbf{e}(\mathbf{q}^i)] = 0 & \text{in } \Omega_s \\ [\mathbf{C} : \mathbf{e}(\mathbf{q}^i)] \cdot \mathbf{n}^i = -\mathbf{n}^i & \text{on } \Gamma^i \\ [\mathbf{C} : \mathbf{e}(\mathbf{q}^i)] \cdot \mathbf{n}^j = 0 & \text{on } \Gamma^j, \quad j \neq i \end{cases} \quad (2.100)$$

Then, the coefficients α^i and B^{ij} can be defined by

$$\begin{aligned}\alpha^i &= -\epsilon^i \mathbf{I} + \langle \mathbf{C} : \mathbf{e}(\mathbf{q}^i) \rangle \\ B^{ij} &= \frac{1}{\Omega} \int_{\Gamma^i} \mathbf{q}^j \cdot \mathbf{n}^j \, ds\end{aligned}\quad (2.101)$$

In the framework of this thesis, the macroscopic coefficients $\bar{\alpha}$, \mathbf{B} (α and β) can be numerically simulated by using the LSM-LBM model for media with one solid and by LSM2S-LBM for two solids which are presented in Chapter 3.

When all four properties are determined, the acoustic velocities in saturated samples can be calculated. Three types of waves can be calculated: fast compressional wave, slow compressional wave and shear waves *Biot* (1956a,b), *Pazdaniakou* (2012).

2.7.4 Gassmann's model

Gassmann's (1951) equations are the relations most widely used to calculate seismic velocity in reservoirs. Gassmann fluid substitution is a simple method used for predicting the acoustic velocities in saturated porous media (*Han and Batzle*, 2004; *Fredy and Alvarado*, 2006). It allows to determine the velocities of the compressional and the shear waves in saturated samples when the effective properties such as the bulk modulus, the shear modulus of dry samples... are fully determined.

As indicated before, in this thesis, the dry samples are calculated by numerical tools and the effective properties are derived; therefore, Gassmann's model can be used to predict the acoustic velocities in saturated samples. For the purpose of comparisons with our numerical results, in this section, this model is summarized.

The pore space stiffness K_ϵ is related to the porosity ϵ , the bulk modulus K_0 of the solid component and the bulk modulus K_d of the dry porous medium by

$$K_\epsilon = \frac{\epsilon}{\frac{1}{K_d} - \frac{1}{K_0}} \quad (2.102)$$

The pore filled by fluids has influences on the macroscopic properties of the medium. For instance, the saturated bulk modulus K_{sat} can be given by

$$K_{sat} = \frac{1}{\frac{1}{K_0} + \frac{\varepsilon}{K_\varepsilon + \frac{K_0 K_f}{K_0 - K_f}}} \quad (2.103)$$

where K_f is the fluid bulk modulus. Then, the density of such saturated medium ρ_{sat} can be expressed as

$$\rho_{sat} = (1 - \varepsilon)\rho_0 + \varepsilon\rho_f \quad (2.104)$$

where ρ_0 is the solid density and ρ_f the fluid density.

In Gassmann's model, the shear modulus is independent of the pore filling, i.e., the shear modulus G_{sat} of saturated medium is equal to the dry one G_d . Therefore, the velocity of shear wave can be derived by

$$V_{sat}^s = \sqrt{\frac{G_{sat}}{\rho_{sat}}} = \sqrt{\frac{G_d}{\rho_{sat}}} \quad (2.105)$$

The compressional wave velocity V_{p2} is more complex; it depends not only on the density and on shear modulus, but also on the saturated bulk modulus K_{sat} . It is expressed as

$$V_{sat}^p = \sqrt{\frac{K_{sat} + 4G_{sat}/3}{\rho_{sat}}} \quad (2.106)$$

In order to apply Gassmann's model to our calculations, the quantities K_d , K_0 , G , ε , ρ_f , ρ_s and K_f are determined. Thanks to equation (2.104), the saturated density of the medium can be calculated. Then, the shear wave velocity V_{sat}^s is determined from (2.105). The pore space stiffness is calculated according to (2.102). Therefore, the compression wave velocity V_{sat}^p can be obtained by (2.106) after determination of the saturated bulk modulus K_{sat} by using (2.103). Hence, the acoustic velocities in saturated porous media can be approximated in a simple way.

Gassmann's model is based on several assumptions which are

- The porous material is isotropic, elastic, homogeneous and composed of a single mineral. It is an issue for the STATOIL samples which are composed of two solid components. However, it can be solved as presented in Chapter 5.

- The porosity is always constant, it means that the porosity does not change with different saturating fluids.
- The pore space is well connected and in pressure equilibrium. This may not be correct for samples with disconnected pores, but correct for our samples as it will be shown in Chapter 4 and Chapter 5.
- The medium is a closed system with no pore-fluid across the boundaries.

It is worth noting that this model takes into account the fluid compressibility; therefore, in the framework of the thesis, it is used for comparison with simulation results obtained by LBM, LSM, LSM2S, LBM-LSM when the samples are saturated by water.

2.8 Summary

The three main works done in this thesis are presented: characterizations of samples, acoustic waves propagating in dry porous media and in saturated media.

The characterizations include calculations of porosity and the correlation function. This is a small part in the overall calculations, but important. A suitable method for each sample can be proposed based on its results.

The acoustic waves in dry porous media is determined from the macroscopic properties of the media. It is based on the calculations of elastic waves in elastic materials when the averaged values are introduced. The velocities can be derived from the effective stiffness tensor C^{eff} which is directly obtained by using numerical tools such as LSM, LSM2S when the sample size is not too large; sometimes the coarsening method must be applied.

The propagation of acoustic waves through saturated porous media was calculated by the homogenization method used by *Malinouskaya* (2007) and *Li* (2010). The effective stiffness tensor C^{eff} , the permeabilities \mathbf{K} , the reaction of the solid matrix on the fluid pressure α and β are calculated first by lattice models such as LSM, LBM, LBM-LSM, LBM-LSM2S (*Pazdniakou*, 2012). The wave velocities are determined by solving the Christoffel equation. These velocities will be compared to the approximate Gassmann's model.

Chapter 3

Lattice models in calculations of porous media

3.1 Introduction

In the field of porous media, there are many problems that can be studied such as flows, mechanical properties... Most of them are very complex and difficult; there are only a few analytical solutions and numerical tools must be used most of the time. The development of computers makes numerical simulations easier and faster. Real experiments which are usually costly, can be partly avoided.

Since the propagation of acoustic waves in porous media is also complex, numerical simulations are needed to obtain results. In order to have simulations which are in good agreement with the real experiments, the models must reproduce correctly the physical situation (i.e., all the necessary physical characteristics which can influence the results have to be known) and the numerical methods have to be precise enough. In this section, lattice models which calculate flows and deformations in dry and in saturated porous media with one or two solid components are presented; they are the Lattice Spring Model (LSM), the Lattice Spring Model for two solids (LSM2S), the coupled LBM-LSM model and the LBM-LSM2S model.

LSM is used to calculate the effective mechanical properties of porous media at a macroscopic level; the medium in this case has only one solid component (*Pazdniakou, 2012*). Solids are modeled by lattice points which are connected to others by springs. Linear and angular springs are used (*Ladd et al., 1997a; Wang, 1989*), together with the concept of elastic elements (*Pazdniakou, 2012; Ladd et al., 1997b*). Then, the macroscopic elastic constants can be obtained by the energy

stored in an elementary cell as described in *Ostoja* (2002).

Lattice Spring Model for two solids is new and is developed based on the basic LSM in order to calculate porous media with two solid components. There are two types of elastic elements in the lattice, one for each solid; this yields many values of elastic constants of springs depending on their location. After determination of all elastic spring constants, LSM2S works in the same way as LSM. In this chapter, LSM2S is developed and validated by comparison with existing methods such as the approximation methods of *Nemat-Nasser and Iwakuma* (1982), *Torquato* (1998, 2000) and *Cohen* (2004), the FFT method of *Hoang-Duc and Bonnet* (2012), and the FMD of *Malinouskaya* (2007).

The coupled LBM-LSM model (*Pazdniakou*, 2012) can study the interactions between fluid and solid phases in saturated porous media. The connection between LBM and LSM is the momentum exchange algorithm (*Buxton et al.*, 2005; *Wu and Aidun*, 2009) which is used to calculate the force exerted by the fluid on a solid surface element point and the reflected distribution function of LBM following the LSM iteration with the Verlet algorithm. This coupled model is used to derive the coefficients α and β which characterize the reaction of the solid matrix on the fluid pressure and they are needed to solve the Christoffel equation. Then, LBM-LSM2S is developed in order to determine these coefficients for media with two solid components.

This chapter is organized as follows. Section 3.2 presents the Lattice Spring Model. Then, the Lattice Spring Model for two solid (LSM2S) is described in Section 3.3. Section 3.4 details the coupled LBM-LSM model and the development of LBM-LSM2S. Finally, some conclusions are discussed in Section 3.5.

3.2 Lattice Spring Model

The Lattice Spring Model (LSM) can be used to simulate elastic media. In this model, the medium is represented by a lattice whose points are connected by linear springs; angular forces between contiguous linear springs can also be included (*Pazdniakou*, 2012). Since LSM describes the elastic medium behaviour at the microscopic level, the behaviour in the continuum limit should be derived. In order to obtain the macroscopic properties, the displacements of lattice points are

supposed small and the strain tensor uniform. The elastic energy stored in an elementary cube yields the macroscopic elastic properties (*Ostoja, 2002*).

3.2.1 3D LSM

In 3D, for isotropic media, a face centered cubic lattice with 18 springs is used (Fig. 3.1.a).

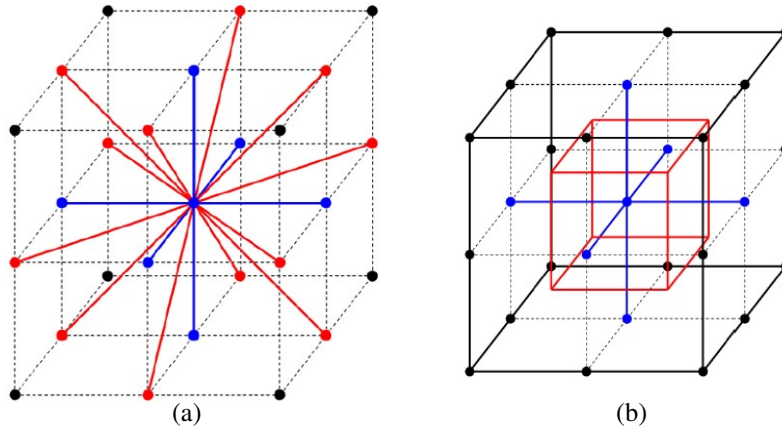


Figure 3.1: (a) The 3D LSM. (b) The elementary cube (red lines).

For a lattice with 18 linear springs, the vectors corresponding to the six first neighbours (blue dots in Fig. 3.1) of any point are given by

$$\mathbf{c}^{(b)} = (\pm a, 0, 0), (0, \pm a, 0), (0, 0, \pm a), b = 1, \dots, 6 \quad (3.1)$$

The twelve second neighbours (red dots in Fig. 3.1) are given by the vectors

$$\mathbf{c}^{(b)} = (\pm a, \pm a, 0), (0, \pm a, \pm a), (\pm a, 0, \pm a), b = 7, \dots, 18 \quad (3.2)$$

where a is the size of the elementary cube. The corresponding unit vectors in the same direction are denoted by

$$\mathbf{n}^{(b)} = \frac{\mathbf{c}^{(b)}}{|\mathbf{c}^{(b)}|} \quad (3.3)$$

Some lattice points can be considered as the centre of an elementary cube whose volume is a^3 (Fig. 3.1.b). The corresponding vectors are denoted by

$$\mathbf{r}^{(b)} = \frac{\mathbf{c}^{(b)}}{2} \quad (3.4)$$

There are also angular springs between some of the linear springs. In the lattice spring model, there are two types of angular springs with angles $\frac{\pi}{4}$ and $\frac{\pi}{3}$ as seen in Fig. 3.2.

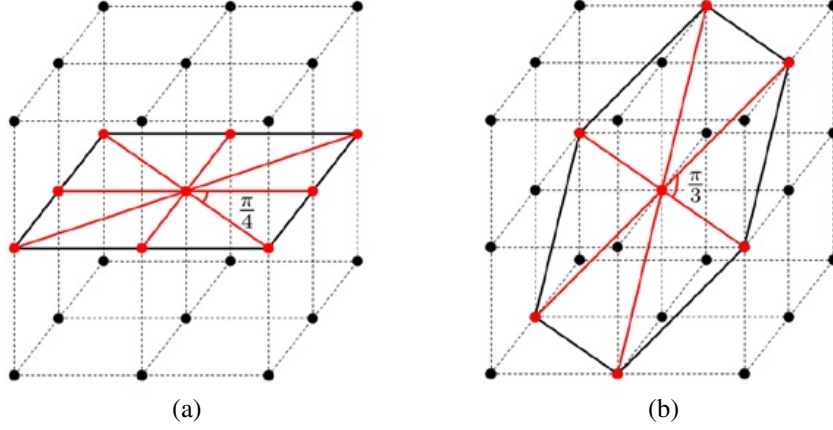


Figure 3.2: Two types of angular springs. (a) The eight angles $\frac{\pi}{4}$ in the xy-plane. (b) The six angles $\frac{\pi}{3}$ in inclined planes.

The energy of an elementary cube can be expressed in terms of displacements and angle changes. If the endpoints of a linear spring are denoted by the indices m and n , the relative displacement is given by

$$\mathbf{u}^b = \mathbf{u}_m - \mathbf{u}_n \quad (3.5)$$

If the angular spring corresponds to two linear springs b and b' , the angle change is given by

$$\Delta\varphi^{(b,b')} = \Delta\theta^{(b')} - \Delta\theta^{(b)} \quad (3.6)$$

In an elementary cube, the length of all the linear springs is equal to half their initial length. Therefore, $\kappa^{(b)} = 2\alpha^{(b)}$ where $\alpha^{(b)}$ is the linear spring constant of the initial spring. The total energy stored in an elementary cube is

$$E = \frac{1}{2} \sum_b \kappa^{(b)} |\mathbf{u}^{(b)}|^2 + \frac{1}{2} \sum_{b,b'} \beta^{(b,b')} (\Delta\varphi^{(b,b')})^2 \quad (3.7)$$

where $\beta^{(b)}$ is the angular spring constant.

3.2.2 Linear springs

The energy of all linear springs stored in an elementary cube is equal to

$$E_c = \frac{1}{2} \sum_b \kappa^{(b)} |\mathbf{u}^{(b)}|^2 \quad (3.8)$$

The relative displacement $\mathbf{u}^{(b)}$ can be expressed by using the strain tensor in the following way

$$u_i^{(b)} = \varepsilon_{ij} r_j^{(b)} = |\mathbf{r}^{(b)}| \varepsilon_{ij} n_j^{(b)} \quad (3.9)$$

For small displacements, we have

$$|\mathbf{u}^{(b)}| = \mathbf{u}^{(b)} \cdot \mathbf{n}^{(b)} = |\mathbf{r}^{(b)}| \varepsilon_{ij} n_j^{(b)} n_i^{(b)} \quad (3.10)$$

Then, the elastic energy of linear springs is

$$E_c = \frac{1}{2} \sum_b \kappa^{(b)} |\mathbf{u}^{(b)}|^2 = \frac{1}{2} \sum_b |\mathbf{r}^{(b)}| n_i^{(b)} n_j^{(b)} |n_k^{(b)} n_l^{(b)}| \varepsilon_{ij} \varepsilon_{kl} \quad (3.11)$$

The elastic energy density is given by

$$W_c = \frac{E_c}{V} = \frac{1}{2} \left[\frac{1}{a^3} \sum_b |\mathbf{r}^{(b)}| n_i^{(b)} n_j^{(b)} |n_k^{(b)} n_l^{(b)}| \right] \varepsilon_{ij} \varepsilon_{kl} \quad (3.12)$$

Therefore, the stiffness tensor relative to the central forces may be expressed as

$$C_{ijkl}^{(cf)} = \frac{1}{a^3} \sum_b |\mathbf{r}^{(b)}| n_i^{(b)} n_j^{(b)} n_k^{(b)} n_l^{(b)} \quad (3.13)$$

With the same value of $\kappa^{(b)}$, the coefficients of the stiffness tensor can be given as follows

$$C_{xxxx}^{cf} = \frac{3\alpha}{a}; \quad C_{xyxy}^{cf} = \frac{\alpha}{a}; \quad C_{xyyx}^{cf} = \frac{\alpha}{a} \quad (3.14)$$

Under such conditions, the Poisson ratio is

$$\nu = \frac{\lambda_s}{2(\lambda_s + \mu_s)} = 0.25 \quad (3.15)$$

3.2.3 Angular springs

Similar to the linear springs, the elastic energy density of angular springs in an elementary cube was found by Pazdniakou (2012)

$$W_a = \frac{1}{2} \left[\frac{\beta}{a^3 \sin^2(\varphi)} \sum_{(b,b')} [\epsilon_{kij} (n_i^{(b')} n_p^{(b')} - n_i^{(b)} n_p^{(b)}) \epsilon_{klm} n_l^{(b)} n_m^{(b')}] \right. \\ \left. [\epsilon_{acd} (n_c^{(b')} n_h^{(b')} - n_c^{(b)} n_h^{(b)}) \epsilon_{afs} n_f^{(b)} n_s^{(b')}] \right] \varepsilon_{jp} \varepsilon_{dh} \quad (3.16)$$

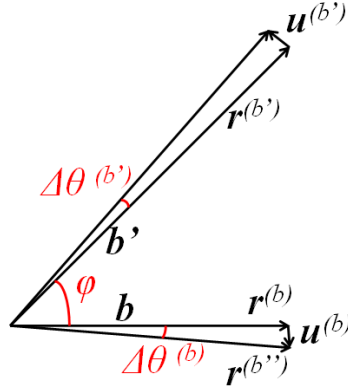


Figure 3.3: The angular displacement of two angular springs.

where ϵ_{ijk} is the Levi-Civita tensor. By using the following tensorial identities

$$\epsilon_{pij}\epsilon_{plk} = \delta_{il}\delta_{jk} - \delta_{ik}\delta_{jl}; \quad \delta_{ij}a_j = a_i \quad (3.17)$$

the angular stiffness tensor $C_{jphd}^{(af)}$ can be simplified as

$$\begin{aligned} C_{jphd}^{(af)} &= \frac{\beta}{a^3 \sin^2} \\ &\cdot \sum_{(b,b')} [n_i^{(b')} n_i^{(b)} n_p^{(b')} n_j^{(b')} - n_i^{(b)} n_i^{(b)} n_p^{(b)} n_j^{(b)} - n_i^{(b')} n_i^{(b')} n_p^{(b')} n_j^{(b)} + n_i^{(b)} n_i^{(b')} n_p^{(b)} n_j^{(b)}] \\ &\cdot [n_l^{(b')} n_l^{(b)} n_h^{(b')} n_d^{(b')} - n_l^{(b)} n_l^{(b)} n_h^{(b)} n_d^{(b)} - n_l^{(b')} n_l^{(b')} n_h^{(b')} n_d^{(b)} + n_l^{(b)} n_l^{(b')} n_h^{(b)} n_d^{(b)}] \quad (3.18) \end{aligned}$$

It is necessary to know the angles between the angular springs in order to calculate the stiffness tensor. There are 24 angular springs with an angle equal to $\frac{\pi}{4}$ which corresponds to the first and second neighbours; they are located in 3 mutually orthogonal planes. Their stiffness tensor coefficients are expressed as

$$C_{xxxx}^{(\frac{\pi}{4})} = \frac{4\beta}{a^3}; \quad C_{xyyy}^{(\frac{\pi}{4})} = -\frac{2\beta}{a^3}; \quad C_{xxxx}^{(\frac{\pi}{4})} = \frac{2\beta}{a^3} \quad (3.19)$$

This tensor is not isotropic since it corresponds to a medium with a cubic symmetry.

In addition, there are too 24 angular springs with an angle equal to $\frac{\pi}{3}$ which correspond to second neighbours; they are located in 4 inclined planes. Their stiffness tensor coefficients are given by

$$C_{xxxx}^{(\frac{\pi}{3})} = \frac{4\beta}{a^3}; \quad C_{xyyy}^{(\frac{\pi}{3})} = -\frac{2\beta}{a^3}; \quad C_{xxxx}^{(\frac{\pi}{3})} = \frac{4\beta}{a^3} \quad (3.20)$$

This tensor is not isotropic for the same reason as before; however, the combination of these two angle sets with the same β yields an isotropic stiffness tensor

$$C_{xxxx}^{(af)} = \frac{8\beta}{a^3}; \quad C_{xxyy}^{(af)} = -\frac{4\beta}{a^3}; \quad C_{xyxy}^{(af)} = \frac{6\beta}{a^3} \quad (3.21)$$

3.2.4 Combination of linear and angular springs

The total stiffness tensor which is the sum of the linear and angular force tensors is expressed by

$$C_{xxxx} = \frac{3\alpha}{a} + \frac{8\beta}{a^3}; \quad C_{xxyy} = \frac{\alpha}{a} - \frac{4\beta}{a^3}; \quad C_{xyxy} = \frac{\alpha}{a} + \frac{6\beta}{a^3} \quad (3.22)$$

The properties of the medium are

$$\lambda_s = \frac{\alpha}{a} - \frac{4\beta}{a^3}; \quad \mu_s = \frac{\alpha}{a} + \frac{6\beta}{a^3}; \quad K = \frac{5\alpha}{a}; \quad \nu = \frac{\alpha - \frac{4\beta}{a^2}}{4\alpha + \frac{4\beta}{a^2}} \quad (3.23)$$

where λ_s and μ_s are the Lamé coefficients, K the bulk modulus and ν the Poisson ratio.

According to *Pazdniakou (2012)*, the force exerted by the linear springs acting on the lattice point i is expressed as

$$\mathbf{F}_i = \alpha \sum_n ((\mathbf{u}_n - \mathbf{u}_i) \cdot \hat{\mathbf{c}}_{i,n}) \hat{\mathbf{c}}_{i,n} \quad (3.24)$$

where $\hat{\mathbf{c}}_{i,n}$ is the normalized vector connecting the nodes i and n .

Then, the forces exerted by angular springs $b - i - b'$ acting on the two endpoints b, b' and the vertex point i are given by

$$\mathbf{F}^{(b)} = \beta \Delta \phi^{(b,b')} \frac{\mathbf{n}^{(b)} \times \hat{\mathbf{n}}^{(b,b')}}{|\mathbf{n}^{(b)} \times \hat{\mathbf{n}}^{(b,b')}| |\mathbf{c}^{(b)}|} \quad (3.25a)$$

$$\mathbf{F}^{(b')} = \beta \Delta \phi^{(b,b')} \frac{\mathbf{n}^{(b')} \times \hat{\mathbf{n}}^{(b,b')}}{|\mathbf{n}^{(b')} \times \hat{\mathbf{n}}^{(b,b')}| |\mathbf{c}^{(b')}|} \quad (3.25b)$$

$$\mathbf{F}^{(i)} = (\mathbf{F}^{(b)} + \mathbf{F}^{(b')}) \quad (3.25c)$$

3.2.5 The problems of the original LSM

In fact, these formulas yield an incorrect Poisson ratio and inadequate boundary conditions.

Problem of Poisson ratio

With the original form of LSM, the Poisson ratio is given by equation (3.23) and it varies between -1 and 0.25 when $\frac{\beta}{\alpha}$ varies from 0 to ∞ . But for real materials, it can be larger than 0.25.

Boundary condition

With the previous formulas, the elastic constants are fixed for all linear and angular springs and they are correct when all the lattice points are located inside the medium. But in most cases, some surface points are presented, such as at the surface of the pores.

In order to prove this, some direct simulations with these formulas were performed and they introduced inaccuracies even for simple geometries as in *Ladd et al. (1997a,b)*. Consider a cube of size L made of an isotropic elastic material and submitted to a simple stretching along the x -direction. According to the linear elastic theory, under the action of this load, the cube will be transformed into a rectangular parallelepiped (Fig. 3.4).

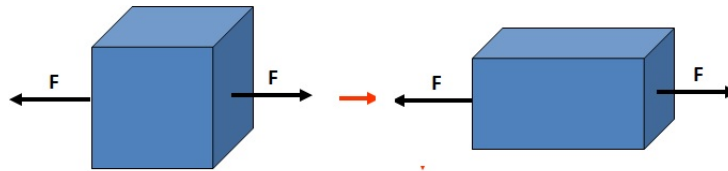


Figure 3.4: A simple stretching along the x -direction of a cube. (a) Original form. (b) Transformed form predicted by the elastic theory.

However, in fact, a direct application of the original LSM is inaccurate and the side surface of size 20 submitted to a simple stretching is deformed as in Fig. 3.5.

Solution by introduction of elastic elements

It is obvious that the elastic constant of the springs located at the surface must be corrected. These problems were solved by introducing "elastic elements" into LSM (*Pazdniakou, 2012*).

An elastic element is an elementary cube which is limited by eight lattice points related by springs (Fig.3.6) and it represents the smallest part of an elastic medium. Depending on the

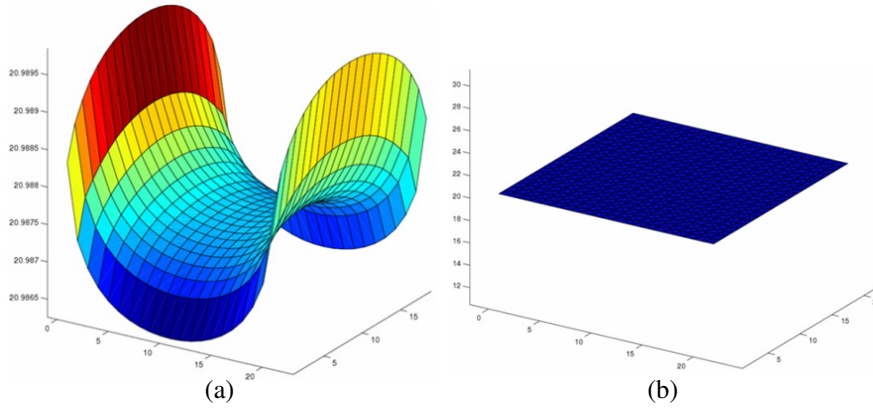


Figure 3.5: Deformation of the top side surface. (a) Inaccurate results with the original LSM (b) Accurate result with elastic elements.

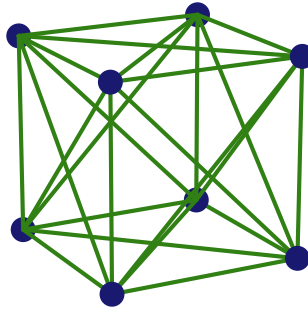


Figure 3.6: An elastic element.

number of neighbours, each spring can belong to several elastic elements. The $[1,0,0]$ type springs can belong to 1, 2, 3 or 4 neighbour elastic elements. The $[1,1,0]$ type springs can belong to 1 or 2 neighbour elastic elements. Therefore, the constant of the considered spring is equal to the sum of the linear spring constants of all the neighbour elastic elements containing the considered spring (Fig. 3.7). A similar approach is applied to the angular springs.

A $[1,0,0]$ linear spring which belongs to an elastic element, has a constant equal to $\frac{1}{4}\alpha$; when it belongs to 2 elements, the constant is equal to $\frac{1}{2}\alpha$; when it belongs to 3 elements, the constant is equal to $\frac{3}{4}\alpha$; the ones located inside the medium have a constant equal to α .

An elastic element contains forty eight $\frac{\pi}{4}$ - and twenty four $\frac{\pi}{3}$ -angular springs. A $\frac{\pi}{3}$ -angular spring can belong only to one elastic element; therefore, its constant is β . A $\frac{\pi}{4}$ -angular spring can belong to 1 or 2 elastic elements; they correspond to $\frac{\beta}{2}$ and β , respectively.

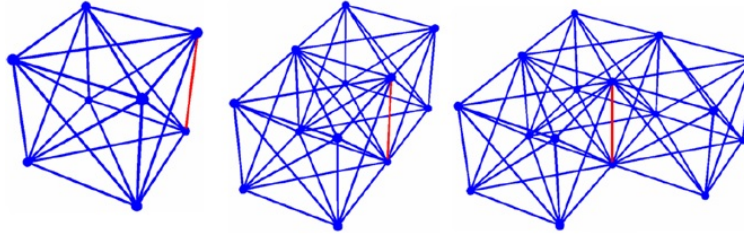


Figure 3.7: The red linear springs belong to one, two, three elastic elements; therefore, the force constants are $\frac{\alpha}{4}$, $\frac{\alpha}{2}$, and $\frac{3\alpha}{4}$, respectively.

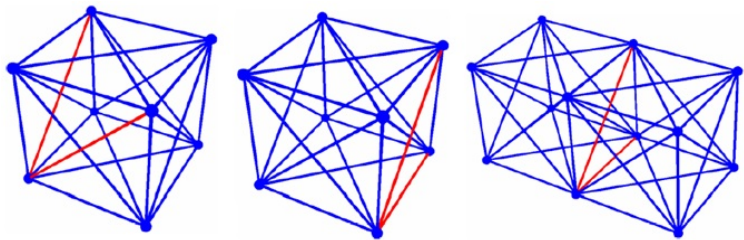


Figure 3.8: The $\frac{\pi}{3}$ -angular springs which belong to only one elastic element correspond to β . The $\frac{\pi}{4}$ -angular springs which belong to one or two elastic elements correspond to $\frac{\beta}{2}$ and β , respectively.

Now, the force constants are different for the springs located inside the medium and at the surface by using the elastic elements. It is possible to solve the problem of the Poisson ratio by assigning negative values to the angular spring elastic constant; then, the Poisson ratio ν becomes larger than 0.25. This can be done because in the elastic element there is always a linear spring between the endpoints of any angular spring which compensates the force exerted by angular springs with a negative constant.

Boundary conditions

In elastostatics problems, the deformations inside an elastic body are usually due to two types of boundary conditions which are either prescribed deformations or prescribed forces.

In the LSM based on elastic elements, an external force is distributed according to the additive principle. The force acting on the side of an elastic element should be uniformly redistributed between the four lattice points composing this side. The total external force acting on a lattice point is the sum of the external forces taken over all the elastic elements containing this lattice point.

If a uniform stress is prescribed on the side of a cube as in Fig. 3.9, there are three types

of lattice points: the points which belong to 3 cube sides where the force is $(\frac{Fx}{4}, 0, 0)$, the points which belong to 2 cube sides where the force is $(\frac{Fx}{2}, 0, 0)$ and the points on 1 cube side where the force is $(Fx, 0, 0)$.

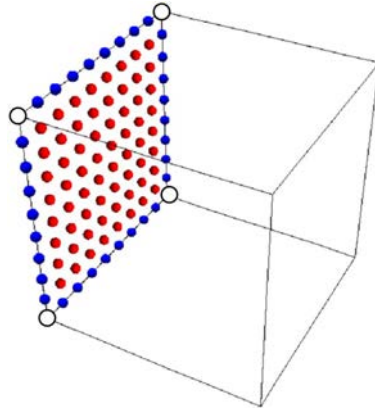


Figure 3.9: Stress boundary condition. The external force is $(\frac{Fx}{4}, 0, 0)$ at the white points, $(\frac{Fx}{2}, 0, 0)$ at the blue points and $(Fx, 0, 0)$ at the red points.

A strain boundary condition can be imposed in the same way as in the original LSM.

3.2.6 Geometry

LSM geometry

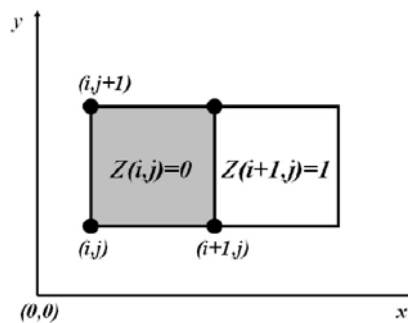


Figure 3.10: Example of LSM geometry in 2D. $Z(i,j)=0$: the corresponding elastic element is grey; the black dots are the solid lattice points. $Z(i+1,j)=1$: the corresponding pore element is white.

The samples are discretized into elementary cubes of size a which are either solid or void. This can be represented by the phase function (2.4). Equivalently, $Z(x)$ can be denoted by $Z(i,j,k)$ where (i,j,k) are the integer coordinates of the voxel. The lattice points of LSM are deduced from

Z ; each solid voxel $Z(i,j,k)=0$ corresponds to one elastic element and eight solid lattice points are the vertices of the elementary cube (Fig. 3.10).

3.2.7 Application of LSM to calculate effective stiffness tensors

The elastic behaviour of porous media is governed by

$$\langle \boldsymbol{\sigma} \rangle = \mathbf{C}^{(eff)} : \langle \boldsymbol{\varepsilon} \rangle \quad (3.26)$$

where $\langle \boldsymbol{\sigma} \rangle$ and $\langle \boldsymbol{\varepsilon} \rangle$ are the average values of stress and strain at the macroscopic level in the porous medium. $\mathbf{C}^{(eff)}$ is the effective stiffness tensor.

In order to calculate the effective stiffness tensors based on LSM with elastic elements, *Pazdniakou* (2012) devised a Fortran simulation program. There are six simulation programs including three simple stretching simulations along the x-, y- and z-directions and three simple shear simulations in the xy-, xz- and yz-planes.

If the medium is isotropic, only 2 simulations are necessary to obtain the effective stiffness tensor, namely a simple stretching and a simple shear.

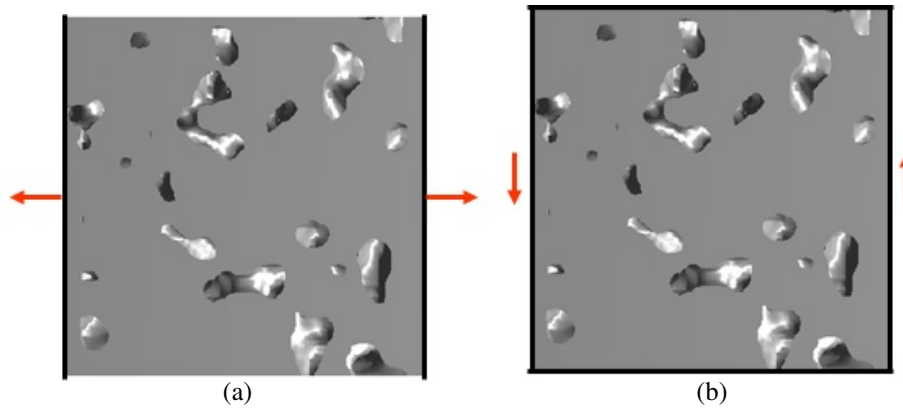


Figure 3.11: Two simple simulations. (a) Simple stretching yields C_{xxxx} and C_{xxyy} . (b) Simple shear yields C_{xyxy} .

In the general case, 6 simulations are necessary to obtain the 9 required values of the effective

stiffness tensor

$$\mathbf{C}^{(eff)} = \begin{pmatrix} C_{xxxx} & C_{xxyy} & C_{xxzz} & 0 & 0 & 0 \\ C_{xxyy} & C_{yyyy} & C_{yyzz} & 0 & 0 & 0 \\ C_{xxzz} & C_{yyzz} & C_{zzzz} & 0 & 0 & 0 \\ 0 & 0 & 0 & C_{yzyz} & 0 & 0 \\ 0 & 0 & 0 & 0 & C_{zxzx} & 0 \\ 0 & 0 & 0 & 0 & 0 & C_{xyxy} \end{pmatrix} \quad (3.27)$$

3.3 The Lattice Spring Model for 2 solid components (LSM2S)

The mechanical properties of porous media are of theoretical and industrial interests. Many methods have been proposed in order to calculate the mechanical properties of porous media on the macroscopic level. However, most methods are limited to media with one solid component and pores, whereas media are often formed by many solid components. Some methods have been proposed to solve this problem, including the approximation methods of *Nemat-Nasser and Iwakuma* (1982), *Torquato* (1998, 2000) and *Cohen* (2004), the FFT method of *Hoang-Duc and Bonnet* (2012), and the FMD of *Malinouskaya* (2007). The analytical methods are limited in applications; calculation of media with more than two solid components is complicated and large samples are difficult to calculate. Based on the basic Lattice Spring Model, a new model called Lattice Spring model with many components (LSM2S) is proposed; it can be used to calculate the macroscopic properties of porous media with two or more solid components.

LSM2S is based on the LSM created by *Pazdniakou* (2012); solids are modeled by springs connected at nodes and the macroscopic elastic constants can be derived by the elastic energy stored in an elementary cell. LSM2S involves the characteristics of the basic LSM, such as the linear springs, the angular springs, the elastic elements, the boundary conditions and the Verlet algorithm. The important point of LSM2S is the presence of interfaces between the different components which induce various values of linear and angular spring constants.

In this section, the descriptions of the resolution of reaction problems between the different solids, the validation of LSM2S, the discussion and the perspectives of the model are presented.

3.3.1 Geometry

The model LSM2S is developed based on the basic Lattice Spring Model in order to calculate the macroscopic properties of heterogeneous media. To achieve this purpose, we must take into account the reaction between the various solids or between solids and pores. The geometry of the sample is discretized in the same way as in LSM. Again the porous medium is discretized into voxels corresponding to the phase function $Z(i, j, k)$ (cf. (2.4)). For media with several components, each solid component is assigned a numerical symbol (0,2...) in the phase function. Therefore, the phase function becomes

$$Z(i, j, k) = \begin{cases} 0 & \text{if the voxel belongs to inclusion} \\ 1 & \text{if the voxel belongs to pore} \\ 2 & \text{if the voxel belongs to matrix} \end{cases} \quad (3.28)$$

In the same way as in LSM, the lattice points of LSM2S are deduced from Z ; each $Z(i,j,k)$ equal to 0 or 2 corresponds to one elastic element of type 0 (blue) or type 2 (green), respectively; eight solid points are the vertices of the elementary cube (Fig. 3.12.b).

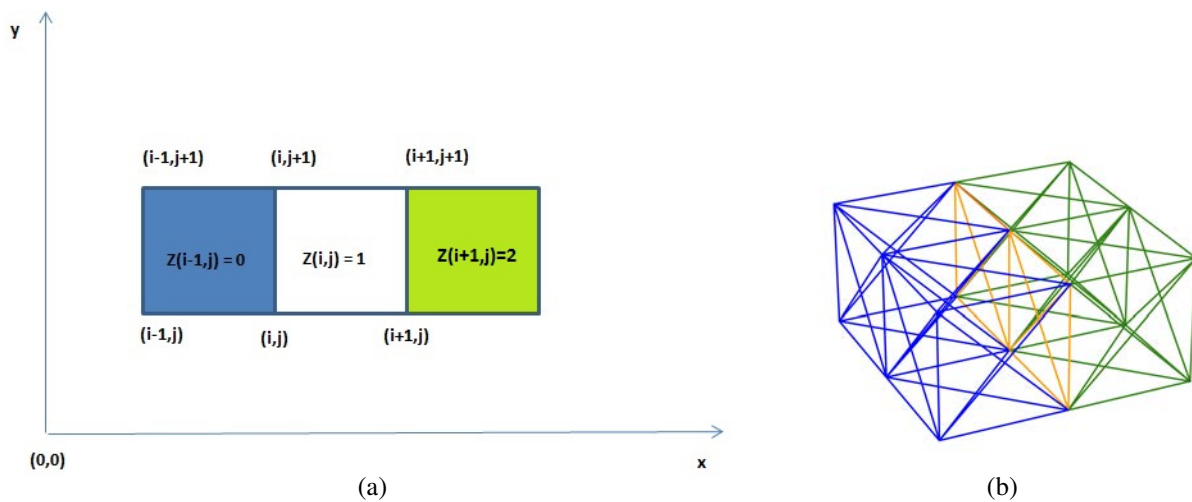


Figure 3.12: Two solids in the lattice. (a) LSM2S geometry and convention. (b) Two types of elastic elements. The blue is inclusion (corresponds to 0). The green is matrix (corresponds to 2). The interface corresponds to the orange springs.

3.3.2 Spring constants with two solids

It is clear that the effective properties depend on the distribution of the matrix and of the inclusions. The springs located at different positions have different values of the elastic constants. According to the elasticity theory and the basic LSM, in an elastic element, the linear spring constant α and the angular spring constant β of each material are given by

$$\alpha = \frac{aE}{5(1-2\nu)} \quad \beta = \frac{a^3E(4\nu-1)}{20(2\nu-1)(1+\nu)} \quad (3.29)$$

where a is the voxel dimension, E the Young modulus, ν the Poisson ratio. Recall that the considered media are composed by pore, matrix and inclusion; their properties are given in Table 3.1.

Elastic modulus (GPa)	Matrix	Inclusion
Young modulus E	E_2	E_0
Poisson ratio ν	ν_2	ν_0

Table 3.1: Elastic properties of matrix and inclusion.

From these values, one can obtain the linear spring constant and the angular spring constant of the inclusion α_0, β_0 and of the matrix α_2, β_2 , respectively.

Due to the complexity of the solid-pore interface, there exist many possible values of elastic constants in the lattice. One spring can belong to an elastic element of type 0, type 2 or both as it can be seen in Fig. 3.12.b (blue, green and orange spring). The elastic constant of a linear spring or an angular spring depends on the number and the type of elastic elements that it belongs to. The results are given in Table 3.2, where η_0 and η_2 are the number of elastic elements of type 0 and 2 to which the selected spring belongs, respectively. The calculations are detailed in Appendix A.1.

3.3.3 The spatially periodic boundary conditions

Usually spatially periodic media are considered. These media can be obtained by translation along the three axes of a unit cell. In order to calculate the macroscopic properties of spatially

Type of springs	η_2	η_0	Elastic constant
(1 0 0) linear springs belong to only one type of elastic element	1	0	$\frac{\alpha_2}{4}$
	2	0	$\frac{\alpha_2}{2}$
	3	0	$\frac{3\alpha_2}{4}$
	4	0	α_2
	0	1	$\frac{\alpha_0}{4}$
	0	2	$\frac{\alpha_0}{2}$
	0	3	$\frac{3\alpha_0}{4}$
	0	4	α_0
(1 0 0) linear springs belong to two types of elastic element	1	1	$\frac{\alpha_2 + \alpha_0}{4}$
	1	2	$\frac{\alpha_2 + 2\alpha_0}{4}$
	1	3	$\frac{\alpha_2 + 3\alpha_0}{4}$
	2	1	$\frac{2\alpha_2 + \alpha_0}{4}$
	3	1	$\frac{3\alpha_2 + \alpha_0}{4}$
	2	2	$\frac{3\alpha_2 + \alpha_0}{2}$
(1 1 0) linear springs	1	0	$\frac{\alpha_2}{2}$
	2	0	α_2
	0	1	$\frac{\alpha_0}{4}$
	0	2	$\frac{\alpha_0}{2}$
	1	1	$\frac{\alpha_2 + \alpha_0}{2}$
$\frac{\pi}{4}$ -angular springs	1	0	$\frac{\beta_2}{2}$
	2	0	β_2
	0	1	$\frac{\beta_0}{4}$
	0	2	$\frac{\beta_0}{2}$
	1	1	$\frac{\beta_2 + \beta_0}{2}$
$\frac{\pi}{3}$ -angular springs	1	0	β_2
	0	1	β_0

Table 3.2: Elastic constants of springs in the lattice.

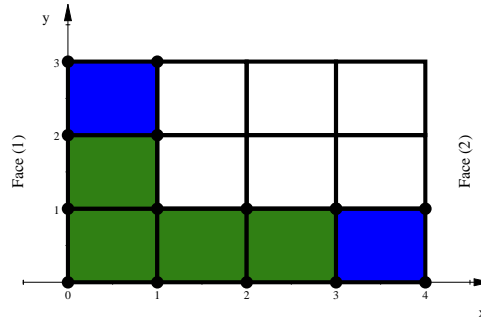


Figure 3.13: The unit cell which fully describes a spatially periodic medium.

periodic media, one has to determine the elastic properties of the unit cell by applying six different macro-strains. In this case, the unit cell is deformed and the displacements of opposite sides depend on each other (*Burla et al.*, 2009). The deformations and the displacements are described in Table 3.3.

These conditions must be applied to pairs of lattice points (two types) at opposite faces of the unit cell. Two opposite faces can be denoted with the superscript ⁽¹⁾ and with the superscript ⁽²⁾ where face ⁽¹⁾ is the first face met in the direction of the normal axis and face ⁽²⁾ is the second one (Figure 3.13). When the opposite faces have the same displacements, all the lattice points from face ⁽²⁾ correspond to lattice point from face ⁽¹⁾ and are connected to the previous layer by springs with spatial periodicity. The transformed unit cell now satisfies the prescribed condition of equal displacements at the opposite faces. However, to apply a nonzero macroscopic strain at the opposite faces, one does not need this step. Before starting the calculations with the Verlet algorithm, displacements corresponding to the desired macro-strain must be prescribed to pairs of solid lattice points at faces ⁽¹⁾ and ⁽²⁾. As a consequence, the total force acting on each point of the pair is equal to the sum of the forces acting on each point of the pair, separately. Then, the spatially periodic boundary conditions are satisfied because the corresponding points undergo the same displacement. A specific example of this problem was given by *Pazdniakou* (2012).

Macro-strain	yz-faces	xz-faces	xy-faces
ε_{xx}	$u_x^2 - u_x^1 = e; u_y^2 = u_y^1; u_z^2 = u_z^1$	$u_x^2 = u_x^1; u_y^2 = u_y^1; u_z^2 = u_z^1$	$u_x^2 = u_x^1; u_y^2 = u_y^1; u_z^2 = u_z^1$
ε_{yy}	$u_x^2 = u_x^1; u_y^2 = u_y^1; u_z^2 = u_z^1$	$u_x^2 = u_x^1; u_y^2 - u_y^1 = e; u_z^2 = u_z^1$	$u_x^2 = u_x^1; u_y^2 = u_y^1; u_z^2 = u_z^1$
ε_{zz}	$u_x^2 = u_x^1; u_y^2 = u_y^1; u_z^2 = u_z^1$	$u_x^2 = u_x^1; u_y^2 = u_y^1; u_z^2 = u_z^1$	$u_x^2 = u_x^1; u_y^2 = u_y^1; u_z^2 - u_z^1 = e$
ε_{xz}	$u_x^2 = u_x^1; u_y^2 = u_y^1; u_z^2 - u_z^1 = e$	$u_x^2 = u_x^1; u_y^2 = u_y^1; u_z^2 = u_z^1$	$u_x^2 = u_x^1; u_y^2 = u_y^1; u_z^2 = u_z^1$
ε_{yx}	$u_x^2 = u_x^1; u_y^2 = u_y^1; u_z^2 = u_z^1$	$u_x^2 - u_x^1 = e; u_y^2 = u_y^1; u_z^2 = u_z^1$	$u_x^2 = u_x^1; u_y^2 = u_y^1; u_z^2 = u_z^1$
ε_{zy}	$u_x^2 = u_x^1; u_y^2 = u_y^1; u_z^2 = u_z^1$	$u_x^2 = u_x^1; u_y^2 = u_y^1; u_z^2 = u_z^1$	$u_x^2 = u_x^1; u_y^2 - u_y^1 = e; u_z^2 = u_z^1$

Table 3.3: Spatially periodic boundary conditions corresponding to the six macro-strains.

3.3.4 Calculation of effective properties of porous media with two solids.

The final purpose of the model LSM2S is to determine the effective properties of porous media with many solid components. As in the basic LSM, they can be obtained by imposing spatially periodic boundary conditions on the unit cell as described above. Then, by using the Verlet algorithm, one can calculate the evolution of the displacement field. But, we must note that it is necessary to introduce a viscosity term θ to damp vibrations; the Verlet algorithm is given by

$$\mathbf{v}_i(t + \frac{\delta t}{2}) = \mathbf{v}_i(t) + \frac{\mathbf{a}_i(t)}{2} \delta t \quad (3.30a)$$

$$\mathbf{u}_i(t + \delta t) = \mathbf{u}_i(t) + \mathbf{v}_i(t + \frac{\delta t}{2}) \delta t \quad (3.30b)$$

$$\mathbf{a}_i(t + \delta t) = \frac{\mathbf{F}_i(t + \delta t)}{m_i} - \theta \mathbf{v}_i(t + \frac{\delta t}{2}) \quad (3.30c)$$

$$\mathbf{v}_i(t + \delta t) = \mathbf{v}_i(t + \frac{\delta t}{2}) + \frac{\mathbf{a}_i(t + \delta t)}{2} \delta t \quad (3.30d)$$

According to *Pazdniakou* (2012), the best value of θ that one can use is 0.5. When equilibrium is reached, the average stress tensor is calculated and the effective moduli can be obtained by

$$\langle \boldsymbol{\sigma} \rangle = \mathbf{C}^{(eff)} : \langle \boldsymbol{\varepsilon} \rangle \quad (3.31)$$

where $\langle \boldsymbol{\sigma} \rangle$ and $\langle \boldsymbol{\varepsilon} \rangle$ are the average values of stress and strain at the macroscopic level. In order to obtain the effective stiffness tensor, six simulations with the six macro-strains presented in Table 3.3 are needed. A code in Fortran was developed and can perform these six simulations.

Calculations of acoustic wave velocities in porous media with many solid components are similar to the ones in the basic LSM. The only difference is the average density over the unit cell $\langle \rho \rangle$ which is

$$\langle \rho \rangle = \frac{1}{V} \int_V \rho dV = \phi_0 \rho_0 + \phi_2 \rho_2 \quad (3.32)$$

where ϕ_0 and ϕ_2 are the proportions of inclusion and matrix in the media; ρ_0 and ρ_2 are the corresponding solid densities.

3.3.5 The algorithm

In this section, we discuss the numerical implementation of LSM2S. The code is developed from the basic LSM code; therefore, it is implemented using Fortran 90. The program flowchart is given in Table 3.4. Similar to LSM, the program spends most time in repeating the Verlet algorithm, in which the calculation of the elastic forces is the most demanding part. In order to decrease the number of objects calculated in the Verlet algorithm and to decrease the memory, loops of elastic force calculations are organized for springs, instead of lattice points. When the number of iterations meets the prescribed values (depending on the simulations) for real time simulations or when a convergence criterion is satisfied for static simulations, the calculations stop.

It is clear that the complexity of LSM2S model lies in the calculation of the spring elastic constants. One must calculate the constants for many types of springs. However, the calculation time for this part is not long; it is much less than the time spent in the Verlet algorithm. Therefore, the use of the LSM program and LSM2S program in order to simulate the media which have the same dimension (the same quantity of elementary cubes), are not very different in terms of simulation times.

The LSM and LSM2S are very often used to simulate real or reconstructed samples; they always have a large size; as a consequence, the required memory can be very large and the simulation time can be very long if the program only works on a single processor. With the same solution as *Pazdniakou* (2012), the OMP parallelization standard is used in our program for the loop of the Verlet algorithm. Thanks to this, the calculation time can be decreased depending on the number of threads. *Pazdniakou* (2012) pointed out that the average speed up $S(p)$ observed in simulations is about 5.2 when 8 threads are used and about 10.4 with 48 threads. The dependence of $S(p)$ on the number of threads according to Amdahl's law (*Che and Nguyen, 2014*) is presented in Fig. 3.14.

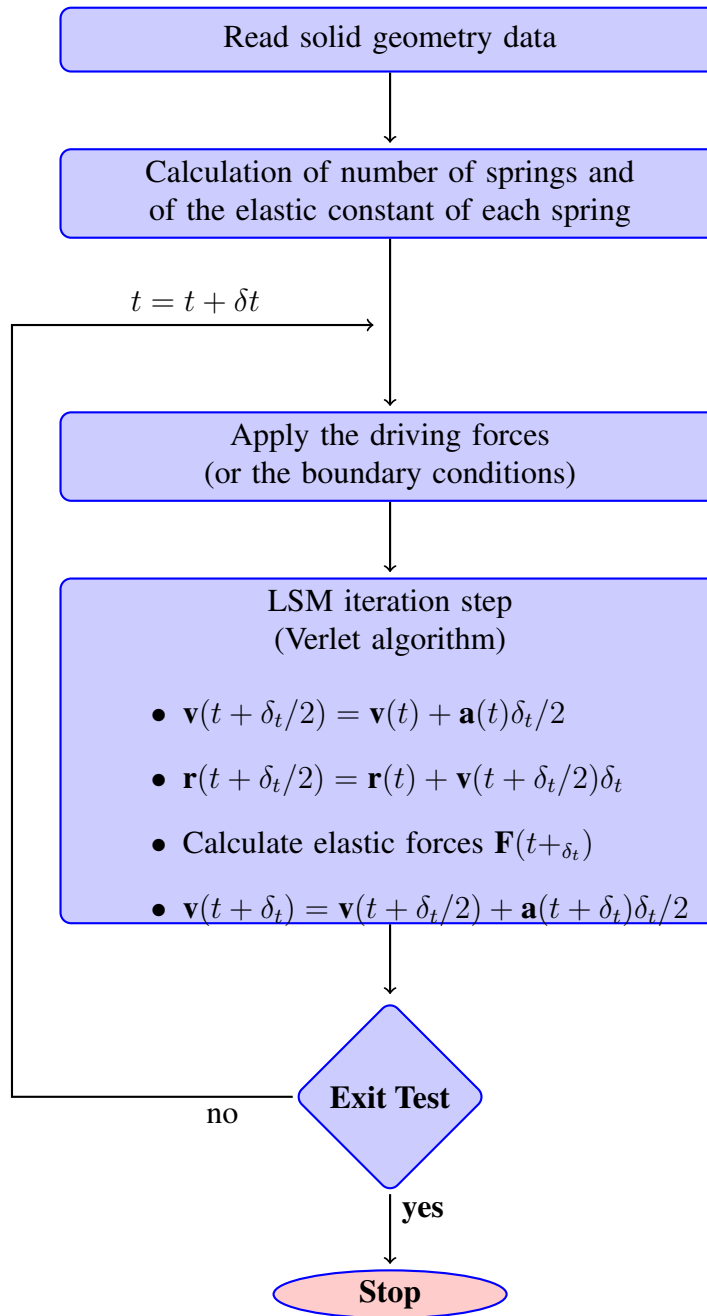


Table 3.4: The LSM2S program flowchart.

3.3.6 Validation

In order to validate LSM2S, some comparisons between our results and other methods are required. In fact, some methods can address media with two components such as the Clausius-Mossotti (CM) approximations of *Cohen* (2004), the approximate numerical solution of *Nemat-Nasser and Iwakuma* (1982) for ellipsoidal inclusions, the new perturbation expansions for the

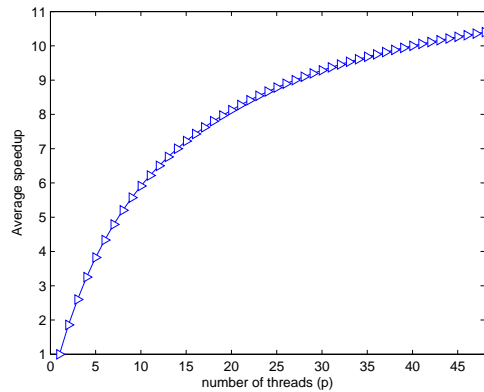


Figure 3.14: Amdahl's law for LSM and LSM2S. The speedup $S(P)$ as a function of the number of processors P .

effective stiffness tensor of *Torquato* (2000), the FFT solution of *Hoang-Duc and Bonnet* (2012), the numerical method FMD of *Malinouskaya* (2007)... These methods are limited; most of them are used for predicting effective properties of media with only two components (one solid - pore; two solids - non pore) and small sizes. Samples which have more than three components (two solids and pores) or with large sizes are more difficult to calculate. Therefore, the validation is performed by comparing the results for some simple samples that can be calculated by these methods.

3.3.6.1 Comparison with Cohen, Iwakuma and Nemat-Nasser and Torquato

Nemat-Nasser and Iwakuma (1982), *Torquato* (1998, 2000) and *Cohen* (2004) proposed approximation methods in order to predict the macroscopic properties of heterogeneous media. *Cohen* (2004) calculated the effective elastic moduli by applying the method of elastostatic resonances to 3D cubic arrays of spheres. One can obtain the leading order in this systematic perturbation expansion in the form of simple algebraic expressions for the elastic moduli. *Nemat-Nasser and Iwakuma* (1982) proposed a method which is applied to cubic arrays of spheres inclusions, of void spheres and of ellipsoidal inclusions. *Torquato* (1998) developed new perturbation expansions for the effective stiffness tensor which are absolutely convergent.

Thanks to these methods, some results for predicting the effective elastic moduli of a simple

cubic array of spheres (Fig. 3.15) were provided to which our results can be compared. These media include two solid components: the matrix and the inclusions.

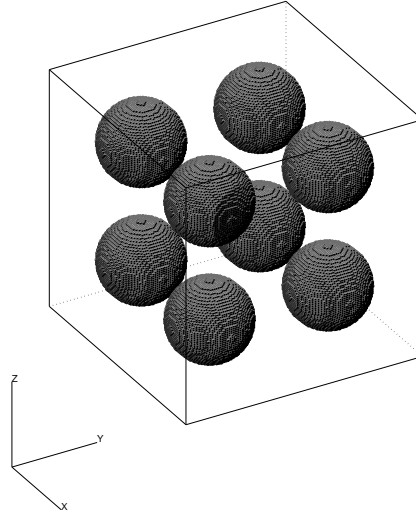


Figure 3.15: Simple cubic array of spheres. The matrix is transparent, the inclusions are grey.

The study is performed for various values of inclusion volume fraction ρ and for two solid components which have properties satisfying the following conditions $\nu_1 = \nu_2 = 0.3$, $G_1/G_2 = 3$. Some sample sizes were used; however, the differences between the results are small. Since the media are isotropic, only two simulations by LSM2S are needed in order to obtain the effective stiffness tensor which is reduced to

$$\mathbf{C}^{(eff)} = \begin{pmatrix} C_{1111} & C_{1122} & C_{1122} & 0 & 0 & 0 \\ C_{1122} & C_{1111} & C_{1122} & 0 & 0 & 0 \\ C_{1122} & C_{1122} & C_{1111} & 0 & 0 & 0 \\ 0 & 0 & 0 & C_{2323} & 0 & 0 \\ 0 & 0 & 0 & 0 & C_{2323} & 0 \\ 0 & 0 & 0 & 0 & 0 & C_{2323} \end{pmatrix} \quad (3.33)$$

Then, the effective bulk modulus K_e , the first effective shear module G_e , the second effective shear module G_e^* are defined by

$$K_e = \frac{C_{1111} + 2C_{1122}}{3}; \quad G_e = C_{2323}; \quad G_e^* = \frac{C_{1111} - C_{1122}}{2} \quad (3.34)$$

The dimensionless effective bulk modulus K_e/K_2 , the first shear modulus G_e/G_2 and the second shear modulus G_e^*/G_2 are gathered and compared in Tables 3.5 and 3.6.

ρ	LSM2S	<i>Cohen</i> (2004)	N & I (1982)	<i>Torquato</i> (2000)	Error (%)
0.05	1.047	1.046	1.046	1.046	0.1
0.1	1.096	1.095	1.095	1.095	0.1
0.15	1.147	1.146	1.147	1.146	0.1
0.2	1.204	1.201	1.202	1.201	0.2
0.25	1.261	1.259	1.260	1.260	0.2
0.3	1.324	1.321	1.323	1.323	0.2
0.4	1.468	1.459	1.461	1.464	0.6
0.5	1.644	1.618	1.620	1.634	1.6

Table 3.5: The effective bulk modulus K_e/K_2 . Comparisons of LSM2S with *Cohen* (2004); *Nemat-Nasser and Iwakuma* (1982); *Torquato* (2000).

ρ	G_e/G_2				G_e^*/G_2			
	LSM2S	<i>Cohen</i>	N & I	Error (%)	LSM2S	<i>Cohen</i>	N & I	Error (%)
0.05	1.053	1.051	1.052	0.2	1.055	1.054	1.054	0.1
0.1	1.105	1.103	1.104	0.2	1.117	1.115	1.116	0.2
0.15	1.159	1.157	1.157	0.2	1.184	1.181	1.182	0.3
0.2	1.214	1.212	1.213	0.2	1.257	1.254	1.255	0.2
0.25	1.273	1.270	1.271	0.2	1.336	1.331	1.333	0.4
0.3	1.336	1.332	1.336	0.3	1.420	1.413	1.415	0.5
0.4	1.478	1.467	1.469	0.7	1.609	1.588	1.590	1.3
0.5	1.659	1.627	1.629	1.9	1.807	1.771	1.774	2.0

Table 3.6: The first shear modulus G_e/G_2 and the second shear modulus G_e^*/G_2 . Comparison of LSM2S with *Cohen* (2004); *Nemat-Nasser and Iwakuma* (1982).

As it can be seen, the differences between LSM2S and the CM-type approximation *Cohen* (2004); *Nemat-Nasser and Iwakuma* (1982) and the third-order approximation *Torquato* (2000) are very small even at high inclusion volume fraction. The maximal error is always less than 2%. The results of LSM2S are very close to the others, and this demonstrates the accuracy of the LSM2S model in the calculation of the effective properties for the media with two solids.

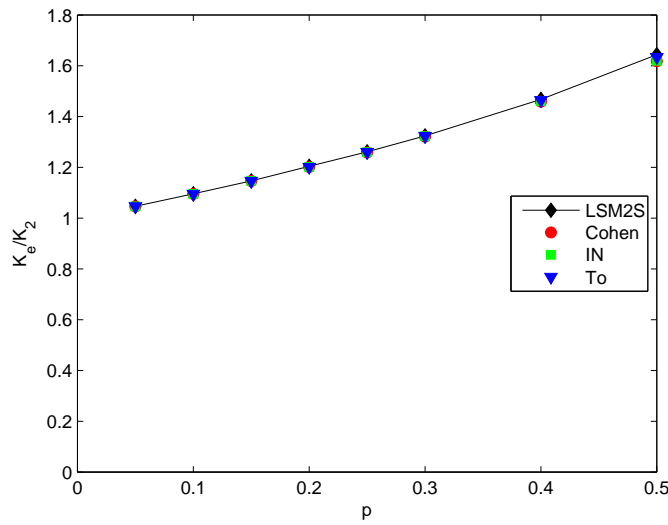


Figure 3.16: The effective bulk modulus K_e/K_2 . Comparison of LSM2S (black) with the results of Cohen (2004) (red), Nemat-Nasser and Iwakuma (1982) (green) and Torquato (2000) (blue).

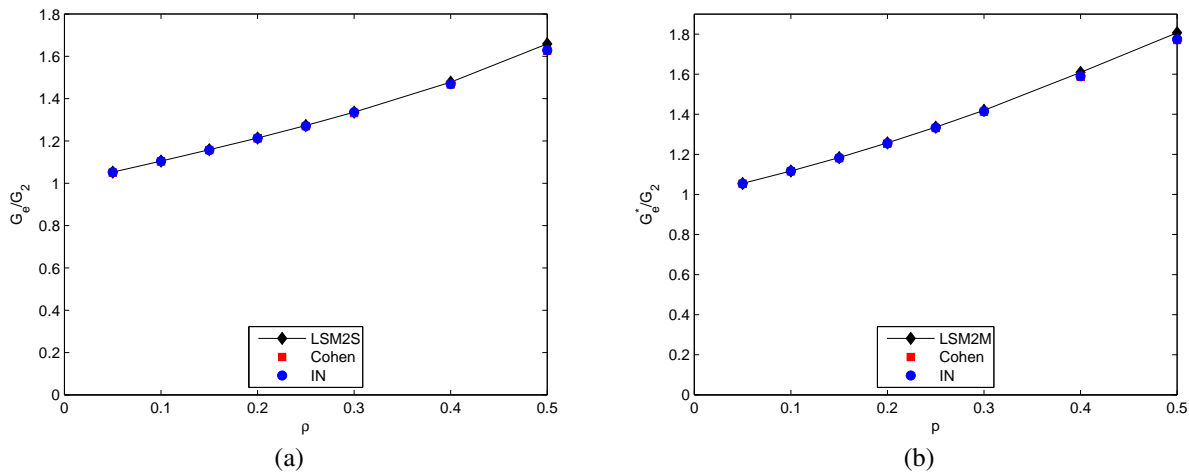


Figure 3.17: (a) The first shear modulus G_e/G_2 , (b) The second shear modulus G_e^*/G_2 . Comparison of LSM2S (black) with the results of Cohen (2004) (red), Nemat-Nasser and Iwakuma (1982) (blue).

3.3.6.2 Comparison with FMD (Malinouskaya, 2007)

Malinouskaya (2007) developed the FMD solver in order to calculate effective properties of heterogeneous materials. FMD which is based on a finite volume formulation, operates on a tetrahedral mesh which can be structured or unstructured; it uses a first order space discretization.

Depending on the ways of splitting the cubic elements into tetrahedra, 4 types of mesh are defined:

- SCT_6 : tetrahedral mesh obtained by splitting cubic elements into a pattern of 6 tetrahedra.
- SCT_{24} : tetrahedral mesh obtained by splitting cubic elements into a pattern of 24 tetrahedra.
- SUT: tetrahedral mesh obtained by an advancing front technique in the solid, starting from a description of the solid surface on a cubic grid.
- TUT: fully unstructured tetrahedral mesh.

These different meshes are shown in Fig. 3.18.

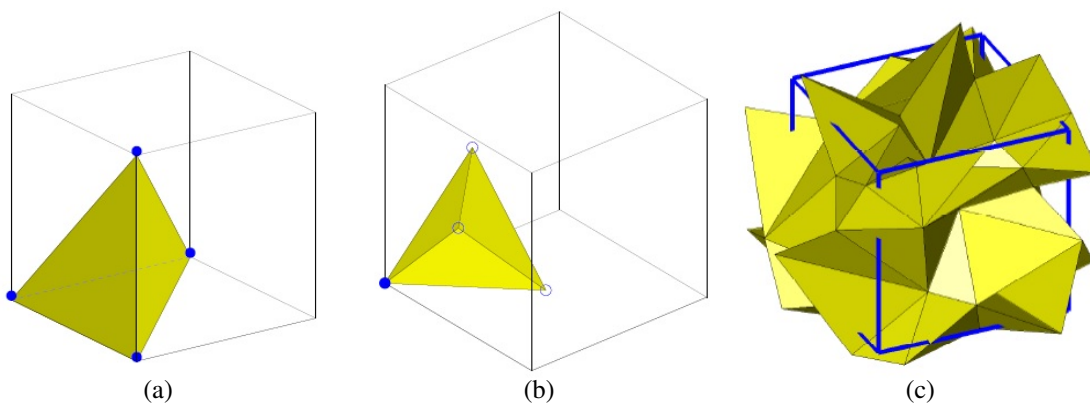


Figure 3.18: Partitions of the elementary cubes into meshes. (a) SCT_6 contains 6 identical tetrahedra. (b) SCT_{24} contains 24 identical tetrahedra. (c) SUT.

A comparison with *Cohen (2004)*; *Nemat-Nasser and Iwakuma (1982)*; *Torquato (2000)* shows that LSM2S works correctly with two components with the same Poisson ratio. For two components with different Poisson ratios, in order to validate LSM2S, some comparisons with the FMD solver are performed. The considered media are the same as *Cohen (2012)*, i.e., a simple cubic array of spheres with various inclusion volume fractions ρ . The elastic properties of the matrix and of the inclusion and the corresponding Young modulus and Poisson ratio are given in Table 3.7.

Elastic modulus	Bulk modulus	Shear modulus	Young modulus	Poisson ratio
Matrix	30	20	49.091	0.2273
Inclusion	100	50	128.57	0.2857

Table 3.7: Elastic properties of the composite material.

According to *Malinouskaya* (2007), SCT24 gives better results than SCT6; therefore, LSM2S and SCT24 are compared. The effective bulk modulus K_e , the first and the second effective shear modulus G_e , G_e^* in GPa are given and compared in Table 3.8.

ρ	K_e			G_e			G_e^*		
	LSM2S	SCT24	Error	LSM2S	SCT24	Error	LSM2S	SCT24	Error
	(GPa)		(%)	(GPa)		(%)	(GPa)		(%)
0.1	33.3813	33.3975	0.05	21.7745	21.7812	0.03	21.9349	21.9490	0.06
0.2	37.1639	37.1914	0.07	23.6346	23.6454	0.05	24.1731	24.1982	0.1
0.3	41.4558	41.4961	0.1	25.6526	25.6683	0.06	26.6904	26.7250	0.13
0.4	46.4316	46.4880	0.12	27.9292	27.9508	0.08	29.4419	29.4548	0.04
0.5	52.7912	52.8714	0.2	30.8012	30.8316	0.1	32.5498	32.8037	0.8

Table 3.8: The effective bulk modulus K_e , the first and the second effective shear modulus G_e , G_e^* . Comparisons of LSM2S with FMD (SCT24).

Figure 3.19 compares the results of LSM2S and FMD solvers. For the samples with small inclusion volume fraction $\rho = 0.1$, the differences of effective bulk moduli, first and second shear moduli are very small and less than 0.1%. The maximal error for the samples with $\rho = 0.5$, the difference between the second effective shear moduli in this case is 0.8%. Thanks to these comparisons, LSM2S is able to calculate the media composed by two solid components with very different elastic properties.

3.3.6.3 Comparison with the FFT solution of *Hoang-Duc and Bonnet* (2012)

Hoang-Duc and Bonnet (2012) presented a new method which allows the prediction of the effective properties of inclusion-matrix heterogeneous media. This method is based on an approx-

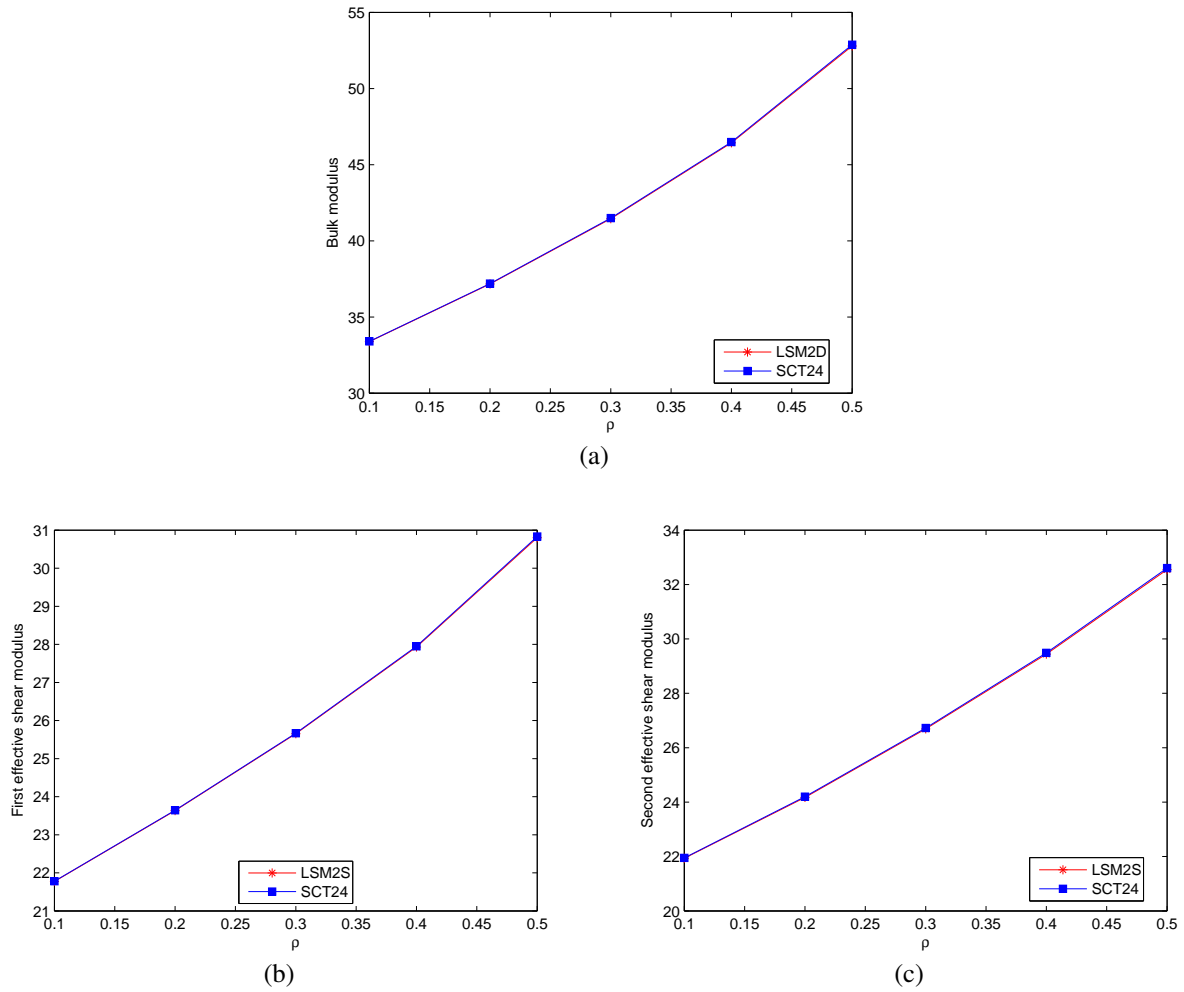


Figure 3.19: Comparisons of LSM2S (red) with the results of the FMD solver (blue). (a) The effective bulk modulus K_e . (b) The first effective shear modulus G_e . (c) The second effective shear modulus G_e^* .

imate FFT based solution which yields the effective properties of elastic media. The considered media are the same as in the previous comparisons; the elastic properties of the matrix and of the inclusion are the same as for the former comparison with FMD (Table 3.7). The effective bulk modulus K_e , the first effective shear modulus G_e are given and compared in Table 3.9.

The results of bulk moduli calculated by LSM2S seem quite close to the FFT solution; the maximal difference is equal to 0.17% when ρ is 0.5. However, a problem is met in the comparison of the first effective shear moduli; for small values of the inclusion volume fraction (0.1 and 0.2), the results are still good and the maximal error is 1.6%; but when ρ increases, the comparison gets

ρ	K_e			G_e		
	LSM2S	FFT	Error	LSM2S	FFT	Error
	(GPa)		(%)	(GPa)		(%)
0.1	33.4443	33.4346	0.03	21.7606	21.831	0.3
0.2	37.1494	37.1963	0.13	23.63	24.01	1.6
0.3	41.467	41.449	0.04	25.716	26.549	3.2
0.4	46.4371	46.3557	0.17	27.965	29.225	4.5
0.5	52.6603	52.5701	0.17	30.7419	32.1127	4.5

Table 3.9: The effective bulk modulus K_e and the first effective shear modulus G_e . Comparison of LSM2S with the results of the FFT solution.

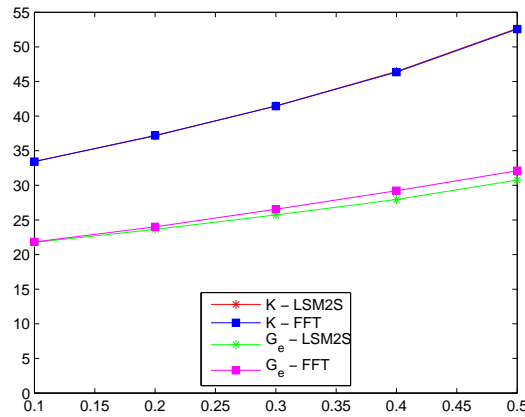


Figure 3.20: The effective bulk modulus K_e and the first effective shear modulus G_e . Comparison of LSM2S with the results of the FFT solution.

worse; the error for $\rho = 0.5$ reaches 4.4%. Note that the results of the FFT solution were only compared with bounds of Voigt and Reuss *Hoang-Duc and Bonnet (2012)*.

3.4 The coupled models: LBM-LSM and LBM-LSM2S

The interactions between the fluid and solid phases in porous media are needed for many practical applications such as the numerical studies of seismic processes in a fluid rock system. In our case, as said before, they are necessary for the determination of coefficients α and β which characterize the reaction of the solid matrix on the fluid pressure. In this thesis, it is solved by the coupled LBM-LSM model.

There are some coupled LBM-LSM models in which the elastic medium is described by LSM (*Pazdaniakou, 2012; Buxton et al., 2005; Wu and Aidun, 2009*). The usual connection between LSM and LBM is to use the momentum exchange algorithm (*Ladd and Verberg, 2001*); this means that the momentum of the solid phase is exchanged with the one of the neighbouring liquid lattice nodes. There are many ways to apply this algorithm; in *O'Brien and Bean. (2004)*, the solid and fluid lattice nodes are considered as in the same lattice, or in *Buxton et al. (2005)*, the solid is described by the LSM free and the solid nodes for momentum exchanged are defined as the LBM lattice nodes located within a distance of the LSM nodes.

This section presents the coupled LBM-LSM model which is used in calculations of acoustic waves velocities in saturated porous media. Then, the development of the coupled LBM-LSM2S model is also described for porous media with two solid components.

3.4.1 Geometry

As for LSM and LBM, the medium geometry is presented by the phase function $Z(i, j, k)$ given by (2.4). Then, each solid voxel is replaced by one elastic element created by eight lattice points as in LSM, while each liquid voxel is presented by a single lattice node located at the centre of the LBM voxel (*Pazdaniakou, 2012*) (Fig. 3.21.a). The same lattice step δ is used for both LBM and LSM; in our calculation, δ is equal to 1 for simplicity. The lattices of LSM and LBM are shifted by $\frac{\delta}{2}$ one with respect to another. Then, the solid is located exactly at half a lattice step for the liquid node (Fig. 3.21.b); thus, the bounce-back boundary condition in LBM can be directly applied in our model.

Since the model is used for calculating the acoustic velocities, the displacement of solid points (LSM lattice nodes) is supposed to be very small; therefore, the geometry of the medium is supposed to be unchanged.

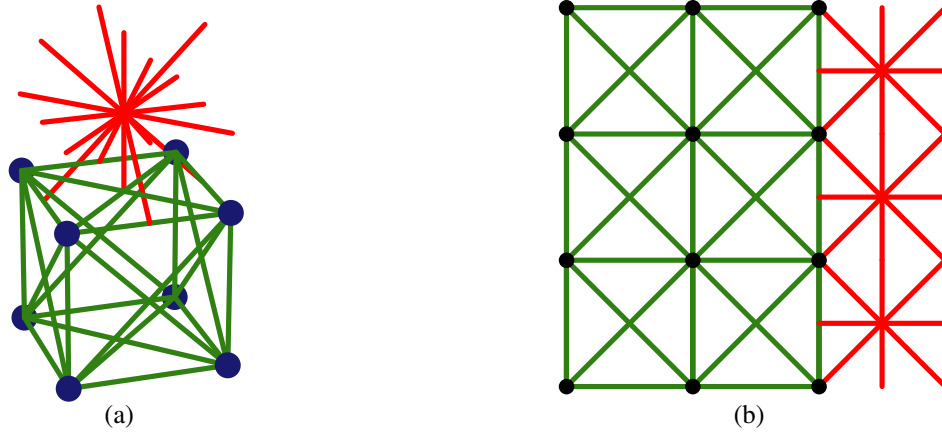


Figure 3.21: (a) The two lattices in the LBM-LSM model. The LSM lattice points (blue) and springs (green) represent the solid, the LBM lattice point (red) represents the fluid. (b) The solid-fluid interface. The solid is located exactly at half a lattice step for the liquid node.

3.4.2 Boundary conditions

In order to couple LBM and LSM, the forces acting on the fluid and solid phases at the interfaces are needed. The volume force $\mathbf{F}^{(s)}$ on an elastic solid medium is given by

$$F_i^{(s)} = \sum_j \partial_j \sigma_{ij}^{(s)} = (\nabla \cdot \sigma^{(s)})_i \quad (3.35)$$

where $\sigma^{(s)}$ is the elastic stress tensor. The equilibrium condition in the case of no external force is given by

$$\nabla \cdot \sigma^{(s)} = 0 \quad (3.36)$$

According to Pazdniakou (2012), the momentum flux tensor for fluids with viscous dissipation is given by

$$\Pi_{ij} = p\delta_{ij} + \rho^{(f)}v_i^f v_j^f - \tau_{ij}^{(f)} \quad (3.37)$$

where p is the fluid pressure, $\rho^{(f)}$ the fluid density, v_i^f the fluid velocity and $\tau_{ij}^{(f)}$ the viscous stress tensor. In the general case, $\tau_{ij}^{(f)}$ is given by

$$\begin{aligned} \tau_{ij}^{(f)} &= \mu^{(f)}(\partial_i v_j^{(f)} + \partial_j v_i^{(f)}) + \lambda^{(f)}(\nabla \cdot \mathbf{v}^{(f)})\delta_{ij} \\ &= \mu^{(f)}(\partial_i v_j^{(f)} + \partial_j v_i^{(f)}) - \frac{2}{3}(\nabla \cdot \mathbf{v}^{(f)})\delta_{ij} + \zeta^{(f)}(\nabla \cdot \mathbf{v}^{(f)})\delta_{ij} \end{aligned} \quad (3.38)$$

where $\mu^{(f)}$ is the dynamic viscosity (the first viscosity coefficient), $\lambda^{(f)}$ the second viscosity coefficient and $\zeta^{(f)}$ the bulk viscosity.

The total fluid stress tensor $\sigma_{ij}^{(f)}$ is defined by

$$\sigma_{ij}^{(f)} = -p\delta_{ij} - \tau_{ij}. \quad (3.39)$$

For an incompressible fluid, it is simplified into

$$\sigma_{ij}^{(f)} = -p\delta_{ij} - \mu^{(f)}(\partial_i v_j^{(f)} + \partial_j v_i^{(f)}) \quad (3.40)$$

According to the no-slip boundary condition, the fluid and solid velocities are the same at the solid-fluid interfaces

$$\mathbf{v}^{(f)} = \mathbf{v}^{(s)} \quad (3.41)$$

The fluid and solid forces acting on the surface element $d\mathbf{s}$ of area $|d\mathbf{s}|$ at the interfaces are expressed as

$$F_i^{(f)} = -|d\mathbf{s}|\sigma_{ij}^{(f)}n_j = |d\mathbf{s}|(n_i p - \tau_{ij}) \quad , \quad (3.42a)$$

$$F_i^{(s)} = |d\mathbf{s}|\sigma_{ij}^{(s)}n_j = \boldsymbol{\sigma}_s \cdot d\mathbf{s} \quad (3.42b)$$

where \mathbf{n} is the unit normal directed from solid into fluid. Thanks to these two relations, the second boundary condition is derived as

$$\boldsymbol{\sigma}^{(f)} \cdot \mathbf{n} = \boldsymbol{\sigma}^{(s)} \cdot \mathbf{n} \quad (3.43)$$

3.4.3 LBM-LSM coupling

The momentum exchange algorithm is an effective way to connect LBM to LSM (*Ladd and Verberg, 2001; Buxton et al., 2005; Wu and Aidun, 2009*). It is used to take into account the forces exerted by fluids on the solid wall. The physical principles of this method can be described quite simply. A particle moving straight with a velocity \mathbf{c}_i collides a perpendicular solid wall moving with a velocity $\mathbf{u}^{(s)} \ll \mathbf{c}_i$. The post-collision particle velocity is $-\mathbf{c}_i + 2\mathbf{u}^{(s)}$ and the force exerted on the wall is proportional to $\mathbf{c}_i - \mathbf{u}^{(s)}$.

According to *Pazdniakou (2012)*, in LBM, the main hydrodynamic variables such as the fluid density $\rho^{(f)}$, the fluid momentum $\mathbf{j}^{(f)}$ and the momentum flux tensor $\boldsymbol{\Pi}$ are expressed by using the particle distribution function \mathbf{f} and the set of discrete velocities \mathbf{c}_i

$$\rho^{(f)} = \sum_i^q f_i = \sum_i^q f_i^{(eq)} \quad , \quad (3.44a)$$

$$j_\alpha^{(f)} = \sum_i^q f_i c_{i\alpha} = \sum_i^q f_i^{(eq)} c_{i\alpha}, \quad (3.44b)$$

$$\Pi_{\alpha\beta} = \sum_i^q f_i c_{i\alpha} c_{i\beta} \quad . \quad (3.44c)$$

The equilibrium momentum flux tensor is given by

$$\Pi_{\alpha\beta}^{(eq)} = \sum_i^q f_i^{(eq)} c_{i\alpha} c_{i\beta} = \rho^{(f)} c_s^2 \delta_{\alpha\beta} + \rho v_\alpha^f v_\beta^f \quad (3.45)$$

where the equilibrium distribution is given by

$$f_i^{(eq)}(\rho, \mathbf{u}) = \rho \omega_i^* + \rho \omega_i \left[\frac{1}{c_s^2} (\mathbf{c}_i \cdot \mathbf{u}) + \frac{1}{2c_s^2} |\mathbf{u}|^2 \right] \quad . \quad (3.46)$$

Then, the viscous stress tensor can be derived as

$$\tau_{\alpha\beta} = -(\Pi_{\alpha\beta} - \Pi_{\alpha\beta}^{(eq)}) = - \sum_i^q f_i^{(neq)} c_{i\alpha} c_{i\beta} \quad , \quad (3.47)$$

where $f_i^{(neq)}$ is the non-equilibrium part of the distribution function.

In our model, the LSM lattice is shifted with respect to the LBM lattice and the no-slip surface is now located exactly at the solid surface; therefore, it is simple to apply the bounce-back boundary conditions in. The solid interface point $\mathbf{r}^{(s)}$ neighbouring some liquid lattice node $\mathbf{r}^{(f)}$ is expressed as

$$\mathbf{r}^{(s)} = \mathbf{r}^{(f)} + \frac{1}{2} \mathbf{c}_i^{(b)} \quad (3.48)$$

According to *Ladd and Verberg (2001)* and *Nguyen and Ladd (2002)*, the reflected particle distribution $f_{i'}$ with the bounce-back boundary conditions is derived as

$$f_{i'}(\mathbf{r}^{(f)}, t + \delta_t) = \tilde{f}_i(\mathbf{r}^{(f)}, t) - \frac{2\omega_i \rho^{(f)} (\mathbf{u}^{(s)} \cdot \mathbf{c}_i)}{c_s^2} \quad , \quad (3.49)$$

where $\mathbf{u}^{(s)}$ is the velocity of the solid interface. It is clear that in our model, $\mathbf{r}^{(s)}$ belongs to the edge of the elastic element or to its face centre; then, $\mathbf{u}^{(s)}$ is calculated as the average of the edge endpoints velocities or average of the face vertices, respectively.

The force exerted by the fluid on the solid wall due to the momentum transferred during the time step δ_t is given by

$$\begin{aligned} \mathbf{F}(\mathbf{r}^{(s)}, t + \frac{\delta_t}{2}) &= [\mathbf{c}_i \tilde{f}_i(\mathbf{r}^{(f)}, t) - \mathbf{c}_{i'} f_{i'}(\mathbf{r}^{(f)}, t + \delta_t)] \frac{\delta_x^3}{\delta_t} \\ &= 2\mathbf{c}_i \left[\tilde{f}_i(\mathbf{r}^{(f)}, t) - \frac{\omega_i \rho^{(f)} (\mathbf{u}^{(s)} \cdot \mathbf{c}_i)}{c_s^2} \right] \frac{\delta_x^3}{\delta_t} \end{aligned} \quad (3.50)$$

This calculated force is equally distributed between the endpoints or face vertices depending on the location of the solid interface point. According to *Pazdaniakou* (2012), if at the equilibrium the fluid does not exert any pressure on the liquid-solid interface, (3.50) becomes

$$\mathbf{F}(\mathbf{r}^{(s)}, t + \frac{\delta_t}{2}) = 2\mathbf{c}_i[\tilde{f}_i(\mathbf{r}^{(f)}, t) - \frac{\omega_i\rho^{(f)}(\mathbf{u}^{(s)} \cdot \mathbf{c}_i)}{c_s^2} - \omega_i\rho_0^{(f)}] \frac{\delta_x^3}{\delta_t} \quad (3.51)$$

where $\omega_i\rho_0^{(f)}$ is the pressure at equilibrium.

3.4.4 Implementation aspects

The code of the coupled LBM-LSM model is based on the Fortran codes of LBM and LSM. The program flowchart is displayed in Fig. 3.22. Since the detailed flowcharts of LBM and LSM are described, this subsection presents only the coupling between them. As can be seen in the flowchart, after reading the solid and liquid geometry of the medium, the main loop starts with the collision step and then the propagation step as in LBM. During the LBM-LSM boundary condition step, the force $\mathbf{F}(\mathbf{r}^{(s)})$ exerted by the liquid on the solid interface point $\mathbf{r}^{(s)}$ is calculated by the momentum exchange algorithm; it is used in order to execute the LSM iteration (Verlet algorithm). The LSM iteration gives $\mathbf{u}^{(s)}$ which is needed to calculate the reflected distribution function $f_i(\mathbf{r}^{(f)}, t + \delta_t)$ by using the bounce-back rule (3.49).

As for LBM and LSM, the LBM-LSM program is parallelized by OMP. The principles of parallelization were presented in the Section 3.2. Some applications of the coupled LBM-LSM model to simple cases are considered in *Pazdaniakou* (2012). The average speedup in the simulations is about 5.1 for 8 processors and it can be considered as a good result.

This model is used to calculate the coefficients $\bar{\alpha}$, \mathbf{B} (α and β) which characterize the reaction of the solid matrix to the fluid pressure. They are used to determine the acoustic velocities by solving the Christoffel equation which is discussed in Chapter 2.

3.4.5 Development of the coupled LBM-LSM2S model

In order to calculate the coefficients α and β of porous samples with two solid components, the coupled LBM-LSM2S model is an extension of the LBM-LSM model. The geometry of the

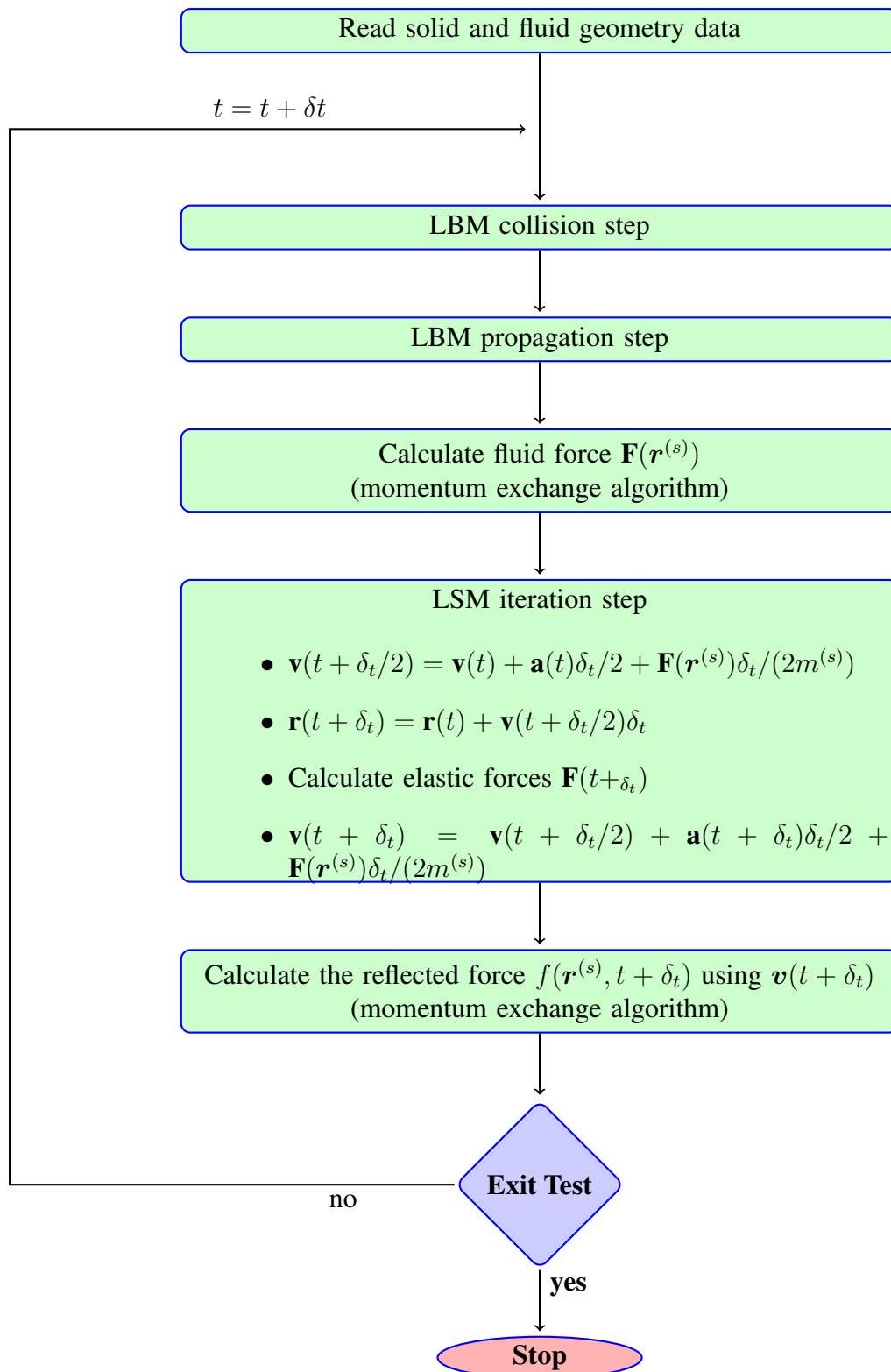


Figure 3.22: The LBM-LSM program flowchart.

medium is similar to the one in LSM2S. The elastic constants of springs are calculated in the same way as in Section 3.3. A code of LBM-LSM2S is developed based on the code of LBM-LSM2S. The required memory for simulations is larger than the LBM-LSM model but the computation time is not very different. A simple comparison is performed when the sample FB18 is simulated by these models and the obtained results are the same.

3.5 Summary

In this chapter, the lattice spring models such as LSM, LSM2S, LBM-LSM and LBM-LSM2S are presented; they can address porous media with one or two solid components. By using these models and LBM, the four necessary quantities (the effective stiffness tensor C^{eff} , the permeabilities K , the reactions of the solid matrix on the fluid pressure α and β) for the Christoffel equation can be determined, from which one can obtain the acoustic velocities in dry and in saturated porous media.

The simulation time and memory requirements of numerical simulations for real samples are large. They are parallelized by OMP and the time is inversely proportional to the number of processors used; the averaged speedup is about 5.1 for 8 processors which is a good result.

All the necessary tools for calculating the acoustic velocities in dry and saturated samples are available. They will be applied to simulate the Fontainebleau samples and Statoil samples and the results will be shown in the next chapters.

Chapter 4

Acoustic wave velocities in Fontainebleau samples

4.1 Introduction

The purpose of this chapter is to study the mechanical behaviour and the propagation of acoustic waves in dry and saturated Fontainebleau sandstones. Fontainebleau is one of the most studied porous media theoretically (*Adler, 1992; Ferréol and Rothman, 1995*)... and experimentally (*Han, 1986; Han et al., 1986; Gomez et al., 2010*)... This study is of importance in many areas of physics and it has various practical applications such as the study of fracturing processes and elastic behaviour of materials.

This chapter is devoted to four measured samples of Fontainebleau sandstone with porosities ranging from 0.08 to 0.23, namely FB8, FB13, FB18 and FB22. They are all cubes of side 2736 μm .

First, their porosities and correlation functions are determined as indicated in Chapter 2. In order to derive the acoustic velocities in dry samples, the macroscopic mechanical properties such as the effective stiffness tensor are needed. The Lattice Spring Model (LSM) developed by *Pazdaniakou (2012)* is used to study mechanical properties as well as propagation of elastic waves in dry samples (*Zhao et al., 2010*). These Fontainebleau samples can be directly simulated by LSM in order to derive the effective stiffness tensors and the acoustic waves velocities. The problem of samples with large sizes can be solved by introducing the coarsening method. Then, the results of coarsened samples can be extrapolated. Our numerical results are the macroscopic Young modulus, the Poisson ratio, the bulk modulus and the acoustic velocities; they are compared

to experimental data (*Han, 1986; Han et al., 1986; Gomez et al., 2010*) and to other simulations (*Arns, 1996; Nur et al., 1991; Krief, 1990*).

Finally, the saturated samples are considered. When there is only one solid (quartz) component, algorithms such as LSM, LBM, LBM-LSM are used to derive the four necessary quantities C , K , α , and β of the Christoffel equation. As indicated in Chapter 2, the calculations are done for the original samples and their mirror configurations in order to estimate them more precisely. Then, three types of waves namely the fast compressional wave, the slow compressional wave and the shear wave with corresponding velocities are calculated by solving the generalized Christoffel equation. In this thesis, the influence of fluids on acoustic properties is also studied; the calculations are performed when the pores are filled by three types of fluids: incompressible, slightly compressible (water in normal conditions) and highly compressible fluids. Some comparisons with the Gassmann's model (*Gassmann, 1951; Fredy and Alvarado, 2006*) which was presented in Chapter 2 are also given.

This chapter is organized as follows. In Section 4.2, the sample porosities and the two point correlation functions *Nguyen (2013)* of the four samples are calculated. In the third Section, the acoustic velocities in dry samples are calculated. Some comparisons are performed in order to study the influence of porosity on the macroscopic properties and on velocities. Some additional comparisons are presented in Section 4.4. The diffusion formation factor F and the characteristic length Λ are calculated in Section 4.5. Section 4.6 yields the four necessary quantities C , K , α , β and solves the Christoffel equation in the samples saturated by the three types of fluids. Then, the acoustic velocities are derived and compared with the ones of the Gassmann's model. Finally, some conclusions are given in the last section.

4.2 Characterizations of Fontainebleau samples

Four reconstructed samples of Fontainebleau sandstones were provided by STATOIL; they are obtained from the real sandstones by micro-CT and have different porosities given by the suffix to their name in percent

- Sample Fontainebleau FB8

- Sample Fontainebleau FB13
- Sample Fontainebleau FB18
- Sample Fontainebleau FB22

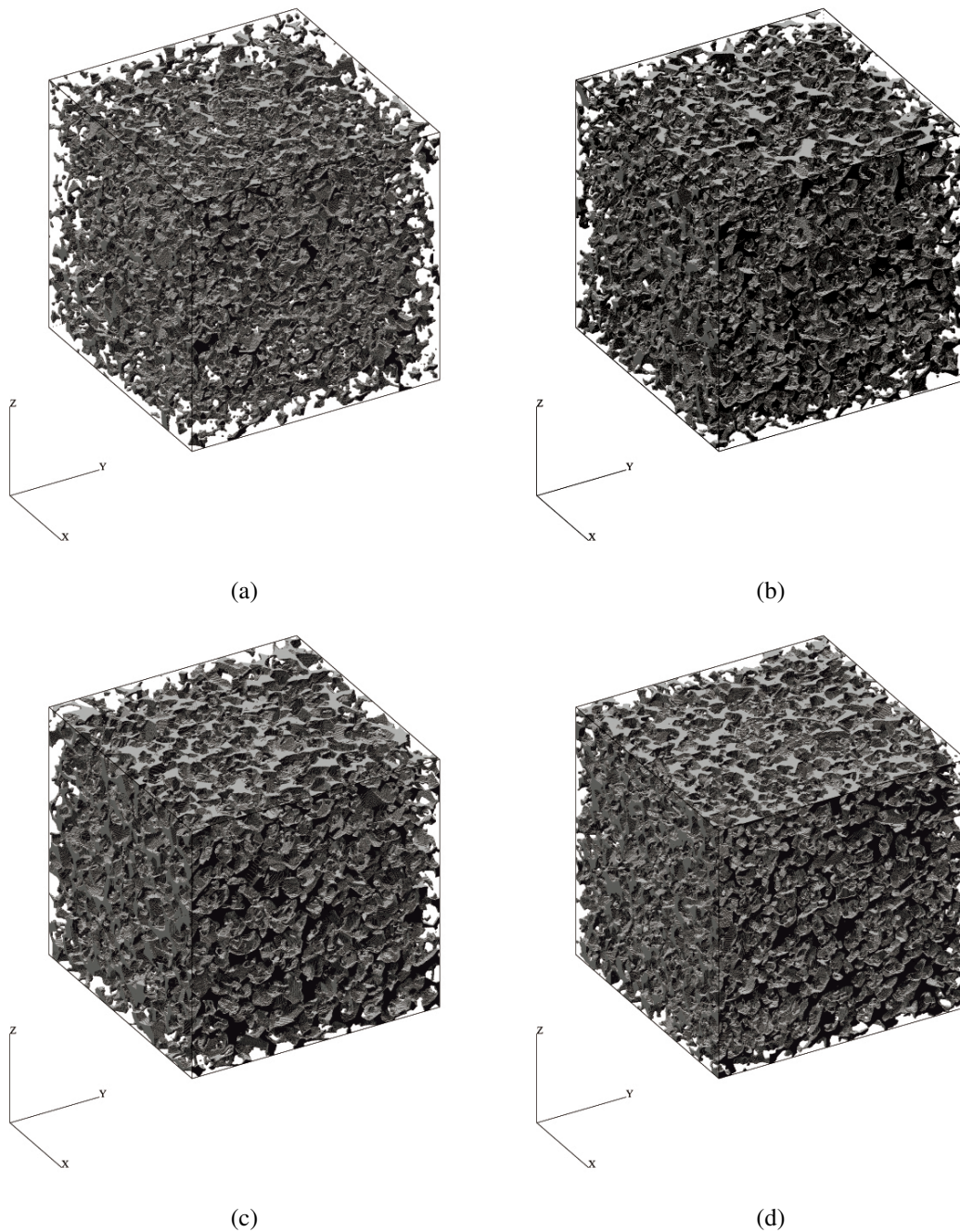


Figure 4.1: (a) Sample FB8. (b) Sample FB13. (c) Samples FB18. (d) Sample FB22. The pores are grey and the solid transparent.

These samples have the same form, namely a cube of side $2736\mu m$; they are divided into $(480)^3$ elementary cubes of size $a = 5.7\mu m$. They include 2 components: 0 is pore and 3 is quartz. In order to make it suitable for our present program, it is necessary to change the labels: 0 is quartz (solid) and 1 is pore. As described in Chapter 2, the pore space of these porous samples can be characterized by the phase function $Z(\mathbf{r})$ given by (2.4).

4.2.1 Sample FB8

The sample FB8 has the smallest porosity among the four Fontainebleau samples. It is displayed in Figure 4.1.a; the pores are grey and the solid transparent.

Sample porosity

As mentioned in Section 2.2 devoted to methodologies, the porosity of the sample is calculated in the following way:

- Calculate porosity for each slice along each direction. The porosities are denoted by $\varepsilon(x)$, $\varepsilon(y)$ and $\varepsilon(z)$.
- Calculate the total number of elements present in the surface $N_{total} = N_{cx} \cdot N_{cy}$
- Calculate the number of porous elements present in the surface: N_{porous} .
- Porosity of each slice:

$$\varepsilon(z_i) = \frac{N_{porous}}{N_{total}} \quad (4.1)$$

where $z = \frac{z'}{a}$ with z' is the distance from the calculation slice to the boundary along the z-axis.

Calculations are performed along the x-,y- and z- directions; the porosities along each direction are displayed in Fig. 4.2. The maximal and minimal values are equal to 0.103 and 0.0603, denoted by $\varepsilon_M(x)$ and $\varepsilon_m(x)$ along the x-direction, respectively; $\varepsilon_M(y) = 0.11$ and $\varepsilon_m(y) = 0.057$ along the y-direction; $\varepsilon_M(z) = 0.1$ and $\varepsilon_m(z) = 0.07$ along the z-direction. The average porosities along the three different directions are equal to $0.08289 \approx 0.083$.

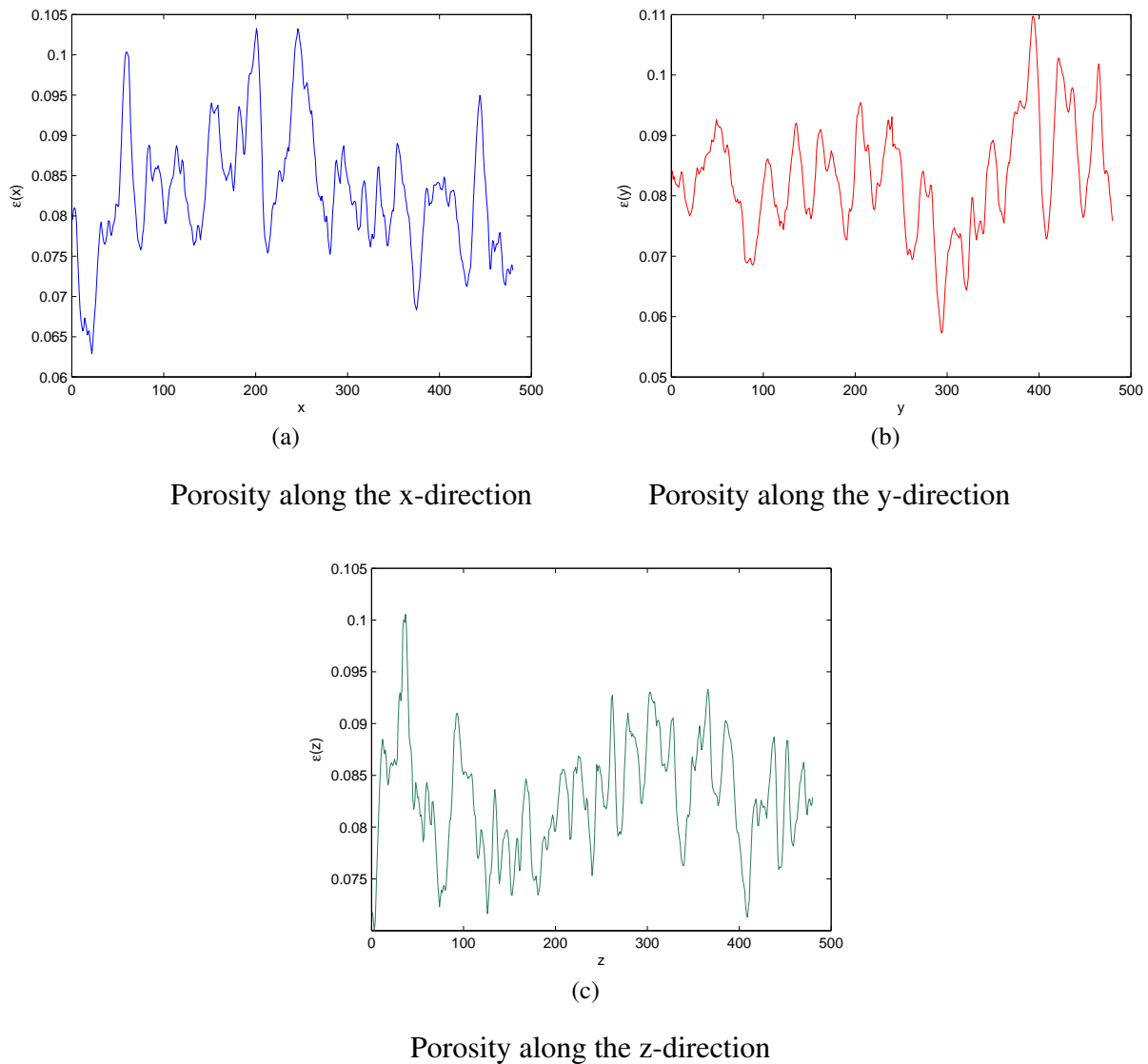


Figure 4.2: Porosity averaged over slices of various directions in sample FB8.

Correlation function

The correlation functions are defined in Chapter 2; $R_z(\mathbf{u})$ and its exponential fit are given by (2.6). For Fontainebleau samples, the two point correlation function is used and the calculations are done for certain slices of samples along three directions.

The calculation program was done by *Nguyen* (2013); it can calculate the correlation function and the least mean square filter for each slice along the three different directions of the sam-

ples. The results are presented in Fig. 4.3. The overall average is displayed in Fig. 4.4. The distance between 2 points is u' , and $u = \frac{u'}{a}$ is dimensionless, where a is the size of the elementary cube. When u is small, the correlation functions of the slices appear to be the same, while for large u there are small differences. Moreover, the results along the three directions are slightly different, but it is not significant. Therefore, the sample can be considered as isotropic.

4.2.2 Samples FB13, FB18 and FB22

The same procedure as for sample FB8 is applied to the next three samples FB13, FB18 and FB22. These samples are cubes of size 480^3 as shown in Fig. 4.1.b-d, respectively.

Calculations of porosities are performed along the x-,y- and z- directions. For each sample, the maximum porosity is 3% - 6.3% larger than the minimum one along the same direction. Since the difference between the three directions is small (nearly 1%) for all samples, they can be considered as isotropic. The porosities vary from 8.3% (FB8) to 21% (FB22). The results are summarized by Table 4.1.

Sample	FB8	FB13	FB18	FB22
ε	0.083	0.129	0.177	0.210
$\varepsilon_M(x); \varepsilon_m(x)$	0.103; 0.0603	0.1471; 0.1117	0.2066; 0.1429	0.2294; 0.1863
$\varepsilon_M(y); \varepsilon_m(y)$	0.11; 0.057	0.1530; 0.1087	0.2016; 0.1555	0.2355; 0.1744
$\varepsilon_M(z); \varepsilon_m(z)$	0.1; 0.07	0.1628; 0.1055	0.2035; 0.1493	0.2437; 0.1856

Table 4.1: The porosity of the 4 Fontainebleau samples.

Similarly, the two points correlation functions of these samples are calculated for several slices along the three directions. The results are given for each slice as in Figure 4.3. Then, the overall average results of the three directions are displayed in Fig. 4.5. As can be seen, these results are similar to FB8.

Another check of the quality of the samples is done with Fourier coefficients (*Adler*, 1992).

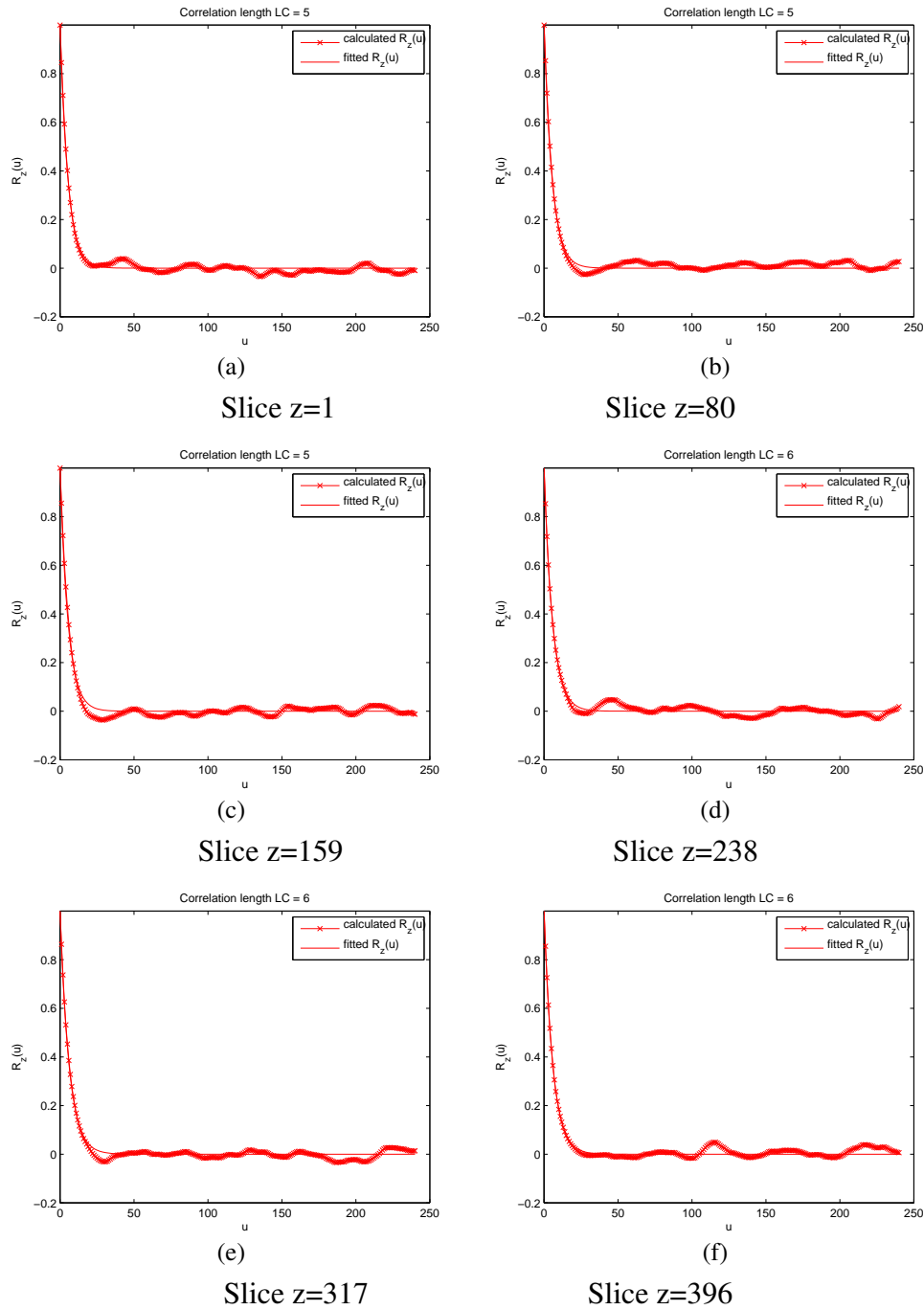


Figure 4.3: The correlation function for different slices in the xy-plane of sample FB8.

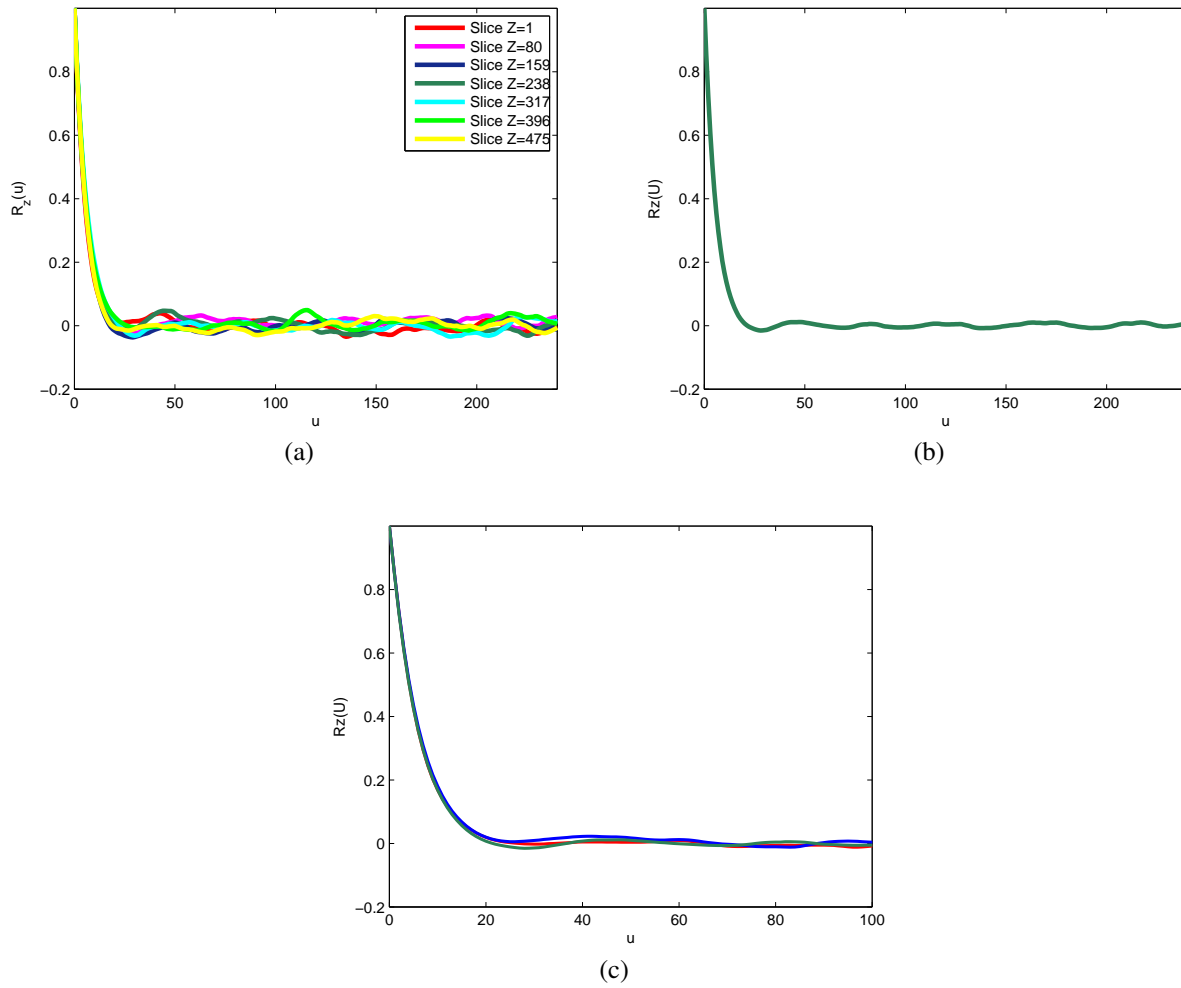


Figure 4.4: (a) The correlation function of various slices. (b) The overall average along the z-direction. (c) The overall averages along the three axes for sample FB8. Data are for: the x-direction (red), the y-direction (blue), the z-direction (green).

For statistically homogeneous media, the Fourier coefficients of the correlation function should be positive. In the four Fontainebleau samples, no negative value observed. For instance, the Fourier components corresponding to the average correlation function along the three directions of sample FB22 varies from 0.12 to 12.3 as can be seen in Fig. 4.5.d. Therefore, the samples can be considered as statistically homogeneous.

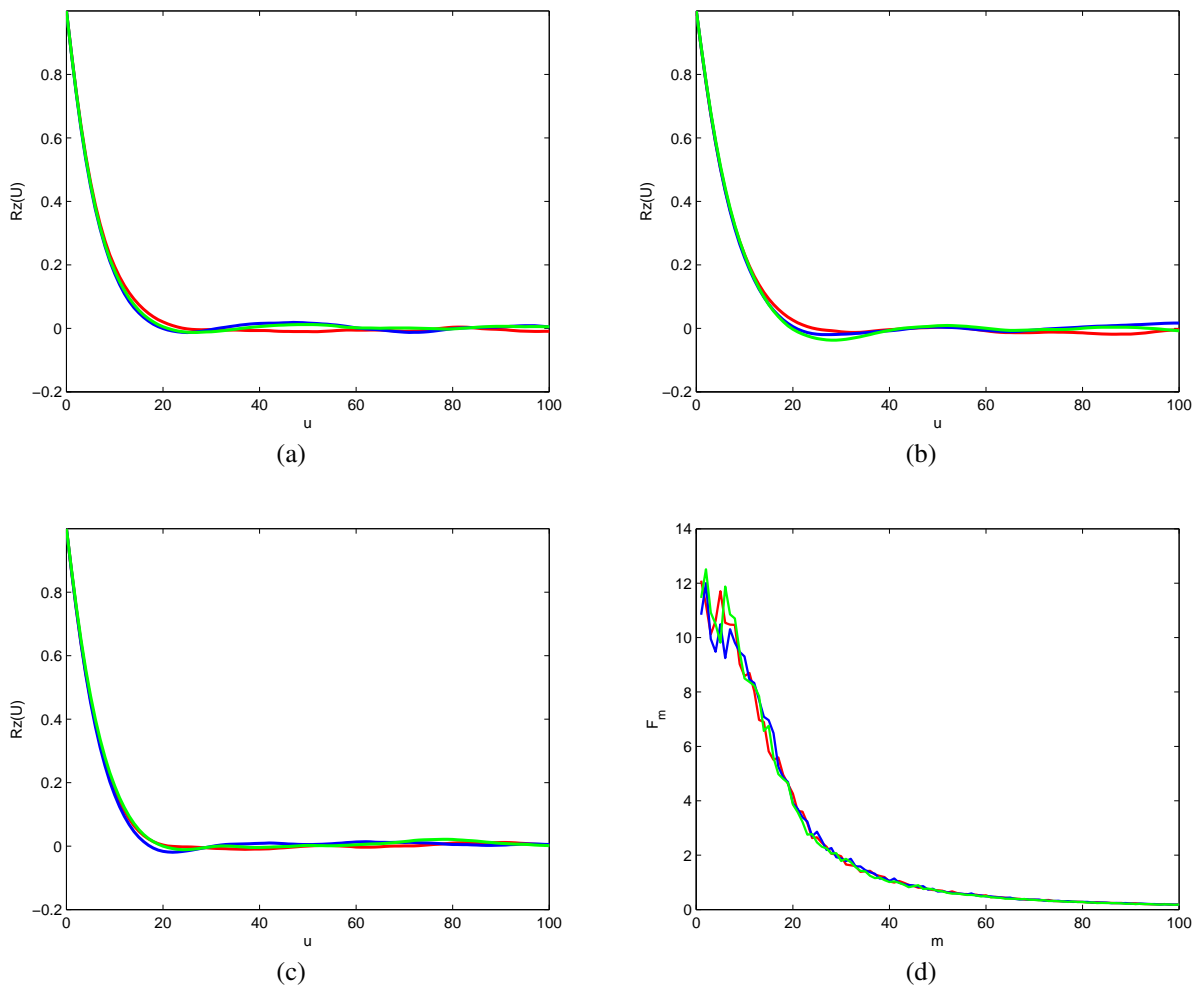


Figure 4.5: The overall average of correlation function along the three axes. (a) Samples FB13. (b) Sample FB18. (c) Sample FB22. (d) The Fourier components corresponding to the average correlation function along the three directions of sample FB22. Data are for: the x-direction (red), the y-direction (blue), the z-direction (green).

4.2.3 The influence of porosity on the correlation function in Fontainebleau sandstones.

Thanks to the previous results, the influence of porosity on the correlation function in Fontainebleau sandstones can be checked. In fact, this problem was often studied; for instance, *Poutet et al.* (1996) found a very small influence. In our case, the same conclusion holds. The correlation function curves are not very different along the three directions as seen in Fig. 4.6. The maximal differences along the x-, y- and z-directions are 18%, 13.3% and 17.1%, respectively.

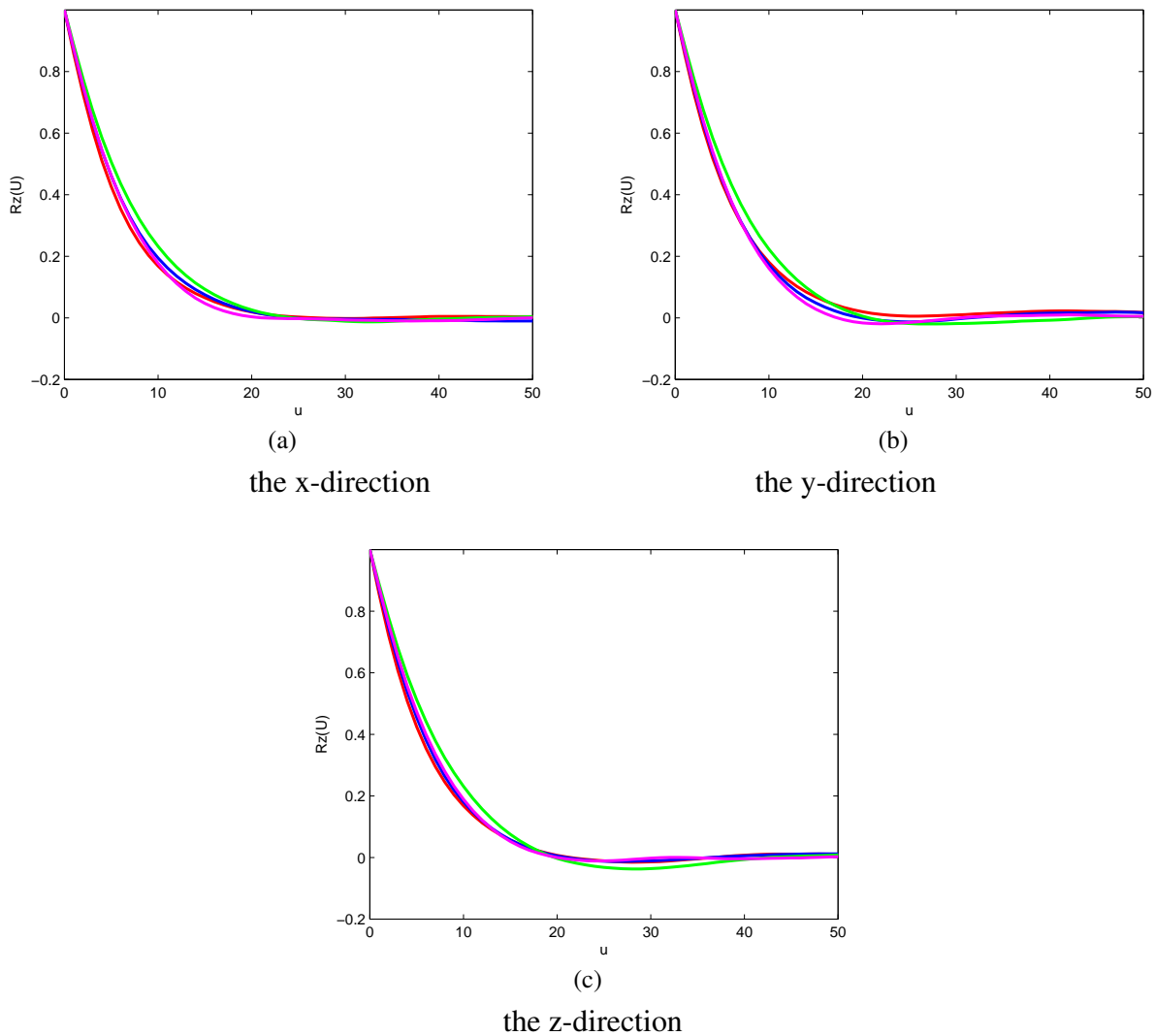


Figure 4.6: The correlation function averaged along the three axes for the four samples: FB8 (red), FB13 (blue), FB18 (green) and FB22 (pink).

4.3 Acoustic wave velocities in the dry Fontainebleau sandstones

4.3.1 Effective stiffness tensor

The acoustic velocities in the dry Fontainebleau samples are derived from the effective stiffness tensors as described in Section 2.6. The calculation of C^{eff} is performed by using the simulation program created by *Pazdniakou* (2012) which is based on the Lattice Spring Model (LSM) with elastic elements (Chapter 3).

Due to the required memory and the simulation time of LSM, two methods are proposed

for calculations: the direct simulations or the coarsening method. The first method is used when computers have a sufficiently large memory and many processors. The second one is for very large samples or for weaker computers. This section presents the calculations obtained by the first way; the second one is presented in Appendix A.2.

The solid component in the Fontainebleau samples is quartz. Its physical properties used in *Han* (1986) and *Arns* (1996) are given by

$$K_s = 37GPa \quad G_s = \mu_{s,H} = 44GPa \quad (4.2)$$

where K_s the solid bulk modulus and G_s the solid shear modulus.

Based on the characterizations in Section 2, the four Fontainebleau samples are considered as isotropic. The coarsening method (see in Section A.2) pointed out that the difference between the three directions is very small, it is always less than 0.5% (Table A.1). Therefore, the calculations for the Fontainebleau samples can be limited to the x-direction. Only one simple stretching and one simple shear are needed to determine the three values of the effective stiffness tensors.

The sample FB22 with the largest porosity is calculated first. For each simulation, the simulation time is over one month and the required memory is 157Gb with a computer with 32 processors. The effective stiffness tensor given in GPa is expressed by

$$\mathbf{C}_{FB22}^{(eff)} = \begin{pmatrix} 47.2990 & 5.7811 & 5.7811 & 0 & 0 & 0 \\ 5.7811 & 47.2990 & 5.7811 & 0 & 0 & 0 \\ 5.7811 & 5.7811 & 47.2990 & 0 & 0 & 0 \\ 0 & 0 & 0 & 20.8307 & 0 & 0 \\ 0 & 0 & 0 & 0 & 20.8307 & 0 \\ 0 & 0 & 0 & 0 & 0 & 20.8307 \end{pmatrix} \quad (4.3)$$

The same simulations are done for the other samples FB18, FB13 and FB8. Then, the three values of \mathbf{C}^{eff} are gathered in Table 4.2.

Sample	C_{xxxx} (GPa)	C_{xxyy} (GPa)	C_{xyxy} (GPa)
FB22	47.2990	5.7811	20.8307
FB18	52.9290	6.1019	23.5346
FB13	64.2706	6.8302	28.8445
FB8	75.6447	7.2287	33.9779

Table 4.2: The three components in the effective stiffness tensors of the 4 Fontainebleau samples.

4.3.2 Acoustic velocities

The acoustic velocities in the dry Fontainebleau samples are derived from their effective stiffness tensor by (2.65). They seem to be a linear function of porosity (see Fig. 4.7). *Arns* (1996) provided the single phase IOS model to calculate acoustic and macroscopic properties of clean sandstones with different porosities. A comparison of the numerical results to the IOS model and to the ones calculated by the coarsening method (Section A.1) is given in Table 4.3. The difference with the IOS model is less than 5.2% for samples FB8, FB13 and FB18, but it is about 8% for sample FB22 with the largest porosity. The two methods (direct and coarsening methods) give close results as seen in Table 4.3.

Han (1986), *Han et al.* (1986) and *Gomez et al.* (2010) also made a number of velocity measurements for dry clean quartz sandstones. The calculated acoustic velocities are slightly larger than the experimental ones. These differences can be due to the small sample size (2736 μm) ; moreover, small fissures which are likely to exist in the real samples might cause these differences. The comparisons are summarized in Fig. 4.7. As it can be seen, the numerical results are in good agreement with the experimental ones.

Since the velocities are mostly linear functions of porosity, approximate linear functions can

Sample	Porosity	Celerities (km/s)	LSM (km/s)	IOS model <i>Arns</i> (1996) (km/s)	Error (%)	Coarsening method (km/s)	Error (%)
FB8	0.083	v_X^p	5.59	5.453	2.5	5.68	1.6
		v_X^s	3.74	3.660	2.1	3.7	1.1
FB13	0.129	v_X^p	5.28	5.113	3.2	5.37	1.7
		v_X^s	3.54	3.41	3.7	3.51	0.9
FB18	0.177	v_X^p	4.93	4.717	4.2	5.03	2.0
		v_X^s	3.29	3.12	5.2	3.27	0.6
FB22	0.21	v_X^p	4.76	4.40	7.6	4.85	1.9
		v_X^s	3.16	2.90	8.2	3.16	0

Table 4.3: Comparison of the acoustic velocities in dry Fontainebleau samples: our numerical results, the single phase IOS (*Arns*, 1996) and the coarsening method.

be built for predictions. They are given by

$$v_p = 6.0218 - 6.018 \varepsilon \quad (4.4)$$

$$v_s = 4.0733 - 4.358 \varepsilon \quad (4.5)$$

with correlation coefficients of 0.9977 and 0.9975, respectively. A good agreement between the numerical results and the predictions is shown in Fig. 4.8.

Since the effective stiffness tensors are determined, the macroscopic properties of the Fontainebleau samples can be derived from (3.34). The effective bulk modulus K_e and the shear modulus G_e of the dry samples are calculated. They are linear functions of porosity and close to the IOS model. The difference for G_e is larger than for K_e especially when the porosity is large as can be seen in Figures 4.7.a-b.

The empirical models are also used to predict the macroscopic properties of dry sandstones. *Nur et al.* (1991, 1995) proposed an empirical model

$$K_{dry} = K_s \left(1 - \frac{\varepsilon}{\varepsilon_c}\right) \quad G_{dry} = G_s \left(1 - \frac{\varepsilon}{\varepsilon_c}\right) \quad (4.6)$$

where ε_c is the critical porosity equal to 0.4.

Krief (1990) derived a more general relationship based on the experimental data of *Raymer et al.* (1980)

$$K_{dry} = K_s (1 - \varepsilon)^{m(\varepsilon)} \quad G_{dry} = G_s (1 - \varepsilon)^{m(\varepsilon)} \quad (4.7)$$

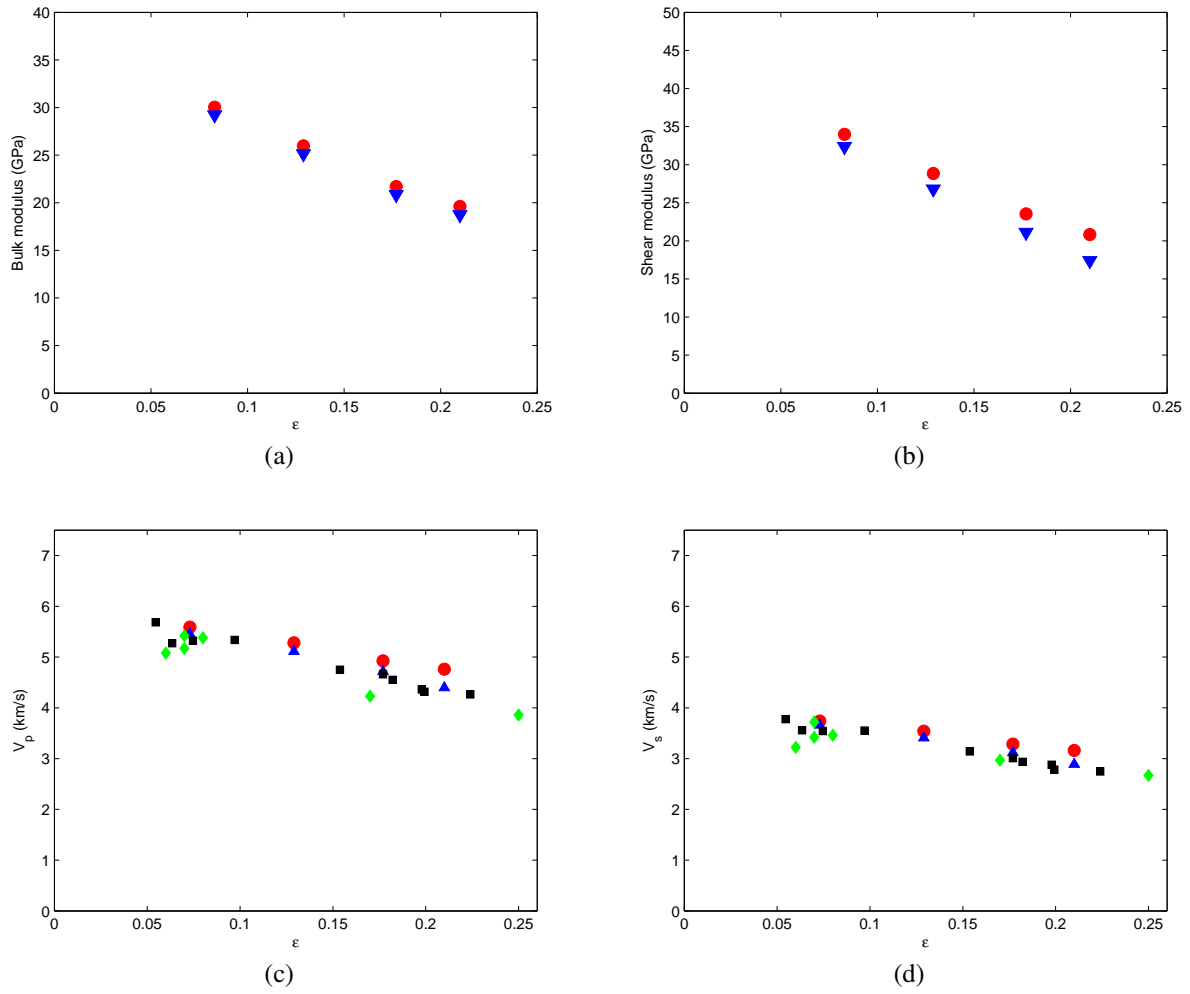


Figure 4.7: Comparisons between the numerical results and the IOS model (*Arns, 1996*), (*Han, 1986*; *Han et al., 1986*) and *Gomez et al. (2010)*. (a) Bulk modulus. (b) Shear modulus. (c) Compressional wave. (d) Shear wave. Data are for: numerical results (red \circ), IOS model (blue \triangle), Han's data (black \square), Gomez's data (green \diamond).

where $m(\varepsilon) = 3/(1 - \varepsilon)$.

For the dry rock Poisson ratio, *Roberts and Garboczi (2000)* proposed a linear function of porosity. Then, *Arns (1996)* proposed a non-linear empirical model which is more reasonable and given by

$$\nu_{dry} = \begin{cases} \nu_s + (2\varepsilon)^{1.5}(0.2 - \nu_s), & \nu_s < 0.2 \\ 0.2 + (1 - 2\varepsilon)^{1.5}(\nu_s - 0.2), & \nu_s > 0.2 \end{cases} \quad (4.8)$$

We first compare the effective bulk modulus. It is slightly larger than (4.6) and (4.7) and closer to Nur's result than Krief's (see Fig. 4.9.a). The shear modulus obtained by LSM lies

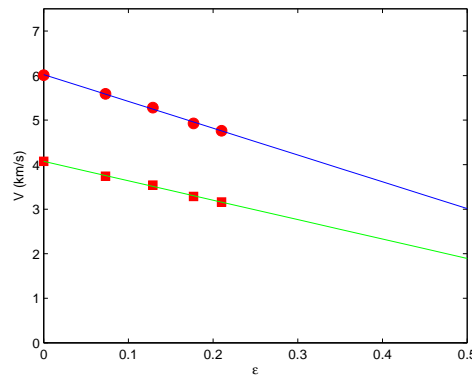


Figure 4.8: Comparison between the numerical results and the linear fits. Data are for: v_p (\circ), v_s (\square), numerical results (red), equation (4.4) (blue), equation (4.5) (green).

between these two empirical models as seen in Fig. 4.9.b. The Poisson ratio is compared with (4.8) in Fig. 4.9.c, the numerical line nearly coincides with the empirical line and the difference decreases when porosity increases.

Summary The effective properties and the acoustic velocities are fully determined for all dry Fontainebleau samples and can be considered to be linear functions of porosity. Some comparisons are given and show that our simulation results are in good agreement with the other numerical, empirical models and the experimental data.

4.4 Additional comparisons

The calculations of Fontainebleau samples are done by two methods: the direct simulations and the coarsening method. The results of the first method were given in Section 4.3. Note that the second method can yield the wave velocities in the samples with an infinite discretization which are close to the real samples; its results are given in Section A.2. A comparison between the results of the coarsened samples with $N_c = \infty$ with the results presented in Section 4.3 is done; the difference is small as it can be seen in Fig. 4.10.

Hence, there is a small difference between our numerical results and the experimental data of Han (1986) or Gomez *et al.* (2010). As mentioned before, it may be due to the presence of small fractures in the real samples. Other possibilities for this discrepancy were investigated. The first solution to improve the numerical results is using the mirror configuration along the three direc-

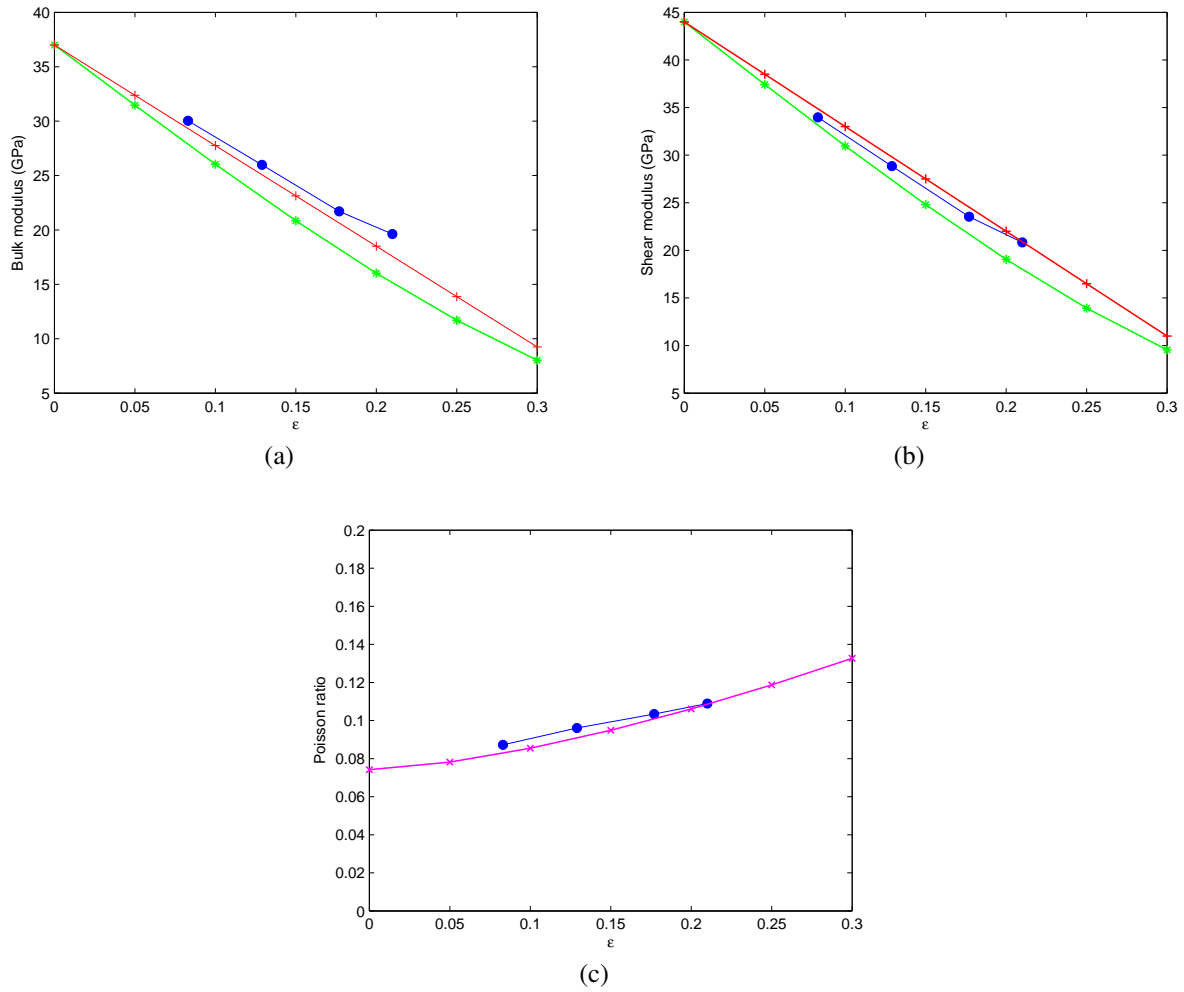


Figure 4.9: Comparisons between the numerical results and the empirical models of *Nur et al.* (1991, 1995), *Krief* (1990) and *Arns* (1996). (a) Bulk modulus. (b) Shear modulus. (c) Poisson ratio. Data are for: numerical results (blue \circ), Nur (red), Krief (blue), Arns (pink).

tions of space in order to ensure the spatially periodic conditions. An example is done for the coarsened sample FB18 with $N_c = 120$; the corresponding mirror configuration of size 240^3 is presented in Fig. 4.11.a. Two simulations are performed for this configuration; the obtained effective stiffness tensor is very close to the original one. For instance, $C_{xxx}^{mirror} = 61.179$ GPa while $C_{xxx}^{original} = 61.015$ GPa.

The second solution is the variation of Lamé coefficients. The Lamé coefficients λ_0 and μ_0 of the quartz can be derived from (4.2). Let us assume that the local values which correspond to

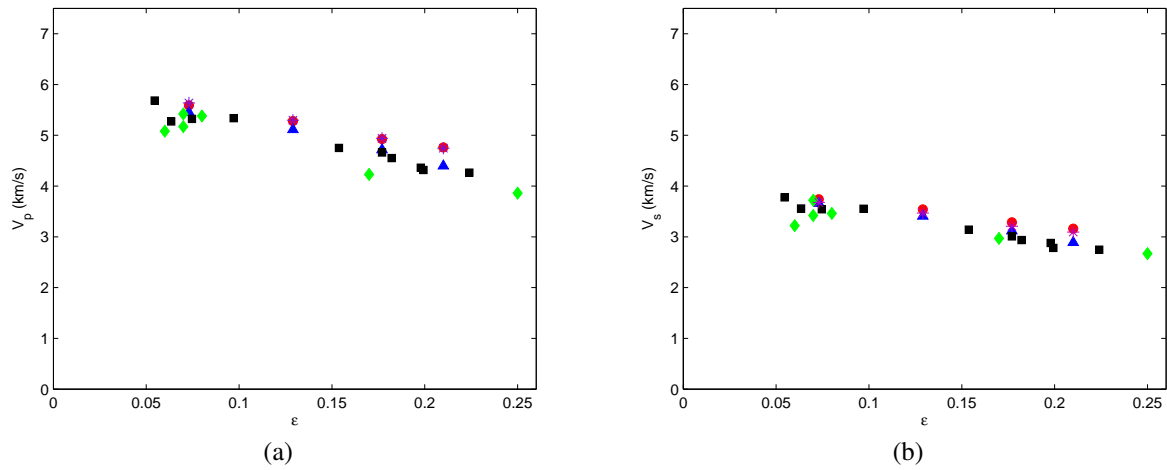


Figure 4.10: Comparisons between the results of the coarsened samples $N_c = \infty$ and the direct simulations, the IOS model (Arns, 1996), (Han, 1986; Han et al., 1986) and Gomez et al. (2010). (a) Compressional wave. (b) Shear wave. Data are for: $N_c = \infty$ (violet *), direct simulations (red o), IOS model (blue Δ), Han's data (black \square), Gomez's data (green \diamond).

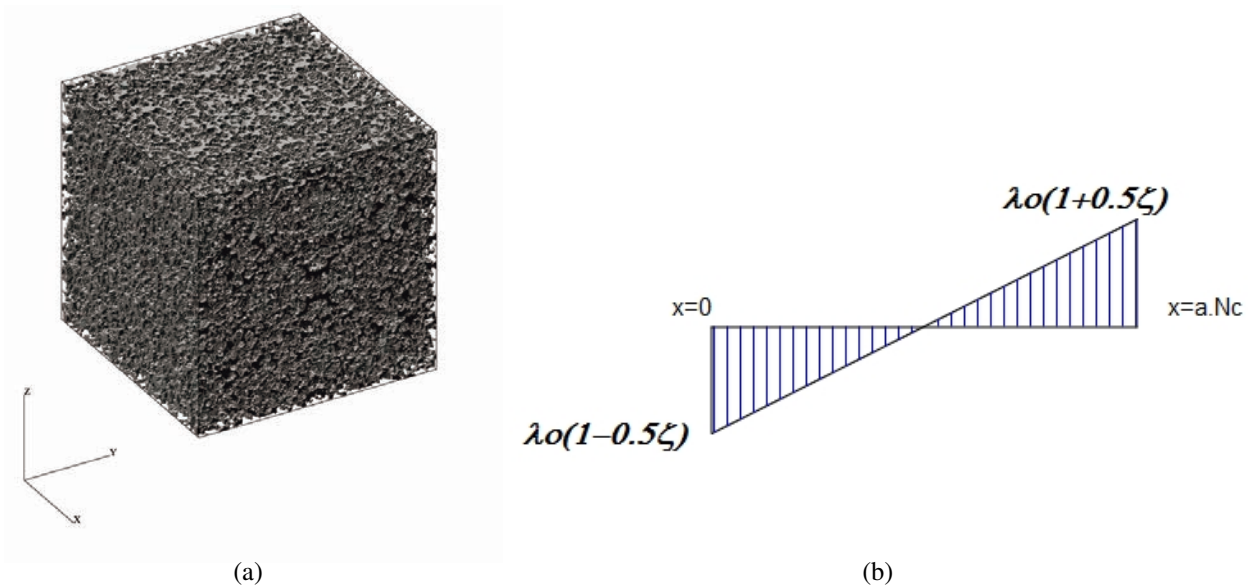


Figure 4.11: (a) The mirror configuration along the three directions of the coarsened sample FB18 with $N_c = 120$. (b) The linear variation of the local Lamé coefficient λ in this sample.

each elementary cube in the lattice vary linearly; the local functions are given by

$$\lambda_x = \lambda_0 \cdot \left(1 + \frac{x - a \cdot N_{cx}/2}{a \cdot N_{cx}} \cdot \zeta\right) \tag{4.9}$$

$$\mu_x = \mu_0 \cdot \left(1 + \frac{x - a \cdot N_{cx}/2}{a \cdot N_{cx}} \cdot \zeta\right)$$

as illustrated in Fig. 4.11.b. Following this supposition, the simulations are done with various values of ζ for the coarsened sample FB22 with $N_c = 120$ and the results are compared with the original result which corresponds to $\zeta = 0$. The difference is negligible even for large variations of λ_x and μ_x as in Table 4.4; it is about 0.3% when $\zeta = 0.2$.

ζ	0	0.02	0.05	0.06	0.1	0.2
C_{xxxx} (GPa)	56.7978	56.7968	56.7883	56.7836	56.7557	56.6206

Table 4.4: Simulation results for the coarsened sample FB22 ($N_c = 120$) when the local Lamé coefficients vary linearly according to (4.9).

Therefore, it seems the fact that the calculated velocities are larger than the measurement ones cannot be explained by these two possibilities.

4.5 The formation factor F and the characteristic length Λ

As mentioned in Chapter 2, the macroscopic conductivity tensor and the length Λ can characterize a porous medium. They are derived by solving the Laplace equation on the pore space by the program based on a second order finite difference approach of *Thovet et al.* (1990).

The calculations are done for the coarsened samples which are provided in Section A.2 for the coarsening method. The computational time varies from some hours to more than one day; the required memory is from 0.1 Gb to 4.4 Gb depending on the sample size. Only one simulation is needed for each sample. The Fontainebleau samples are close to isotropic; therefore, the results are given only for the x-direction. The dimensionless length Λ/a and conductivity tensor $\frac{\bar{\Sigma}}{\Sigma_0}$ are determined and given in Table 4.5.

Valfouskaya et al. (2005) showed that if the field $\psi(r)$ (see (2.9)) does not vary too much in the pore space, the length scale Λ can be approximated by

$$\Lambda \sim 2 \frac{\Omega_p}{S} \quad (4.10)$$

where Ω_p is the pore volume, S the pore surface. A comparison with the simulation results is presented Table 4.5 and the difference is at most 21.4% as it can be seen.

Sample	N_c	$\frac{\bar{\Sigma}}{\Sigma_0}$	$\frac{\Lambda}{a}$	$\frac{2 \cdot \Omega_p}{S \cdot a}$
FB22	120	0.0255	1.143	0.942
	240	0.0473	2.067	1.7253
	480	0.0576	4.287	3.3667
FB18	120	0.020	1.198	0.986
	240	0.0361	2.169	1.8182
	480	0.0437	4.475	3.5521
FB13	120	0.0037	0.9959	0.8342
	240	0.0134	1.690	1.5136
	480	0.0183	3.4656	2.9402
FB8	120	0	0	0.7544
	240	0.0016	1.3469	1.3369
	480	0.00327	2.6907	2.5461

Table 4.5: The dimensionless conductivity components $\frac{\bar{\Sigma}}{\Sigma_0}$ and the characteristic length Λ/a of the Fontainebleau samples.

The formation factor F is derived from the conductivity tensor by (2.11). Archie (1942) postulated a relationship between interconnected porosity ε and the factor F; it is given by

$$F = \frac{1}{\varepsilon^m} \quad (4.11)$$

Archie further noted that m is close to 2 (Worthington, 1993). This is called the "first Archie equation". A comparison with this equation is presented in Fig. 4.12.a. The numerical results are close to Archie's law.

Another form of Archie equation is given by

$$F = \frac{a}{\varepsilon^m} \quad (4.12)$$

The quantities a and m have been reported to vary widely for various formations. For the original Fontainebleau samples ($N_c = 480$), the best fit for our numerical data is obtained when $a = 0.2034$ and $m = 2.7747$ (see Fig. 4.12.b). They are in good agreement with Gomez-Rivero (1977) who proposed $a = 0.04 - 17.7$ and $m = 0.02 - 5.67$ for sandstones.

Gomez *et al.* (2010) also made some measurements of the formation factor F for Fontainebleau sandstones while STATOIL measured for the mCT samples whose porosities are close to our sam-

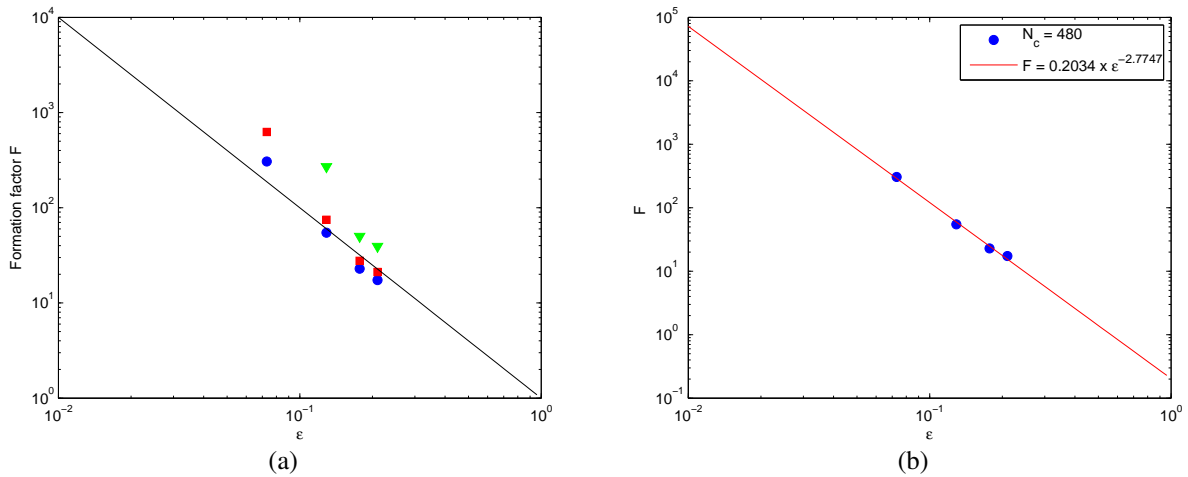


Figure 4.12: The formation factor F of Fontainebleau samples. (a) Comparison with "first Archie equation" (4.11). (b) Comparison with (4.12) when $a = 0.2034$ and $m = 2.7747$. Data are for: $N_c = 480$ (blue \circ), 240 (red \square), 120 (green ∇), (4.11) (black line), (4.12) (red line).

ples. Obviously, our numerical results are very close to STATOIL data and in good agreement with the experimental ones of *Gomez et al.* (2010) as shown in Fig. 4.13.

4.6 Acoustic wave velocities in saturated Fontainebleau samples

The calculations of acoustic wave velocities in saturated Fontainebleau samples are done according to the methodology presented in Chapter 2. Therefore, the four quantities C , K , α , and β which are presented in the Christoffel equation are derived by LBM, LSM, LBM-LSM.

4.6.1 Permeabilities

4.6.1.1 Absolute permeability

The absolute permeability of Fontainebleau samples was calculated by a program based on the Lattice Boltzmann Model (*Pazdniakou, 2012*). The program code is written in Fortran. Since the samples can be considered as isotropic, one only needs a single simulation to calculate the absolute permeability of each Fontainebleau sample. Moreover, the memory requirements for a simulation by LBM is smaller than for LSM; therefore, the coarsening method is not necessary in this case.

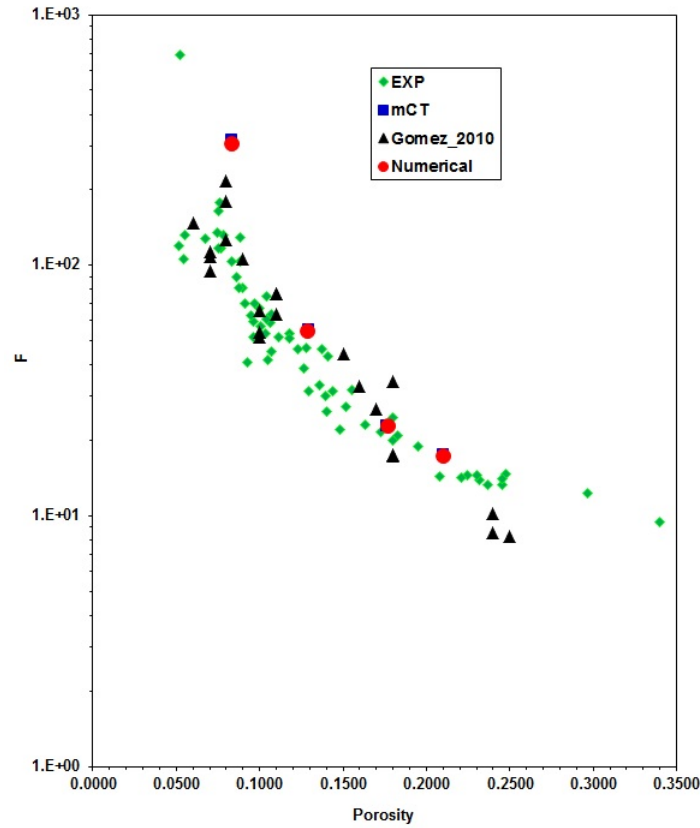


Figure 4.13: The formation factor F of the Fontainebleau samples compared with the data provided by STATOIL and the experimental data of *Gomez et al. (2010)* and STATOIL. Data are for: numerical (red \circ), STATOIL data for mCT samples (blue \square), *Gomez et al. (2010)* (black \triangle), STATOIL data for various subsamples (green \diamond).

As mentioned before, in order to ensure the connection between two opposite sample faces, the original sample and its mirror image along the corresponding axis are used for simulations. If the medium is spatially periodic, we use it; otherwise, the mirror image is used. For Fontainebleau samples, we simulate both configurations and compare the results in order to show the influence of the boundary conditions. The original sample FB22 (480 x 480 x 480) and its mirror configuration along the x-direction (960 x 480 x 480) are displayed in Fig 4.14.

For the sake of completeness, the absolute permeability of the four samples FB8, FB13, FB18 and FB22 with the same size $N_{cx} \cdot N_{cy} \cdot N_{cz} = 480 \times 480 \times 480$ was calculated. The simulations are performed on computers with 32 processors; the memory requirements are about 40 Gb and the simulation time is more than two weeks. The result K is dimensionless; the real value of the

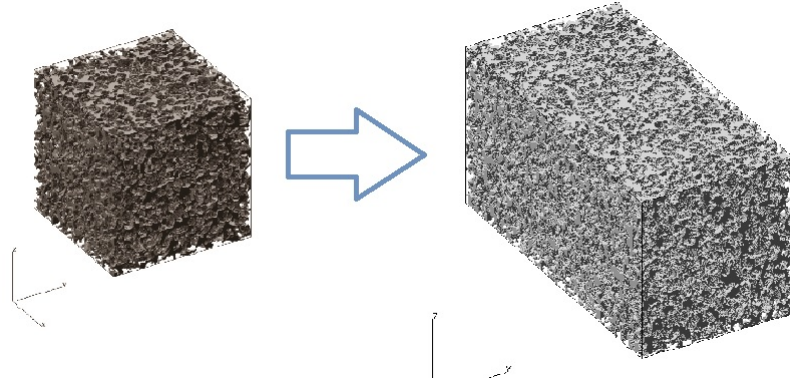


Figure 4.14: The mirror configuration along the x-direction of sample FB22 ($N_{cx} \cdot N_{cy} \cdot N_{cz} = 960 \times 480 \times 480$).

absolute permeability K_0 is given by

$$K_0 = K \cdot a^2 \quad (4.13)$$

The results are given in Table 4.6.

Permeability K_0 (mD)	FB8	FB13	FB18	FB22
The original sample	29.0	397.6	1834	2251.5
The mirror configuration	49	494.65	2152.73	2570.61

Table 4.6: Absolute permeabilities of the original Fontainebleau samples and of their mirror configurations.

The simulations of the mirror configurations are performed by the same program on the computers with 32 processors, the memory requirements and simulation time are about twice the ones necessary for the original samples. The real values of permeabilities (mD) for mirror images along the x-direction of 4 Fontainebleau samples are given in Table 4.6.

Gomez et al. (2010) measured the absolute permeability of these 4 samples. The comparison with the simulation results is presented in Fig. 4.15.

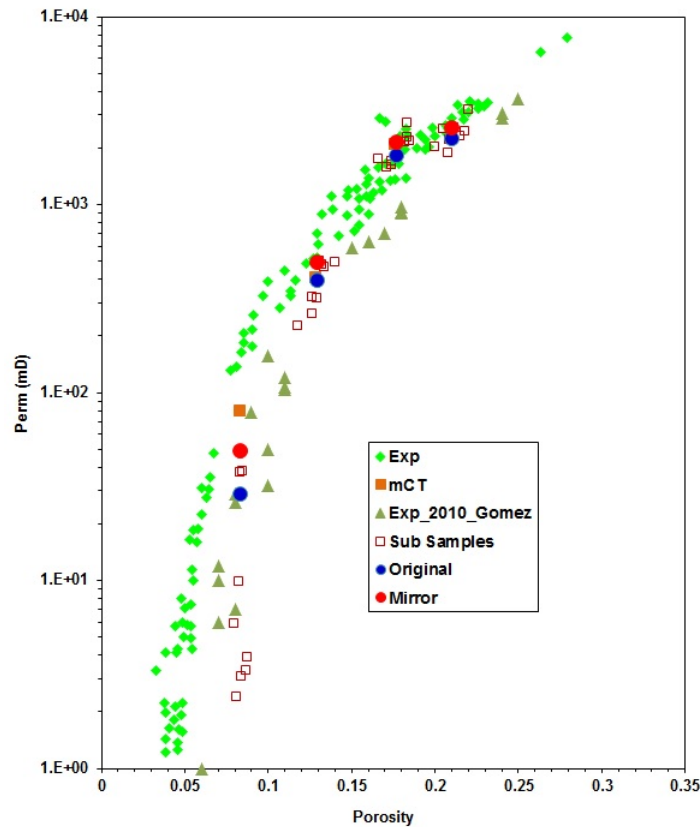


Figure 4.15: The permeability of the Fontainebleau samples (blue \circ) and of their mirror images along the x-direction (red \circ) compared with the experimental data of *Gomez et al.* (2010) (green \triangle), the data provided by STATOIL for subsamples (green \diamond) and mCT samples (brown \square).

It can be seen that the results of the mirror images are better and larger than the ones of the original samples. In fact, the mirror configurations ensure connection between two opposite sample faces and therefore the continuity of the flow; as a result, there is no artificial loss of permeability in this case and the results are larger than in the corresponding original sample. However, the results of both types are close to the experimental results.

4.6.1.2 Dynamic permeability

The same program based on LBM is used to calculate the dynamic permeability. However, due to the dependence on the frequency ω , it is necessary to simulate with several values of ω . Furthermore, the first simulations indicated that the computation time depends on the frequency

and is often larger than the ones for absolute permeability. For these reasons, it is difficult for our computers to simulate directly the original samples with large sizes. In order to solve this problem, the coarsening method is applied to the calculation of dynamic permeability and the coarsened samples are the same as for dry samples (Section A.2).

The sample FB22 with the maximum porosity is calculated first. The original and coarsened samples are displayed in Fig. A.5. The chosen kinematic viscosity, the frequencies in simulations have to satisfy the condition of Knudsen number Kn and of high frequency (*Pazdniakou*, 2012).

The memory requirements for a simulation of the coarsened samples of size $N_{cx} \cdot N_{cy} \cdot N_{cz} = 120 \times 120 \times 120$ is about 0.5 Gb; the simulation time depends on the frequency. For small frequencies, a larger number of iterations is needed; therefore, the computation time becomes longer. All the simulations were done with the same parameters

$$c_s^2 = \frac{1}{3} \frac{a^2}{\delta t^2}; \quad \rho_0 = 1 \frac{m_u}{a^3}; \quad \nu = 10^{-3} \frac{a^2}{\delta t}; \quad \mathbf{b}_f = [10^{-7}, 0, 0] \frac{m_u a}{\delta t^2} \quad (4.14)$$

where c_s is the sound speed (the maximum value is $\sqrt{0.5}$, $\sqrt{1/3}$ is recommended), ρ_0 the initial fluid density, ν the fluid kinematic viscosity, \mathbf{b}_f the fluid body force, and ϵ the convergence parameter. All the physical properties are given in lattice units a (a is the size of the elementary cubes), time step δt and mass unit m_u . The dimensionless permeability K/a^2 is calculated; the simulation is stopped when $|A_{i+1} - A| < 10^{-8}$ (*Nguyen*, 2013).

The dimensionless real and imaginary parts of permeability \mathbf{K} of the coarsened sample FB22 with $N_c = 120$ are simulated for various frequencies; the results are given in Table 4.7.

Similarly to the calculation along the x-direction, the dynamic permeability along the y- and z-directions are simulated, with a fluid body force equal to $[0, 10^{-7}, 0]$ and $[0, 0, 10^{-7}]$ ($\frac{m_u a}{\delta t^2}$), respectively. The simulation results are given in Table 4.7.

The results of dynamic permeability along the x-, y-, z-directions are close (see Fig. 4.16); therefore, it is not necessary to calculate for all three directions. The calculations of dynamic permeability for the other samples will be performed only along the x-direction.

Frequency	$N_c = 120$					
	x-axis		y-axis		z-axis	
ω	K_r/a^2	K_i/a^2	K_r/a^2	K_i/a^2	K_r/a^2	K_i/a^2
0.05	3.783e-5	-2.492e-4	3.735e-5	-2.478e-4	3.818e-5	-2.596e-4
0.025	1.247e-4	-4.829e-4	1.338e-4	-4.794e-4	1.372e-5	-5.011e-4
0.01	6.665e-4	-7.943e-4	6.698e-4	-7.530e-4	6.906e-4	-8.015e-4
0.005	0.0013	-9.597e-4	0.0012	-9.061e-4	0.0013	-9.778e-4
0.0025	0.0018	-7.724e-4	0.0018	-7.274e-4	0.0019	-7.894e-4
0.001	0.0021	-3.863e-4	0.0021	-3.621e-4	0.0022	-3.933e-4
0.0005	0.0022	-2.013e-4	0.0021	-1.884e-4	0.0023	-2.045e-4
0.00025	0.0022	-1.017e-4	0.0021	-9.513e-5	0.0023	-1.033e-4
0.0001	0.0022	-4.082e-5	0.0021	-3.819e-5	0.0023	-4.144e-5
5e-05	0.0022	-2.042e-5	0.0021	-1.910e-5	0.0023	-2.073e-5
2.5e-05	0.0022	-1.021e-5	0.0021	-9.552e-6	0.0023	-1.037e-5
1e-05	0.0022	-4.084e-6	0.0021	-3.820e-6	0.0023	-4.147e-6

Table 4.7: The dimensionless dynamic permeability K/a^2 along the x-, y- and z-directions for the coarsened samples FB22 with $N_c = 120$.

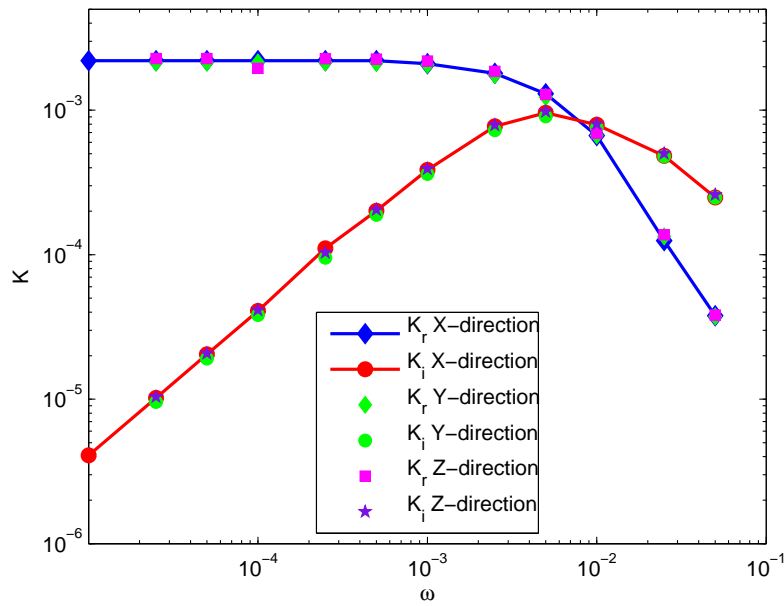


Figure 4.16: Comparison of dynamic permeability along the three directions of the coarsened samples FB22 (size 120 x 120 x 120).

The coarsened sample FB22 of size 240 x 240 x 240 and the original sample $N_c = 480$ are calculated, but only along the x-direction. The input parameters are the same as for the sample with $N_c = 120$. For a simulation with $N_c = 240$, the memory requirement is about 5.1 Gb; the simulation time which depends on the frequency can vary from several hours to more than one week with a computer with 8 processors, while the necessary ones for $N_c = 480$ are about 8 times larger. The dimensionless real K_r/a^2 and imaginary parts K_i/a^2 of the calculated dynamic permeability are given in Table 4.8; the dimensionless quantities K/K_0 (K_0 is the absolute permeability) are presented in Figures 4.17.a and 4.17.b. The dimensional values of the dynamic permeability in mD of these coarsened samples are calculated by (4.13). The coarsening method has more influence on the imaginary part than on the real part of permeability as can be seen in Figure 4.17.c.

The universal scaling behaviour presented in Section 2.4 can be verified. Since the length Λ and the formation factor F are calculated for all samples by solving the Laplace equation in the pore space by the method of *Thovert et al.* (1990), the frequency value ω_c which corresponds to the

Frequency	$N_c = 240$		$N_c = 480$	
	x-axis		x-axis	
ω	K_r/a^2	K_i/a^2	K_r/a^2	K_i/a^2
0.05	5.343e-5	-6.297e-4	6.70e-5	-0.0009
0.025	1.891e-4	-0.0013	1.32e-4	-0.0018
0.01	0.0011	-0.0026	0.0013	-0.0040
0.005	0.0026	-0.0043	0.0024	-0.0079
0.0025	0.0054	-0.0056	0.0059	-0.0139
0.001	0.0100	-0.0053	0.0174	-0.0239
0.0005	0.0124	-0.0036	0.0327	-0.286
0.00025	0.0134	-0.0021	0.0498	-0.0264
0.0001	0.0137	-8.574e-4	0.0641	-0.0156
5e-05	0.0138	-4.315e-4	0.0678	-0.0086
2.5e-05	0.0138	-2.161e-4	0.0689	-0.0044
1e-05	0.0138	-8.649e-5	-	-

Table 4.8: The dimensionless dynamic permeability K/a^2 along the x-direction of the coarsened samples FB22 with $N_c = 240$ ($a_{240} = 11.4 \mu m$) and $N_c = 480$ ($a_{480} = 5.7 \mu m$).

transition from the viscous dominated flow regime to the inertia dominated flow regime (*Pazdniakou*, 2012) can be determined. Thanks to that, the rescaled dimensionless dynamic permeability and frequency (K' and ω'_c) are derived and compared to the Poiseuille flow in Fig. 4.17d. A good universal scaling behaviour is observed. The points corresponding to the coarsened sample FB22 are gathered around the curves corresponding to the plane Poiseuille flow. This is in good agreement with *Zhou and Sheng* (1989) and *Pazdniakou and Adler* (2013) who pointed out that this behaviour is nearly independent of the microstructure of the porous media.

The mirror configurations along the x-direction are also calculated. The mirrored original sample FB22 is displayed in Figure 4.14, its size is $N_{cx} \times N_{cy} \times N_{cz} = 960 \times 480 \times 480$. As for the absolute permeability, the results of mirror configurations are a little larger than the originals

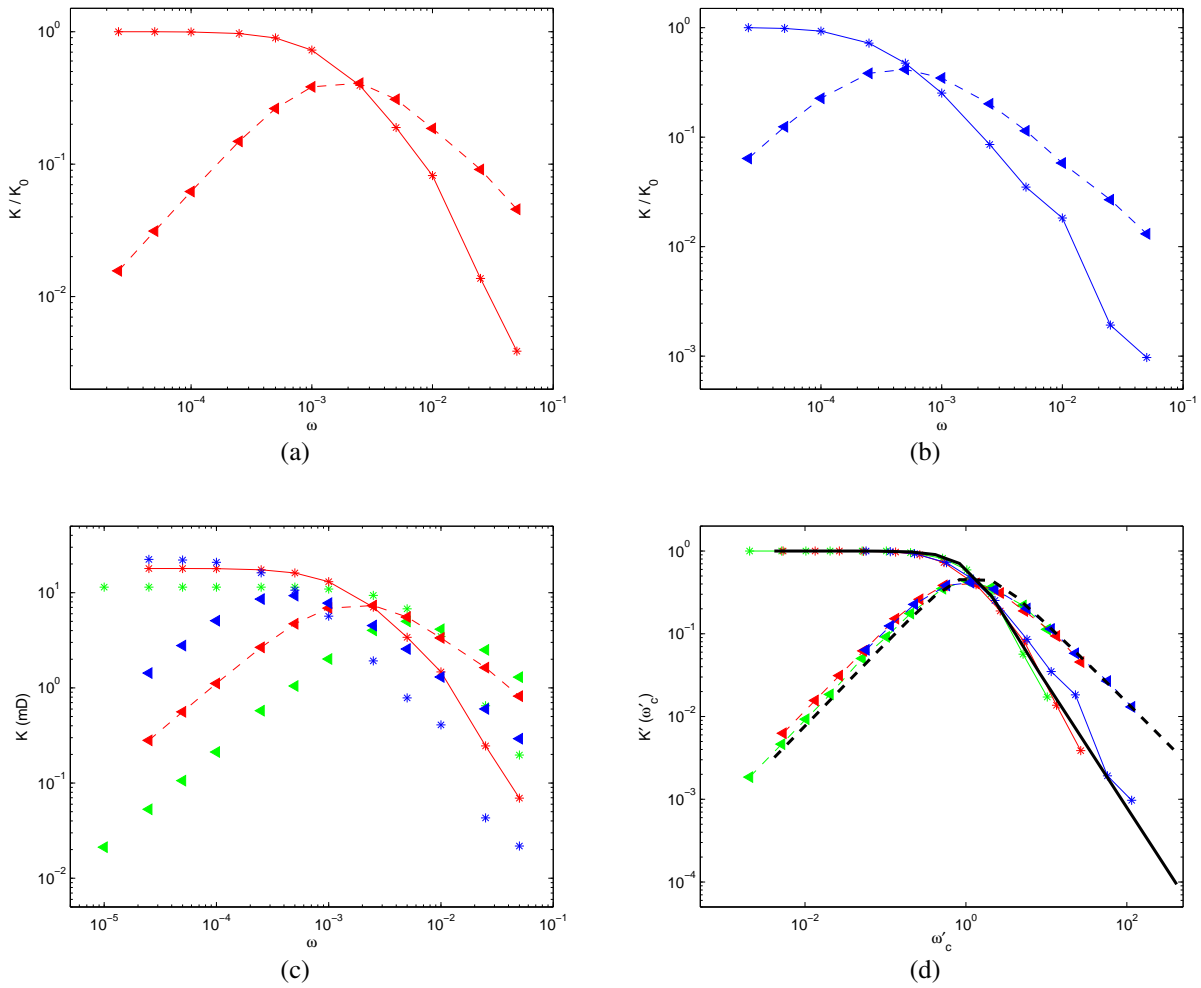


Figure 4.17: (a) The dynamic permeability K/a^2 along the x-direction of the coarsened sample FB22 with $N_c=240$. (b) The results of the original sample with $N_c=480$. (c) Comparison of the real values K along the x-direction of the three coarsened samples. (d) Dynamic permeability in the universal scaling. Data are for: $N_c=120$ (green), 240 (red), 480 (blue), Poiseuille flow (black), real part (—), imaginary part (- -).

as can be seen in Table 4.9. For instance with $\omega = 2.5e - 5$, the difference of the real part Kr/a^2 is 12% when $N_c = 120$ and 12.3 % when $N_c = 480$. This difference is shown in Fig. 4.18 which displays real dynamic permeabilities for all the coarsened samples FB22 (mirror and original).

	$N_c = 120$		$N_c = 240$		$N_c = 480$	
Frequency	x-axis		x-axis		x-axis	
ω	K_r/a^2	K_i/a^2	K_r/a^2	K_i/a^2	K_r/a^2	K_i/a^2
0.05	0.00004	-2.7982e-04	0.00006	-6.8015e-04	0.00005	-9.7397e-04
0.025	0.00015	-5.3616e-04	0.00020	-1.3583e-03	0.00014	-1.9927e-03
0.01	0.0007	-9.0788e-04	0.0012	-2.8539e-03	0.0013	-4.3177e-03
0.005	0.0014	-1.0631e-03	0.0028	-4.7032e-03	0.0024	-8.6469e-03
0.0025	0.0020	-8.6184e-04	0.0059	-6.2850e-03	0.0062	-1.5183e-02
0.001	0.0024	-4.3436e-04	0.0111	-6.0861e-03	0.0186	-2.6473e-02
0.0005	0.0025	-2.2690e-04	0.0138	-4.2731e-03	0.0355	-3.2494e-02
0.00025	0.0025	-1.1479e-04	0.0151	-2.4544e-03	0.0551	-3.0734e-02
0.0001	0.0025	-4.6069e-05	0.0156	-1.0315e-03	0.0724	-1.8774e-02
5e-05	0.0025	-2.3046e-05	0.0156	-5.1972e-04	0.0772	-1.0445e-02
2.5e-05	0.0025	-1.1524e-05	0.0156	-2.6037e-04	0.0786	-5.3934e-03

Table 4.9: The dimensionless dynamic permeability K/a^2 for the mirror configurations along the x-direction of the coarsened samples FB22 with $N_c = 120$ ($a_{120} = 22.8 \mu m$), $N_c = 240$ ($a_{240} = 11.4 \mu m$) and $N_c = 480$ ($a_{480} = 5.7 \mu m$).

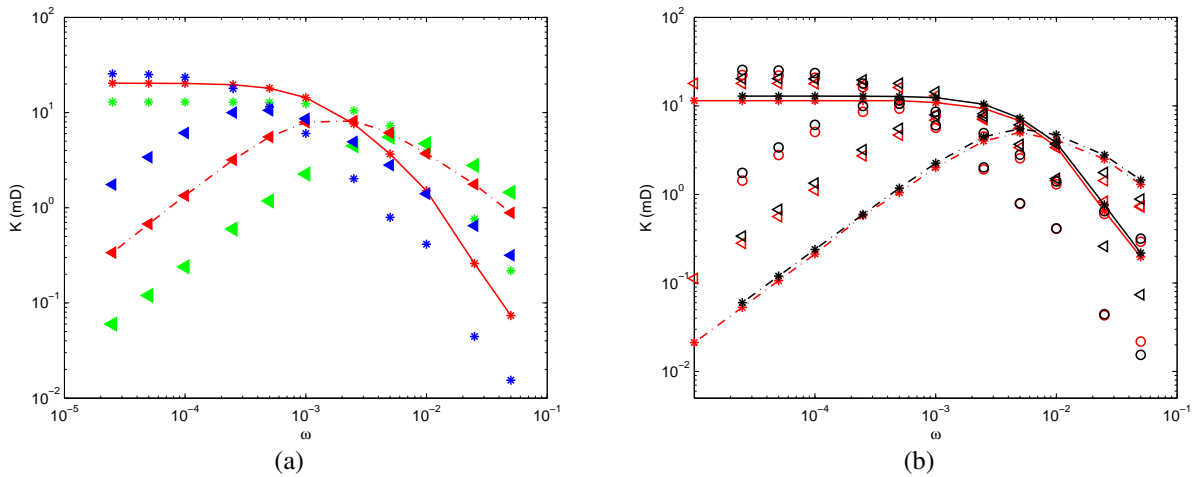


Figure 4.18: (a) The comparison of real dynamic permeability of the mirror configurations along the x-direction of the three coarsened samples. Data are for: $N_c=120$ (green), 240 (red), 480 (blue). (b) Comparison between the mirror configurations and the original ones of the coarsened samples. Data are for: $N_c = 120$ (*), 240 (\triangleright), 480 (\diamond), original (red), mirror (black), real part (—), imaginary part (- -).

In the same way, the dynamic permeability is calculated for the other samples, the results of the coarsened samples FB18 ($N_c = 120, 240$ and 480) are presented in Table 4.10 for the original configuration and in Table 4.11 for the mirror one. The results for sample FB13 are given in Table 4.12; it should be noted that, due to the small porosity, the smallest discretization $N_c = 120$ creates problems in calculating \mathbf{K} . Therefore, for this sample, only the results for $N_c = 240$ and $N_c = 480$ are presented. The same problem occurs with sample FB8. Then, some comparisons between the real values of their permeabilities are given in Figure 4.19.

Frequency	$N_c = 120$		$N_c = 240$		$N_c = 480$	
	x-axis		x-axis		x-axis	
ω	K_r/a^2	K_i/a^2	K_r/a^2	K_i/a^2	K_r/a^2	K_i/a^2
0.05	0.00003	-1.9278e-04	0.00007	-4.4710e-04	0.00006	-7.1045e-04
0.025	0.00010	-3.8130e-04	0.00014	-9.5103e-04	0.00010	-1.3445e-03
0.01	0.00059	-6.1433e-04	0.00096	-1.9250e-03	0.00142	-3.0604e-03
0.005	0.00101	-7.1967e-04	0.00206	-3.2453e-03	0.00202	-5.9250e-03
0.0025	0.00144	-5.9157e-04	0.00415	-4.4372e-03	0.00446	-1.0296e-02
0.001	0.00169	-2.9820e-04	0.00790	-4.3898e-03	0.01285	-1.8601e-02
0.0005	0.00174	-1.5536e-04	0.00995	-3.0826e-03	0.02475	-2.3137e-02
0.00025	0.00176	-7.8521e-05	0.01084	-1.7576e-03	0.03894	-2.2209e-02
0.0001	0.00176	-3.1504e-05	0.01116	-7.3479e-04	0.05165	-1.3586e-02
5e-05	0.00176	-1.5759e-05	0.01120	-3.6986e-04	0.05508	-7.5085e-03
2.5e-05	0.00176	-7.8803e-06	0.01122	-1.8524e-04	0.05609	-3.8637e-03

Table 4.10: The dimensionless dynamic permeability K/a^2 for the original configurations of the coarsened samples FB18 with $N_c = 120$ ($a_{120} = 22.8 \mu m$), $N_c = 240$ ($a_{240} = 11.4 \mu m$) and $N_c = 480$ ($a_{480} = 5.7 \mu m$).

Frequency	$N_c = 120$		$N_c = 240$		$N_c = 480$	
	x-axis		x-axis		x-axis	
ω	K_r/a^2	K_i/a^2	K_r/a^2	K_i/a^2	K_r/a^2	K_i/a^2
0.05	0.00003	-2.2229e-04	0.00004	-5.2303e-04	0.00007	-7.3790e-04
0.025	0.00012	-4.3390e-04	0.00015	-1.0652e-03	0.00010	-1.5118e-03
0.01	0.00063	-7.0305e-04	0.00102	-2.2021e-03	0.00124	-3.4227e-03
0.005	0.00113	-8.5822e-04	0.00219	-3.7031e-03	0.00203	-6.5206e-03
0.0025	0.00165	-7.1701e-04	0.00458	-5.1778e-03	0.00461	-1.1701e-02
0.001	0.00196	-3.6502e-04	0.00900	-5.2661e-03	0.01401	-2.1270e-02
0.0005	0.00203	-1.9063e-04	0.01153	-3.7703e-03	0.02753	-2.6993e-02
0.00025	0.00204	-9.6413e-05	0.01267	-2.1722e-03	0.04432	-2.6589e-02
0.0001	0.00205	-3.8690e-05	0.01307	-9.1194e-04	0.06006	-1.6705e-02
5e-05	0.00205	-1.9354e-05	0.01313	-4.5934e-04	0.06447	-9.3149e-03
2.5e-05	0.00205	-9.6782e-06	0.01315	-2.3010e-04	0.06579	-4.8075e-03

Table 4.11: The dimensionless dynamic permeability K/a^2 for the mirror configurations along the x-direction of the coarsened sample FB18 with $N_c = 120$ ($a_{120} = 22.8 \mu m$), $N_c = 240$ ($a_{240} = 11.4 \mu m$) and $N_c = 480$ ($a_{480} = 5.7 \mu m$).

Frequency	Original				Mirror			
	$N_c = 240$		$N_c = 480$		$N_c = 240$		$N_c = 480$	
	x-axis		x-axis		x-axis		x-axis	
ω	K_r/a^2	K_i/a^2	K_r/a^2	K_i/a^2	K_r/a^2	K_i/a^2	K_r/a^2	K_i/a^2
0.05	0.00004	-1.3219e-04	0.00012	-2.4503e-04	0.00003	-1.6690e-04	0.00003	-9.1208e-05
0.025	0.00006	-2.8225e-04	0.00009	-5.2811e-04	0.00007	-3.4188e-04	0.00007	-1.8853e-04
0.01	0.00061	-5.0992e-04	0.00097	-1.1362e-03	0.00063	-5.9018e-04	0.00104	-1.2336e-03
0.005	0.00090	-7.1878e-04	0.00147	-1.9544e-03	0.00099	-9.1795e-04	0.00137	-2.2733e-03
0.0025	0.00140	-8.0783e-04	0.00230	-3.2142e-03	0.00162	-1.0494e-03	0.00249	-3.9380e-03
0.001	0.00194	-5.5492e-04	0.00520	-4.8438e-03	0.00235	-7.5465e-04	0.00602	-6.0712e-03
0.0005	0.00210	-3.1805e-04	0.00832	-4.8332e-03	0.00259	-4.3844e-04	0.00993	-6.1843e-03
0.00025	0.00215	-1.6553e-04	0.01071	-3.4978e-03	0.00267	-2.2934e-04	0.01307	-4.6000e-03
0.0001	0.00217	-6.7002e-05	0.01194	-1.6472e-03	0.00269	-9.2979e-05	0.01479	-2.2118e-03
5e-05	0.00217	-3.3559e-05	0.01216	-8.4724e-04	0.00270	-4.6581e-05	0.01511	-1.1430e-03
2.5e-05	0.00217	-1.6787e-05	0.01222	-4.2675e-04	0.00270	-2.3302e-05	0.01520	-5.7645e-04

Table 4.12: The dimensionless dynamic permeability K/a^2 for the original and mirror configurations along the x-direction of the coarsened sample FB13 with $N_c = 240$ ($a_{240} = 11.4 \mu m$) and $N_c = 480$ ($a_{480} = 5.7 \mu m$).

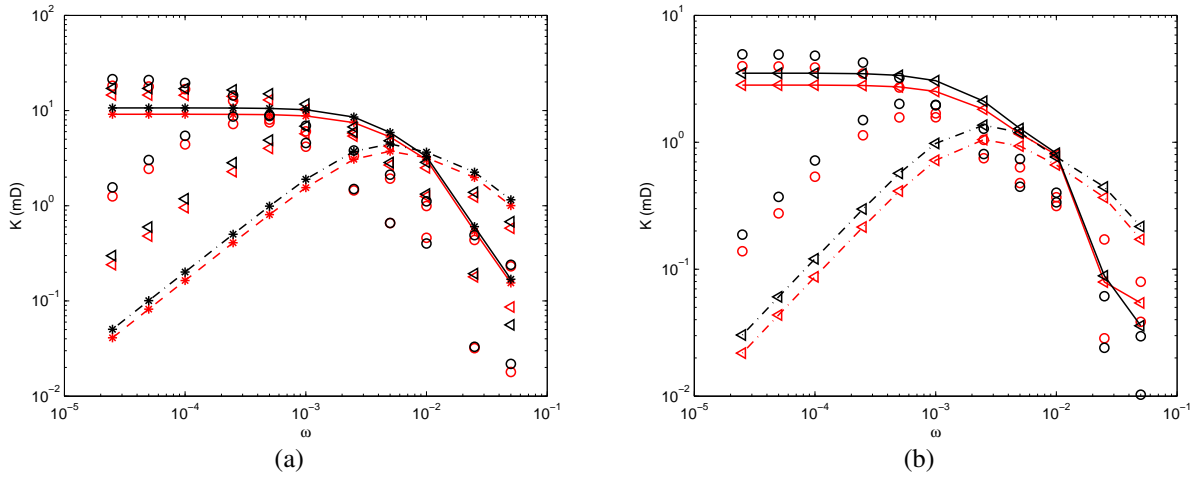


Figure 4.19: (a) The comparison of real dynamic permeability between the mirror configurations and the original ones of the coarsened sample FB18. Data are for $N_c = 120$ (*), $N_c = 240$ (\triangleright), $N_c = 480$ (\circ), original (red), mirror (black), real part (—), imaginary part (- - -). (b) The results for sample FB13.

4.6.2 The coefficients α , β and the velocities in the saturated samples

As presented in Chapter 2 and Chapter 3, the macroscopic coefficients α and β are calculated by the LBM-LSM coupled model. It is important to note that only the percolating component of the pore space is left in all four Fontainebleau samples; the closed porosity is eliminated. Then, the tensor α is computed by imposing a unit pressure in the pore and measuring the resulting mean stress in the solid matrix (2.101a). The coefficient β is numerically calculated by imposing a unit pressure in the pore and measuring the volume change of the pore (2.101b). Now, the necessary quantities of the generalized Christoffel equation (2.99) are fully determined and it allows us to calculate the acoustic velocities in saturated samples.

According to Pazdaniakou (2012) and Li (2010), the velocity of the waves propagation c_p and the attenuation coefficient a_h are given by

$$c_p = \frac{|c|^2}{c_r} \quad ; \quad a_h = \frac{\omega c_i}{|c|^2} \quad (4.15)$$

where c_r and c_i are the real and imaginary parts of c , respectively. Then, the attenuation effects

can be considered by studying the penetration depth h given by

$$h = a_h^{-1} \quad (4.16)$$

The physical constants of quartz and fluid used in simulations are given by

$$\begin{aligned} K_s = 37GPa & \quad G_s = 44GPa & \quad \rho_s = 2650kgm^{-3} \\ \mu_f = 10^{-3}Pa.s & \quad \rho_f = 1000kgm^{-3} \end{aligned} \quad (4.17)$$

As the macroscopic stiffness tensor, in this section, these coefficients are calculated by the coarsening method with the same coarsened samples as in the previous sections. The first calculations are for sample FB22 with the largest porosity. The simulation results of α and β for the coarsened sample FB22 with $N_c = 120$ are expressed as

$$\alpha = \begin{pmatrix} -0.3730 & 3.17 \times 10^{-3} & -1.11 \times 10^{-3} \\ 3.17 \times 10^{-3} & -0.2723 & -5.42 \times 10^{-5} \\ -1.11 \times 10^{-3} & -5.42 \times 10^{-5} & -0.3694 \end{pmatrix} \quad (4.18a)$$

$$\beta = -0.004504 \quad GPa^{-1} \quad (4.18b)$$

The tensor α is nearly spherical; the largest components are located on its diagonal. This corresponds well to the form presented by *Pazdniakou* (2012) and *Li* (2010). Since the effective stiffness tensor is calculated and the dynamic permeability with various values of frequency are given in Table 4.7, the generalized Christoffel equation can be solved. Then, the velocity c , the solid displacement \hat{U} and the fluid displacement \hat{W} are determined. For instance, when the frequency $\omega = 0.001$ and \mathbf{p} along the x-direction, the eigenvalue problem has four solutions

$$c = 6.17 + 2.0 \times 10^{-11}i \quad \hat{U} = \begin{pmatrix} 0.9999 \\ -0.0042 - 1.3 \times 10^{-13}i \\ -0.0015 - 4.7 \times 10^{-14}i \end{pmatrix} \quad \hat{W} = \begin{pmatrix} 2.3 \times 10^{-12} + 1.3 \times 10^{-11}i \\ 8.4 \times 10^{-15} + 4.6 \times 10^{-11}i \\ 2.9 \times 10^{-15} + 1.6 \times 10^{-14}i \end{pmatrix} \quad (4.19a)$$

$$c = 3.319 + 7.8 \cdot 10^{-12}i \quad \hat{U} = \begin{pmatrix} -1.8 \cdot 10^{-14} - 4.9 \cdot 10^{-17}i \\ -0.3294 - 1.2 \cdot 10^{-14}i \\ 0.9422 \end{pmatrix} \quad \hat{W} = \begin{pmatrix} -3.1 \\ , 10^{-22} - 1.3 \cdot 10^{-24}i \\ 6.6 \cdot 10^{-13} + 3.6 \cdot 10^{-12}i \\ -1.9 \cdot 10^{-12} - 1.0 \cdot 10^{-11}i \end{pmatrix} \quad (4.19b)$$

$$c = 3.319 + 7.8 \cdot 10^{-12}i \quad \hat{U} = \begin{pmatrix} 0.0045 + 4.9 \cdot 10^{-13}i \\ 0.9442 \\ 0.3294 + 1.2 \cdot 10^{-14}i \end{pmatrix} \quad \hat{W} = \begin{pmatrix} -7.7 \cdot 10^{-14} - 4.2 \cdot 10^{-13}i \\ -1.9 \cdot 10^{-12} - 1.0 \cdot 10^{-11}i \\ -6.6 \cdot 10^{-13} - 3.6 \cdot 10^{-12}i \end{pmatrix} \quad (4.19c)$$

$$c = 3.06 \cdot 10^{-5} + 2.6 \cdot 10^{-5}i \quad \hat{U} = \begin{pmatrix} -0.685 - 2.0 \cdot 10^{-11}i \\ 0.131 - 4.5 \cdot 10^{-12}i \\ 0.005 + 5.9 \cdot 10^{-13}i \end{pmatrix} \quad \hat{W} = \begin{pmatrix} 0.727 \\ -2.1 \cdot 10^{-12} + 1.1 \cdot 10^{-13}i \\ -4.3 \cdot 10^{-15} - 4.9 \cdot 10^{-14}i \end{pmatrix} \quad (4.19d)$$

As can be seen, in the first solution, the velocity is mostly real; the imaginary part is very small and the attenuation is very weak. The solid displacement \hat{U} is nearly purely real along the x-direction. Therefore, we can say that this is an almost pure compression wave. Moreover, the fluid displacement \hat{W} is small compared to \hat{U} , i.e., the wave propagates mostly through the solid matrix. This corresponds to the fast compressional wave and the velocity is denoted by $c_{||}^{fast}$.

In the second and third solutions, the solid displacement \hat{U} is nearly purely real along the y-direction or the z-direction, i.e., U oscillates along a single direction which is nearly orthogonal to p . They are called the shear waves and the velocity is denoted by c_{\perp} . These two solutions are almost identical, and from now on, only one of them is considered.

In the last solution, both solid and fluid displacements occur mostly along the x-direction, but the velocity is much smaller than $c_{||}^{fast}$; therefore, it is the slow compressional wave and the velocity is $c_{||}^{slow}$. Due to the large imaginary part, it has a strong attenuation. Of course, these three types correspond well to the ones presented by *Biot* (1956a,b).

Note that these results are relative to an incompressible fluid; then, the influence of the fluid compressibility can be studied by introducing the compressibility coefficient c_f (Li, 2010). The calculations of saturated samples are performed with three types of fluids: incompressible ($c_f = 0$), slightly compressible ($c_f = 4.6 \times 10^{-10} Pa^{-1}$; it corresponds to water in normal conditions) and highly compressible ($c_f = 100 \times 10^{-10} Pa^{-1}$). Based on the simulation results for incompressible fluids, the dependency of β on c_f can be calculated by (2.98). The velocities of the three waves (given in km/s) are given in Table 4.13.

It is clear that c_f has an influence on compressional waves while the shear wave does not depend on it as it will be demonstrated later.

C_f	$c_{ }^{fast}$	c_{\perp}	$c_{ }^{slow}$
$c_f = 100 \times 10^{-10} Pa^{-1}$	$4.968 + 1.2 \times 10^{-11}i$	$3.319 + 7.8 \times 10^{-12}i$	$1.76 \times 10^{-6} + 1.5 \times 10^{-6}i$
$c_f = 4.6 \times 10^{-10} Pa^{-1}$	$5.025 + 8.6 \times 10^{-12}i$	$3.319 + 7.8 \times 10^{-12}i$	$7.94 \times 10^{-6} + 6.6 \times 10^{-6}i$
Gassmann's model	5.2087	3.319	-
Error (%)	0.1	0	-

Table 4.13: The velocities in sample FB22 of $N_c = 120$ saturated by a slightly compressible fluid ($c_f = 4.6 \times 10^{-10} Pa^{-1}$) and highly compressible fluid $c_f = 100 \times 10^{-10} Pa^{-1}$. Comparison to Gassmann's model.

As discussed in Section 2.7, in order to evaluate our simulation results, the Gassmann's model (Gassmann, 1951; Han and Batzle, 2004; Fredy and Alvarado, 2006) is used for comparison. It allows us to calculate the velocities in the coarsened sample FB22 with $N_c = 120$ saturated by water (1 bar). The method is presented in Chapter 2; the value of K_{dry} and G_{dry} are obtained from simulations. The equations (2.102), (2.103) and (2.104) imply

$$\rho_{b2} = 2304 \text{ } kgm^{-3}; \quad K_{\phi} = 12.738 \text{ } GPa; \quad K_{sat2} = 24.421 \text{ } GPa; \quad G = 25.376 \text{ } GPa \quad (4.20)$$

Then, the velocities of compressional and shear wave are derived according to (2.105) and (2.106) and compared to the numerical results in Table 4.13. It is obvious that our results are in very good agreement with the Gassmann's model when the error for the fast compressional wave is less than 0.1% and the shear wave velocities are identical.

The other simulations are done for various frequencies in the same way. The velocities of these three waves are calculated and presented in Tables 4.14 , 4.15 and 4.16. The dynamic permeabilities correspond to the original and the mirror configurations (Table 4.7).

Figures 4.20 and 4.21 show the influence of the frequency, of the compressibility coefficient and also of the configuration type on the acoustic velocities and on the attenuation effect in this saturated sample. It can be seen that the frequency has almost no influence on the fast compressional wave and shear wave velocities while $c_{||}^{slow}$ increases with frequency. The penetration depth h is always a decreasing function of frequency (Figure 4.21) in good agreement with *Pazdniakou* (2012).

With the other fluids, the velocity $c_{||}^{fast}$ is depending on the compressibility coefficient and is a decreasing function of c_f . *Li* (2010) pointed out that the fast compressional wave in the saturated medium with compressible fluids is slower than in the dry medium, because of the additional inertia due to the interstitial fluid. The change of $h_{||}^{fast}$ is of interest since

$$h_{||}^{fast}(c_f = 4.6) > h_{||}^{fast}(c_f = 100) > h_{||}^{fast}(c_f = 0) \quad (4.21)$$

Therefore, the variations of $h_{||}^{fast}(c_f)$ are not monotonous. For the slow wave, the dependence $c_{||}^{slow}$ is similar to $c_{||}^{fast}$ but the compressibility of fluids has no influence on $h_{||}^{slow}$. Finally, the velocity c_{\perp} and the depth h_{\perp} of the shear wave is independent in this case.

The original and mirror configurations have the same velocities except for the slow compressional wave velocity. $c_{||}^{slow}$ of the mirror is slightly larger than the one of the original; this difference is clearly shown for the high frequencies in Figure 4.20.b.

ω	Original $N_{cx} = 120$						Mirror $N_{cx} = 240$					
	$C_f = 0$		$C_f = 4.6$		$C_f = 100$		$C_f = 0$		$C_f = 4.6$		$C_f = 100$	
	C_r	C_i	C_r	C_i	C_r	C_i	C_r	C_i	C_r	C_i	C_r	C_i
0.05	6.17	1.8e-11	5.025	7.8e-12	4.968	1.0e-11	6.17	2.0e-11	5.025	8.6e-12	4.968	1.2e-11
0.025	6.17	3.0e-11	5.025	1.3e-11	4.968	1.7e-11	6.17	3.5e-11	5.025	1.5e-11	4.968	2.0e-11
0.01	6.17	6.4e-11	5.025	2.7e-11	4.968	3.7e-11	6.17	7.0e-11	5.025	3.0e-11	4.968	4.0e-11
0.005	6.17	6.2e-11	5.025	2.7e-11	4.968	3.6e-11	6.17	6.7e-11	5.025	2.9e-11	4.968	3.8e-11
0.0025	6.17	4.3e-11	5.025	1.9e-11	4.968	2.5e-11	6.17	4.8e-11	5.025	2.1e-11	4.968	2.8e-11
0.001	6.17	2.0e-11	5.025	8.6e-12	4.968	1.2e-11	6.17	2.3e-11	5.025	9.8e-12	4.968	1.3e-11
0.0005	6.17	1.1e-11	5.025	4.5e-12	4.968	6.0e-12	6.17	1.2e-11	5.025	5.0e-12	4.968	6.7e-12
0.00025	6.17	5.3e-12	5.025	2.3e-12	4.968	3.0e-12	6.17	5.9e-12	5.025	2.5e-12	4.968	3.4e-12
0.0001	6.17	2.1e-12	5.025	9.0e-13	4.968	1.2e-12	6.17	2.4e-12	5.025	1.0e-12	4.968	1.4e-12
5e-05	6.17	1.1e-12	5.025	4.5e-13	4.968	6.0e-13	6.17	1.2e-12	5.025	5.1e-13	4.968	6.8e-13
2.5e-05	6.17	5.3e-13	5.025	2.3e-13	4.968	3.0e-13	6.17	5.9e-13	5.025	2.6e-13	4.968	3.4e-13

Table 4.14: The fast compressional wave velocities in the original and mirror configurations of the coarsened sample FB22 ($N_{cx} = 120$) saturated by the three types of fluids: incompressible fluid ($C_f = 0$), low compressibility ($C_f = 4.6$, water in pressure of 1b) and high compressibility ($C_f = 100$).

ω	Original $N_{cx} = 120$						Mirror $N_{cx} = 240$					
	$C_f = 0$		$C_f = 4.6$		$C_f = 100$		$C_f = 0$		$C_f = 4.6$		$C_f = 100$	
	C_r	C_i	C_r	C_i	C_r	C_i	C_r	C_i	C_r	C_i	C_r	C_i
0.05	9.65e-05	7.29e-06	2.50e-05	1.89e-06	5.55e-06	4.19e-07	1.02e-04	7.62e-06	2.65e-05	1.98e-06	5.88e-06	4.38e-07
0.025	9.55e-05	1.21e-05	2.48e-05	3.15e-06	5.49e-06	6.98e-07	1.01e-04	1.36e-05	2.61e-05	3.51e-06	5.79e-06	7.79e-07
0.01	8.25e-05	3.00e-05	2.14e-05	7.78e-06	4.74e-06	1.73e-06	8.79e-05	3.12e-05	2.28e-05	8.08e-06	5.05e-06	1.79e-06
0.005	6.92e-05	3.49e-05	1.79e-05	9.05e-06	3.98e-06	2.01e-06	7.24e-05	3.59e-05	1.88e-05	9.31e-06	4.16e-06	2.06e-06
0.0025	5.04e-05	3.32e-05	1.31e-05	8.61e-06	2.90e-06	1.91e-06	5.32e-05	3.51e-05	1.38e-05	9.10e-06	3.06e-06	2.02e-06
0.001	3.06e-05	2.55e-05	7.94e-06	6.61e-06	1.76e-06	1.47e-06	3.26e-05	2.72e-05	8.44e-06	7.04e-06	1.87e-06	1.56e-06
0.0005	2.12e-05	1.93e-05	5.49e-06	5.01e-06	1.22e-06	1.11e-06	2.24e-05	2.04e-05	5.80e-06	5.29e-06	1.29e-06	1.17e-06
0.00025	1.47e-05	1.39e-05	3.80e-06	3.61e-06	8.43e-07	8.01e-07	1.55e-05	1.48e-05	4.02e-06	3.84e-06	8.92e-07	8.51e-07
0.0001	9.13e-06	8.96e-06	2.37e-06	2.32e-06	5.25e-07	5.15e-07	9.69e-06	9.51e-06	2.51e-06	2.47e-06	5.57e-07	5.47e-07
5e-05	6.42e-06	6.37e-06	1.67e-06	1.65e-06	3.69e-07	3.66e-07	6.82e-06	6.76e-06	1.77e-06	1.75e-06	3.92e-07	3.88e-07
2.5e-05	4.53e-06	4.51e-06	1.17e-06	1.17e-06	2.60e-07	2.59e-07	4.81e-06	4.79e-06	1.25e-06	1.24e-06	2.77e-07	2.75e-07

Table 4.15: The slow compressional wave velocities of the coarsened sample FB22 ($N_{cx} = 120$) saturated by the three types of fluids.

ω	Original $N_{cx} = 120$						Mirror $N_{cx} = 240$					
	$C_f = 0$		$C_f = 4.6$		$C_f = 100$		$C_f = 0$		$C_f = 4.6$		$C_f = 100$	
	C_r	C_i	C_r	C_i	C_r	C_i	C_r	C_i	C_r	C_i	C_r	C_i
0.05	3.319	7.0e-12	3.319	7.0e-12	3.319	7.0e-12	3.319	7.8e-12	3.319	7.8e-12	3.319	7.8e-12
0.025	3.319	1.2e-11	3.319	1.2e-11	3.319	1.2e-11	3.319	1.4e-11	3.319	1.4e-11	3.319	1.4e-11
0.01	3.319	2.5e-11	3.319	2.5e-11	3.319	2.5e-11	3.319	2.7e-11	3.319	2.7e-11	3.319	2.7e-11
0.005	3.319	2.4e-11	3.319	2.4e-11	3.319	2.4e-11	3.319	2.6e-11	3.319	2.6e-11	3.319	2.6e-11
0.0025	3.319	1.7e-11	3.319	1.7e-11	3.319	1.7e-11	3.319	1.9e-11	3.319	1.9e-11	3.319	1.9e-11
0.001	3.319	7.8e-12	3.319	7.8e-12	3.319	7.8e-12	3.319	8.9e-12	3.319	8.9e-12	3.319	8.9e-12
0.0005	3.319	4.1e-12	3.319	4.1e-12	3.319	4.1e-12	3.319	4.6e-12	3.319	4.6e-12	3.319	4.6e-12
0.00025	3.319	2.0e-12	3.319	2.0e-12	3.319	2.0e-12	3.319	2.3e-12	3.319	2.3e-12	3.319	2.3e-12
0.0001	3.319	8.2e-13	3.319	8.2e-13	3.319	8.2e-13	3.319	9.2e-13	3.319	9.2e-13	3.319	9.2e-13
5e-05	3.319	4.1e-13	3.319	4.1e-13	3.319	4.1e-13	3.319	4.6e-13	3.319	4.6e-13	3.319	4.6e-13
2.5e-05	3.319	2.0e-13	3.319	2.0e-13	3.319	2.0e-13	3.319	2.3e-13	3.319	2.3e-13	3.319	2.3e-13

Table 4.16: The shear wave velocities in the original and mirror configurations of the coarsened sample FB22 ($N_{cx} = 120$) saturated by the three types of fluids.

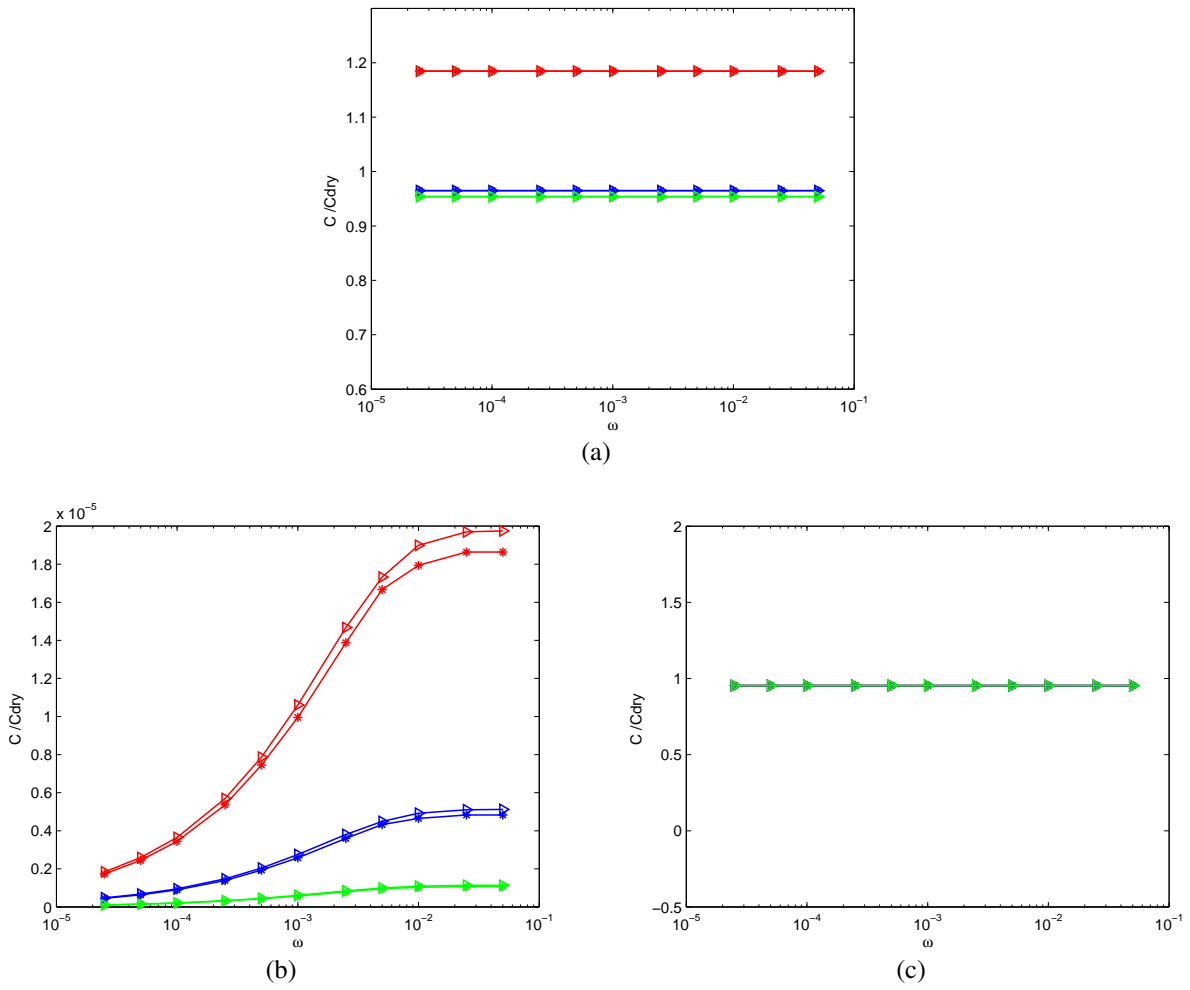


Figure 4.20: The acoustic velocities in the coarsened sample FB22 ($N_c = 120$) saturated by three types of fluids. (a) Fast compressional wave. (b) Slow compressional wave. (c) Shear wave. Data are for: original configuration (*), mirror configuration (\triangleright), incompressible fluid $c_f = 0$ (red), normal water $c_f = 4.6 \times 10^{-10}$ (blue), highly compressible fluid $c_f = 100 \times 10^{-10}$ (green).

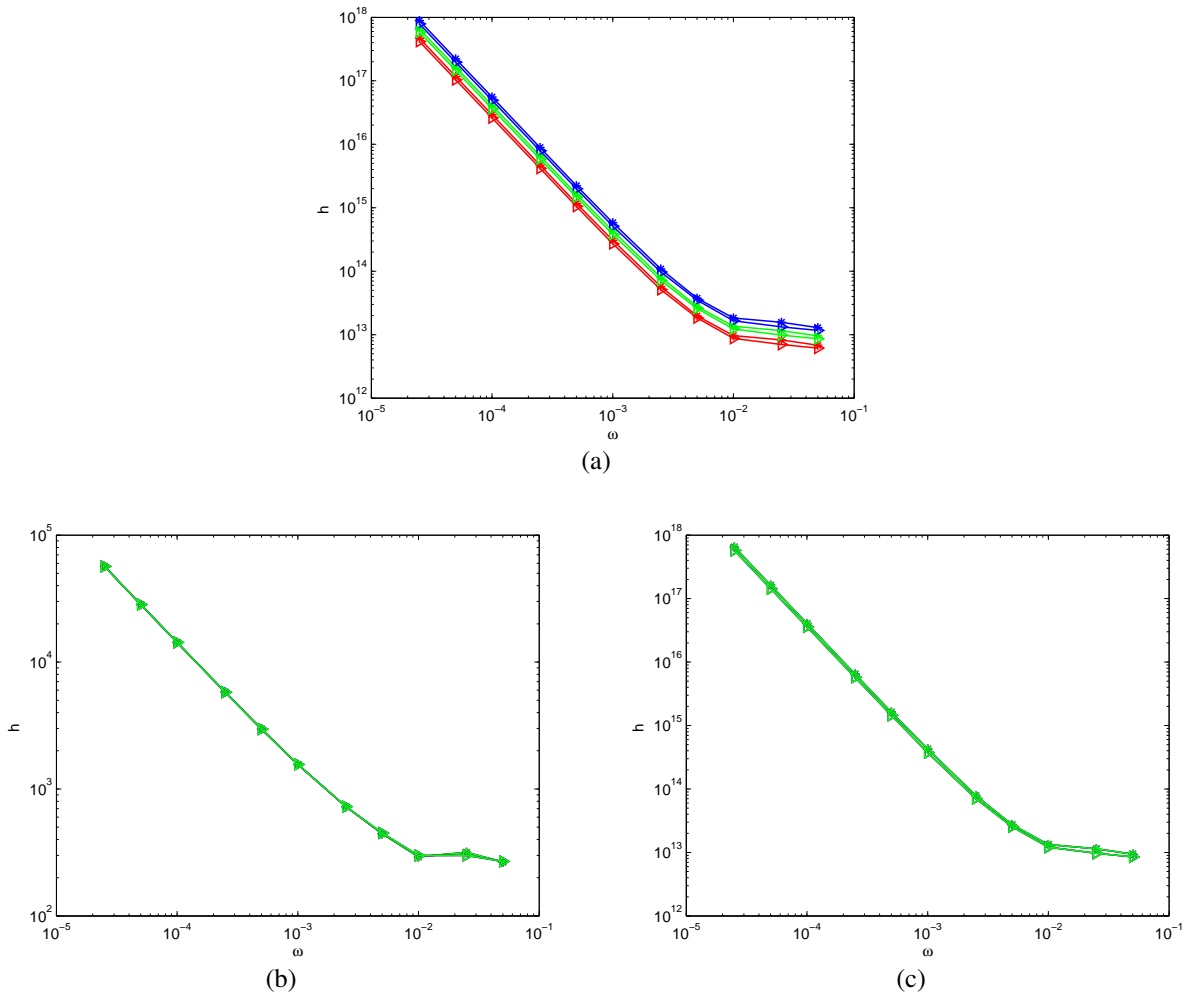


Figure 4.21: The penetration depth h characterizes the attenuation effects in the coarsened sample FB22 ($N_c = 120$) saturated by three types of fluids. (a) Fast compressional wave. (b) Slow compressional wave. (c) Shear wave. Data are for: original configuration (*), mirror configuration (\triangleright), incompressible fluid $c_f = 0$ (red), normal water $c_f = 4.6 \times 10^{-10}$ (blue), highly compressible fluid $c_f = 100 \times 10^{-10}$ (green).

The calculations for the other coarsened samples FB22 with larger discretizations are done in the same way. The results for $N_c = 240$ are given in Tables A.7, A.8 and A.9; the ones for $N_c = 480$ are given in Tables A.10, A.11 and A.12. Then, Figures 4.22 and 4.23 compare the results between the various discretizations. The velocity of the fast compressional wave with an incompressible fluid is about 1.18 times the dry velocity for $N_c = 120$ and about 1.22 for $N_c = 240$ and 480; this ratio decreases when c_f increases and the difference between these discretizations can be ignored

for high compressibility ($c_f = 100$) as seen in Fig. 4.22.a. The same behaviour is seen in the slow compressional wave; the difference is larger for high frequencies; however, the shear wave velocity does not depend on c_f . Finally, the penetration depth $h(120) > h(240) > h(480)$ for the fast compressional and shear waves, but the reverse is true for the slow wave as shown in Fig. 4.23.

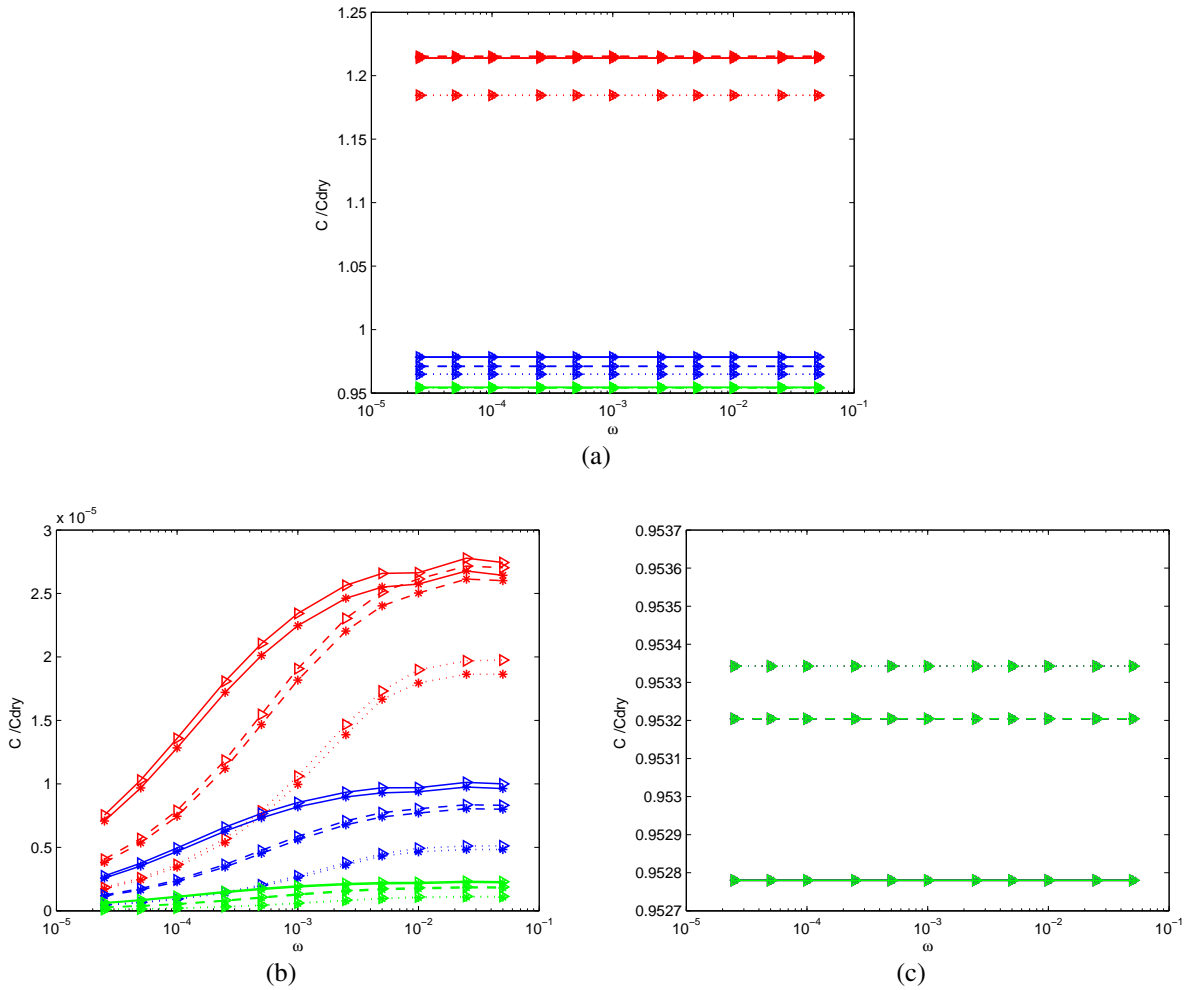


Figure 4.22: Comparison of acoustic velocities between the coarsened samples FB22 with $N_c = 120$, $N_c = 240$ and $N_c = 480$. (a) Fast compressional wave. (b) Slow compressional wave. (c) Shear wave. Data are for: $N_c = 120$ (.), 120 (- -), 480 (-), original configuration (*), mirror configuration (>), $c_f = 0$ (red), $c_f = 4.6 \times 10^{-10}$ (blue), $c_f = 100 \times 10^{-10}$ (green).

Similarly to sample FB22, since \mathbf{C}^{eff} , \mathbf{K} , α and β are fully determined, the acoustic velocities and the penetration depth h of the other samples as FB18 and FB13 can be derived from the generalized Christoffel equation. The results are gathered in Tables A.13, A.14, A.15, A.16, A.17,

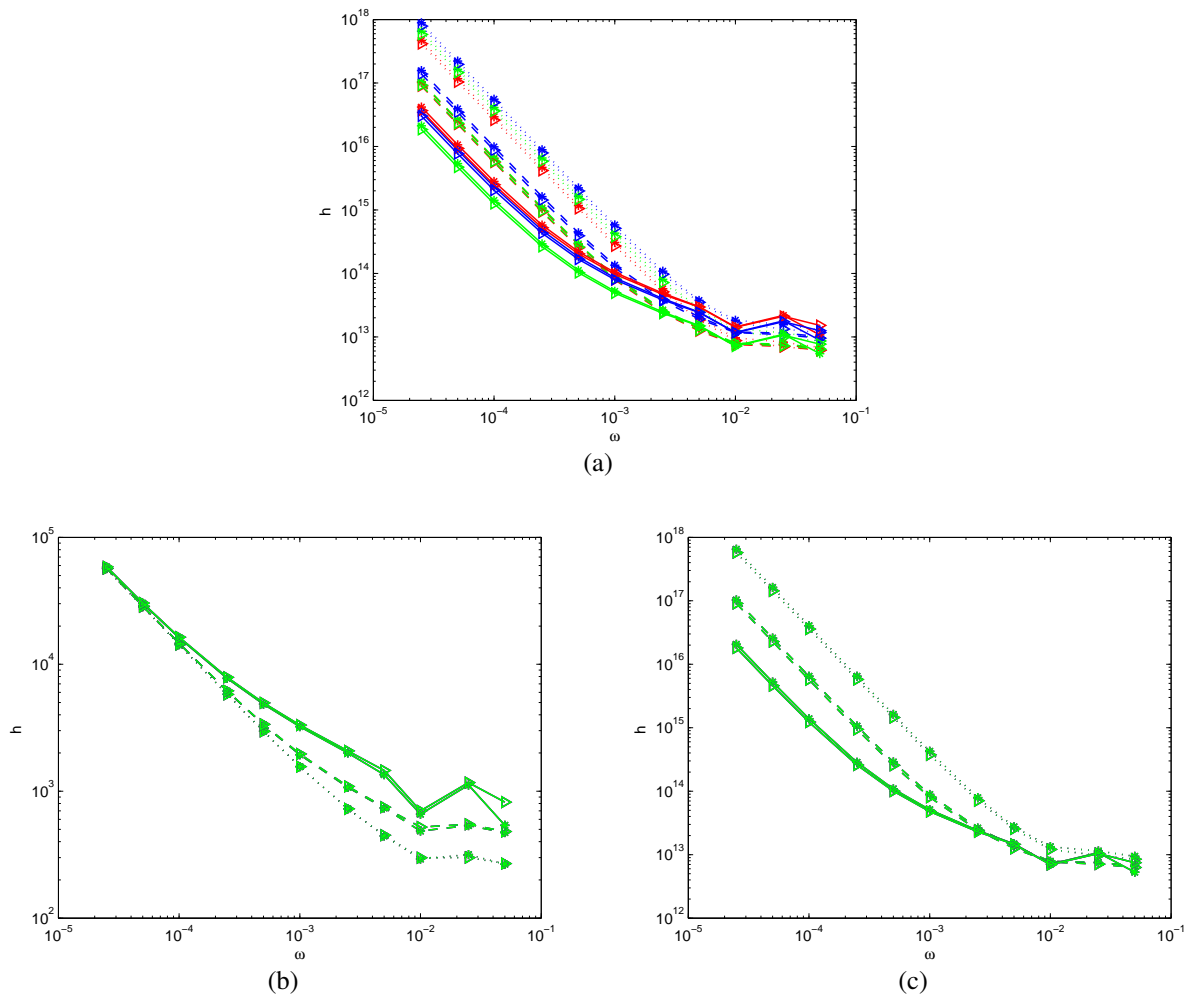


Figure 4.23: The penetration depth h for the coarsened samples FB22 with $N_c = 120$, $N_c = 240$ and $N_c = 480$. (a) Fast compressional wave. (b) Slow compressional wave. (c) Shear wave. Data are for: $N_c = 120$ (.), 120 (- -), 480 (-), original configuration (*), mirror configuration (\triangleright), $c_f = 0$ (red), $c_f = 4.6 \times 10^{-10}$ (blue), $c_f = 100 \times 10^{-10}$ (green).

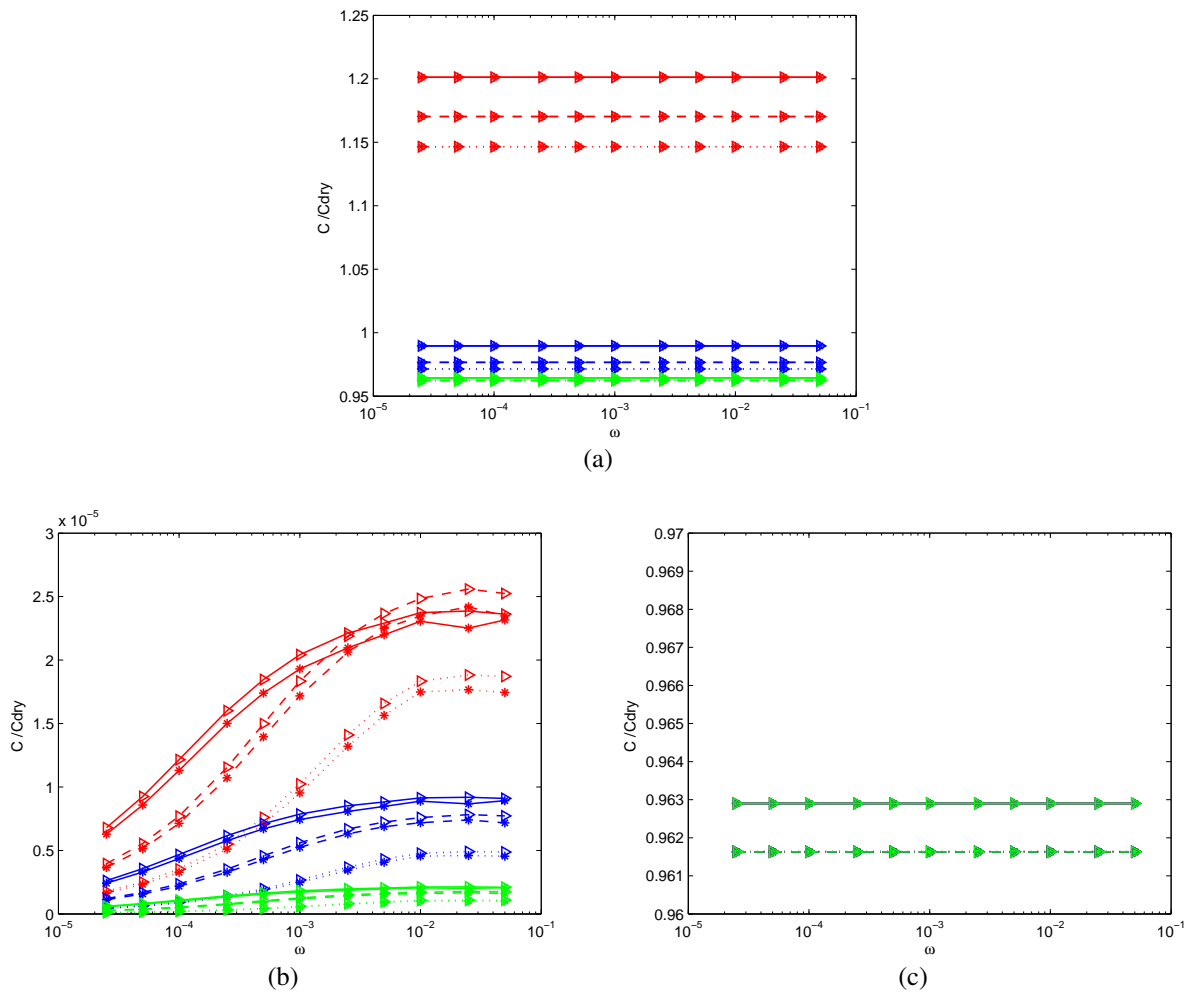


Figure 4.24: Comparison of acoustic velocities between the coarsened samples FB18 with $N_c = 120$, $N_c = 240$ and $N_c = 480$. (a) Fast compressional wave. (b) Slow compressional wave. (c) Shear wave. Data are for: $N_c = 120$ (.), 120 (- -), 480 (-), original configuration (*), mirror configuration (>), $c_f = 0$ (red), $c_f = 4.6 \times 10^{-10}$ (blue), $c_f = 100 \times 10^{-10}$ (green).

A.18, A.19, A.20 and A.21 for the coarsened samples FB18 with $N_c = 120$, 240 and 480; in Tables A.22, A.23, A.24, A.25, A.26 and A.27 for the coarsened samples FB 13 with $N_c = 240$ and 480. The results for samples FB8 are not available yet due to problems difficulties in the determination of the dynamic permeability.

Then, Figures 4.24, 4.25, 4.26 and 4.27 compare these results for samples FB18 and FB13. We can note that the ratio $c_{||}^{fast}/c_{dry}$ decreases when the sample porosity decreases. For instance, for the coarsened samples $N_c = 240$ saturated by the incompressible fluid, it is equal to 1.22 for FB22 ($\varepsilon = 0.21$), 1.17 for FB18 ($\varepsilon = 0.177$) and 1.075 for FB13 ($\varepsilon = 0.129$). However, this ratio

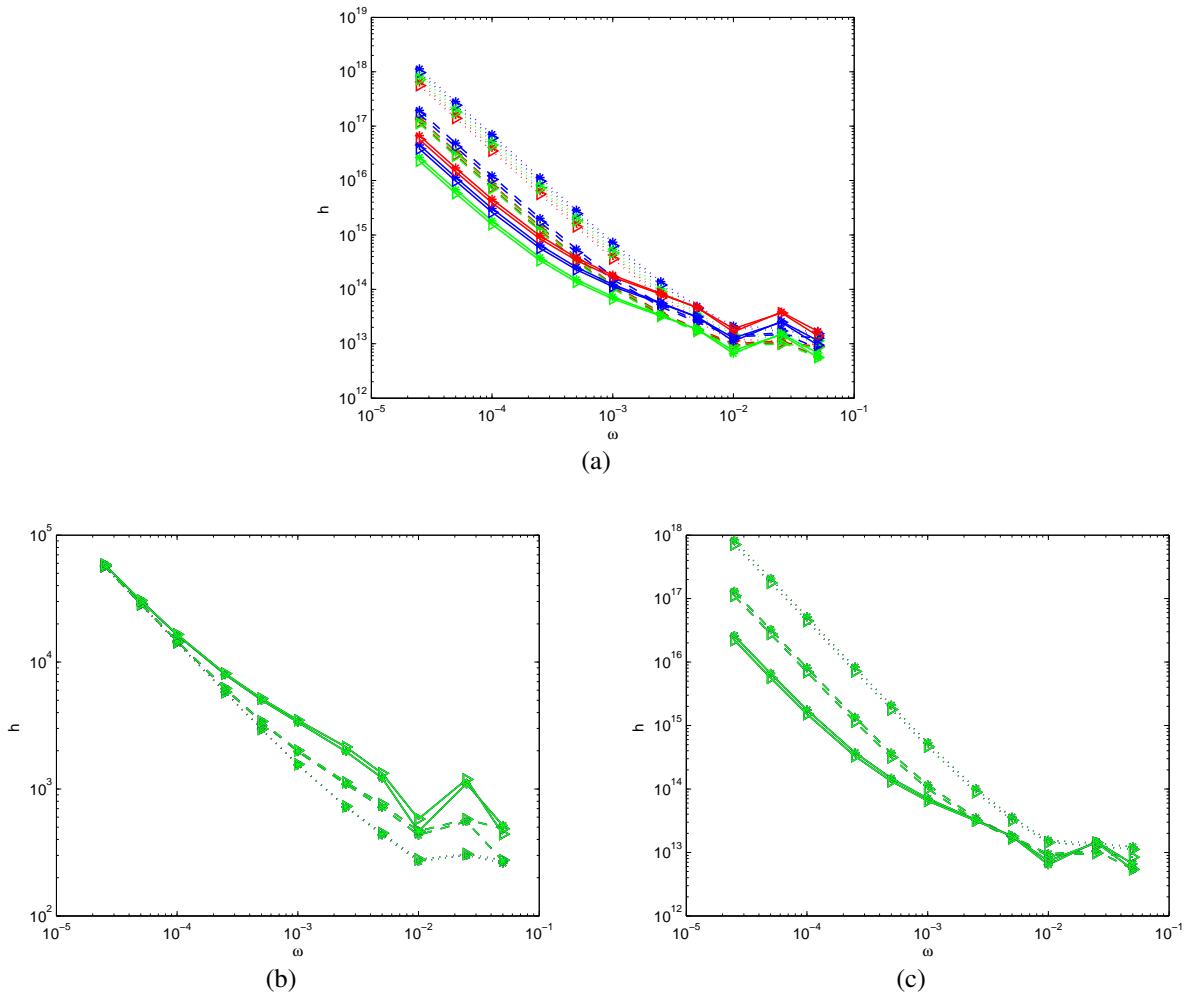


Figure 4.25: Penetration depths for coarsened samples FB18 with $N_c = 120$, $N_c = 240$ and $N_c = 480$. (a) Fast compressional wave. (b) Slow compressional wave. (c) Shear wave. Data are for: $N_c = 120$ (.), 120 (- -), 480 (-), original configuration (*), mirror configuration (\triangleright), $c_f = 0$ (red), $c_f = 4.6 \times 10^{-10}$ (blue), $c_f = 100 \times 10^{-10}$ (green).

is almost independent on the porosity for the slow compressional and shear waves.

Some noisy results for the penetration depth h occur for high frequencies as can be seen in Figures 4.25 and 4.27. It might be due to problems of the determination of the dynamic permeability \mathbf{K} since some changes were applied to satisfy the conditions on the Knudsen number.

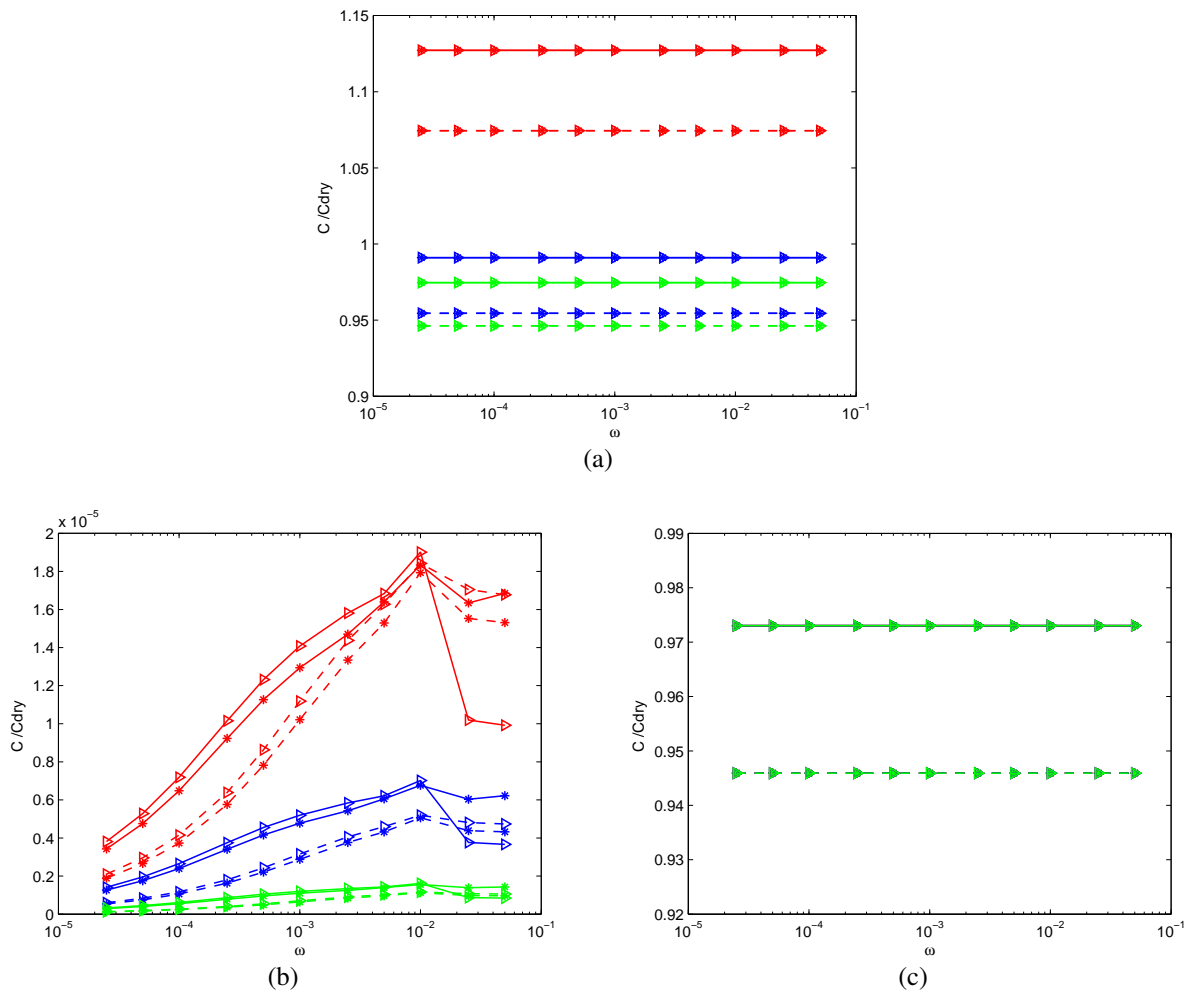


Figure 4.26: The acoustic velocities of the coarsened samples FB13 with $N_c = 240$ and $N_c = 480$. (a) Fast compressional wave. (b) Slow compressional wave. (c) Shear wave. Data are for: $N_c = 240$ (- -), 480 (-), original configuration (*), mirror configuration (\triangleright), $c_f = 0$ (red), $c_f = 4.6 \times 10^{-10}$ (blue), $c_f = 100 \times 10^{-10}$ (green).

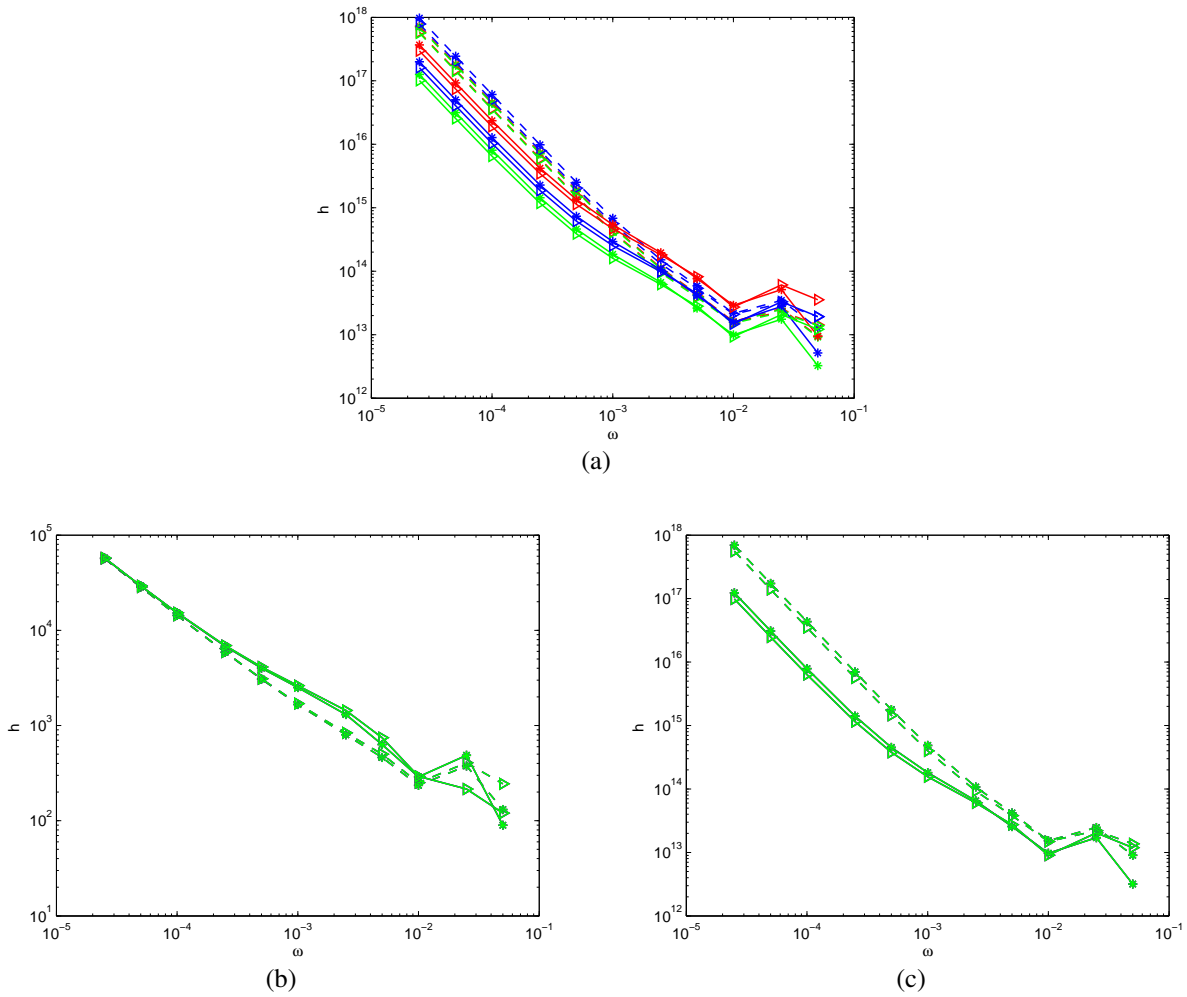


Figure 4.27: Penetration depths for the coarsened samples FB13 with $N_c = 240$ and $N_c = 480$. (a) Fast compressional wave. (b) Slow compressional wave. (c) Shear wave. Data are for: $N_c = 240$ (- -), 480 (-), original configuration (*), mirror configuration (\triangleright), $c_f = 0$ (red), $c_f = 4.6 \times 10^{-10}$ (blue), $c_f = 100 \times 10^{-10}$ (green).

As mentioned above, our simulation results can be compared with the compressional and shear wave velocities derived from the Gassmann's model presented in Chapter 2. The comparisons are done for the coarsened samples saturated by normal water (1bar) and the slightly compressible fluid. Then, Table 4.17 shows that the simulation velocities are very close to the Gassmann's model, the maximal relative difference is about 0.76 % for the fast compressional waves and always equal to 0% for the shear waves. This is consistent with the fact that the saturated shear wave velocity mostly depends on the shear modulus of the medium.

Samples	N_c	Simulation		Gassmann's model		Error	
		v_p	v_s	v_p	v_s	v_p	v_s
		km/s	km/s	km/s	km/s	%	%
FB 22	120	5.025	3.319	5.0287	3.319	0.1	0
	240	4.754	3.105	4.7622	3.105	0.2	0
	480	4.657	3.011	4.643	3.011	0.3	0
FB 18	120	5.152	3.414	5.1588	3.414	0.13	0
	240	4.921	3.236	4.9312	3.236	0.21	0
	480	4.875	3.163	4.838	3.163	0.76	0
FB 13	240	5.271	3.505	5.2791	3.505	0.15	0
	480	5.204	3.445	5.233	3.445	0.56	0

Table 4.17: The comparison between our simulation results and the Gassmann's model. The coarsened samples are saturated by water in normal conditions (1bar), $c_f = 4.6 \times 10^{-10}$.

Another comparison is performed for the samples saturated by air in normal conditions (1b). According to *Li* (2010) and *Denny* (1993), the physical properties of the air in this condition are given by

$$\rho_a = 1.16 \text{Kg.m}^{-3}; \quad \mu_a = 1.8 \times 10^{-5} \text{Pa.s}; \quad c_a^f = 10^{-5} \text{Pa}^{-1}; \quad K_a = 1.01 \times 10^5 \text{Pa} \quad (4.22)$$

Obviously, the samples which are saturated by air (1b) correspond to the dry samples. A comparison between the numerical results, the dry samples and Gassmann's model is given in Table 4.18; they have the same velocities since the maximal difference is equal to 0.2%.

Samples	N_{cx}	Numerical results		Dry		Error		Gassmann's model		Error	
		v_p	v_s	v_p	v_s	v_p	v_s	v_p	v_s	v_p	v_s
		km/s	km/s	km/s	km/s	%	%	km/s	km/s	%	%
FB22	120	5.208	3.4860	5.216	3.4811	0.2	0.1	5.2091	3.4812	0.2	0.1
	240	4.895	3.2575	4.895	3.2577	0	0	4.9028	3.2575	0.2	0
	480	4.759	3.16	4.76	3.16	0	0	4.764	3.16	0.1	0
FB18	120	5.303	3.550	5.303	3.5502	0	0	5.3046	3.550	0	0
	240	5.039	3.3653	5.039	3.3655	0	0	5.0481	3.3653	0.2	0
	480	4.933	3.29	4.93	3.29	0.1	0	4.94	3.29	0.1	0
FB13	240	5.367	3.6018	5.368	3.6019	0	0	5.3750	3.6018	0.1	0
	480	5.284	3.54	5.28	3.54	0.1	0	5.291	3.54	0.1	0

Table 4.18: The comparison between the coarsened samples saturated by air (1b), the dry ones and Gassmann's model.

As for the coarsening method used in Section A.2, since the acoustic velocities in the coarsened samples are determined, the ones for samples with an infinite discretization ($N_c = \infty$) can be derived by extrapolation. The same procedure is repeated and the results are given in Table 4.19. The compressional and shear wave velocities were also measured in some saturated clean sandstone samples by *Han* (1986). Due to the same reasons which are discussed in Section 4.3 devoted to dry samples, these experimental data are slightly smaller than the numerical ones as shown in Fig. 4.28.

N_c	Velocity	FB8	FB13	FB18	FB22
∞	v_p (km/s)	-	5.195	4.7595	4.5215
	v_s (km/s)	-	3.385	3.074	2.904

Table 4.19: The acoustic velocities in saturated samples with an infinite discretization.

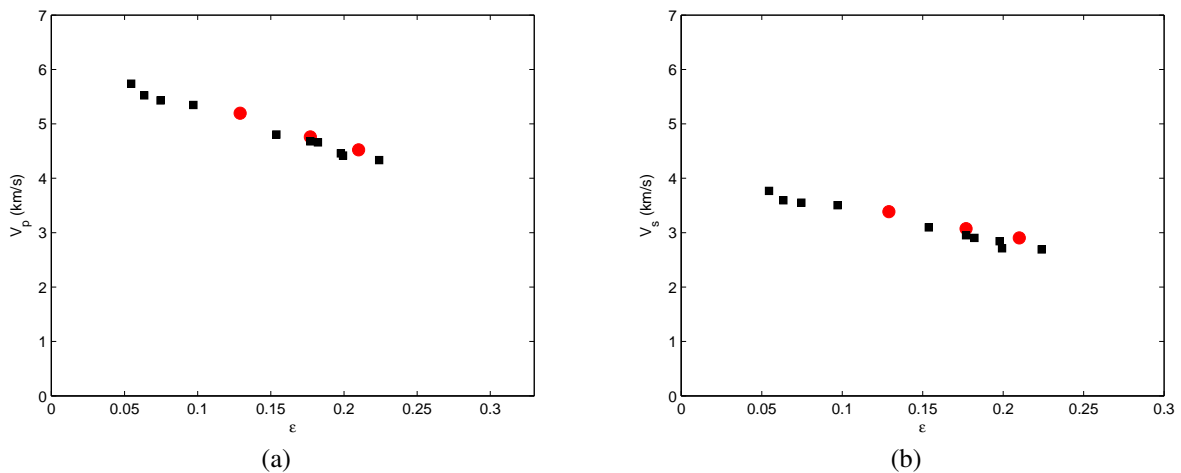


Figure 4.28: Comparison between the acoustic velocities in Fontainebleau samples with an infinite discretization and the experimental data of *Han* (1986). (a) The compressional wave velocity. (b) The shear wave velocity. Data are for: numerical (red \circ), *Han* (1986) (black \square).

4.7 Conclusions

This chapter presents the calculations for the four Fontainebleau samples FB22, FB18, FB13 and FB8. The sample porosities and the two point correlation functions are calculated and they indicate that the samples are close to isotropic and statistically homogeneous. The macroscopic properties such as the effective stiffness tensor C^{eff} , the bulk modulus K , the shear modulus G and the acoustic velocities in dry samples are determined by LSM. The results are close to the other numerical or empirical models (Arns, 1996; Nur *et al.*, 1991; Krief, 1990) and the experimental data (Han, 1986; Han *et al.*, 1986; Gomez *et al.*, 2010). The maximal difference for velocities is less than 8.2%.

The macroscopic conductivity tensor and the characteristic length Λ are calculated by the method of Thovert *et al.* (1990) and close to Archie's law. The absolute and dynamic permeabilities are calculated by LBM with the original and the mirror configurations and then compared to one another; the mirror one is considered to be more precise. The universal scaling behaviour is also verified and they are in good agreement with the Poiseuille flow. The coefficients α and β which characterize the interaction solid -fluid are determined by the LBM-LSM coupled model. Then, the acoustic velocities and the penetration depth of the fast and slow compressional as well as shear waves are calculated for the coarsened samples saturated by three types of fluid: incompressible fluid, slightly compressible fluid and highly compressible fluid. The slightly compressible fluid corresponds to water in normal conditions; therefore, the simulation results in this case are compared with the Gassmann's model and a very good agreement is obtained since the relative difference is always less than 0.3%. Another comparison between the dry samples and the ones saturated by air in normal conditions is performed and the maximal difference is only about 0.2%. Finally, the velocities in the saturated samples with an infinite discretization which are determined by extrapolations are in good agreement with the experimental data of Han (1986).

Chapter 5

Acoustic wave velocities in STATOIL samples with two solid components

5.1 Introduction

In this chapter, the calculations of wave propagations in four dry and saturated STATOIL samples X2, X7, Y5, Y13 are presented. These samples have three components, namely pore, clay and quartz.

The study of acoustic and dynamic properties of composite media has been an important and difficult problem for a long time. *Hashin and Shtrikman* (1962a,b), *Torquato* (1998, 2000), *Garboczi* (1993)... obtained some results, but with limitations; the geometry must be simple such as a cubic array of spheres, the solid components must have the same Poisson ratio, there is no pore in the media... In the recent years, there are some efficient numerical codes such as FMD (*Malinouskaya*, 2007),... but only for dry samples with a size limit. In this chapter, a homogenization approach (Chapter 2) associated with numerical tools such as LSM2S and LBM-LSM2S is used to solve this problem.

The calculations are done by the same procedure as for Fontainebleau samples. The acoustic properties in dry samples can be obtained from the effective stiffness tensors which are calculated by LSM2S. Furthermore, due to the large sample size, the coarsening method is also applied. The conductivity tensor and the characteristic length are calculated as for the porous media with one solid component. Then, the acoustic velocities in saturated samples are derived from the Christoffel equation after determining the 4 quantities C^{eff} , K , α and β . The samples are saturated by

slightly, highly and incompressible fluids; the influence of air under normal conditions (1b) is also studied. The calculations are performed with the original and mirror configurations as in the previous chapter. It is important to note that two comparisons are done in order to evaluate our simulation results; the first one is with Gassmann's model since the fluid is water (1b) and the second one is between the dry samples and the ones saturated by air (1b).

The organization of this chapter is as follows. Section 5.2 provides some details on the samples. The acoustic properties of dry samples are determined in Section 5.3. The formation factor F and the length Λ are given in Section 5.4. Then, the calculations of saturated samples are presented in Section 5.5, together with some comparisons. Finally, some conclusions are given in Section 5.6.

5.2 Characterizations of samples

Since these four samples are provided by STATOIL, they are called STATOIL samples. They are reconstructed from real porous media by micro-CT. Unlike the Fontainebleau samples, they are parallelepipedons of various sizes (as in Fig.5.1) and are divided into $N_{cx} \times N_{cy} \times N_{cz}$ elementary cubes of size $a = 5.7 \mu m$. Their names are X2, X7, Y5 and Y13 and the corresponding dimensions are given in Table 5.1.

Sample	N_{cx}	N_{cy}	N_{cz}
X2	1200	1200	436
X7	1200	1132	485
Y5	1200	1200	371
Y13	1000	1000	554

Table 5.1: The dimensions of the STATOIL samples. $a = 5.7 \mu m$.

As presented in Chapter 2, these samples contain three components: 0 is pore, 1 clay and 3 quartz. However, these labels are changed to make them suitable with our convention; 0 is clay, 1 pore and 2 quartz. Then, the phase function $Z(\mathbf{r})$ characterizing the pore space in such samples is

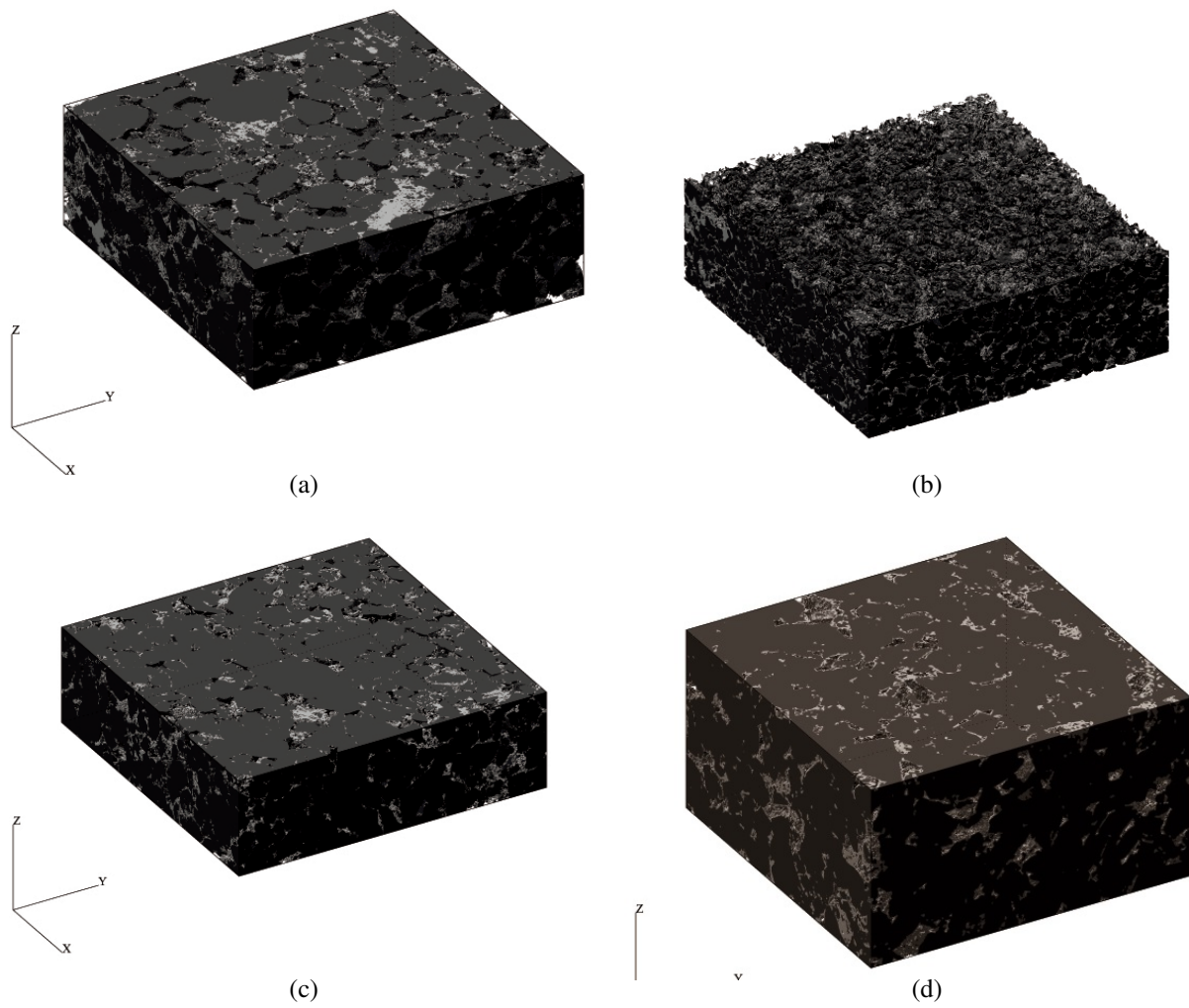


Figure 5.1: The four first samples from STATOIL: (a) X2, (b) X7, (c) Y5, (d) Y13.

given by

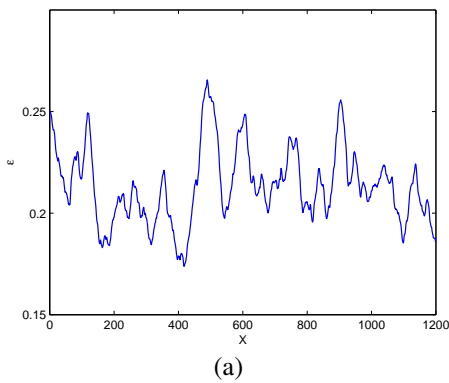
$$Z(\mathbf{r}) = \begin{cases} 0 & \text{if } \mathbf{r} \text{ belongs to clay} \\ 1 & \text{if } \mathbf{r} \text{ belongs to pore} \\ 2 & \text{if } \mathbf{r} \text{ belongs to quartz} \end{cases} \quad (5.1)$$

The STATOIL samples are characterized by the porosities and the correlation functions as the Fontainebleau samples.

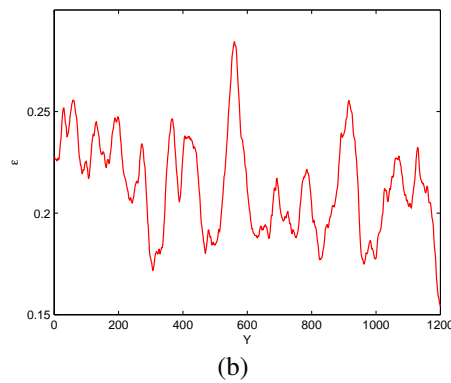
5.2.1 Porosities and component proportions

The size of sample X2 is $6480 \times 6480 \times 2485 \mu\text{m}^3$ and divided into $1200 \times 1200 \times 436$ elementary cubes. It is shown in Fig.5.1.a; the pores are transparent, the clay grey and the quartz black.

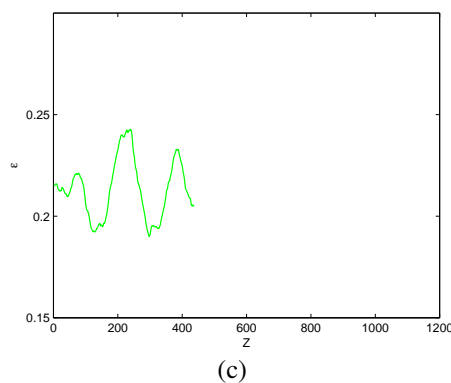
In the same way as in Section 4.2, the porosities of each slice along the x-, y-, z-direction of X2 are calculated and displayed in Fig.5.2. The maximal and the minimal values $\varepsilon_M(x)$ and $\varepsilon_m(x)$ are equal to 0.2656 and 0.1738 along the x-direction. These values are 0.2844, 0.1541 and 0.2428, 0.19 along the y- and z-direction, respectively. The average porosities along these directions are the same and equal to 0.2133.



The porosity along the x-direction



The porosity along the y-direction



The porosity along the z-direction

Figure 5.2: Porosity averaged over slices along the three axes in the sample X2.

The same calculations are performed for the other samples X7, Y5 and Y13. The results

are given in Table 5.4. The sample X7 has the maximal porosity (0.2712) and the Y13 has the minimal one (0.0739). The differences between the maximal and minimal porosities of slices along the three directions are significant in sample X2 (from 5.2% to 13%) and Y5 (from 14% to 18%); these differences are less than 7% in the samples X7 and Y13. Since the difference between the three directions is small (from 1% to 4%), these samples can be considered to be isotropic.

Sample	X2		X7		Y5		Y13	
ε	0.2133		0.2712		0.1781		0.0739	
$\varepsilon_M(x); \varepsilon_m(x)$	0.2656;	0.1738	0.2974;	0.2393	0.2612;	0.1154	0.1159;	0.0421
$\varepsilon_M(y); \varepsilon_m(y)$	0.2844;	0.1541	0.2953;	0.2329	0.2828;	0.1097	0.1222;	0.0382
$\varepsilon_M(z); \varepsilon_m(z)$	0.2428;	0.19	0.2849;	0.2571	0.2050;	0.1550	0.0935;	0.0515

Table 5.2: The maximal and minimal slice porosities of the 4 STATOIL samples.

In order to study the influence of the component proportions on the macroscopic properties, the proportions are calculated in the same way as the porosities and the results are given in Table 5.3. It is clear that the proportion of clay is very small in comparison with quartz; therefore, quartz is the main solid component which controls the effective properties.

Sample	Pore	Clay	Quartz
X2	0.2133	0.0522	0.7345
X7	0.2712	0.0501	0.6787
Y5	0.1781	0.0413	0.7806
Y13	0.0739	0.0757	0.8504

Table 5.3: The component proportions of the 4 STATOIL samples.

5.2.2 Correlation functions

As for the Fontainebleau samples, the two point correlation functions are calculated for each slice (**2D**) and then the averages are compared between the three directions. The results of six slices along the z-direction of the sample X2 are presented in Fig.5.3. As it can be seen in the superposition of all these results (Fig.5.4.a), when the distance u is small, the correlation functions of slices seem to be the same, while for large u , differences are significant. Then, the averaged

results along the three directions are calculated and compared in Fig.5.4.a, the difference between them is small when u is less than 200.

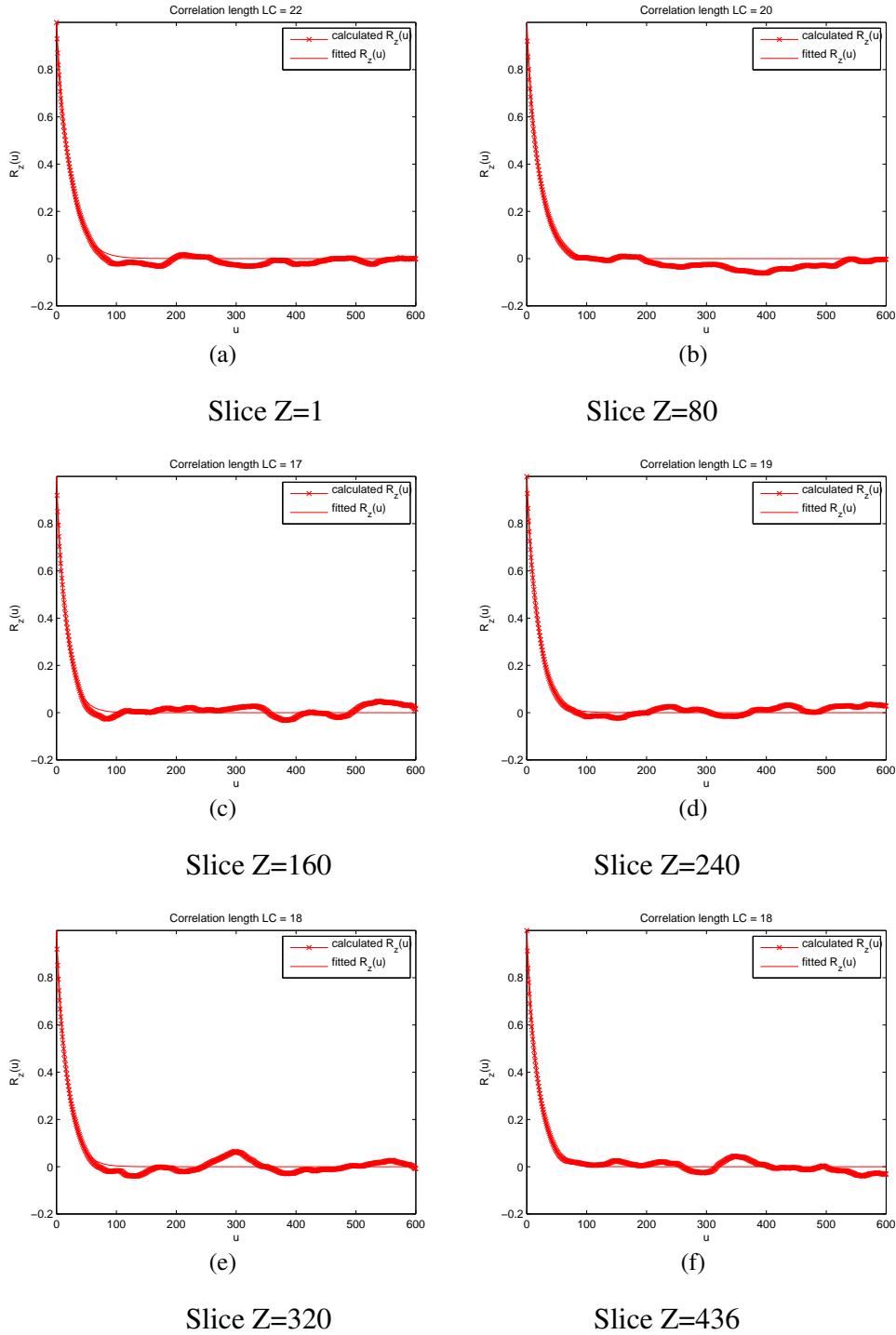


Figure 5.3: The correlation function of some slices in the x-y plane. STATOIL sample X2.

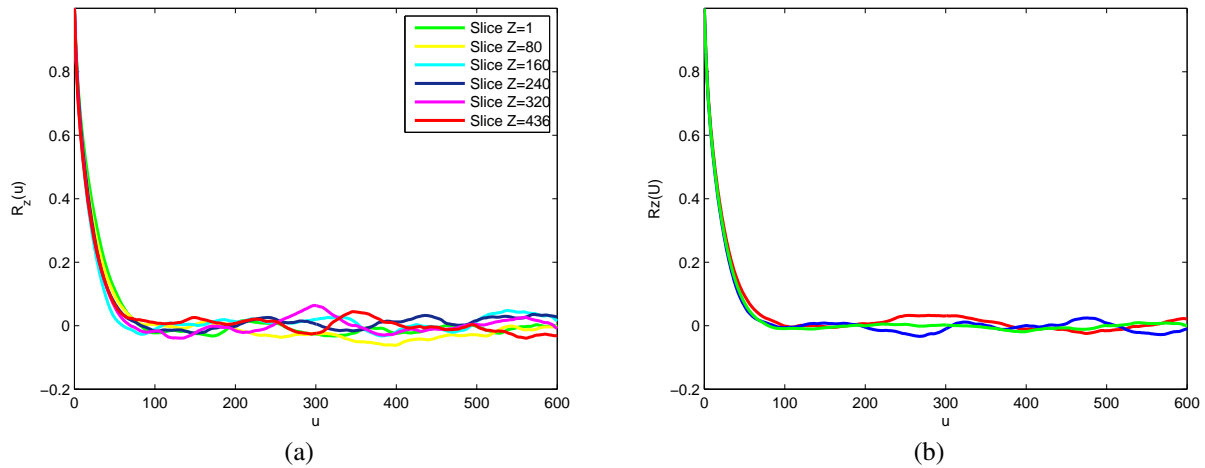


Figure 5.4: (a) The overall correlation functions of some slices in the x-y plane of the sample X2. (b) The averaged results along the three directions. Data are for: the x-direction (red), y-direction (blue) and z-direction (green).

Similarly, the two point correlation functions of X7, Y5 and Y13 are determined and presented in Fig.5.5. The results along the three directions of X7 and Y5 are close to each other as in the sample X2. However, for the sample Y13, the averaged one along the x-direction is different with the y- and z-directions even when u is small as it can be seen in Fig.5.5.c.

The Fourier components of the correlation functions R_Z are also checked as for the Fontainebleau samples. For all slices, the results which are always positive show that the four STATOIL samples can be considered homogeneous. For instance, the Fourier components corresponding to the correlation function of the slice $Z = 240$ of sample X2 are positive as it can be seen Fig. 5.6.a.

Thanks to these calculations, the correlation functions along the x-direction of all STATOIL samples are compared in Fig.5.6.b. The results of X2, Y5 and Y13 are closer than the one of X7.

5.3 Acoustic velocities in the dry samples

As for the Fontainebleau samples, the acoustic velocities in dry STATOIL samples are derived from the effective stiffness tensors. However, the difference is that they have two solid components; therefore, we must use the Lattice Spring Model for two solid components (LSM2S) which is developed from the basic LSM presented in Chapter 3. The accuracy of LSM2S has been

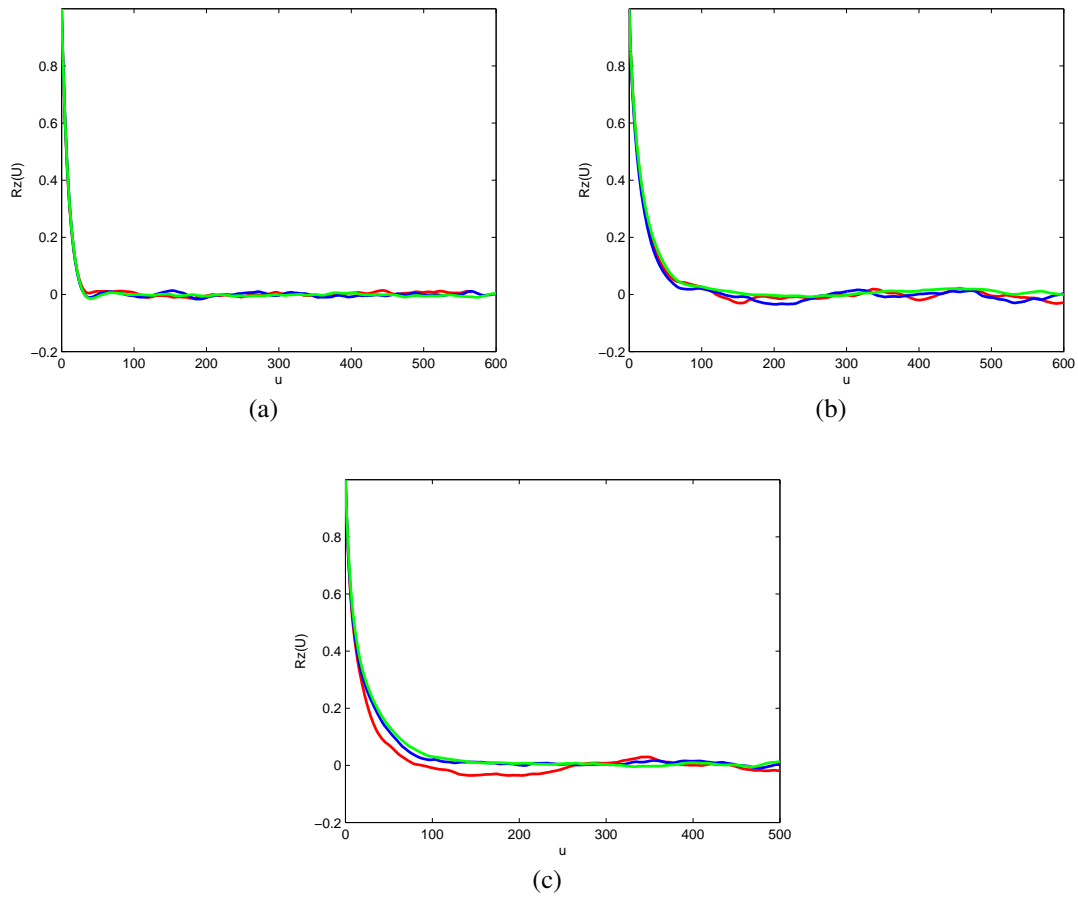


Figure 5.5: The averaged correlation functions along the three directions. Data for the x-direction (red), y-direction (blue) and z-direction (green). (a) Sample X7. (b) Sample Y5. (c) Sample Y13.

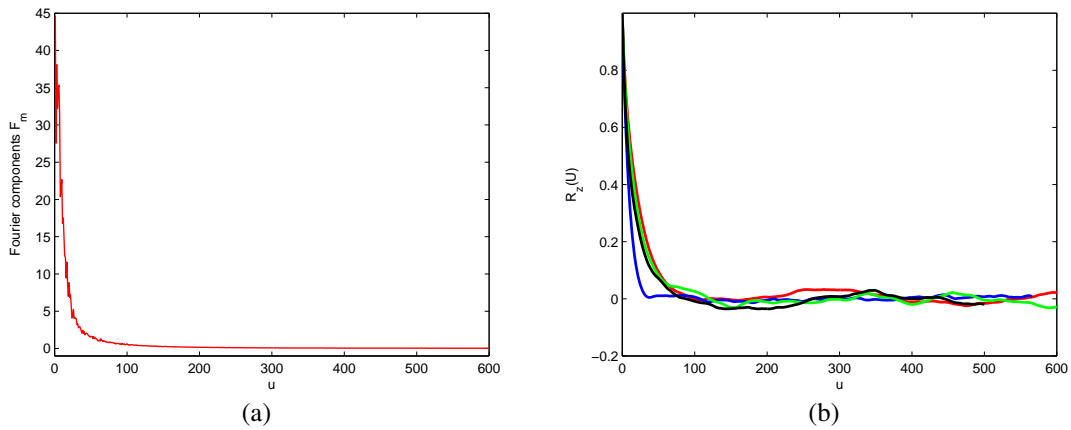


Figure 5.6: (a) The Fourier components corresponding to the correlation function of the slice $Z = 240$ of sample X2. (b) The averaged correlation functions along the x-direction of STATOIL samples. Data are for: X2 (red), X7 (blue) Y5 (green) and Y13 (black).

checked by comparison with others such as *Nemat-Nasser and Iwakuma (1982)*, *Torquato (1998)* and *Cohen (2004)*, the FFT method of *Hoang-Duc and Bonnet (2012)*, and the FMD of *Malinouskaya (2007)*. Moreover, simulations by LSM2S and FMD for the same coarsened samples X2 will be compared in Subsection 5.3.1.4.

These samples contain three components: pore, clay and quartz which correspond to 1, 0 and 2 (1-pore, 0-clay and 2-quartz). Their properties are given by *Arns (1996)* and recalled in Table 5.4.

Solid	K (GPa)	μ (GPa)	ρ [g/cm^{-3}]
Clay	20.8	6.9	2.6
Quartz	37.0	44.0	2.65

Table 5.4: The properties of solid components.

5.3.1 Samples X2

The simulation of simple stretching along the x-direction is carried out by LSM2S for the original sample X2, but due to the large sample size, the memory requirements are too large and exceed the computer memories.

Therefore, the coarsening method must be used, the principles of this method is presented in Section A.1. Then, for each coarsened sample, six simulations are needed to calculate nine values of the effective stiffness tensor for three simple stretchings and three simple shears.

5.3.1.1 The coarsened samples

The coarsened samples of size 150 x 150 x 54; 300 x 300 x 109 and 600 x 600 x 218 were derived from the original samples (Fig.5.7).

The coarsening method slightly changes the component proportions in the samples as shown in Table 5.5 and Fig.5.8.

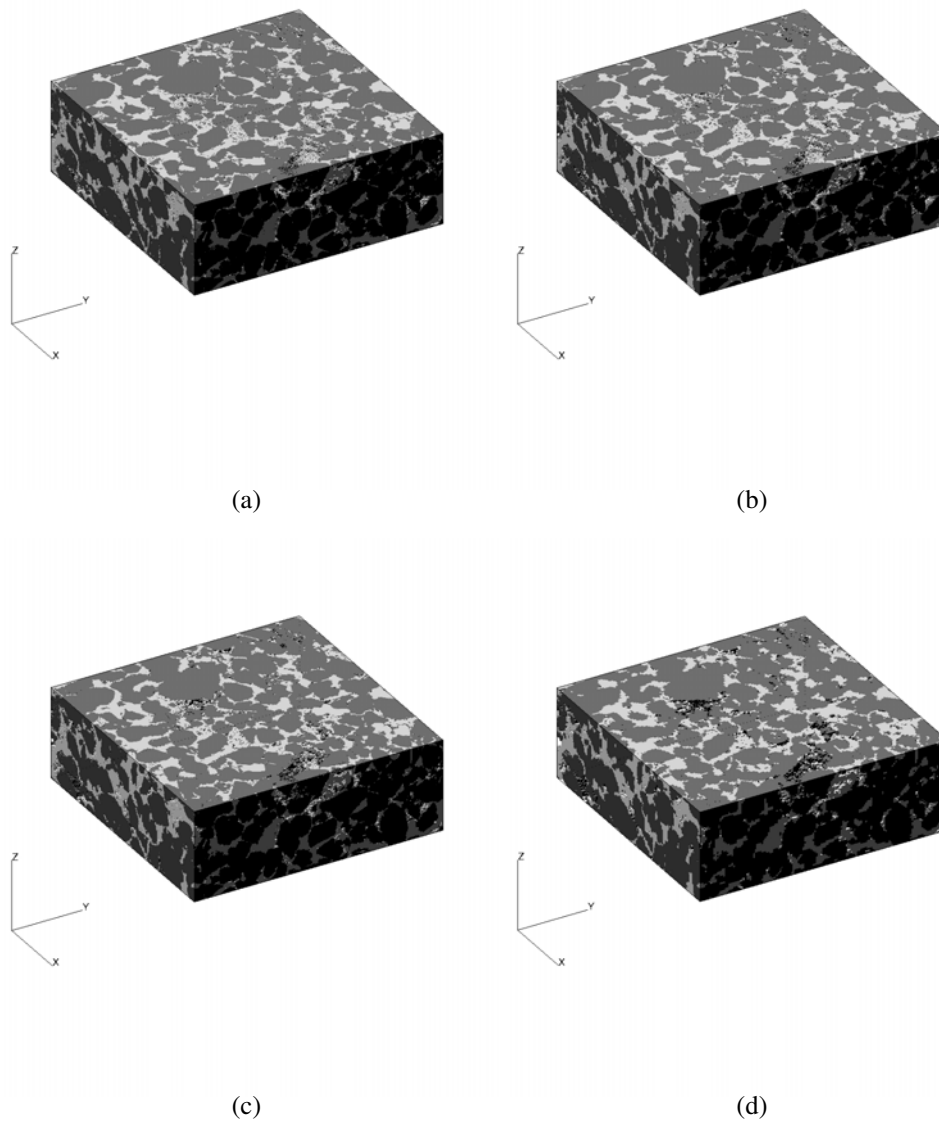


Figure 5.7: The coarsened samples X2. (a) The original sample $N_{cx}=1200$. (b) The sample $N_{cx}=600$. (c) The sample $N_{cx}=300$. (d) The sample $N_{cx}=150$.

Sample	N_{cx}	Pore	Clay	Quartz
X2	1200	0.2133	0.0522	0.7345
	600	0.2174	0.0561	0.7265
	300	0.2223	0.0562	0.7215
	150	0.2306	0.0518	0.7176
X7	1200	0.2712	0.0501	0.6787
	600	0.2764	0.0537	0.6699
	300	0.2887	0.0501	0.6612
	150	0.3085	0.0378	0.6537
Y13	1000	0.0739	0.0757	0.8504
	500	0.0734	0.0812	0.8454
	250	0.0711	0.0872	0.8471
	125	0.0679	0.0878	0.8443
Y5	1200	0.1781	0.0413	0.7806
	600	0.1769	0.0444	0.7787
	300	0.1808	0.0430	0.7762
	150	0.1886	0.0357	0.7757

Table 5.5: The change of component proportions in the coarsened STATOIL samples.

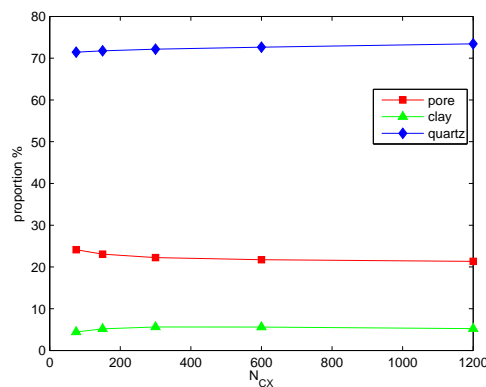


Figure 5.8: The component proportions in the coarsened samples X2.

For comparison, the middle slices of the coarsened samples are displayed in Fig.5.9. We can see that the coarsening method does not change much the spatial distribution of the components in the medium.

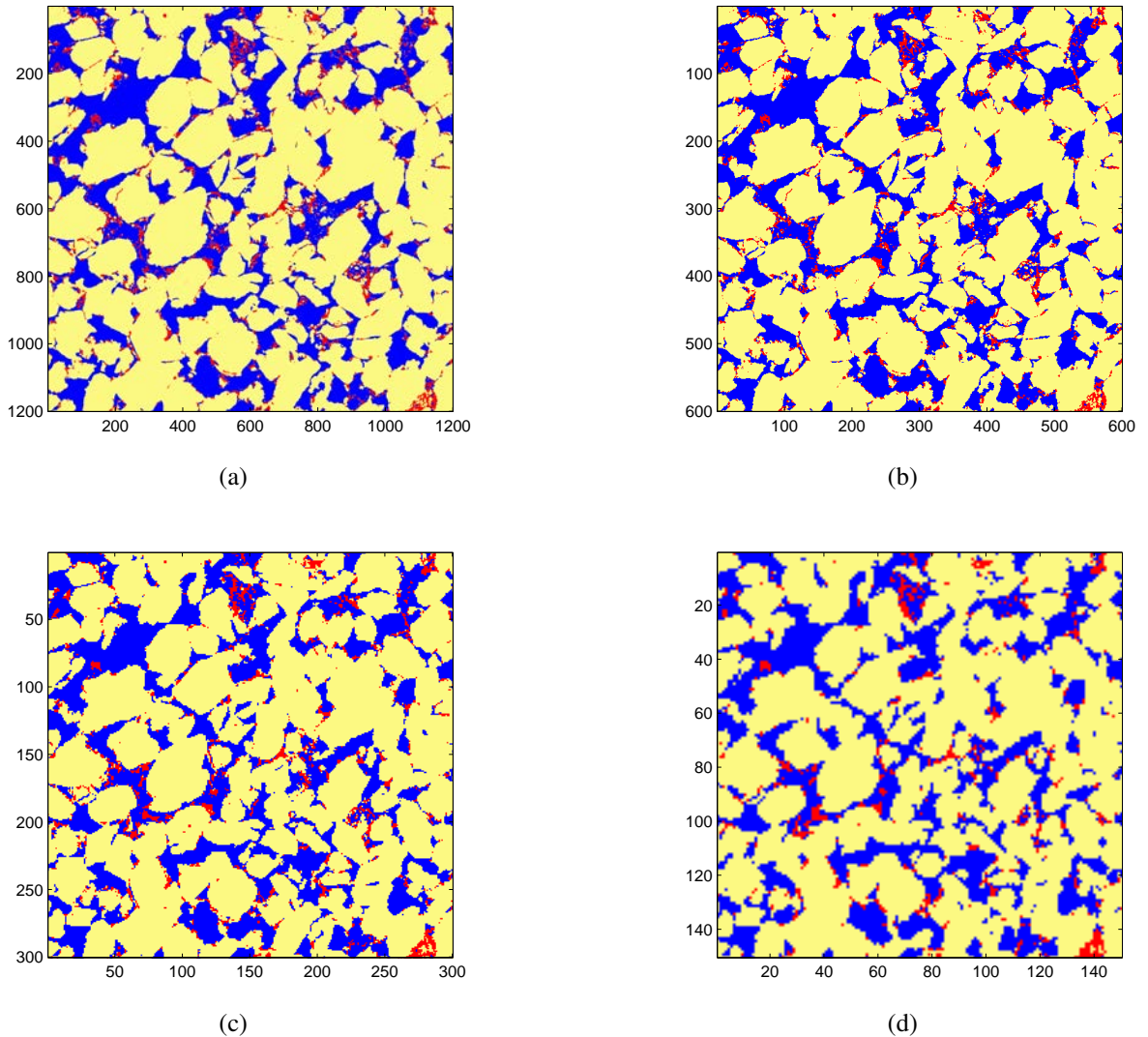


Figure 5.9: The middle slices of the coarsened samples X2. (a) The original sample $N_{cx}=1200$. (b) The sample $N_{cx}=600$. (c) The sample $N_{cx}=300$. (d) The sample $N_{cx}=150$.

The simulations were performed for the coarsened samples $N_{cx} = 150$, $N_{cx} = 300$ and $N_{cx} = 600$. The results for the original sample and the sample with an infinite discretization are obtained by extrapolations.

5.3.1.2 Results for the coarsened samples X2

Sample of size $150 \times 150 \times 54$

The effective stiffness tensor of this sample is calculated by 6 simulations. The calculation time is about 2 days and the memory requirement is 2.56 Gb for each simulation with a computer with 8 processors. Since all the components are numerically determined, the effective stiffness tensor is shown as symmetric and the large components are located only on the diagonal. The result expressed in GPa is given by

$$\mathbf{C}^{(eff)} = \begin{pmatrix} 43.58 & 5.99 & 5.83 & 0 & 0 & 0 \\ 5.99 & 45.64 & 5.93 & 0 & 0 & 0 \\ 5.83 & 5.93 & 41.68 & 0 & 0 & 0 \\ 0 & 0 & 0 & 18.52 & 0 & 0 \\ 0 & 0 & 0 & 0 & 18.09 & 0 \\ 0 & 0 & 0 & 0 & 0 & 19.08 \end{pmatrix} \quad (5.2)$$

The proportions of clay and quartz in the sample are equal to 0.052 and 0.718, respectively.

The average solid density is given by

$$\langle \rho \rangle = \frac{1}{V} \int_V \rho dV = \phi_0 \rho_0 + \phi_2 \rho_2 = 2036.3 \text{ kg/m}^3 \quad (5.3)$$

As for Fontainebleau samples, the acoustic velocities in this dry coarsened sample along the various directions are calculated according to (2.65) and presented in Table 5.6.

Size	x-axis		y-axis		z-axis		Erros	
	v_p^X (km/s)	v_s^X (km/s)	v_p^Y (km/s)	v_s^Y (km/s)	v_p^Z (km/s)	v_s^Z (km/s)	v_p %	v_s %
150 x 150 x 54	4.63	3.02	4.73	2.98	4.52	3.06	4.4	2.6
300 x 300 x 109	4.39	2.86	4.52	2.82	4.28	2.90	5.3	2.7
600 x 600 x 218	4.23	2.74	4.36	2.71	4.12	2.79	5.5	2.9

Table 5.6: The velocities of compressional and shear waves along the three directions in the coarsened samples X2.

Sample of size $300 \times 300 \times 109$

Calculations are done by 5 computers with 8 processors and 1 computer with 32 processors. The simulation time is about 11 days with a computer with 8 processors and the memory requirement is 22.01 Gb. The effective stiffness tensor expressed in GPa is given by

$$\mathbf{C}^{(eff)} = \begin{pmatrix} 39.72 & 5.65 & 5.48 & 0 & 0 & 0 \\ 5.65 & 41.96 & 5.61 & 0 & 0 & 0 \\ 5.48 & 5.61 & 37.77 & 0 & 0 & 0 \\ 0 & 0 & 0 & 16.37 & 0 & 0 \\ 0 & 0 & 0 & 0 & 16.80 & 0 \\ 0 & 0 & 0 & 0 & 0 & 17.34 \end{pmatrix} \quad (5.4)$$

Since the proportions of clay and quartz in the sample is equal to 0.056 and 0.722, the average density $\langle \rho \rangle$ is equal to 2058.1 kg/m^3 . The acoustic velocities in this dry coarsened sample along different directions are calculated and presented in Table 5.6.

Sample of size $600 \times 600 \times 218$

The memory requirement for a simulation with $N_{cx} = 600$ reaches 161.8 Gb. It takes over 1 month for one simulation with 32 processors. The effective stiffness tensor expressed in GPa is given by

$$\mathbf{C}^{(eff)} = \begin{pmatrix} 37.0 & 5.33 & 5.13 & 0 & 0 & 0 \\ 5.33 & 39.40 & 5.30 & 0 & 0 & 0 \\ 5.13 & 5.30 & 35.08 & 0 & 0 & 0 \\ 0 & 0 & 0 & 15.55 & 0 & 0 \\ 0 & 0 & 0 & 0 & 15.19 & 0 \\ 0 & 0 & 0 & 0 & 0 & 16.17 \end{pmatrix} \quad (5.5)$$

The proportions of clay and quartz is equal to 0.056 and 0.727, the average density $\langle \rho \rangle$ is equal to 2071.1 kg/m^3 . The acoustic velocities are given in Table 5.6.

5.3.1.3 Extrapolation to the original size

After the calculation of these three coarsened samples, the acoustic velocities of the three compressional and the three shear waves along the x-, y- and z-directions are displayed in Table 5.6 and can be extrapolated to the original sample with $N_{cx} = 1200$ or to a sample with an infinite discretization $N_{cx} = \infty$ in the same way as Fontainebleau samples (cf Section A.1). The two point and three point lines will be used to find the best linear predicted function of these velocities. The best fits (three points lines), together with their correlation coefficient r and the velocities along the three directions are calculated and given in Table 5.7.

Velocities	linear function	r	$N_c = 1200$	$N_c = \infty$
v_p^X	$78.86/N_{cx} + 4.11$	0.9952	4.17	4.11
v_p^Y	$71.12/N_{cx} + 4.26$	0.9948	4.32	4.26
v_p^Z	$78.86/N_{cx} + 4.0$	0.9972	4.07	4.0
v_s^X	$54.86/N_{cx} + 2.66$	0.9942	2.71	2.66
v_s^Y	$53.14/N_{cx} + 2.63$	0.9947	2.67	2.63
v_s^Z	$53.14/N_{cx} + 2.71$	0.9965	2.75	2.71

Table 5.7: The best fits and their correlation coefficients for acoustic velocities in the sample X2.

The lines through the last two points ($N_{cx} = 300$ and 600) are also calculated. The velocities for $N_{cx} = \infty$ derived from the three and two points lines are 4.11 and 4.06 (km/s), respectively. They are in a very good agreement since the difference is equal to 1.2%. These lines are close to each other as can be seen in Fig.5.10.

The accuracy of the extrapolation and of the coarsening method was demonstrated in the calculations of Fontainebleau samples (where the difference between the extrapolation and the direct simulation is about 1.28 %); therefore, it is clear that these methods can be applied to the STATOIL samples with two solids.

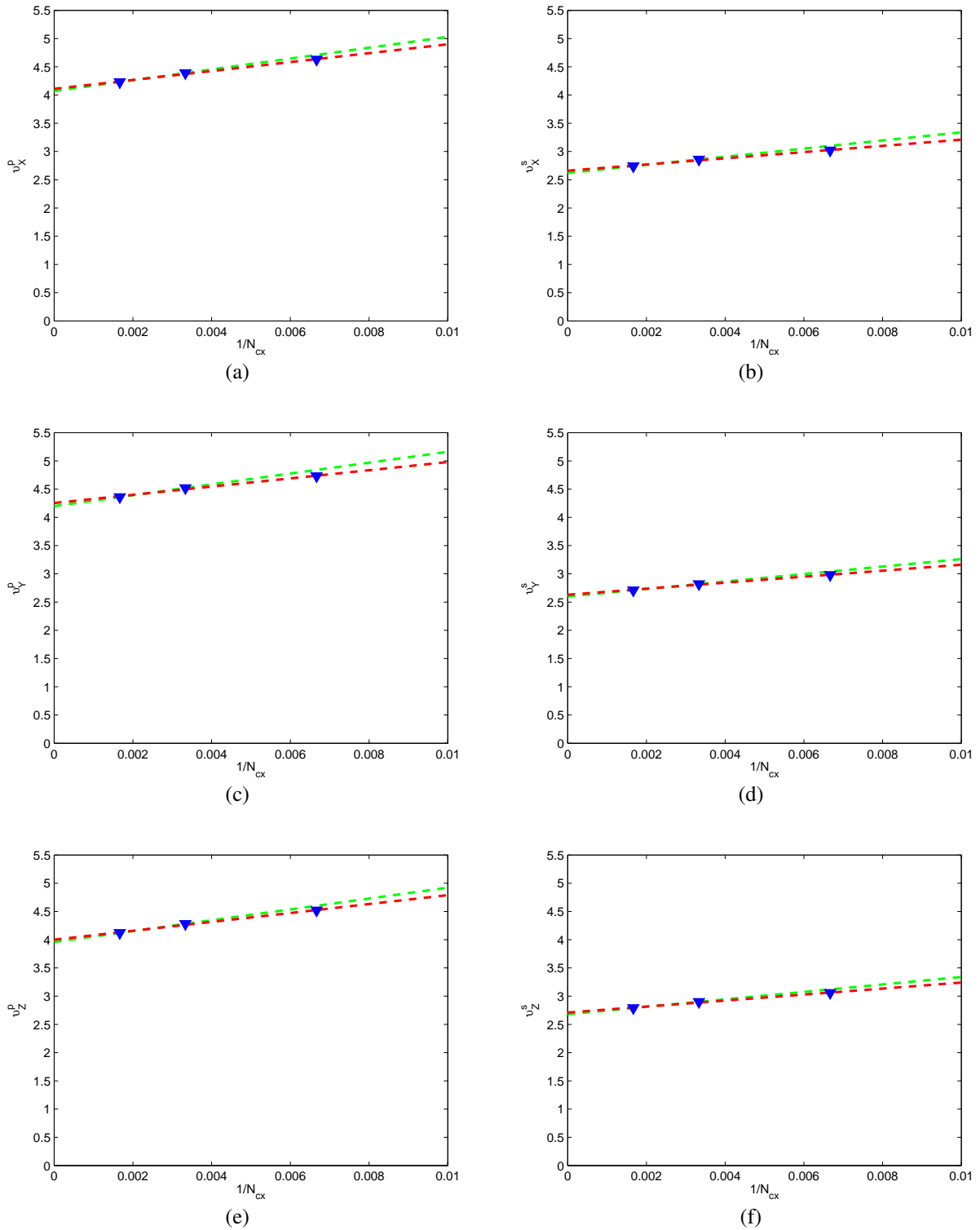


Figure 5.10: The acoustic waves velocities and their extrapolated functions. (a) The compressional wave along the x-direction v_p^x . (b) The shear wave v_s^x . (c) The compressional wave v_p^y . (d) The shear wave v_s^y . (e) The compressional wave v_p^z . (f) The shear wave v_s^z . Data are for: 2 points line (green), 3 points line (red), numerical results (∇).

5.3.1.4 Comparison of LSM2S and LSM, FMD for the STATOIL samples with two solid components

LSM2S was shown to be able to calculate the macroscopic properties of samples with two solid components by comparison with the other methods in Section 3.3. However, the accuracy of simulations by LSM2S to calculate the real STATOIL samples was still an issue. Therefore, three comparisons are performed in order to verify the accuracy of LSM2S.

The first comparison: LSM2S and LSM

The comparison was done for the coarsened sample X2 of size $150 \times 150 \times 54$. Because LSM is only able to calculate the sample with one solid, we have to change the sample for a suitable comparison. The sample which is simulated by LSM2S does not change (three components: 0 - 1 -2), but the elastic properties of phase 0 are equal to the ones of phase 2 (Fig.5.11a).

The sample which is simulated by LSM is derived from the coarsened sample X2 with $N_{cx} = 150$; the clay is changed into quartz (0 is changed into 2) and the sample has only two components, pore and quartz, and it is now suitable for LSM (Fig.5.11.b). Therefore, these two samples are identical

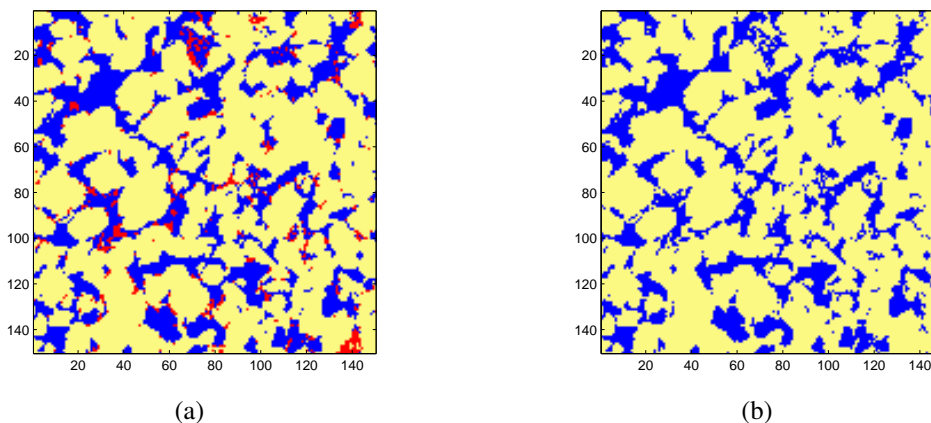


Figure 5.11: Coarsened sample X2 with $N_{cx} = 150$ for simulation by LSM2S (elastic properties of the red phase are equal to the yellow phase) (a). Then, clay (red) is assimilated to quartz (yellow) (b).

The simulations for simple stretching along the x-direction of these two samples were done. The first sample is simulated by LSM2S, the second by LSM. The simulation times are similar and about 1 day; the results are identical as seen in Table 5.8.

The second comparison: LSM2S and FMD of Malinouskaya for the coarsened sample X2 of size 150 x 150 x 54

The samples with two solid components can be calculated with the model FMD. This model was presented by *Malinouskaya* (2007) and *Li* (2010).

The coarsened sample X2 (Fig.5.9.d) with $N_{cx} = 150$ was used for comparison. We performed two simulations: a simple stretching and a simple shear along the y-direction. The results are given in Table 5.8; the errors are always less than 3% which is very good since FMD is a first order scheme.

The third comparison: LSM2S and FMD for the coarsened sample X2 of size 300 x 300 x 109

The second comparison is very good; it is enough to validate the model LSM2S. For an additional comparison, we used a sample with a twice smaller mesh, namely the coarsened samples X2 of size 300 x 300 x 109 (Fig.5.9.c). The same simulations were performed. Their results are given in Table 5.8; the errors are less than 2.1%. Therefore, the Lattice Spring Model for two solids can be used to calculate the real reconstructed STATOIL samples with confidence.

Comparison	Effective property	LSM	LSM2S	FMD	Errors (%)
1	C_{xxxx}	49.19	49.19	-	0
2	C_{yyyy}	-	45.64	46.84	2.5
	C_{zzxz}	-	18.09	18.63	3.0
3	C_{yyyy}	-	41.96	42.83	2.06
	C_{zzxz}	-	16.80	16.75	0.2

Table 5.8: Comparisons of LSM, LSM2S and FMD on the coarsened X2 samples.

5.3.2 Sample X7

As for sample X2, the macroscopic physical properties of X7 were calculated by the coarsening method. The coarsened samples with $N_{cx} = 150$, $N_{cx} = 300$ and $N_{cx} = 600$ were derived from the original sample with $N_{cx} = 1200$.

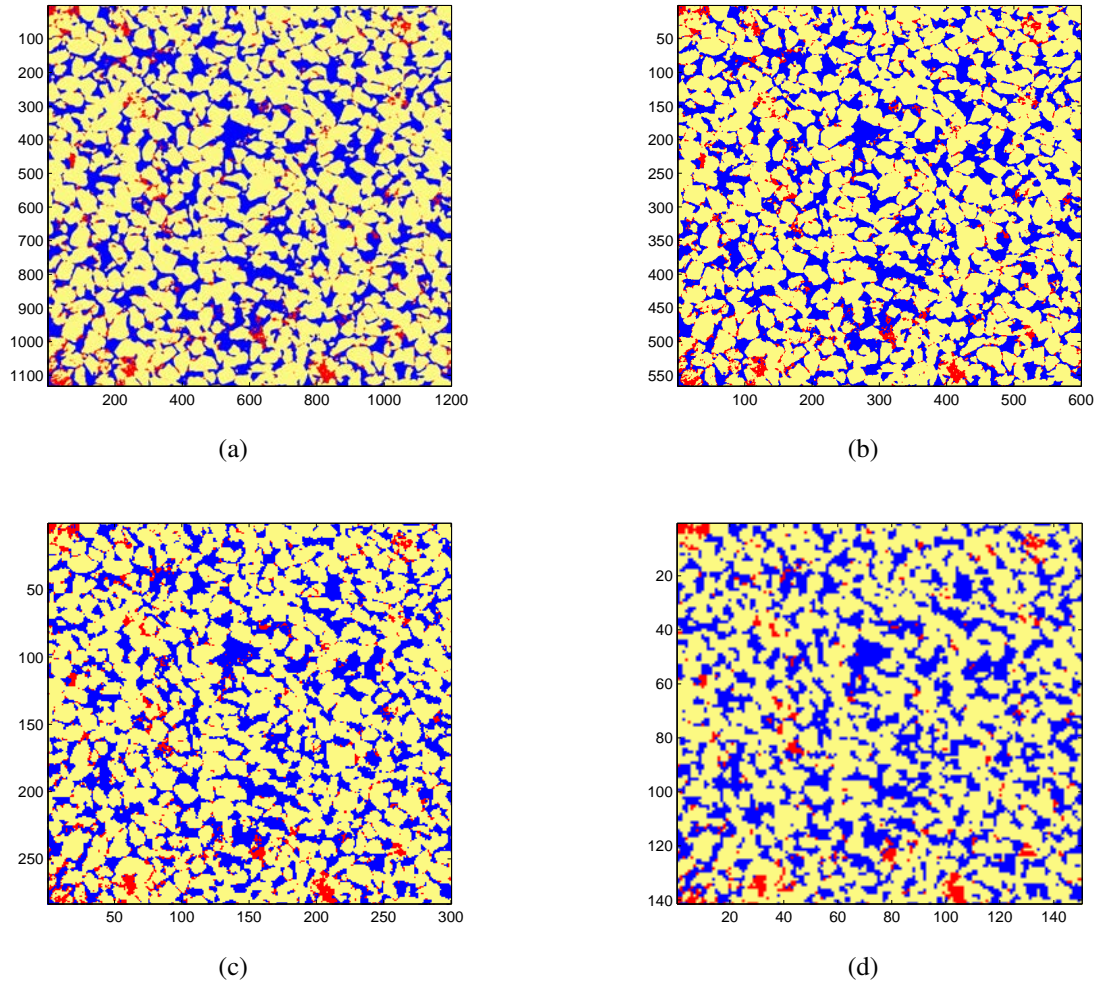


Figure 5.12: The middle slices of the coarsened samples X7. (a) The original sample $N_{cx} = 1200$. (b) The sample $N_{cx} = 600$ (c.) The sample $N_{cx} = 300$. (d) The sample $N_{cx} = 150$.

The change of component proportions of these samples is given in Table 5.5. The calculations were done from the sample with the smallest to the largest N_{cx} . The original and larger sample ($N_{cx} > 1200$) are derived by extrapolations.

5.3.2.1 Simulation results

The effective stiffness tensors are determined by six simulations for each coarsened sample of size $150 \times 141 \times 60$ and $300 \times 283 \times 121$. Then, velocities of compressional and shear waves along the three directions are derived from (2.65) and given in Table 5.9. It should be noted that the difference between the x-, y- and z-directions is always less than 1.4% for v_p and 0.4% for v_s ; therefore, the results are similar along these directions. Thanks to this conclusion, for the coarsened sample with $N_{cx} = 600$, due to the large required memory and the simulation time, the calculation is done only for the x-direction. It means that only one simple stretching and one simple shear simulation are needed. Then, the acoustic velocities of these samples are given in Table 5.9.

Size	x-axis		y-axis		z-axis		Erros	
	v_p^X	v_s^X	v_p^Y	v_s^Y	v_p^Z	v_s^Z	v_p	v_s
	(km/s)	(km/s)	(km/s)	(km/s)	(km/s)	(km/s)	%	%
150 x 141 x 60	4.7	3.09	4.75	3.09	4.77	3.08	1.4	0.3
300 x 283 x 121	4.29	2.80	4.34	2.81	4.28	2.81	1	0.4
600 x 566 x 242	4.07	2.64	4.07	2.6	4.07	2.64	-	-

Table 5.9: The velocities of compressional and shear waves along the three directions in the coarsened samples X7.

5.3.2.2 Extrapolation to the original sample

With the same method as for X2, the acoustic velocity can be presented as a function of $1/N_{cx}$. The three point linear functions of $1/N_{cx}$ are calculated. As mentioned above, the extrapolation is done only for the x-direction, the results with the corresponding correlation coefficient r and the velocities for $N_{cx} = 1200$ and ∞ are derived and presented in Table 5.10. Note that the correlation coefficients are nearly equal to 1; therefore, these functions are trusted to be accurate.

Velocities	linear function	r	$N_c = 1200$	$N_c = \infty$
v_p^X	$125.57/N_{cx} + 3.865$	0.9988	3.9696	3.865
v_s^X	$90.12/N_{cx} + 2.4981$	0.9996	2.567	2.492

Table 5.10: The best fits with the corresponding correlation coefficients and the acoustic velocities along the x-direction of the sample X7.

5.3.3 Sample Y5 and Y13

The sample Y5 has the same form as the samples X2 and X7; its dimensions are $N_{cx} \times N_{cy} \times N_{cz} = 1200 \times 1200 \times 371$. The coarsened samples of sizes $N_{cx} \times N_{cy} \times N_{cz} = 150 \times 150 \times 46$, $300 \times 300 \times 92$ and $600 \times 600 \times 185$ were derived from the original sample.

The sample Y13 has a different size: $N_{cx} \times N_{cy} \times N_{cz} = 1000 \times 1000 \times 554$. The coarsened samples are of sizes $N_{cx} \times N_{cy} \times N_{cz} = 125 \times 125 \times 69$, $250 \times 250 \times 138$ and $500 \times 500 \times 277$.

In the same way, the velocities in these coarsened samples are calculated as in Table 5.11. Note that for the coarsened samples with larger sizes ($N_{cx} = 500$ and 600), only the calculations along the x-direction are performed.

Velocities km/s	Sample Y5			Sample Y13		
	$N_{cx} = 150$	$N_{cx} = 300$	$N_{cx} = 600$	$N_{cx} = 125$	$N_{cx} = 250$	$N_{cx} = 500$
v_p^X	5.08	4.90	4.82	5.45	5.33	5.27
v_p^Y	5.03	4.85	-	5.37	5.26	-
v_p^Z	5.07	4.88	-	5.40	5.28	-
v_s^X	3.32	3.19	3.13	3.57	3.49	3.45
v_s^Y	3.34	3.20	-	3.60	3.51	-
v_s^Z	3.33	3.20	-	3.58	3.50	-

Table 5.11: Acoustic velocities of compressional and shear waves along the three directions in coarsened samples Y5 and Y13.

Then, the extrapolations are made in order to determine the wave velocities along the x-direction in the original sample and the sample with $N_{cx} = \infty$. The results are given in Table 5.12.

Velocities (km/s)	Sample Y5		Sample Y13	
	$N_c = 1200$	$N_c = \infty$	$N_c = 1000$	$N_c = \infty$
v_p^X	4.77	4.73	5.24	5.21
v_s^X	3.09	3.06	3.43	3.41

Table 5.12: Acoustic velocities extrapolated to the original samples Y5 and Y13 and to an ∞ discretization.

Finally, the velocities are determined for all the coarsened STATOIL samples. Unlike the Fontainebleau samples, these samples have different forms and dimensions; therefore, it is difficult to compare them. The velocities are decreasing functions of porosity for the original samples. However, when N_{cx} is small, the velocity can increase with porosity (see Fig.5.13.a). A comparison with the velocities in a no-pore medium v_0 is given in Fig.5.13.b; the ratio v/v_0 is also a decreasing function of porosity and the difference $v_p/v_0^p - v_s/v_0^s$ is always nearly equal to 0.03.

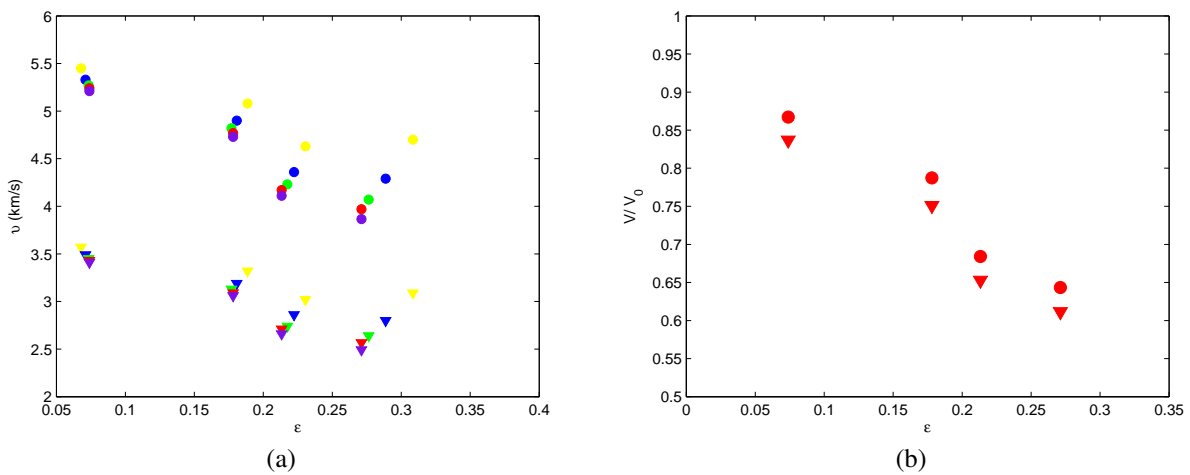


Figure 5.13: (a). The comparison of velocities between STATOIL samples. (b) The ratio V/V_0 for the original samples. Data are for: $N_{cx} = 150$ or 125 (yellow), $N_{cx} = 300$ or 250 (blue), $N_{cx} = 600$ or 500 (green), $N_{cx} = 1200$ or 1000 (red), $N_{cx} = \infty$ (violet), compressional wave (\circ) and shear wave (∇).

Han (1986) also measured the wave velocities in various composite sandstones with porosity ranging from 2% to 30% and clay content ranging from 0 to 50%. Their component proportions are

close to our samples as shown in the clay content-porosity relation (see Fig. 5.14.c). Furthermore, some linear functions to predict the velocities in the considered sandstones (*Han et al.*, 1986) are also provided

$$V_p = 5.41 - 6.35\varepsilon - 2.87C \quad \text{km/s} \quad (5.6a)$$

$$V_s = 3.57 - 4.57\varepsilon - 1.83C \quad \text{km/s} \quad (5.6b)$$

where C is the clay proportion.

The numerical results of the compressional and the shear velocities are slightly larger than the experimental data as can be seen in Fig. 5.14.a-b. The differences are from 6% to 12% for V_p and from 7% to 13% for V_s in comparisons with the predictions (5.6). They are due to the small size and mostly to the small fissures which are likely to exist in the real samples. A more precise comparison is shown in Fig. 5.14.d, the ratio V_p/V_s of simulations is close to the predictions since the difference is less than 3%.

Since the effective stiffness tensors were calculated for all coarsened samples, the ones for the original samples are determined by extrapolations. Then, the effective bulk modulus and shear modulus can be derived from (3.34). The upper Hashin-Shtrickman's bounds (*Wall*, 1997; *Hashin and Shtrickman*, 1962b) for a composite medium with two materials are given by

$$K_u = K_1 + \frac{m_2}{\frac{1}{K_2 - K_1} + \frac{m_1}{K_1 + G_1}}, \quad G_u = G_1 + \frac{m_2}{\frac{1}{G_2 - G_1} + \frac{m_1(K_2 + 2G_1)}{2G_1(K_1 + G_1)}} \quad (5.7)$$

where K_1 , K_2 are the bulk moduli, G_1 , G_2 the shear moduli, m_1 , m_2 the volume fraction of the first and the second materials, respectively, with the condition: $(K_1 \times K_2)(G_1 \times G_2) \geq 0$. For comparisons, the clay in our samples is considered as quartz; then, the first material is quartz and the second is pore ($K_2 = G_2 = 0$, $m_2 = \varepsilon$). The numerical results are under the upper bounds; the effective shear modulus is closer to the HS bound than the bulk modulus as shown in Fig. 5.15.a-b. They are also compared to the empirical equations (4.6) (*Nur et al.*, 1991, 1995) and (4.7) (*Krief*, 1990) in Fig 5.15.c-d. K_e is in a good agreement with the empirical results. The difference for G_e is significant; but it should be noted that these equations are for media with only one solid component.

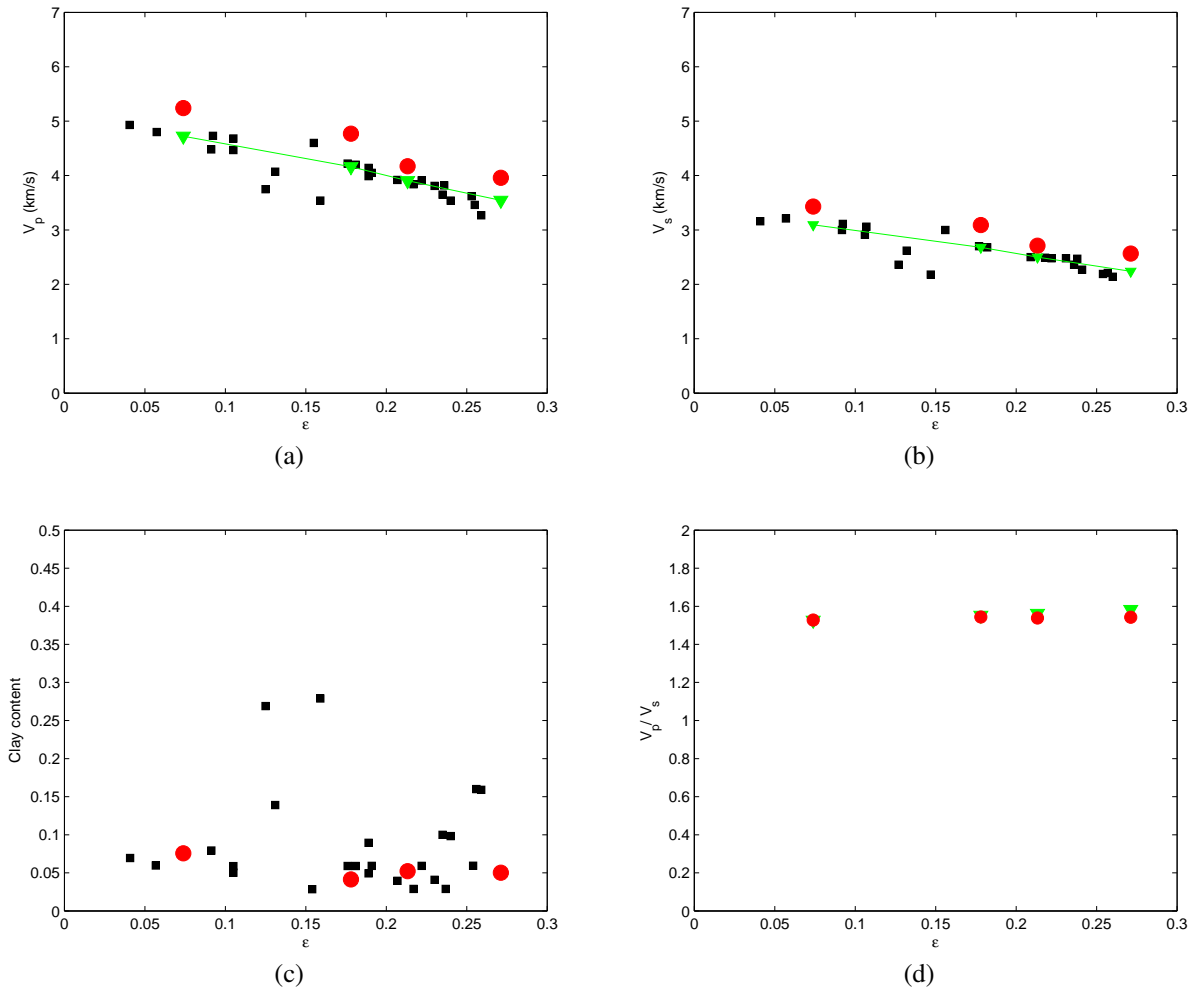


Figure 5.14: Comparisons between numerical results, Han's data and Han's predictions. (a) Compressional wave velocity. (b) Shear wave velocity. (c) The clay content-porosity function. (d) Comparison of ratio V_p/V_s with Han's predictions. Data are for: numerical results (red \circ), Han's data (black \square), Han's prediction (5.6) (green ∇).

5.4 Additional comparisons

The calculations of dry STATOIL samples are done by the coarsening methods; this authorize us to obtain the acoustic velocities in the samples with an infinite discretization ($N_{cx} = \infty$). The results are given in Tables 5.7, 5.10 and 5.12. It is clear that these samples are closer to the real samples than the original samples with $N_{cx} = 1200$. Therefore, a further comparison between these results and the data given in Section 5.3 is presented in Fig. 5.16; the difference is quite smaller than the one in Fig. 5.14.

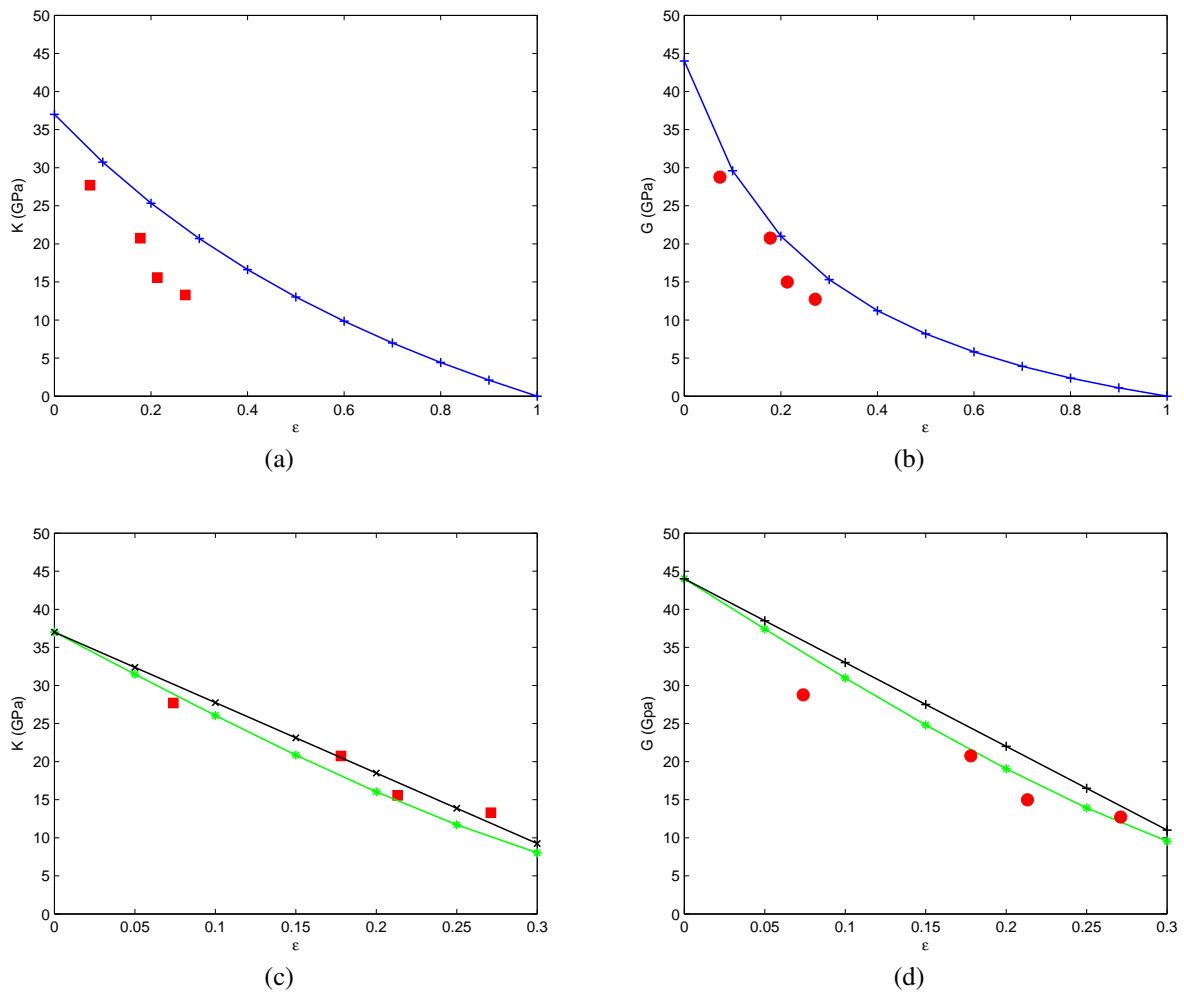


Figure 5.15: Comparisons of the effective moduli with the Hashin-Shtrickman's bounds and the empirical equations. (a) K_e with the HS bounds. (b) G_e with the HS bounds. (c) K_e with the empirical equations (4.6), (4.7). (d) G_e with the empirical equations (4.6), (4.7). Data are for: numerical results (red), HS bounds (blue), Nur (black), Krief (green).

The samples X2, X7, Y5 and Y13 are provided by STATOIL and they also made some measurements for real samples whose components are clay, quartz and pore. There are two classes of samples that called the X-samples and the Y-samples. Obviously, X2 and X7 belong to the first class and Y5, Y13 to the second class. A comparison with the experimental data is given in Fig. 5.17. It can be observed that the results of Y5 and Y13 are close to the Y-samples but the ones of X2 and X7 are larger than the X-samples. This difference can be due to the small samples size, to the appearance of small fissures in samples, to the difference of solids proportions and to the difference of clay properties...

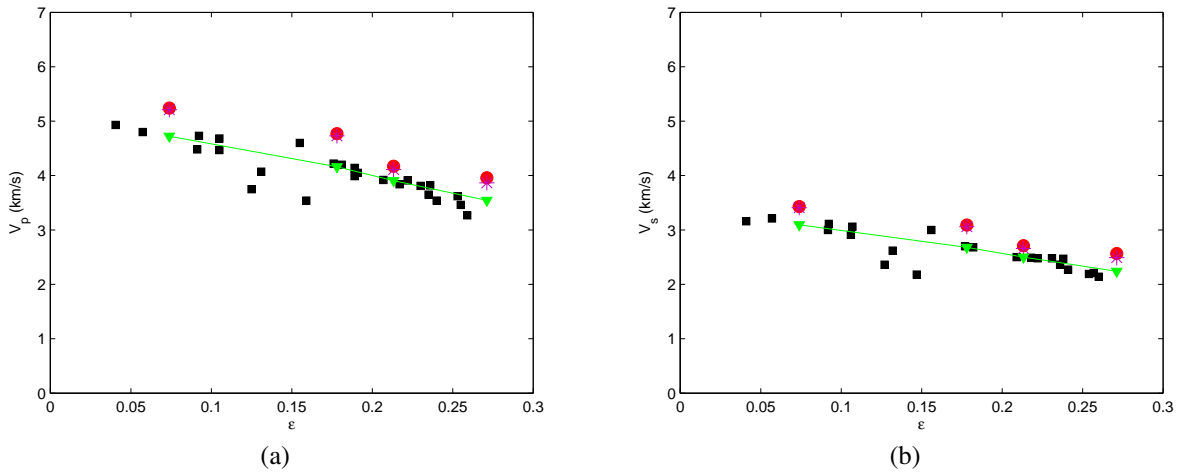


Figure 5.16: Comparisons between the results of the coarsened samples $N_c = \infty$ and the original samples and experimental data of (Han, 1986; Han et al., 1986). (a) Compressional wave. (b) Shear wave. Data are for: $N_c = \infty$ (violet *), original samples (red o), Han’s experimental data (black □), Han’s predictions (green ▽).

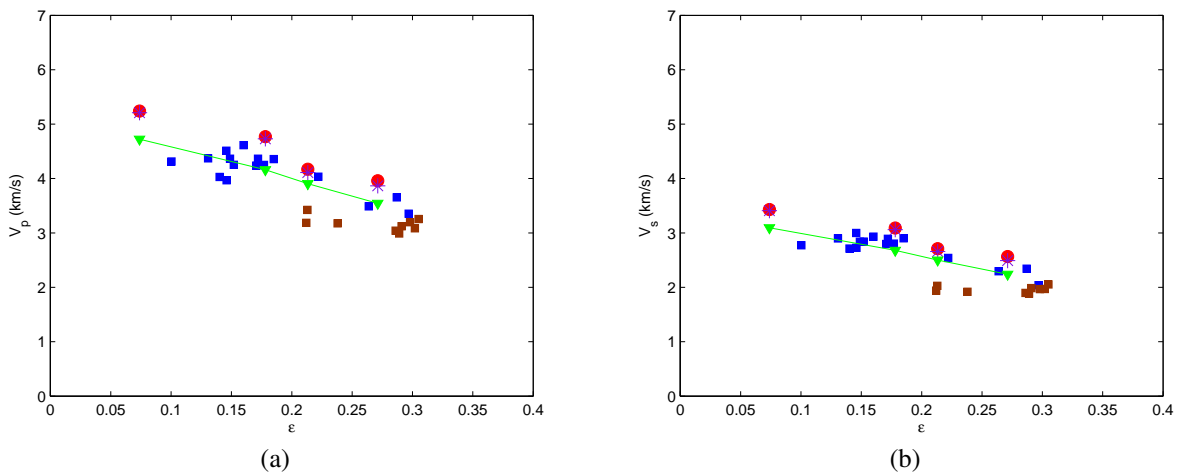


Figure 5.17: Comparisons between the results of the coarsened samples $N_c = \infty$ and the original samples, the predictions of Han (1986) and the experimental data of STATOIL. (a) Compressional wave. (b) Shear wave. Data are for: $N_c = \infty$ (violet *), original samples (red o), Y-samples (blue □), X-samples (brown □), Han’s predictions (green ▽).

As for the Fontainebleau samples, the mirror configurations along the three directions of the samples were also used to check the spatially periodic conditions. The obtained results are about the same as the original one. Another attempt is to check the influence of clay on the velocities. In this case, the clay is considered as pores. The verifications are done for the coarsened samples

X2 with $N_{cx} = 150$ and in two different ways. In the first way, the clay is changed into pore and the simulation is done by LSM. In the second way, the properties of clay are assigned to be equal to the ones of air and the simulations is performed by LSM2S. Both ways yield the same results: $C_{xxxx} = 38.653$ GPa and $C_{yzyz} = 16.4635$ GPa. They are smaller in comparison with the obtained results in Section 5.3: $C_{xxxx} = 43.58$ GPa and $C_{yzyz} = 18.52$ GPa. However, it is important to note that when the clay is changed into pore, the averaged density $\langle \rho \rangle$ is also decreased; therefore, this has an influence the velocities. The new compressional and shear wave velocities are 4.51 (km/s) and 2.94 (km/s), respectively. They are about 2.7% smaller than the original results which are equal to 4.63 (km/s) and 3.02 (km/s), respectively. This comparison shows that the clay proportion does not have a heavy influence on the acoustic velocities of dry samples when the quartz proportion is unchanged.

5.5 The formation factor F and the characteristic length Λ

As for the Fontainebleau samples, the macroscopic conductivity tensor, the formation factor F and the characteristic length Λ are needed in order to study flows in STATOIL samples. The same program of *Thovert et al.* (1990) is used for calculations. The numerical results of dimensionless length Λ/a and conductivity component $\frac{\Sigma}{\Sigma_0}$ along the x-direction are determined. Then, they are compared with the approximate results calculated by (4.10) in Table 5.13.

The formation factor F of the coarsened STATOIL samples is derived from the conductivity tensor. They are close to the prediction of the "first Archie equation" when $m = 2$ as can be seen in Fig. 5.18.

5.6 Acoustic velocities in saturated STATOIL samples

The problem of wave propagations in saturated composite media is difficult. The method usually used is homogenization (*Juan, 2006; Malinouskaya, 2007; Li, 2010*). As described in Chapter 2, the generalized Christoffel equation (2.99) is obtained and the acoustic velocities can be derived after determining the four quantities C^{eff} , K , α and β .

The effective stiffness tensors C^{eff} are determined in Section 5.3. In this Section, the other

Sample	N_{cx}	$\frac{\bar{\Sigma}}{\Sigma_0}$	$\frac{\Lambda}{a}$	$\frac{2\Omega_p}{S.a}$
X2	150	0.0453	1.759	1.3326
	300	0.0509	2.6628	1.9982
	600	0.0559	4.2452	3.2211
X7	150	0.0606	1.2323	0.9825
	300	0.0772	1.9803	1.5182
	600	0.0846	3.5931	2.6117
Y5	150	0.0131	1.3829	1.2379
	300	0.0172	2.1883	1.8786
	600	0.0191	3.7007	2.9930
Y13	125	0	0	0.906
	250	0	0	-
	500	0.0002	2.2959	2.3278

Table 5.13: The dimensionless conductivity components $\frac{\bar{\Sigma}}{\Sigma_0}$ and the characteristic length Λ/a of the STATOIL samples.

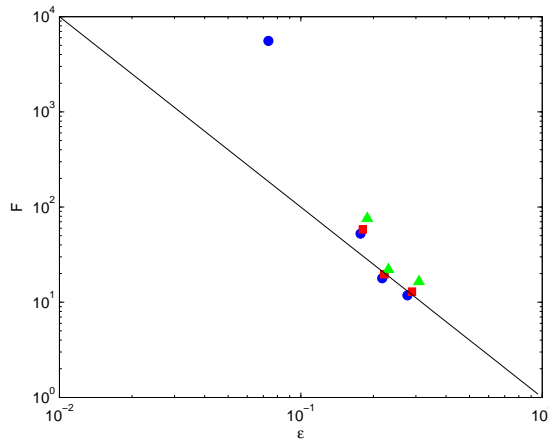


Figure 5.18: Comparison of numerical results of the formation factor F with the first Archie equation (4.11). Data are for: $N_{cx}=600$ (blue \circ), 300 (red \square), 150 (green \triangle), equation (4.11) (black line).

calculations are presented. The dynamic permeability is calculated by LBM; the fluid reaction α , β by LBM-LSM2S.

5.6.1 Permeabilities

5.6.1.1 Absolute permeability

In permeability calculations, the difference between the solid components does not matter. The quartz and clay components are considered as the same solid component. Therefore, the absolute permeability of the STATOIL samples is calculated by the same LBM program (*Pazdriakou, 2012*).

The calculations of absolute permeability are performed by the coarsening method; the coarsened samples are the same as in Section 5.3. As for Fontainebleau samples, only one simulation is needed for each sample. The time and memory requirement depend on the sample size. For example with a computer with 8 processors, the time is less than 10 hours and the memory is 0.6 Gb for the coarsened sample X2 of size $150 \times 150 \times 54$ and more than a week and 36.7 Gb for $N_{cx} = 600$. Normally, if N_{cx} increases by a factor of 2, the memory and time is about 8 times larger. The calculations are done for the original and mirror configurations. Then, the absolute permeability can be derived by (4.13) and is given in Table 5.14. Some points can be observed: the results of the mirror configurations are larger than the original ones, the permeability of the sample X2 is larger than the others.

Sample	N_{cx}	Original			Mirror
		K	a	K_0	K_0
		(dimensionless)	(μm)	(real value) (mD)	(real value) (mD)
X2	150	0.00942	45.6	195.88	245.99
	300	0.02761	22.8	143.5	182.98
	600	0.09270	11.4	120.475	-
X7	150	0.00583	45.6	121.23	133.08
	300	0.01971	22.8	102.46	111.35
Y5	150	0.00132	45.6	27.45	39.92
	300	0.0042	22.8	21.83	33.37

Table 5.14: The absolute permeability of the coarsened STATOIL samples.

5.6.1.2 Dynamic permeability

As for the Fontainebleau samples, we used the same program based on LBM (Pazdniakou, 2012) in order to calculate the dynamic permeability. Therefore, the input parameters are the same. These calculations are for the original and mirror configurations with various values of frequency ω , but only along the x-direction.

For the original configuration of the coarsened sample X2 of size $150 \times 150 \times 54$, the required memory is about 0.8 Gb for each simulation with 8 processors; the simulation time varies from some hours to 3 days. The results are given in Table 5.15 and the forms of the real part and imaginary parts are presented in Fig.5.19.a.

The simulations of the coarsened sample X2 of size $300 \times 300 \times 109$ ($a_{300} = 22.8\mu m$) are done with a memory requirement of 6.8 Gb, the simulation time can vary from one day to more than two weeks with a computer with 8 processors. The ones for the coarsened sample of size $600 \times 600 \times 218$ ($a_{600} = 45.6\mu m$) are about 8 times larger. Then, two dimensionless values $\frac{K}{K_0}$ and $\omega' = \frac{\omega K_0}{\nu}$ which can be determined from the absolute permeability K_0 (Pazdniakou, 2012) are used for comparisons as it can be seen in Fig.5.19.a.

A comparison between the dimensionless dynamic permeability $K'(\omega'_c)$ (Pazdniakou and Adler, 2013) of the coarsened samples with $N_{cx} = 150$ and 300 and the plane Poiseuille flow is shown in Fig. 5.19.b. It can be seen that they are in good agreement since the simulation points are close to the curve corresponding to the analytical solution of the Poiseuille flow. However, a significant difference is observed for the real part K_r' when $\omega'_c > 1$; this may due to the reduction of the viscosity to satisfy the conditions on Knudsen number.

Then, the calculations for the mirror configuration are also performed; the sample sizes are now $300 \times 150 \times 54$ and $600 \times 300 \times 109$. The simulation time and memory are about two times larger than the original one. The results are a little larger than the original; the difference is about 20% for the real part K_r/a^2 with $\omega = 2.5e - 5$ and $N_{cx} = 150$; this is reasonable as explained in Chapter 2. The real values (in mD) of dynamic permeability (K_r and K_i) are calculated according to (4.13); a comparison between the coarsened samples X2 and between the configurations are presented in Fig.5.19.c.

Frequency	Original				Mirror			
	$N_{cx} = 150$		$N_{cx} = 300$		$N_{cx} = 300$		$N_{cx} = 600$	
	x-axis		x-axis		x-axis		x-axis	
ω	K_r/a^2	K_i/a^2	K_r/a^2	K_i/a^2	K_r/a^2	K_i/a^2	K_r/a^2	K_i/a^2
0.05	0.00006	-5.6311e-04	0.00011	-8.0617e-04	0.00007	-6.6791e-04	0.00006	-8.0988e-04
0.025	0.00021	-1.1209e-03	0.00018	-1.4243e-03	0.00023	-1.2973e-03	0.00020	-1.6503e-03
0.01	0.00123	-2.2278e-03	0.00146	-3.1610e-03	0.00126	-2.6201e-03	0.00135	-3.3832e-03
0.005	0.00259	-3.3126e-03	0.00301	-5.3552e-03	0.00286	-4.0927e-03	0.00293	-6.2015e-03
0.0025	0.00481	-3.9628e-03	0.00574	-7.9191e-03	0.00556	-4.9525e-03	0.00634	-9.7685e-03
0.001	0.00775	-3.1241e-03	0.01266	-1.0870e-02	0.00933	-4.1630e-03	0.01461	-1.3538e-02
0.0005	0.00888	-1.9116e-03	0.01922	-1.0463e-02	0.01098	-2.6576e-03	0.02281	-1.3679e-02
0.00025	0.00927	-1.0204e-03	0.02425	-7.5980e-03	0.01159	-1.4459e-03	0.02980	-1.0575e-02
0.0001	0.00940	-4.1645e-04	0.02697	-3.6229e-03	0.01179	-5.9403e-04	0.03409	-5.3056e-03
5e-05	0.00941	-2.0884e-04	0.02748	-1.8699e-03	0.01182	-2.9819e-04	0.03496	-2.7714e-03
2.5e-05	0.00942	-1.0450e-04	0.02761	-9.4276e-04	0.01183	-1.4924e-04	0.03520	-1.4020e-03

Table 5.15: The dimensionless dynamic permeability K/a^2 along the x-direction of the coarsened samples X2 of size 150 x 150 x 54 ($a_{150} = 45.6\mu m$) and of size 300 x 300 x 109 ($a_{300} = 22.8\mu m$).

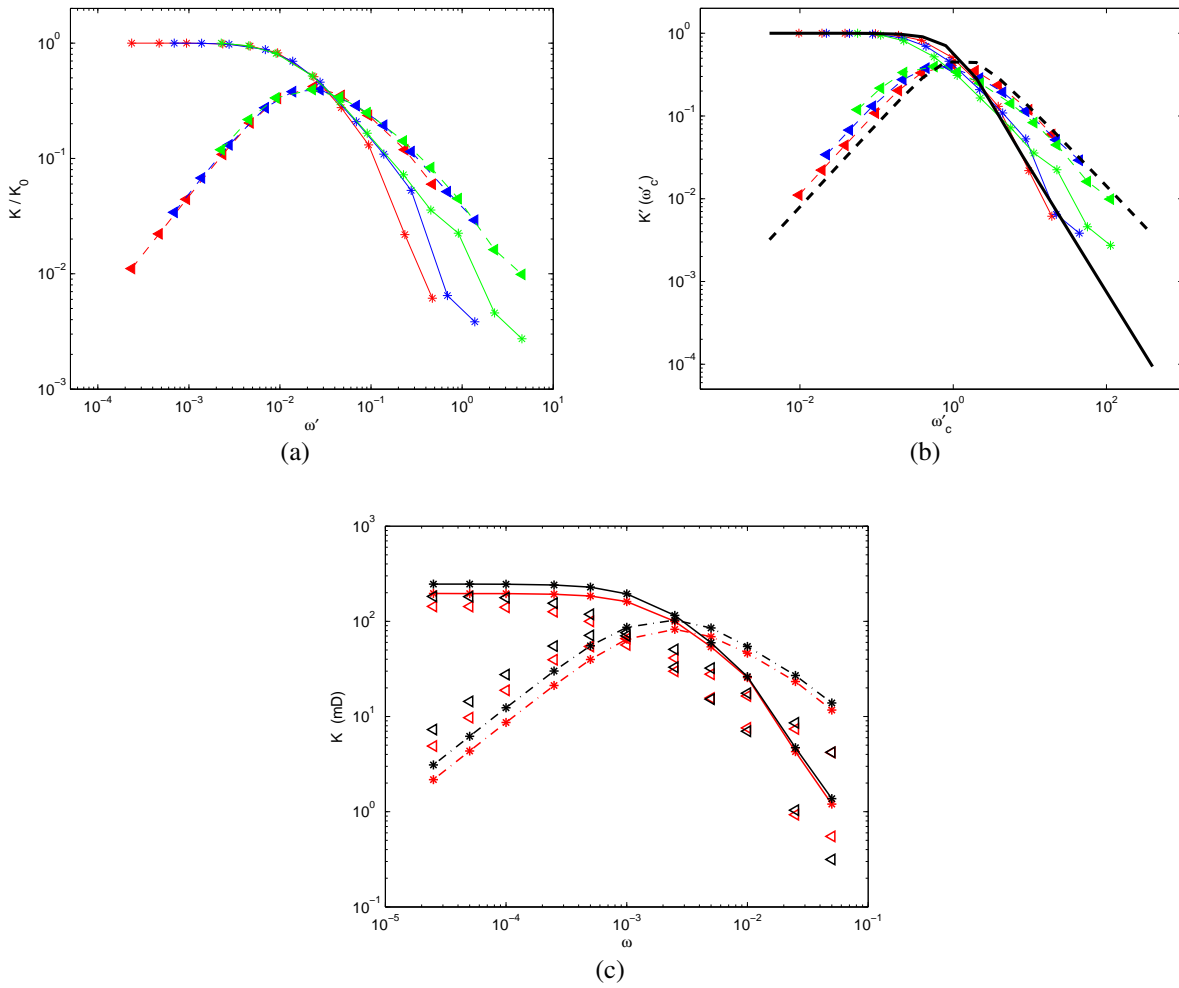


Figure 5.19: (a) The dimensionless dynamic permeability of the original configurations X2 with $N_{cx}= 150$, $N_{cx}= 300$ and $N_{cx}= 600$. (b) Comparison of $K'(\omega'_c)$ with the Poiseuille flow. Data are for: $N_{cx} = 150$ (red), $N_{cx} = 300$ (blue), $N_{cx} = 600$ (green), Poiseuille flow (black), real part (—), imaginary part (- - -). (c) Comparison of the real dynamic permeability between the mirror configurations and the original ones of the coarsened samples X2. Data for $N_{cx} = 150$ (*), $N_{cx} = 300$ (\triangleright), original (red), mirror (black), real part (—), imaginary part (- - -).

Frequency	Original				Mirror			
	$N_{cx} = 150$		$N_{cx} = 300$		$N_{cx} = 300$		$N_{cx} = 600$	
	x-axis		x-axis		x-axis		x-axis	
ω	K_r/a^2	K_i/a^2	K_r/a^2	K_i/a^2	K_r/a^2	K_i/a^2	K_r/a^2	K_i/a^2
0.05	0.00009	-6.4404e-04	0.00016	-1.0266e-03	0.00009	-6.9286e-04	0.00009	-1.1006e-03
0.025	0.00032	-1.2319e-03	0.00033	-2.0527e-03	0.00034	-1.3183e-03	0.00034	-2.1620e-03
0.01	0.00151	-2.2458e-03	0.00180	-4.3479e-03	0.00156	-2.4182e-03	0.00180	-4.5661e-03
0.005	0.00312	-2.6305e-03	0.00449	-6.8544e-03	0.00330	-2.9162e-03	0.00455	-7.2736e-03
0.0025	0.00464	-2.1543e-03	0.00898	-8.4244e-03	0.00501	-2.4251e-03	0.00939	-9.1501e-03
0.001	0.00558	-1.0937e-03	0.01549	-7.0875e-03	0.00610	-1.2466e-03	0.01655	-7.8805e-03
0.0005	0.00576	-5.7147e-04	0.01828	-4.5015e-03	0.00632	-6.5343e-04	0.01974	-5.0804e-03
0.00025	0.00581	-2.8909e-04	0.01931	-2.4453e-03	0.00638	-3.3085e-04	0.02095	-2.7784e-03
0.0001	0.00583	-1.1602e-04	0.01964	-1.0043e-03	0.00640	-1.3281e-04	0.02135	-1.1438e-03
5e-05	0.00583	-5.8037e-05	0.01969	-5.0412e-04	0.00640	-6.6441e-05	0.02141	-5.7437e-04
2.5e-05	0.00583	-2.9022e-05	0.01971	-2.5231e-04	0.00640	-3.3225e-05	0.02142	-2.8749e-04

Table 5.16: The dimensionless dynamic permeability K/a^2 for the original and mirror configurations along the x-direction of the coarsened samples X7 with $N_c = 150$ ($a_{150} = 45.6 \mu m$) and $N_c = 300$ ($a_{300} = 22.8 \mu m$).

Frequency	Original				Mirror			
	$N_{cx} = 150$		$N_{cx} = 300$		$N_{cx} = 300$		$N_{cx} = 600$	
	x-axis		x-axis		x-axis		x-axis	
ω	K_r/a^2	K_i/a^2	K_r/a^2	K_i/a^2	K_r/a^2	K_i/a^2	K_r/a^2	K_i/a^2
0.05	0.00005	-1.0747e-04	0.00011	-2.2562e-04	0.00007	-1.4152e-04	0.00006	-2.3125e-04
0.025	0.00007	-2.1441e-04	0.00031	-4.0436e-04	0.00009	-3.1353e-04	0.00010	-5.0309e-04
0.01	0.00071	-3.4872e-04	0.00126	-6.6351e-04	0.00065	-3.8577e-04	0.00040	-1.2095e-03
0.005	0.00094	-3.2215e-04	0.00172	-1.2228e-03	0.00107	-6.8693e-04	0.00157	-1.4590e-03
0.0025	0.00110	-2.8699e-04	0.00248	-1.2941e-03	0.00151	-6.0692e-04	0.00268	-2.1978e-03
0.001	0.00126	-1.7568e-04	0.00332	-1.1043e-03	0.00182	-3.3415e-04	0.00461	-2.2834e-03
0.0005	0.00130	-9.7294e-05	0.00385	-8.1174e-04	0.00189	-1.7922e-04	0.00570	-1.6351e-03
0.00025	0.00131	-5.0145e-05	0.00410	-4.7138e-04	0.00191	-9.1554e-05	0.00620	-9.4911e-04
0.0001	0.00132	-2.0243e-05	0.00419	-1.9877e-04	0.00192	-3.6865e-05	0.00639	-4.0083e-04
5e-05	0.00132	-1.0135e-05	0.00420	-1.0022e-04	0.00192	-1.8451e-05	0.00642	-2.0216e-04
2.5e-05	0.00132	-5.0692e-06	0.00420	-5.0220e-05	0.00192	-9.2275e-06	0.00642	-1.0131e-04

Table 5.17: The dimensionless dynamic permeability K/a^2 for the original and mirror configurations along the x-direction of the coarsened samples Y5 with $N_c = 150$ ($a_{150} = 45.6 \mu m$) and $N_c = 300$ ($a_{300} = 22.8 \mu m$).

The dynamic permeability of original and mirror configurations are similarly determined for the samples X7 and Y5. The results of coarsened samples X7 of size $150 \times 141 \times 60$ and $300 \times 283 \times 121$ are given in Table 5.16. Then, the real values are calculated and compared in Fig.5.20.a. The imaginary and real parts of K/a^2 of the coarsened samples Y5 of size $150 \times 150 \times 46$ and $300 \times 300 \times 92$ are presented in Table 5.17, and the results are compared in Fig.5.20.b. Some noisy results are obtained for high frequencies although the viscosity was decreased in order to improve the Knudsen number (*Pazdniakou, 2012*). Problems occur for samples with a small porosity such as sample Y13; some solutions are being studied to solve it.

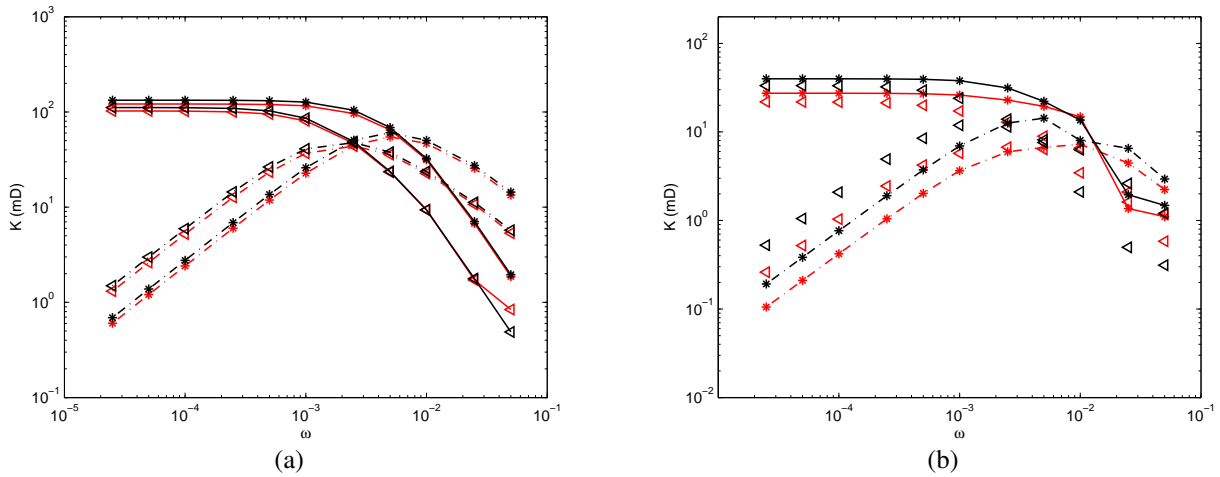


Figure 5.20: (a) Comparison of real dynamic permeability between the mirror configurations and the original ones of the coarsened samples X7. Data for $N_c = 150$ (*), $N_c = 300$ (\triangleright), original (red) and mirror (black), real part (—), imaginary part (- - -). (b) The results for sample Y5.

5.6.2 Coefficients α , β and acoustic velocities in saturated samples

The coefficients characterize the fluid action; α and β are derived by LBM-LSM2S as presented in Chapter 3. The physical properties of clay, quartz and fluid are described in (4.17) and in Table 5.4. As for Fontainebleau samples, very small pores which are disconnected are eliminated; α and β are calculated by imposing a unit pressure in the pore as in Section 4.4.

The calculations are done by the coarsening methods with the same coarsened samples. A sample needs only one simulation to obtain these coefficients. For dry samples, the coarsened

samples X2 are calculated first. The simulation for $N_{cx} = 150$ takes about 4 days; the memory requirements is 2.92 Gb. The results are

$$\alpha = \begin{pmatrix} -0.4831 & 6.964e-3 & 4.776e-3 \\ 6.964e-3 & -0.4644 & 7.015e-5 \\ 4.776e-3 & 7.015e-5 & -0.5002 \end{pmatrix} \quad (5.8a)$$

$$\beta = -0.00135 \quad GPa^{-1} \quad (5.8b)$$

The four needed quantities C^{eff} , K , α and β are fully determined; therefore, the acoustic velocities can be derived from the generalized Christoffel equation (2.99). Similarly to sample FB22, the calculations are done for various frequencies ω and three solutions are obtained for three types of waves. Furthermore, the STATOIL samples are saturated by three types of fluids: incompressible, slightly compressible and highly compressible with the same properties as for Fontainebleau samples. The results of $v_{||}^{fast}$, $v_{||}^{slow}$ and v_{\perp} calculated for original and mirror configurations are presented in Tables 5.18, 5.19 and 5.20, respectively.

It is worth noting that the relations between compressibility coefficients of fluids, type of configurations, frequency... in this coarsened sample are the same as in the Fontainebleau samples (Section 4.4). The velocities and the penetration depth h of wave propagation are derived by (4.15) and (4.16) and then compared in Figures 5.21 and 5.22. It is seen that the ratio $v_{||}^{fast}/v_{dry}$ in this sample is larger than the one of Fontainebleau samples; it is about 2.1 in this case but only equal to 1.2 in the coarsened sample FB22 with $N_c = 120$. The other ratios such as $v_{||}^{slow}/v_{dry}$ or v_{\perp}/v_{dry} are not very different from the Fontainebleau ones.

ω	Original $N_{cx} = 150$						Mirror $N_{cx} = 300$					
	$C_f = 0$		$C_f = 4.6$		$C_f = 100$		$C_f = 0$		$C_f = 4.6$		$C_f = 100$	
	C_r	C_i	C_r	C_i	C_r	C_i	C_r	C_i	C_r	C_i	C_r	C_i
0.05	9.77	2.4e-10	4.492	8.9e-12	4.389	1.4e-11	9.77	2.8e-10	4.492	1.0e-11	4.389	1.6e-11
0.025	9.77	4.3e-10	4.492	1.6e-11	4.389	2.5e-11	9.77	4.8e-10	4.492	1.8e-11	4.389	2.8e-11
0.01	9.77	1.0e-09	4.492	3.8e-11	4.389	6.0e-11	9.77	1.1e-09	4.492	3.9e-11	4.389	6.2e-11
0.005	9.77	1.1e-09	4.492	4.0e-11	4.389	6.4e-11	9.77	1.2e-09	4.492	4.4e-11	4.389	7.0e-11
0.0025	9.77	1.0e-09	4.492	3.7e-11	4.389	5.9e-11	9.77	1.2e-09	4.492	4.3e-11	4.389	6.8e-11
0.001	9.77	6.5e-10	4.492	2.4e-11	4.389	3.8e-11	9.77	7.8e-10	4.492	2.9e-11	4.389	4.6e-11
0.0005	9.77	3.7e-10	4.492	1.4e-11	4.389	2.2e-11	9.77	4.6e-10	4.492	1.7e-11	4.389	2.7e-11
0.00025	9.77	1.9e-10	4.492	7.2e-12	4.389	1.1e-11	9.77	2.4e-10	4.492	9.0e-12	4.389	1.4e-11
0.0001	9.77	7.9e-11	4.492	2.9e-12	4.389	4.6e-12	9.77	9.9e-11	4.492	3.6e-12	4.389	5.8e-12
5e-05	9.77	4.0e-11	4.492	1.5e-12	4.389	2.3e-12	9.77	5.0e-11	4.492	1.8e-12	4.389	2.9e-12
2.5e-05	9.77	2.0e-11	4.492	7.3e-13	4.389	1.2e-12	9.77	2.5e-11	4.492	9.2e-13	4.389	1.4e-12

Table 5.18: The fast compressional wave velocities in the original and mirror configurations of the coarsened sample X2 ($N_{cx} = 150$) saturated by the three types of fluids: incompressible fluid ($C_f = 0$), slightly compressible ($C_f = 4.6$, water in pressure of 1b) and highly compressible ($C_f = 100$).

ω	Original $N_{cx} = 150$						Mirror $N_{cx} = 300$					
	$C_f = 0$		$C_f = 4.6$		$C_f = 100$		$C_f = 0$		$C_f = 4.6$		$C_f = 100$	
	C_r	C_i	C_r	C_i	C_r	C_i	C_r	C_i	C_r	C_i	C_r	C_i
0.05	1.47e-04	7.55e-06	3.60e-05	1.84e-06	7.94e-06	4.07e-07	1.61e-04	7.91e-06	3.92e-05	1.93e-06	8.65e-06	4.26e-07
0.025	1.48e-04	1.34e-05	3.60e-05	3.28e-06	7.95e-06	7.24e-07	1.59e-04	1.37e-05	3.87e-05	3.35e-06	8.55e-06	7.40e-07
0.01	1.36e-04	3.50e-05	3.31e-05	8.54e-06	7.31e-06	1.89e-06	1.46e-04	3.34e-05	3.56e-05	8.14e-06	7.86e-06	1.80e-06
0.005	1.20e-04	4.15e-05	2.94e-05	1.01e-05	6.48e-06	2.24e-06	1.32e-04	4.17e-05	3.23e-05	1.02e-05	7.13e-06	2.25e-06
0.0025	9.91e-05	4.68e-05	2.42e-05	1.14e-05	5.34e-06	2.52e-06	1.09e-04	4.90e-05	2.67e-05	1.19e-05	5.89e-06	2.64e-06
0.001	6.65e-05	4.49e-05	1.62e-05	1.09e-05	3.58e-06	2.42e-06	7.44e-05	4.83e-05	1.82e-05	1.18e-05	4.01e-06	2.60e-06
0.0005	4.60e-05	3.72e-05	1.12e-05	9.07e-06	2.48e-06	2.00e-06	5.18e-05	4.08e-05	1.26e-05	9.95e-06	2.79e-06	2.20e-06
0.00025	3.16e-05	2.83e-05	7.70e-06	6.90e-06	1.70e-06	1.52e-06	3.56e-05	3.14e-05	8.67e-06	7.66e-06	1.92e-06	1.69e-06
0.0001	1.95e-05	1.86e-05	4.74e-06	4.54e-06	1.05e-06	1.00e-06	2.19e-05	2.08e-05	5.33e-06	5.07e-06	1.18e-06	1.12e-06
5e-05	1.36e-05	1.33e-05	3.32e-06	3.25e-06	7.33e-07	7.17e-07	1.53e-05	1.49e-05	3.73e-06	3.64e-06	8.23e-07	8.03e-07
2.5e-05	9.58e-06	9.47e-06	2.34e-06	2.31e-06	5.16e-07	5.10e-07	1.07e-05	1.06e-05	2.62e-06	2.59e-06	5.79e-07	5.71e-07

Table 5.19: The slow compressional wave velocities of the coarsened sample X2 ($N_{cx} = 150$) saturated by the three types of fluids.

ω	Original $N_{cx} = 150$						Mirror $N_{cx} = 300$					
	$C_f = 0$		$C_f = 4.6$		$C_f = 100$		$C_f = 0$		$C_f = 4.6$		$C_f = 100$	
	C_r	C_i	C_r	C_i	C_r	C_i	C_r	C_i	C_r	C_i	C_r	C_i
0.05	2.858	9.4e-12	2.858	9.4e-12	2.858	9.4e-12	2.858	1.1e-11	2.858	1.1e-11	2.858	1.1e-11
0.025	2.858	1.7e-11	2.858	1.7e-11	2.858	1.7e-11	2.858	1.8e-11	2.858	1.8e-11	2.858	1.8e-11
0.01	2.858	4.0e-11	2.858	4.0e-11	2.858	4.0e-11	2.858	4.1e-11	2.858	4.1e-11	2.858	4.1e-11
0.005	2.858	4.2e-11	2.858	4.2e-11	2.858	4.2e-11	2.858	4.7e-11	2.858	4.7e-11	2.858	4.7e-11
0.0025	2.858	3.9e-11	2.858	3.9e-11	2.858	3.9e-11	2.858	4.5e-11	2.858	4.5e-11	2.858	4.5e-11
0.001	2.858	2.5e-11	2.858	2.5e-11	2.858	2.5e-11	2.858	3.0e-11	2.858	3.0e-11	2.858	3.0e-11
0.0005	2.858	1.4e-11	2.858	1.4e-11	2.858	1.4e-11	2.858	1.8e-11	2.858	1.8e-11	2.858	1.8e-11
0.00025	2.858	7.6e-12	2.858	7.6e-12	2.858	7.6e-12	2.858	9.4e-12	2.858	9.4e-12	2.858	9.4e-12
0.0001	2.858	3.1e-12	2.858	3.1e-12	2.858	3.1e-12	2.858	3.8e-12	2.858	3.8e-12	2.858	3.8e-12
5e-05	2.858	1.5e-12	2.858	1.5e-12	2.858	1.5e-12	2.858	1.9e-12	2.858	1.9e-12	2.858	1.9e-12
2.5e-05	2.858	7.7e-13	2.858	7.7e-13	2.858	7.7e-13	2.858	9.6e-13	2.858	9.6e-13	2.858	9.6e-13

Table 5.20: The shear wave velocities in the original and mirror configurations of the coarsened sample X2 ($N_{cx} = 150$) saturated by the three types of fluids.

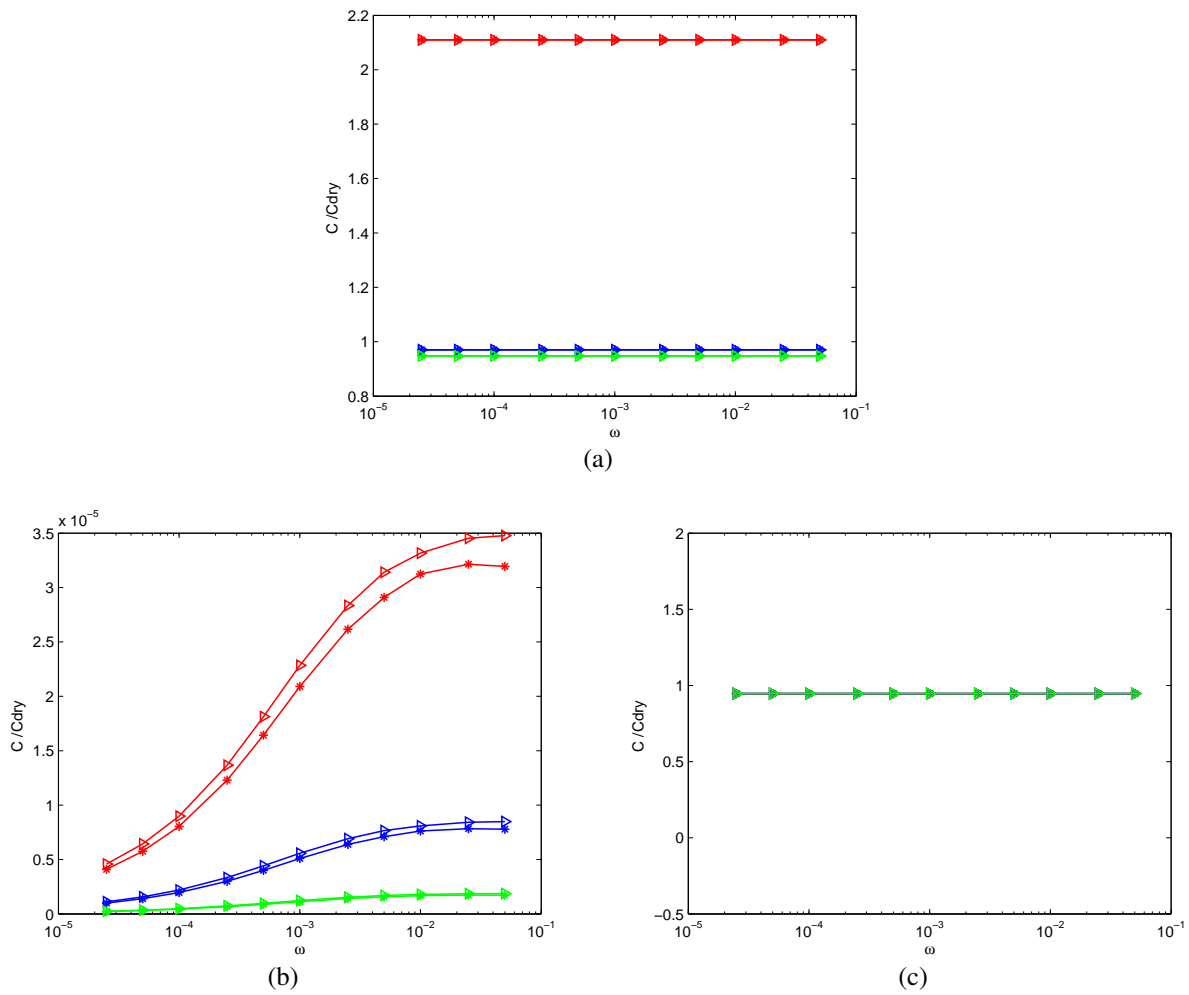


Figure 5.21: The acoustic velocities in the coarsened sample X2 ($N_{cx} = 150$) saturated by the three types of fluids. (a) Fast compressional wave. (b) Slow compressional wave. (c) Shear wave. Data are for: original configuration (*), mirror configuration (\triangleright), incompressible fluid $c_f = 0$ (red), normal water $c_f = 4.6 \times 10^{-10}$ (blue) , highly compressible fluid $c_f = 100 \times 10^{-10}$ (green).

The calculations for coarsened samples X2 of size $300 \times 300 \times 109$ and $600 \times 600 \times 218$ are done in the same way. The wave velocities are determined for various frequencies and for both configuration types; they are given in Tables 5.21, 5.22 and 5.23 for $N_{cx} = 300$ and in Table 5.24 for $N_{cx} = 600$.

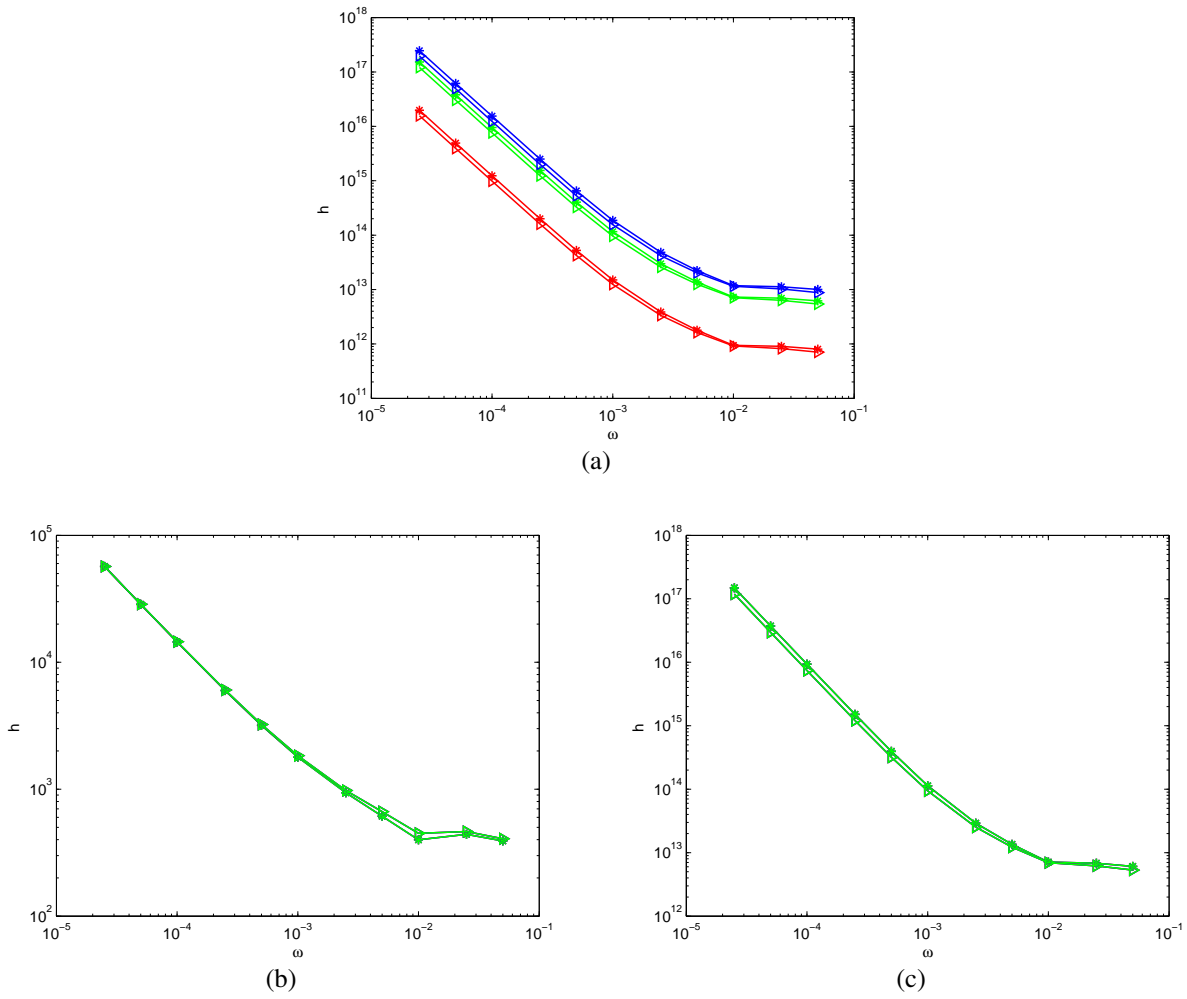


Figure 5.22: The penetration depth h of the coarsened sample X2 ($N_{cx} = 150$) saturated by the three types of fluids. (a) Fast compressional wave. (b) Slow compressional wave. (c) Shear wave. Data are for: original configuration (*), mirror configuration (\triangleright), incompressible fluid $c_f = 0$ (red), normal water $c_f = 4.6 \times 10^{-10}$ (blue), highly compressible fluid $c_f = 100 \times 10^{-10}$ (green).

ω	Original $N_{cx} = 150$						Mirror $N_{cx} = 300$					
	$C_f = 0$		$C_f = 4.6$		$C_f = 100$		$C_f = 0$		$C_f = 4.6$		$C_f = 100$	
	C_r	C_i	C_r	C_i	C_r	C_i	C_r	C_i	C_r	C_i	C_r	C_i
0.05	8.84	3.0e-10	4.310	1.4e-11	4.180	2.4e-11	8.84	1.7e-10	4.310	7.9e-12	4.180	1.4e-11
0.025	8.84	2.5e-10	4.310	1.2e-11	4.180	2.1e-11	8.84	2.8e-10	4.310	1.3e-11	4.180	2.3e-11
0.01	8.84	8.3e-10	4.310	3.8e-11	4.180	6.7e-11	8.84	7.6e-10	4.310	3.5e-11	4.180	6.2e-11
0.005	8.84	8.5e-10	4.310	3.9e-11	4.180	6.9e-11	8.84	8.3e-10	4.310	3.8e-11	4.180	6.8e-11
0.0025	8.84	8.1e-10	4.310	3.7e-11	4.180	6.6e-11	8.84	9.0e-10	4.310	4.1e-11	4.180	7.3e-11
0.001	8.84	7.2e-10	4.310	3.3e-11	4.180	5.8e-11	8.84	8.3e-10	4.310	3.8e-11	4.180	6.7e-11
0.0005	8.84	5.4e-10	4.310	2.5e-11	4.180	4.4e-11	8.84	6.5e-10	4.310	3.0e-11	4.180	5.3e-11
0.00025	8.84	3.4e-10	4.310	1.6e-11	4.180	2.8e-11	8.84	4.2e-10	4.310	1.9e-11	4.180	3.4e-11
0.0001	8.84	1.5e-10	4.310	7.0e-12	4.180	1.2e-11	8.84	1.9e-10	4.310	8.9e-12	4.180	1.6e-11
5e-05	8.84	7.8e-11	4.310	3.6e-12	4.180	6.3e-12	8.84	9.9e-11	4.310	4.5e-12	4.180	8.1e-12
2.5e-05	8.84	3.9e-11	4.310	1.8e-12	4.180	3.2e-12	8.84	5.0e-11	4.310	2.3e-12	4.180	4.1e-12

Table 5.21: The fast compressional wave velocities in the original and mirror configurations of the coarsened sample X2 ($N_{cx} = 300$).

ω	Original $N_{cx} = 150$						Mirror $N_{cx} = 300$					
	$C_f = 0$		$C_f = 4.6$		$C_f = 100$		$C_f = 0$		$C_f = 4.6$		$C_f = 100$	
	C_r	C_i	C_r	C_i	C_r	C_i	C_r	C_i	C_r	C_i	C_r	C_i
0.05	1.53e-04	1.00e-05	4.34e-05	2.84e-06	9.68e-06	6.34e-07	1.53e-04	5.73e-06	4.34e-05	1.62e-06	9.69e-06	3.62e-07
0.025	1.44e-04	9.01e-06	4.08e-05	2.55e-06	9.10e-06	5.69e-07	1.55e-04	9.35e-06	4.39e-05	2.65e-06	9.79e-06	5.91e-07
0.01	1.39e-04	3.05e-05	3.93e-05	8.63e-06	8.77e-06	1.93e-06	1.43e-04	2.74e-05	4.04e-05	7.75e-06	9.02e-06	1.73e-06
0.005	1.29e-04	3.38e-05	3.66e-05	9.57e-06	8.16e-06	2.14e-06	1.38e-04	3.08e-05	3.90e-05	8.74e-06	8.70e-06	1.95e-06
0.0025	1.13e-04	3.68e-05	3.21e-05	1.04e-05	7.16e-06	2.32e-06	1.25e-04	3.69e-05	3.53e-05	1.04e-05	7.87e-06	2.33e-06
0.001	8.94e-05	4.11e-05	2.53e-05	1.16e-05	5.65e-06	2.60e-06	9.85e-05	4.30e-05	2.79e-05	1.22e-05	6.23e-06	2.72e-06
0.0005	6.85e-05	4.07e-05	1.94e-05	1.15e-05	4.33e-06	2.57e-06	7.64e-05	4.33e-05	2.16e-05	1.23e-05	4.83e-06	2.73e-06
0.00025	4.89e-05	3.59e-05	1.39e-05	1.02e-05	3.09e-06	2.27e-06	5.53e-05	3.91e-05	1.57e-05	1.11e-05	3.50e-06	2.47e-06
0.0001	2.99e-05	2.62e-05	8.47e-06	7.41e-06	1.89e-06	1.65e-06	3.40e-05	2.91e-05	9.62e-06	8.24e-06	2.15e-06	1.84e-06
5e-05	2.06e-05	1.93e-05	5.85e-06	5.46e-06	1.31e-06	1.22e-06	2.34e-05	2.16e-05	6.63e-06	6.13e-06	1.48e-06	1.37e-06
2.5e-05	1.44e-05	1.39e-05	4.08e-06	3.94e-06	9.10e-07	8.79e-07	1.63e-05	1.57e-05	4.61e-06	4.43e-06	1.03e-06	9.90e-07

Table 5.22: The slow compressional wave velocities of the coarsened sample X2 ($N_{cx} = 300$) saturated by the three types of fluids.

ω	Original $N_{cx} = 150$						Mirror $N_{cx} = 300$					
	$C_f = 0$		$C_f = 4.6$		$C_f = 100$		$C_f = 0$		$C_f = 4.6$		$C_f = 100$	
	C_r	C_i	C_r	C_i	C_r	C_i	C_r	C_i	C_r	C_i	C_r	C_i
0.05	2.714	1.6e-11	2.714	1.6e-11	2.714	1.6e-11	2.714	9.3e-12	2.714	9.3e-12	2.714	9.3e-12
0.025	2.714	1.4e-11	2.714	1.4e-11	2.714	1.4e-11	2.714	1.5e-11	2.714	1.5e-11	2.714	1.5e-11
0.01	2.714	4.5e-11	2.714	4.5e-11	2.714	4.5e-11	2.714	4.1e-11	2.714	4.1e-11	2.714	4.1e-11
0.005	2.714	4.6e-11	2.714	4.6e-11	2.714	4.6e-11	2.714	4.5e-11	2.714	4.5e-11	2.714	4.5e-11
0.0025	2.714	4.4e-11	2.714	4.4e-11	2.714	4.4e-11	2.714	4.9e-11	2.714	4.9e-11	2.714	4.9e-11
0.001	2.714	3.9e-11	2.714	3.9e-11	2.714	3.9e-11	2.714	4.5e-11	2.714	4.5e-11	2.714	4.5e-11
0.0005	2.714	3.0e-11	2.714	3.0e-11	2.714	3.0e-11	2.714	3.5e-11	2.714	3.5e-11	2.714	3.5e-11
0.00025	2.714	1.9e-11	2.714	1.9e-11	2.714	1.9e-11	2.714	2.3e-11	2.714	2.3e-11	2.714	2.3e-11
0.0001	2.714	8.3e-12	2.714	8.3e-12	2.714	8.3e-12	2.714	1.0e-11	2.714	1.0e-11	2.714	1.0e-11
5e-05	2.714	4.2e-12	2.714	4.2e-12	2.714	4.2e-12	2.714	5.4e-12	2.714	5.4e-12	2.714	5.4e-12
2.5e-05	2.714	2.1e-12	2.714	2.1e-12	2.714	2.1e-12	2.714	2.7e-12	2.714	2.7e-12	2.714	2.7e-12

Table 5.23: The shear wave velocities in the original and mirror configurations of the coarsened sample X2 ($N_{cx} = 300$) saturated by the three types of fluids.

ω	Fast compressional velocity						Shear wave velocity					
	$C_f = 0$		$C_f = 4.6$		$C_f = 100$		$C_f = 0$		$C_f = 4.6$		$C_f = 100$	
	C_r	C_i	C_r	C_i	C_r	C_i	C_r	C_i	C_r	C_i	C_r	C_i
0.05	8.335	5.4e-10	4.182	2.8e-11	4.028	5.5e-11	2.607	3.6e-11	2.607	3.6e-11	2.607	3.6e-11
0.025	8.335	4.5e-10	4.182	2.3e-11	4.028	4.6e-11	2.607	3.1e-11	2.607	3.1e-11	2.607	3.1e-11
0.01	8.335	8.9e-10	4.182	4.6e-11	4.028	9.0e-11	2.607	6.0e-11	2.607	6.0e-11	2.607	6.0e-11
0.005	8.335	7.1e-10	4.182	3.6e-11	4.028	7.1e-11	2.607	4.8e-11	2.607	4.8e-11	2.607	4.8e-11
0.0025	8.335	7.1e-10	4.182	3.7e-11	4.028	7.2e-11	2.607	4.8e-11	2.607	4.8e-11	2.607	4.8e-11
0.001	8.335	6.6e-10	4.182	3.4e-11	4.028	6.6e-11	2.607	4.4e-11	2.607	4.4e-11	2.607	4.4e-11
0.0005	8.335	6.1e-10	4.182	3.1e-11	4.028	6.2e-11	2.607	4.1e-11	2.607	4.1e-11	2.607	4.1e-11
0.00025	8.335	5.1e-10	4.182	2.6e-11	4.028	5.2e-11	2.607	3.5e-11	2.607	3.5e-11	2.607	3.5e-11
0.0001	8.335	3.2e-10	4.182	1.7e-11	4.028	3.3e-11	2.607	2.2e-11	2.607	2.2e-11	2.607	2.2e-11
5e-05	8.335	1.9e-10	4.182	9.7e-12	4.028	1.9e-11	2.607	1.3e-11	2.607	1.3e-11	2.607	1.3e-11
2.5e-05	8.335	9.9e-11	4.182	5.1e-12	4.028	1.0e-11	2.607	6.7e-12	2.607	6.7e-12	2.607	6.7e-12

Table 5.24: The fast compressional and shear wave velocities in the original configuration of the coarsened sample X2 ($N_{cx} = 600$) saturated by the three types of fluids.

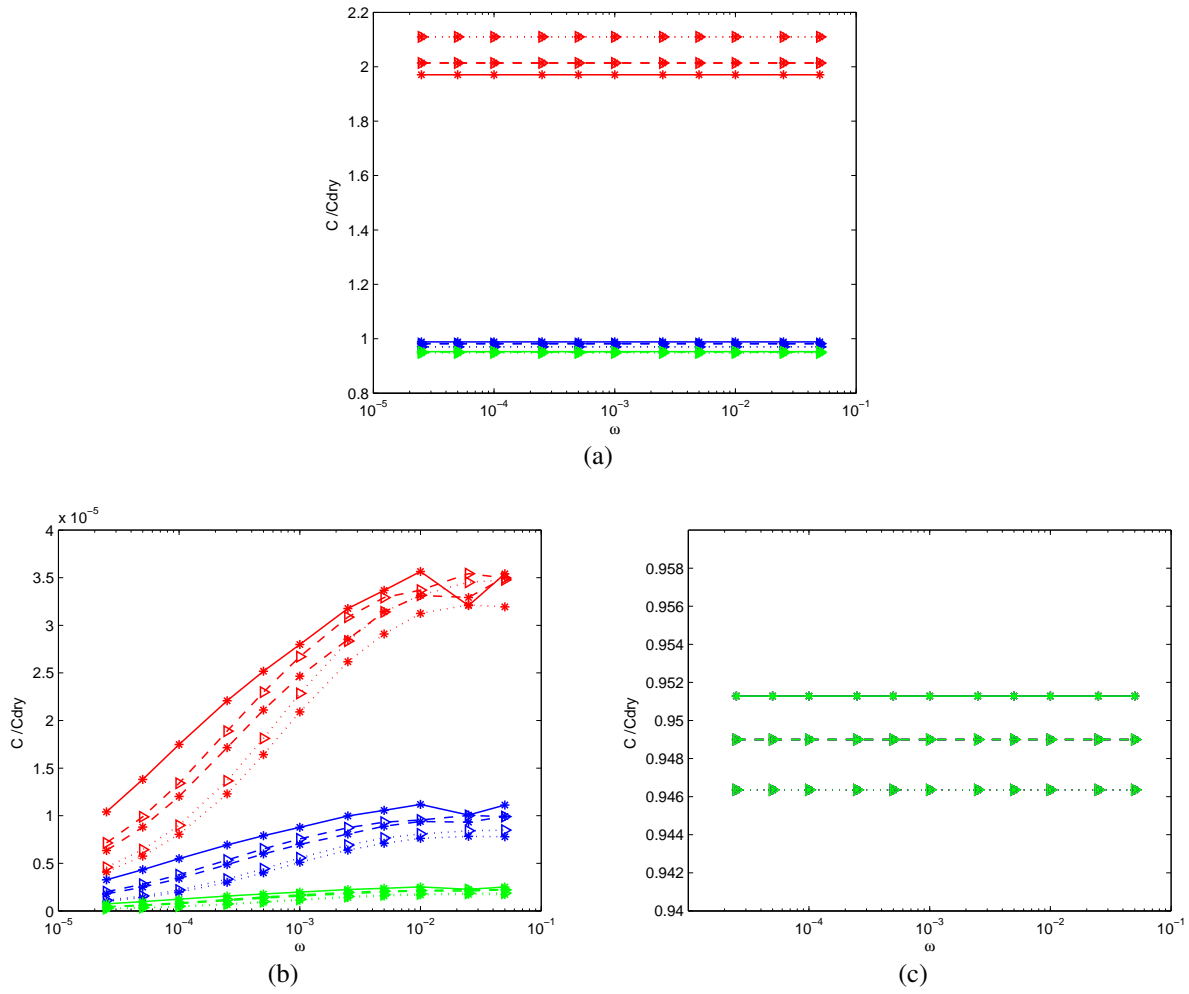


Figure 5.23: The acoustic velocities in the coarsened samples X2 with $N_{cx} = 150$, $N_{cx} = 300$ and $N_{cx} = 600$. (a) Fast compressional wave. (b) Slow compressional wave. (c) Shear wave. Data are for: $N_{cx} = 600$ (—), $N_{cx} = 300$ (- - -), 150 (. . .), original configuration (*), mirror configuration (\triangleright), $c_f = 0$ (red), $c_f = 4.6 \times 10^{-10}$ (blue), $c_f = 100 \times 10^{-10}$ (green).

Then, the comparisons of the velocities between the coarsened samples X2 with $N_{cx} = 150$, 300 and 600 are presented in Fig.5.23 and the ones for the attenuation depth h are in Fig.5.24. It can be seen that due to the very small imaginary part, $v_{||}^{fast}$ and v_{\perp} seem to be constant when ω increases. However, $v_{||}^{slow}$ is an increasing function in this case, some noisy results are obtained with high frequencies for the sample $N_{cx} = 300$ and 600 as seen in Fig.5.23.b. It can be attributed to the values of \mathbf{K} when some changes are applied to fulfill the condition on the Knudsen number.

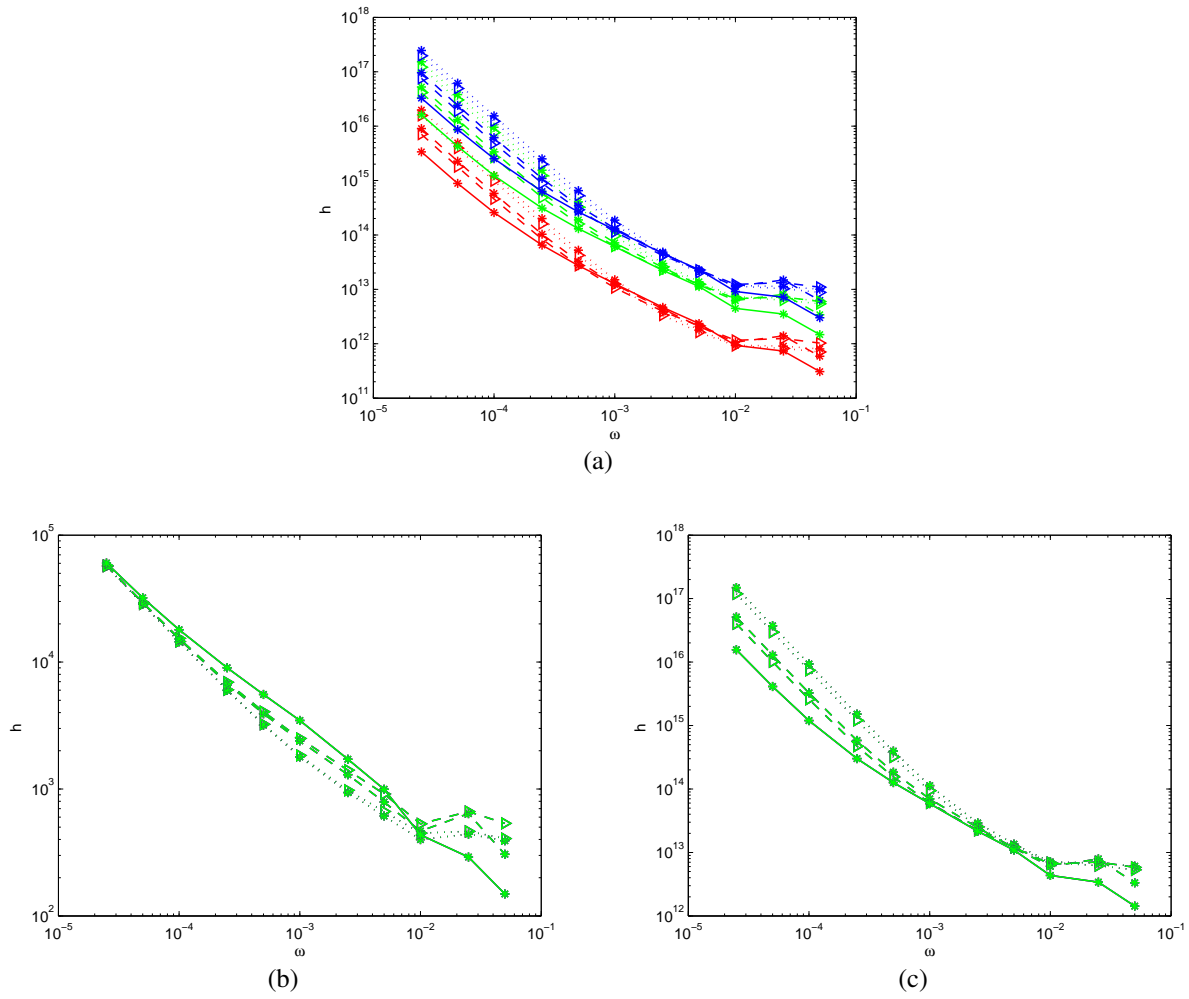


Figure 5.24: The penetration depths of the coarsened samples X2 with $N_{cx} = 150$, $N_{cx} = 300$ and $N_{cx} = 600$. (a) Fast compressional wave. (b) Slow compressional wave. (c) Shear wave. Data are for: $N_{cx} = 600$ (—), $N_{cx} = 300$ (- - -), 150 (. . .), original configuration (*), mirror configuration (\triangleright), $c_f = 0$ (red), $c_f = 4.6 \times 10^{-10}$ (blue), $c_f = 100 \times 10^{-10}$ (green).

Similarly, since the four quantities of the Christoffel equation are fully determined, the acoustic velocities and the penetration depth h can be derived for the samples X7 and Y5. The results for the coarsened sample X7 of size $150 \times 141 \times 60$ are presented in Tables A.28, A.29 and A.30; the ones for sample of size $300 \times 283 \times 121$ are in Tables A.31, A.32, A.33 and in Table A.34 for $600 \times 566 \times 242$. The velocities and h of fast, slow compressional and shear waves are compared in Figures 5.25 and 5.26.

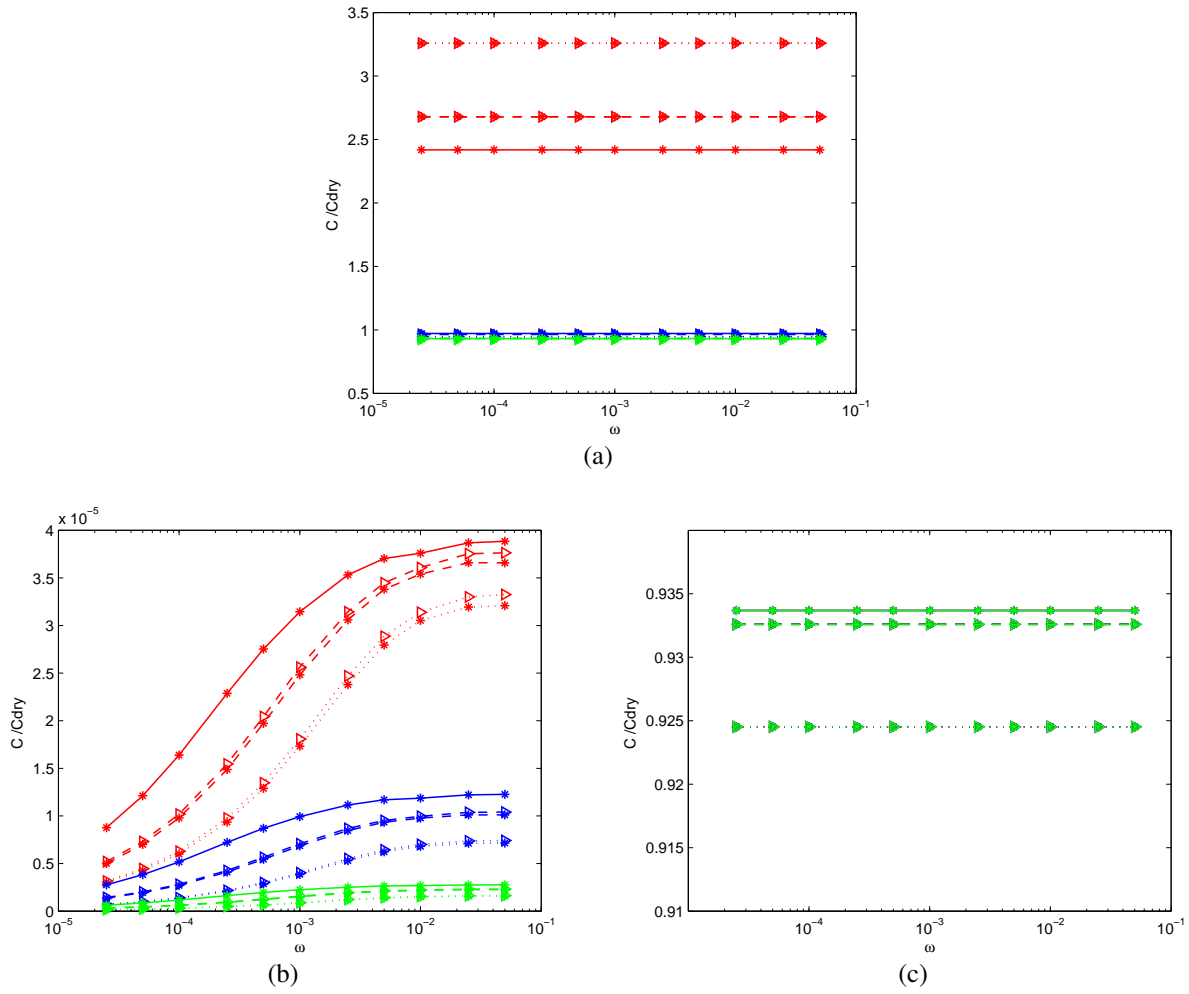


Figure 5.25: The acoustic velocities in the coarsened samples X7 with $N_{cx} = 150$, $N_{cx} = 300$ and $N_{cx} = 600$. (a) Fast compressional wave. (b) Slow compressional wave. (c) Shear wave. Data are for: $N_{cx} = 600$ (—), $N_{cx} = 300$ (- - -), 150 (. . .), original configuration (*), mirror configuration (\triangleright), $c_f = 0$ (red), $c_f = 4.6 \times 10^{-10}$ (blue), $c_f = 100 \times 10^{-10}$ (green).

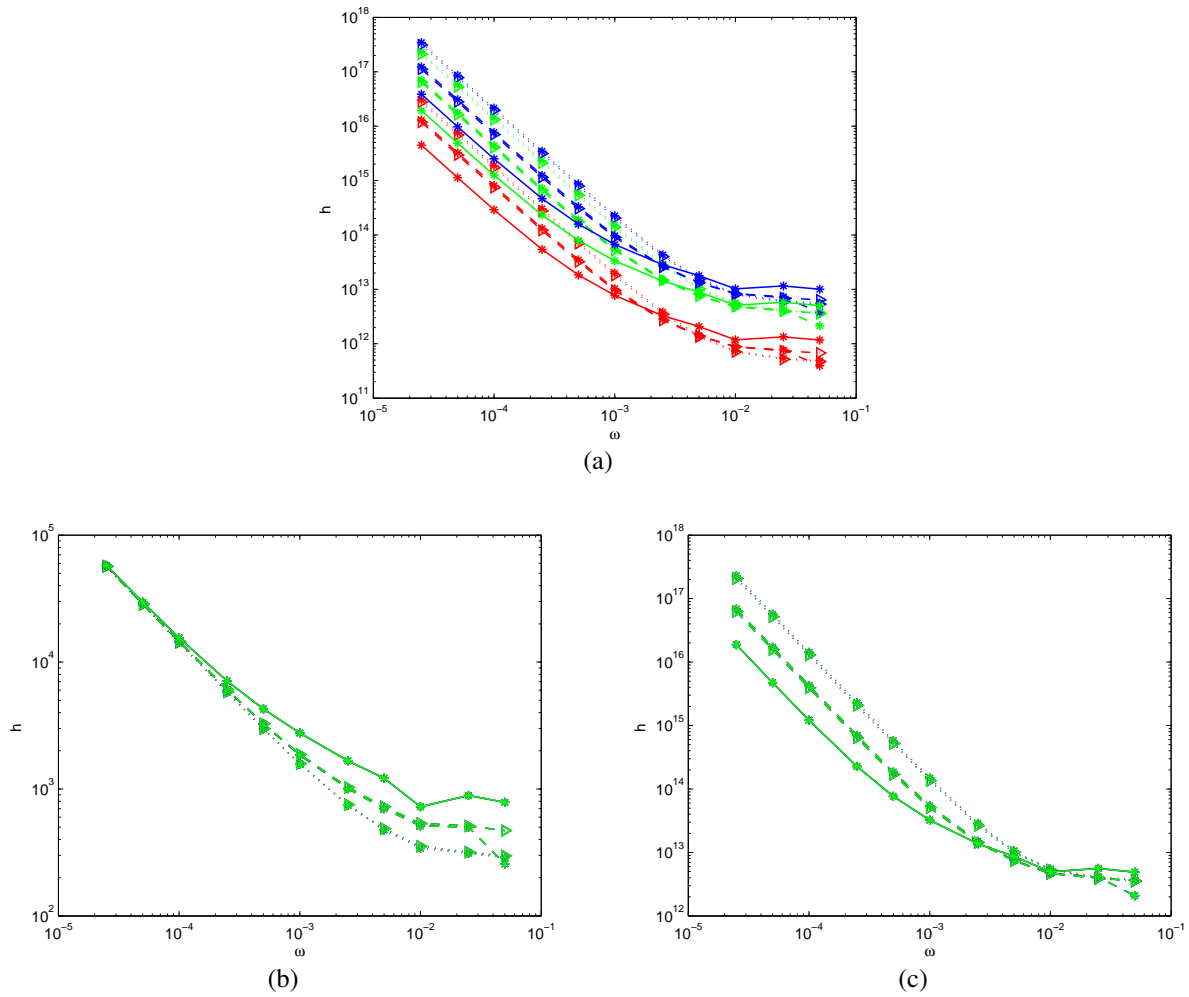


Figure 5.26: The penetration depths of the coarsened samples X7 with $N_{cx} = 150$, $N_{cx} = 300$ and $N_{cx} = 600$. (a) Fast compressional wave. (b) Slow compressional wave. (c) Shear wave. Data are for: $N_{cx} = 600$ (—), $N_{cx} = 300$ (- - -), 150 (. . .), original configuration (*), mirror configuration (\triangleright), $c_f = 0$ (red), $c_f = 4.6 \times 10^{-10}$ (blue), $c_f = 100 \times 10^{-10}$ (green).

The fast compressional, slow compressional and shear wave velocities of the coarsened samples Y5 with $N_{cx} = 150$, 300 and 600 are given in turn in Tables A.35, A.36, A.37, A.38, A.39, A.40 and A.41. Together with the corresponding penetration depth h , they are compared to each other as shown in Figures 5.27 and 5.28.

Due to the same reasons for sample X2, some noisy results can be observed for the slow compressional velocity and the depth h for high frequencies. Furthermore, as for sample FB8, the acoustic velocities in the saturated sample Y13 with the smallest porosity are not yet available

because of problems of the determination of the dynamic permeability.

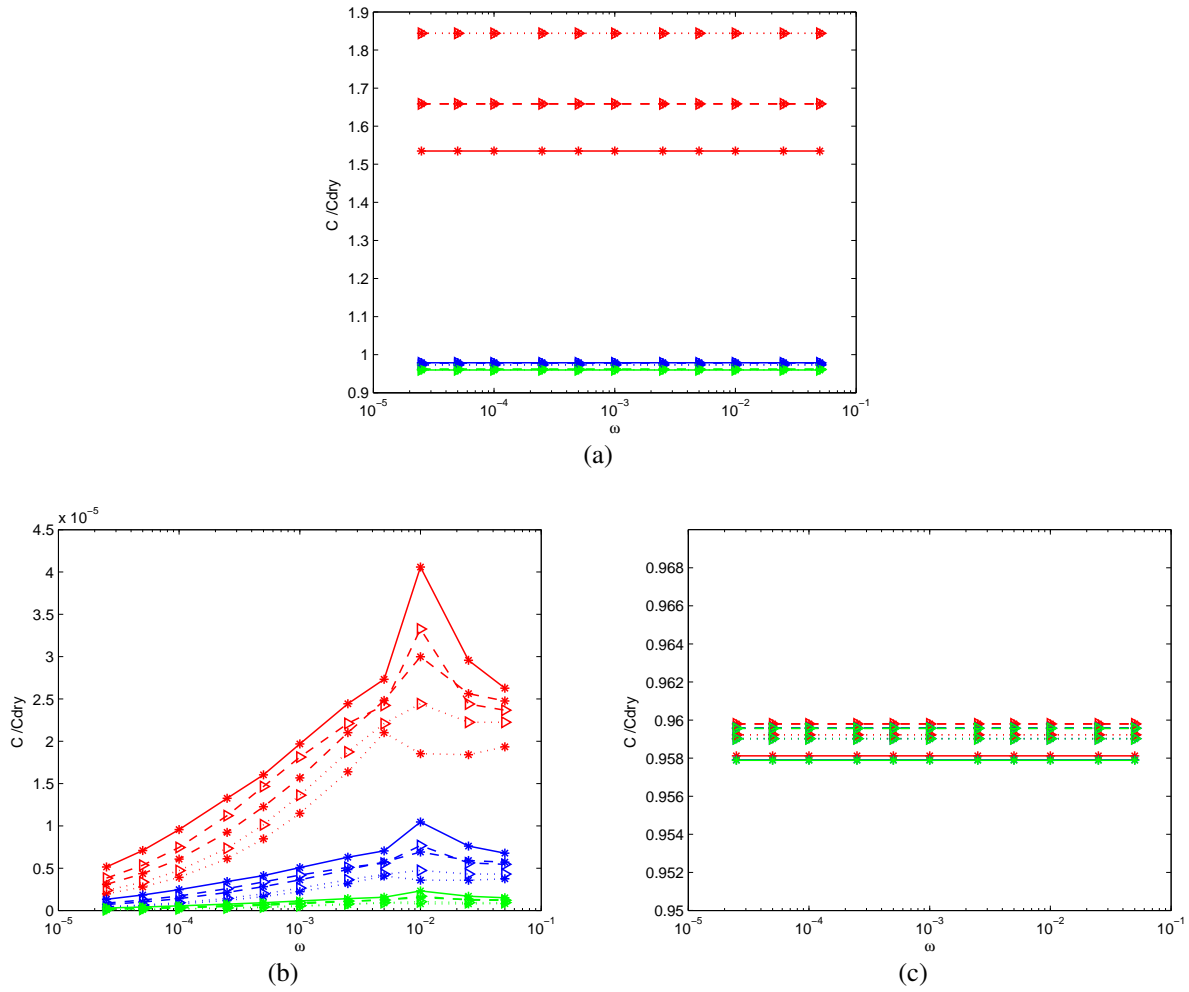


Figure 5.27: The acoustic velocities in the coarsened samples Y5 with $N_{cx} = 150$, $N_{cx} = 300$ and $N_{cx} = 600$. (a) Fast compressional wave. (b) Slow compressional wave. (c) Shear wave. Data are for: $N_{cx} = 600$ (—), $N_{cx} = 300$ (- - -), 150 (. . .), original configuration (*), mirror configuration (\triangleright), $c_f = 0$ (red), $c_f = 4.6 \times 10^{-10}$ (blue), $c_f = 100 \times 10^{-10}$ (green).

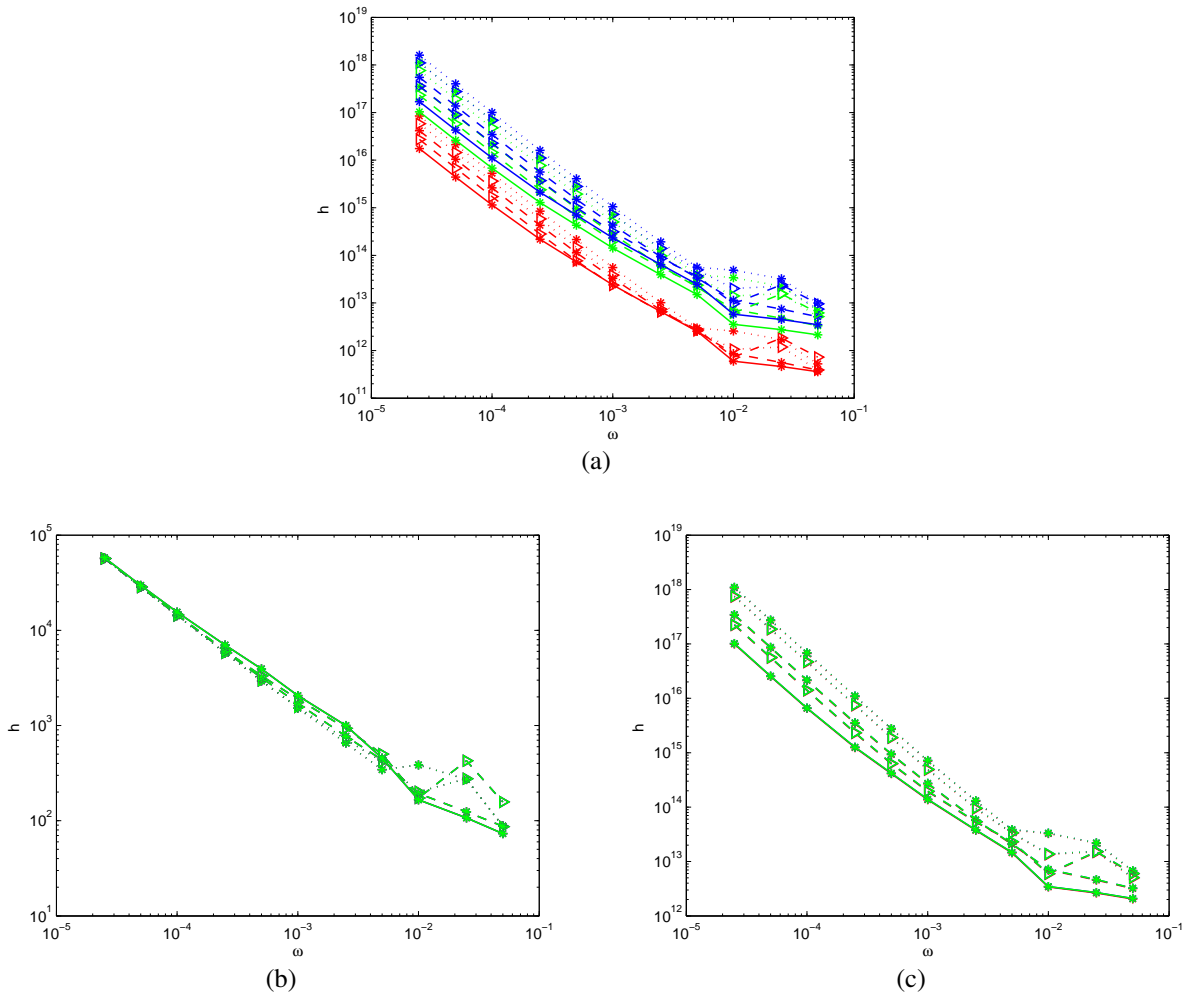


Figure 5.28: The penetration depths of the coarsened samples Y5 with $N_{cx} = 150$, $N_{cx} = 300$ and $N_{cx} = 600$. (a) Fast compressional wave. (b) Slow compressional wave. (c) Shear wave. Data are for: $N_{cx} = 600$ (—), $N_{cx} = 300$ (- - -), 150 (...), original configuration (*), mirror configuration (\triangleright), $c_f = 0$ (red), $c_f = 4.6 \times 10^{-10}$ (blue), $c_f = 100 \times 10^{-10}$ (green).

As mentioned, two comparisons are done to evaluate our results. In the first case, Gassmann's model is used. It should be noted that this model is only for media with one solid component; therefore, in order to apply to the STATOIL samples, clay should be changed into quartz. The bulk modulus of dry samples are the results of Section 5.3. This is possible because the clay proportion in our samples is very small in comparison with quartz as can be seen in Table 5.5. The comparisons are done when our samples saturated by water under normal conditions (1b) correspond to the slightly compressible fluid with $c_f = 4.6 \times 10^{-10} Pa^{-1}$. The results are given in Table

5.25. Our results are very close to Gassmann's predictions since the maximal difference is 1.0% for the compressional wave and 0.1% for the shear wave.

Samples	N_{cx}	Simulation		Gassmann's model		Error	
		v_p	v_s	v_p	v_s	v_p	v_s
		km/s	km/s	km/s	km/s	%	%
X2	150	4.493	2.858	4.474	2.856	0.4	0.07
	300	4.310	2.714	4.293	2.713	0.4	0.04
	600	4.182	2.607	4.163	2.610	0.5	0.1
X7	150	4.451	2.857	4.446	2.856	0.11	0.04
	300	4.138	2.611	4.143	2.610	0.12	0.04
	600	3.955	2.465	3.961	2.463	0.15	0.08
Y5	150	4.944	3.184	4.90	3.183	0.89	0.03
	300	4.794	3.061	4.748	3.060	0.95	0.03
	600	4.717	2.999	4.669	2.997	1.0	0.07

Table 5.25: The comparison between our simulation results and Gassmann's model. These coarsened samples are saturated by water under normal conditions (1b), $c_f = 4.6 \times 10^{-10} Pa^{-1}$.

The first comparison is done when the medium is saturated by water. Then, the second comparison is performed for samples filled with air (1b). The physical properties of the air are given in (4.22).

Obviously, the samples saturated by air (1b) can be considered as dry. Thanks to that, a comparison between the numerical results, the dry samples obtained in Section 5.3 and Gassmann's model is done. They are about the same since the difference is always less than 1% as seen in Table 5.26.

Now, the acoustic velocities are fully determined for the coarsened samples X2, X7, Y5 with $N_{cx} = 150, 300$; therefore, the ones for the original samples ($N_{cx} = 1200$) and for the samples with an infinite discretization ($N_{cx} = \infty$) can be derived. The extrapolations are done in the same ways as for dry samples. The fast compressional and shear wave velocities are presented in Table

Samples	N_{cx}	Air (1b)		Dry		Error		Gassmann		Error	
		v_p	v_s	v_p	v_s	v_p	v_s	v_p	v_s	v_p	v_s
		km/s	km/s	km/s	km/s	%	%	km/s	km/s	%	%
X2	150	4.63	3.02	4.63	3.02	0	0	4.603	3.01	0.6	0.3
	300	4.39	2.86	4.39	2.86	0	0	4.37	2.85	0.5	0.3
	600	4.23	2.74	4.23	2.74	0	0	4.22	2.75	0.2	0.4
X7	150	4.70	3.09	4.70	3.09	0	0	4.70	3.09	0	0
	300	4.29	2.80	4.29	2.80	0	0	4.30	2.80	0.2	0
	600	4.05	2.64	4.07	2.64	0.5	0	4.05	2.63	0	0.4
Y5	150	5.08	3.32	5.08	3.32	0	0	5.04	3.32	0.8	0
	300	4.90	3.19	4.90	3.19	0	0	4.85	3.18	1.0	0.3
	600	4.80	3.12	4.82	3.13	0.4	0.3	4.75	3.12	1.0	0

Table 5.26: The acoustic velocities for the coarsened samples saturated by air (1b). Comparison between the simulations, the dry samples and Gassmann’s model.

5.27.

N_c	Velocity	Y13	Y5	X2	X7
1200	v_p (km/s)	-	4.6798	4.1415	3.8805
	v_s (km/s)	-	2.9683	2.576	2.4068
∞	v_p (km/s)	-	4.642	4.095	3.7985
	v_s (km/s)	-	2.9375	2.535	2.342

Table 5.27: The acoustic velocities in saturated samples with the original dimension ($N_{cx}=1200$) and in the samples with an infinite discretization.

Note that various samples whose the quartz and clay proportions are close to our STATOIL as described in Fig. 5.14.c were also measured by Han (1986). Then, Han et al. (1986) provided

the prediction functions for velocities in saturated samples; they are expressed as

$$V_p = 5.59 - 6.93\varepsilon - 2.18C \quad \text{km/s} \quad (5.9a)$$

$$V_s = 3.52 - 4.91\varepsilon - 1.89C \quad \text{km/s} \quad (5.9b)$$

Let us compare the extrapolated results and the experimental data of *Han* (1986). Fig. 5.29 indicates that they are in good agreement but the numerical data are slightly larger than the measurement ones. We believe that this is for the reasons which are mentioned in Chapter 4.

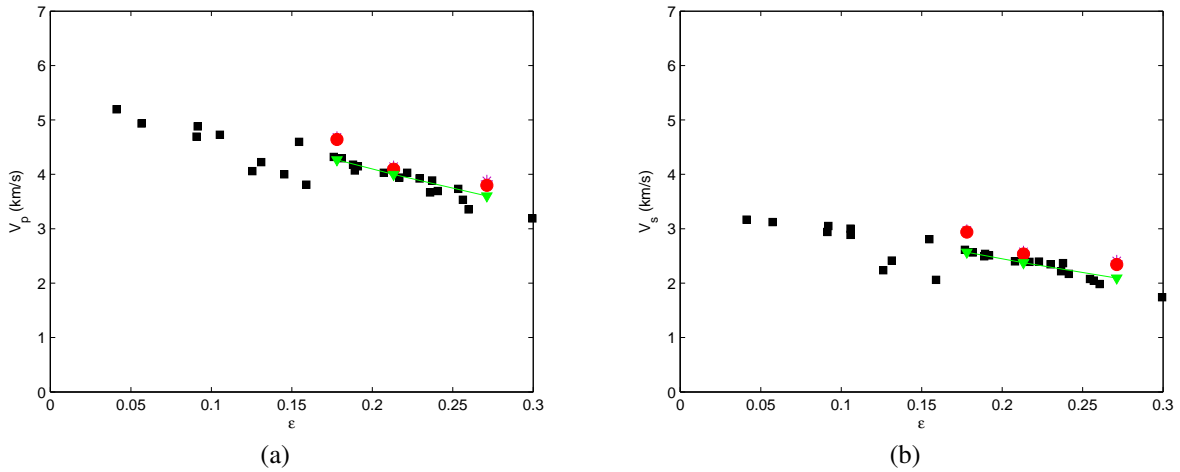


Figure 5.29: Comparison between the acoustic velocities in STATOIL samples with $N_{cx} = 1200$ and $N_{cx} = \infty$ and the experimental data of *Han* (1986). (a) The compressional wave velocity. (b) The shear wave velocity. Data are for: $N_{cx} = 1200$ (red \circ), $N_{cx} = \infty$ (violet $*$), experimental data of *Han* (1986) (black \square), Han's predictions (5.9) (green ∇).

5.7 Conclusion

In this chapter, four STATOIL samples X2, X7, Y5 and Y13 are calculated. The acoustic velocities in dry samples are derived from the effective stiffness tensor which are calculated by LSM2S. Some comparisons are provided in calculations of the coarsened sample X2 in order to demonstrate the accuracy of this code. The calculations are done by the coarsening method and the results of the original samples are obtained by extrapolation. The results are slightly larger than

the experimental data of *Han* (1986) and of STATOIL, but in good agreement with the Hashin-Shtrickman's bounds and the empirical models of *Nur et al.* (1991); *Krief* (1990).

The acoustic properties in saturated samples are determined by the Christoffel equation. The calculations are done with the original and mirror configurations of the coarsened samples for three types of fluids: slightly, highly and incompressible fluids. Then, as for Fontainebleau samples, the influences of frequency, of compressibility coefficients, of discretization on the acoustic velocities and on the penetration depth h of fast, slow compressional and shear waves are also considered. Two comparisons are performed: the first is with Gassmann's model and the second is between the dry samples and the ones saturated by air under normal conditions. The maximal difference is about 1.0% in both cases; this coincidence allows us to evaluate the precision of our method. Finally, the acoustic velocities in the original samples and in the samples with an infinite discretization are determined by extrapolations. A comparison with the experimental data of *Han* (1986); *Han et al.* (1986) is done and this shows that they are close to each other but the numerical results are still slightly larger than the experimental ones.

Chapter 6

Conclusions

In this thesis, the lattice models are used to calculate the acoustic velocities in dry and in saturated porous media. The numerical tools may avoid some of the experiments which are usually more expensive. The basic models LBM, LSM, LBM-LSM (*Pazdniakou, 2012*) are extended to address the porous media with two solid components. The new models whose names are LSM2S and LBM-LSM2S are validated by comparison with the other methods such as the approximation methods of *Nemat-Nasser and Iwakuma (1982)*, *Torquato (1998, 2000)* and *Cohen (2004)*, the FFT method of *Hoang-Duc and Bonnet (2012)*, and the FMD of *Malinouskaya (2007)*. The codes are parallelized in order to work with large samples; the averaged speedup can be predicted according to Amdahl's law (*Che and Nguyen, 2014*).

Two types of porous media are addressed in this work. The first type, which includes quartz and pore, corresponds to Fontainebleau samples and is named FB8, FB13, FB18 and FB22. The second one is composed by clay, quartz and pore; their names are X2, X7, Y5, Y13. For each type, three problems have been studied numerically. The first problem is devoted to characterizations of samples. The second one addresses wave propagation in dry samples. The third one corresponds to samples saturated by incompressible or compressible fluids.

The characterizations include the determination of the porosity and of the correlation function. They are calculated for each slice along the three directions of the samples. The Fourier components corresponding to the correlation function are also determined. The calculations are done for all samples in the same way and they can be considered to be isotropic and statistically homogeneous.

For the dry samples, the wave propagation is ruled by the elastic behaviour. The acoustic velocities are derived from the effective stiffness tensor C^{eff} which can be determined numerically by LSM (for Fontainebleau samples) or by LSM2S (for STATOIL samples). The calculations are done by the direct simulations or by the coarsening method depending on the sample size. Then, the compressional, shear wave velocities and the effective bulk, shear modulus are determined for the original samples or the samples with an infinite discretization. It is shown that the results are in good agreement with the IOS model of *Arns* (1996), the experimental data of *Han* (1986) and *Gomez et al.* (2010) and the empirical models of *Nur et al.* (1991) and *Krief* (1990). The numerical results are slightly larger than the experimental data that may be due to the small size of real samples, to the appearance of small fissures in samples, to the difference of solids proportions and to the difference of clay properties...

For the saturated samples, the system of the local equations is more complicated. It includes elastic and Navier-Stokes equations in the solid and the fluid phases, respectively. The acoustic velocities can be obtained by solving the Christoffel equations for a single pore filled by an incompressible fluid or for many pores filled by a compressible fluid. Four quantities, namely the effective stiffness tensor C^{eff} , the dynamic permeability \mathbf{K} , the solid-fluid reactions α and β , are needed. They are calculated by LSM (LSM2S), LBM, LBM-LSM (LBM-LSM2S), respectively. The fast compressional, slow compressional and shear velocities are determined for Fontainebleau and STATOIL samples which are saturated by incompressible, slightly compressible (water), highly compressible fluids and by air. The analysis of the influence of frequency, compressible coefficient, discretization and mirror configurations on the velocities and on the attenuation effect is studied. The obtained results are in very good agreement with Gassmann's model since the difference is always less than 1.2%; as for the dry samples, the result slightly larger the measurement data of *Han* (1986).

It is clear that the numerical study has some advantages in comparison with the experiments such as the low cost, the reduction of errors... However, some problems still remain which can be listed as follows.

- There is always a difference between numerical results and the experimental data. As it

is shown in Chapter 4 and 5, our results are slightly larger than the experimental ones.

- The determination of the dynamic permeability for samples with a small porosity (FB8 and Y13) is difficult. Until now, the results are not yet available. As a consequence, one cannot obtain the acoustic velocities in these samples.
- The computational time is usually very long for samples with a large size though the codes were parallelized.
- The required memory is still large (161 Gb for a sample of dimension 480^3); therefore, some computers are not strong enough to calculate.

In the future, we believe that these problems can be solved as a result of the development of technologies. Moreover, the present models can be developed to calculate porous media with many solid components and partially or fully saturated by two fluids. It must be also noted that this purpose is a complex problem because of various fluid-fluid, fluid-solid interface effects.

Bibliography

- Achenbach, J. (1973), Wave propagation in elastic solids, *North-Holland Publishing Company, Amsterdam*.
- Adler, P. M. (1992), *Porous Media: Geometry and Transports*, Butterworth-Heinemann, Stoneham, MA.
- Adler, R. J. (1981), The geometry of random fields, *John Wiley, New York*.
- Archie, G. E. (1942), The electrical resistivity log as an aid in determining some reservoir characteristics, *Trans. AIME*, 146: 54-62.
- Arns, C. (1996), The influence of morphology on physical properties of reservoir rocks, Ph.D. thesis, University of technology, Aachen.
- Artola, F. A., and V. Alvaradob (2006), Sensitivity analysis of gassmann's fluid substitution equations: Some implications in feasibility studies of time-lapse seismic reservoir monitoring, *Journal of Applied Geophysics*, 59(1), 47 – 62.
- Bhartnagar, P. L., E. P. Gross, and M. Krook (1954), A model for collision processes in gases. i. small amplitude processes in charged and neutral one-component systems, *Phys. Rev.*94, 511.
- Biot, M. (1941), General theory of three dimensional consolidation, *J. Appl. Physic*, 12: 155-164.
- Biot, M. (1956a), Theory of propagation of elastic waves in a fluid-saturated porous solid. low-frequency range, *J. Acoust. Soc. Am.* 28, 179.
- Biot, M. (1956b), Theory of propagation of elastic waves in a fluid-saturated porous solid. high-frequency range, *J. Acoust. Soc. Am.* 28, 179.
- Boutin, C., and J. Auriault (1990), Dynamic behaviour of porous media saturated by viscoelastic fluid. application to bituminous concretes, *Int. J. Eng. Sci.* 28, 1157.
- Burla, R. K., A. V. Kumar, and B. V. Sankar (2009), Implicit boundary method for determination of effective properties of composite microstructures, *Journal of Solid and Structures* 46, 2514,.
- Buxton, G. A., R. Verberg, D. Jasnow, and A. C. Balazs (2005), Newtonian fluid meets an elastic solid: Coupling lattice boltzmann and lattice-spring models, *Phys. Rev. E* 71, 056707.
- Che, H., and M. Nguyen (2014), Amdahl's law for multithreaded multicore processors, *Journal of Parallel and Distributed Computing Volume 74, Issue 10, October 2014, Pages 3056–3069*.

- Christensen, R. (1979), Mechanics of composite materials, *John Wiley & Sons, Inc.*
- Clearly, M. P., I.-W. Chen, and S.-M. Lee (1980), Self-consistent techniques for heterogeneous media., *J. Engng Mech., ASCE 106*, 861-887.
- Cohen, I. (2004), Simple algebraic approximations for the effective elastic moduli of cubic arrays of spheres, *Journal of the Mechanics and Physics of Solids 52 (2004)* 2167-2183.
- Datta, S. K. (1977), Diffraction of a plane elastic waves by ellipsoidal inclusions, *J. Acoust. Soc. Am., 61(6)*, 1432-1437.
- Denny, M. W. (1993), *Air and water : the biology and physics of life's media*, Princeton, N.J. : Princeton University Press.
- d'Humières, D., P. Lallemand, and U. Frisch (1986), Lattice gas models for 3d hydrodynamics, *Europhys. Letters 2*, 291.
- d'Humières, D., I. Ginzburg, M. Krafczyk, P. Lallemand, and L.-S. Luo (2002), Multiple-relaxationtime lattice boltzmann models in three dimensions, *Phil. Trans. R. Soc. Lond. A 360*, 437.
- Ferréol, B., and D. H. Rothman (1995), Lattice-boltzmann simulations of flow through fontainebleau sandstone, *Transport in Porous Media 20: 3-20, 1995. Kluwer Academic Publishers.*
- Fredy, A., and V. Alvarado (2006), Sensitivity analysis of gassmann's fluid substitution equations: Some implications in feasibility studies of time-lapse seismic reservoir monitoring, *Journal of Applied Geophysics 59 (2006)* 47– 62.
- Frisch, U., B. Hasslacher, and Y. Pomeau (1986), Lattice-gas automata for the navier-stokes equation, *Phys. Rev. Lett. 56*, 1505.
- Garboczi, B. D., E.J (1993), Computational materials science of cement-basedmaterials, *Mat. Rrs. Sot. Bull. 18*, 50-54.
- Gassmann, F. (1951), Uber die elastizitat proposer medien, viertel, *Naturforsch. Ges. Zurich 96*, 1-23.
- Ginzbourg, I., and P. M. Adler (1991), Boundary condition analysis for the three dimensional lattice boltzmann model, *J. Phys. II France 4*, 191.
- Ginzburg, I., and D. d'Humières (2003), Multireflection boundary conditions for lattice boltzmann models, *Phys. Rev. E 68*, 066614.
- Gomez, C. T., J. Dvorkin, and T. Vanorio (2010), Laboratory measurements of porosity, permeability, resistivity, and velocity on fontainebleau sandstones, *Geophysics, Vol. 75, No. 6 (november-december 2010); P. E191–E204.*
- Gomez-Rivero, O. (1977), Some considerations about the possible use of the parameters a and m as a formation evaluation tool through well logs, *Trans. SPWLA 18th Ann. Logging Symp., pp. J 1-24.*

- Han, D. (1986), Effects of porosity and clay content on acoustic properties of sandstones and unconsolidated sediments, Ph.D. thesis, University of Stanford.
- Han, D., and M. L. Batzle (2004), Gassmann's equation and fluidsaturation effects on seismic velocities, *GEOPHYSICS*, 69(2), 398–405.
- Han, D., A. Nur, and D. Morgan (1986), Effect of porosity and clay content on wave velocities in sandstones, *Geophysics V51, N11, Nov 1986, P2093–210*.
- Hashin, Z., and S. Shtrikman (1962a), On some variational principles in anisotropic and non homogeneous elasticity, *J. Mech. Phys. Solids 10, 335-342*.
- Hashin, Z., and S. Shtrikman (1962b), On some variational approach to the theory of the elastic behaviour of polycrystal, *J. Mech. Phys. Solids 10, 343-352*.
- Hoang-Duc, H., and G. Bonnet (2012), Effective properties of viscoelastic heterogeneous periodic media: An approximate solution accounting for the distribution of heterogeneities, *Mechanics of Materials Volume 56, January 2013, Pages 71–83*.
- Johnson, D. L., J. Koplik, and L. M. Schwartz (1986), New pore-size parameter characterizing transport in porous media, *Physical Review Letters 57, 2564*.
- Juan, C. L. J. G., E. S (2006), On the static and dynamic behavior of fluid saturated composite porous solids: A homogenization approach, *International Journal of Solids and Structures 43 (2006) 1224–1238*.
- Junk, M., and Z. Yang (2009), Convergence of lattice boltzmann methods for navier-stokes flows in periodic and bounded domains, *Numer. Math. 112, 65*.
- Krief, G. J. S. J. V. J., M. (1990), A petrophysical interpretation using the velocities of p and s waves (full waveform sonic), *The Log Analyst, 31:355-369*.
- Ladd, A. J. C., and R. Verberg (2001), Lattice-boltzmann simulations of particle-fluid suspensions, *J. Stat. Phys. 104, 1191*.
- Ladd, A. J. C., J. H. Kinney, and T. M. Breunig (1997a), Deformation and failure in cellular materials, *Phys. Rev. E 55, 3271*.
- Ladd, A. J. C., J. H. Kinney, and T. M. Breunig (1997b), Elastic constants of cellular structures, *Physica A 240, 349*.
- Landau, L. D., and E. M. Lifshitz (1986), Theory of elasticity, *Pergamon Press, New York*.
- Li, X.-Y. (2010), Propagation des ondes acoustiques dans les milieux hétérogènes, Ph.D. thesis, Université Pierre et Marie Curie.
- Luo, L.-S. (2000), Theory of the lattice boltzmann method: Lattice boltzmann models for non ideal gases, *Phys. Rev. E 62, 4982*.
- Malinouskaya, I. (2007), Propagation des ondes acoustiques dans les milieux hétérogènes, Ph.D. thesis, Université Pierre et Marie Curie.

- Nemat-Nasser, S., and H. M. Iwakuma, T. (1982), On composite with periodic structure, *Mech. Mater. 1*, 239-267.
- Nguyen, K. T. (2013), Direct samples, Ph.D. thesis, Université Pierre et Marie Curie.
- Nguyen, N.-Q., and A. J. C. Ladd (2002), Lubrication corrections for lattice-boltzmann simulations of particle suspensions, *Phys. Rev. E 66*, 046708.
- Nie, X., Y. H. Qian, G. Doolen, and S. Chen (1998), Lattice boltzmann simulation of the two-dimensional rayleigh-taylor instability, *Phys. Rev. E 58*, 6861.
- Nur, A., D. Marion, and Y. H. (1991), Wave velocities in sediments, In J. Hovem, M. D. Richardson, and R. D. Stoll, editors, *Shear Waves in Marine sediments*, pages 131-140. Kluwer Academic, Dordrecht.
- Nur, A., G. Mavko, J. Dvorkin, and D. Galmundi (1995), Critical porosity: the key to relating physical properties to porosity in rocks, In *Proc. 65th Ann Int. Meeting Soc. Expl. Geophys.*, page 878.
- O'Brien, G. S., and C. J. Bean. (2004), A discrete numerical method for modeling volcanic earthquake source mechanisms, *J. Geophys. Res. 109*, B09301.
- Ostoja, M. S. (2002), Lattice models in micromechanics, *Appl. Mech. Rev.*55,35.
- Pan, C., L.-S. Luo, and T. M. Cass (2006), An evaluation of lattice boltzmann schemes for porous medium ow simulation, *Computers and Fluids 35*, 898.
- Pazdniakou, A. (2012), Lattice model in porous media studies, Ph.D. thesis, Université Pierre et Marie Curie.
- Pazdniakou, A., and P. M. Adler (2013), Dynamic permeability of porous media by the lattice boltzmann method, *Advances in Water Resources 62* (2013) 292–302.
- Poutet, J., D. Manzoni, F. Hage-Chahade, C. J. Jacquin, M. Bouteca, J.-F. Thovert, and P. M. Adler (1996), The effective mechanical properties of random porous media, *J.Mech. Phys. Solid*, Vol.44, No.10, Elsevier Science Ltd.
- Raymer, L. L., E. R. Hunt, and J. S. Gardner (1980), An improved sonic transit time to porosity transform, In *Trans. Soc. Prof. Well Log Analysts, 21st annual logging symposium*, page Paper P.
- Roberts, A. P., and E. J. Garboczi (2000), Elastic properties of model porous ceramics, *J. Amer. Ceramic Society*, 83(12):3041-3048.
- Roberts, G. E. J., A P. (2002), Computation of the linear elastic properties of random porous materials with a wide variety of microstructure, *Proc. R. Soc. London, Ser. A*, 458, 1033-1054.
- Saenger, E. H., N. Gold, and S. A. Shapiro (1977), Diffraction of a plane elastic waves by ellipsoidal inclusions, *J. Acoust. Soc. Am.*, 61(6), 1432-1437.
- Sanchez, P. E. (1980), Non homogeneous media and vibration theory, *Springer-Verlag, Berlin*.

- Thovert, J. F., F. Wary, and P. M. Adler (1990), Thermal conductivity of random media and regular fractals, *Journal of Applied Physics* 68, 3872.
- Torquato, S. (1998), Effective stiffness tensor of composite media: II. application to isotropic dispersion, *J. Mech. Phys. Solids* 46, 1441-1440.
- Torquato, S. (2000), Modeling of physical properties of composite materials, *International Journal of Solids and Structures* 37 (2000) 411-422.
- Valfouskaya, A., P. M. Adler, J.-F. Thovert, and M. Fleury (2005), Nuclear-magnetic-resonance diffusion simulations in porous media, *Journal of applied physics* 97, 083510.
- Wall, P. (1997), A comparison of homogenization, hashin-shtrikman bounds and the halpin-tsai equations, *Applications of Mathematics*. August 1997, Volume 42, Issue 4, pp 245-257.
- Wang, J. (1989), The bond-bending model in three dimensions, *J. Phys. A: Math. Gen.* 22, L291.
- Worthington, P. F. (1993), The uses and abuses of the archie equations, 1: The formation factor-porosity relationship, *Journal of Applied Geophysics* Volume 30, Issue 3, May 1993, Pages 215-228.
- Wu, J., and C. K. Aidun (2009), Simulating 3d deformable particle suspensions using lattice boltzmann method with discrete external boundary force, *Int. J. Numer. Meth. Fluids*.
- Zanetti, G. (1989), Hydrodynamics of lattice-gas automata, *Phys. Rev. A* 40, 1539.
- Zhao, G. F., J. Fang, and J. Zhao (2010), 3d distinct lattice spring model for elasticity and dynamic failure, *International journal for numerical and analytical methods in geomechanics*.
- Zhou, M.-Y., and P. Sheng (1989), First-principles calculations of dynamic permeability in porous media, *Phys. Rev. B* 39, 12017.

Appendix A

APPENDIX

A.1 Spring constants in the LSM2S model

In the basic LSM, each spring can belong to several elastic elements. Therefore, the force constant of springs is equal to the sum of spring constants of all neighbouring elastic elements containing this spring.

There are two types of linear springs in the lattice: $[1\ 0\ 0]$ type and $[1\ 1\ 0]$ type. One linear spring of $[1\ 0\ 0]$ type can belong to at most four neighbour elements; one linear spring of $[1\ 1\ 0]$ type can belong to at most two neighbour elements. As in the basic LSM, linear spring constants are multiplied by the number of elastic elements the spring belongs to. For one $[1\ 0\ 0]$ linear spring, its constant is equal to $\frac{\alpha_2}{4}$, $\frac{\alpha_2}{2}$, $\frac{3\alpha_2}{4}$, α_2 , if it belongs to one, two, three or four elastic elements of type 2 (Fig. A.1a-d). For one $[1\ 1\ 0]$ linear spring, if it belongs to one elastic element of type 2 (Fig. A.1e), its constant is $\frac{\alpha_2}{2}$; if it belongs to two elastic elements (Fig. A.1f), the constant is α_2 . This calculation is done in the same way for the elements of type 0 (for the inclusion); the elastic constant of linear springs in this case has 4 values: $\frac{\alpha_0}{4}$, $\frac{\alpha_0}{2}$, $\frac{3\alpha_0}{4}$, α_0 .

As mentioned above, in an elastic element, there are two types of angular springs: $\frac{\pi}{3}$ -angular spring and $\frac{\pi}{4}$ -angular spring; the junction of two elastic elements side by side does not create any new angular spring. A $\frac{\pi}{3}$ -angular spring can belong to only one elastic element while a $\frac{\pi}{4}$ -angular spring can belong to at most two elastic elements. When springs only belong to elements of type 2 (matrix), the $\frac{\pi}{3}$ -angular spring constant is equal to β_2 (Fig. A.2a); the $\frac{\pi}{4}$ -angular spring constant is equal to $\frac{\beta_2}{2}$ if it belongs to one element (Fig. A.2b), and equal to β_2 if it belongs to two elements

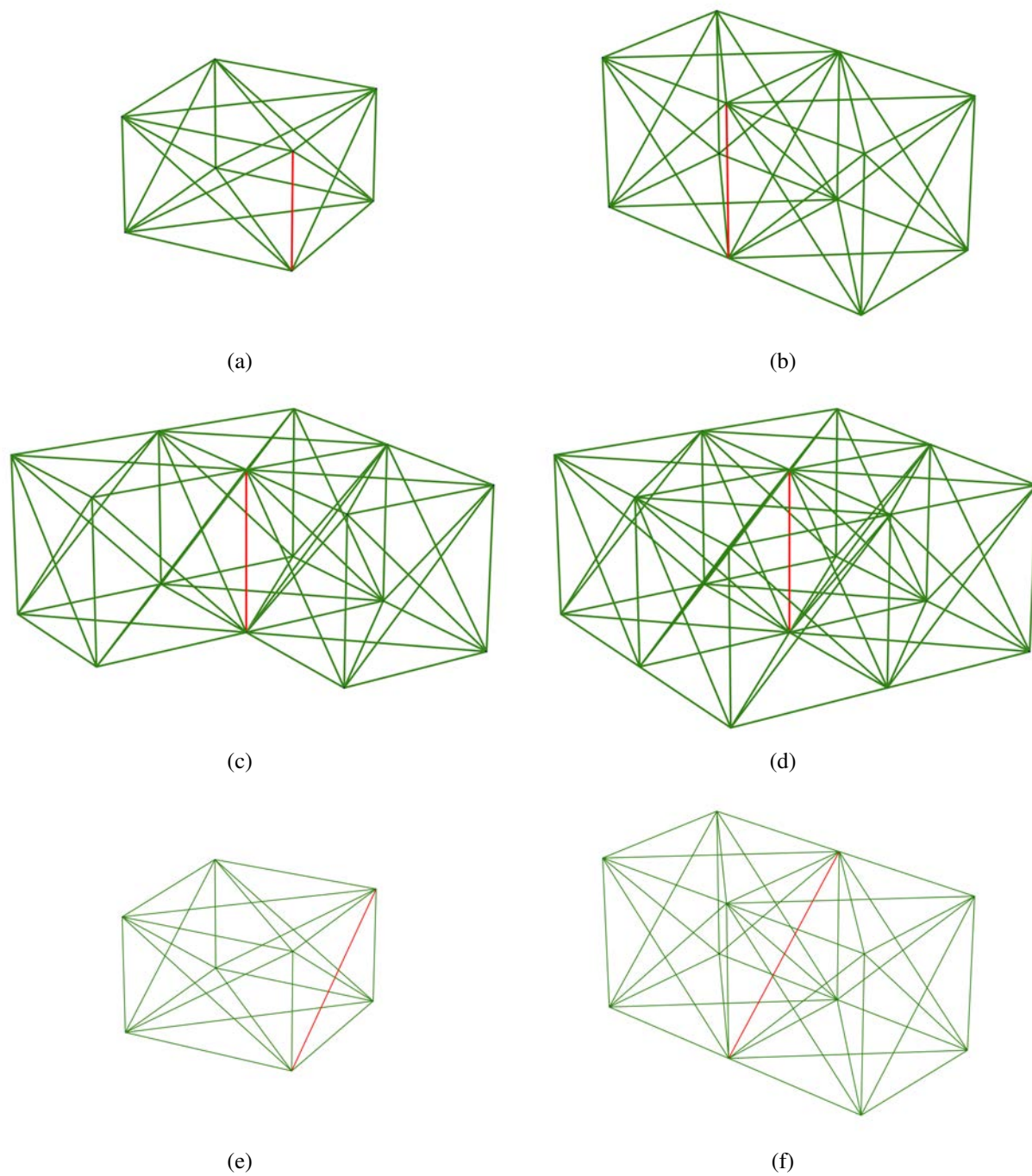


Figure A.1: The $[1\ 0\ 0]$ and $[1\ 1\ 0]$ linear springs with the elastic elements of type 2.

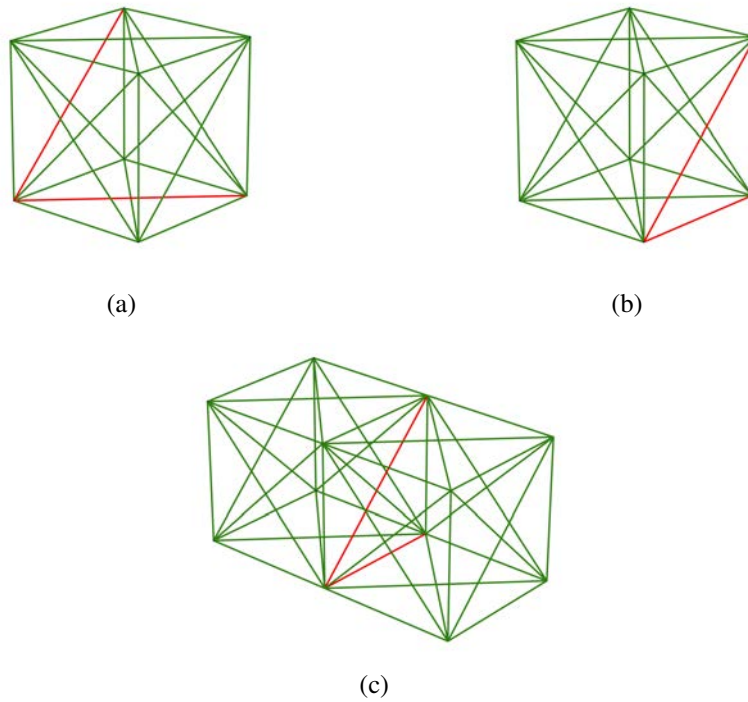


Figure A.2: The angular springs with the elastic elements of type 2.

(Fig. A.2c). The same holds for springs which only belong to elements of type 0 (inclusion); the angular spring constant is equal to β_0 or $\frac{\beta_0}{2}$.

The difference between LSM2S and LSM is due to the interfaces matrix - inclusion and solids - pores. Now, we consider springs which belong to two types of elastic elements.

If one $[1\ 0\ 0]$ linear spring belongs to one element of type 2 and one element of type 0 (Fig. A.3a), its constant is equal to $\frac{\alpha_0 + \alpha_2}{4}$; if it belongs to one element of type 2 and two elements type 0 (Fig. A.3b), the constant is $\frac{2\alpha_0 + \alpha_2}{4}$; if it belongs to one element of type 2 and three elements of type 0 (Fig. A.3c), the constant is $\frac{3\alpha_0 + \alpha_2}{4}$; if it belongs to two elements of type 2 and one element of type 0 (Fig. A.3d), the constant is $\frac{\alpha_0 + 2\alpha_2}{4}$; if it belongs to three elements of type 2 and one element of type 0 (Fig. A.3e), the constant is $\frac{\alpha_0 + 3\alpha_2}{4}$ and if it belongs to two elements of type 2 and two elements of type 0 (Fig. A.3f), the constant is $\frac{\alpha_0 + \alpha_2}{2}$.

For one $[1\ 1\ 0]$ linear spring (see Fig. A.3g), its elastic constant is equal to $\frac{\alpha_0 + \alpha_2}{2}$. An angular spring which belongs to one element of type 2 and one element of type 0 (Fig. A.3h) has a constant equal to $\frac{\beta_0 + \beta_2}{2}$.

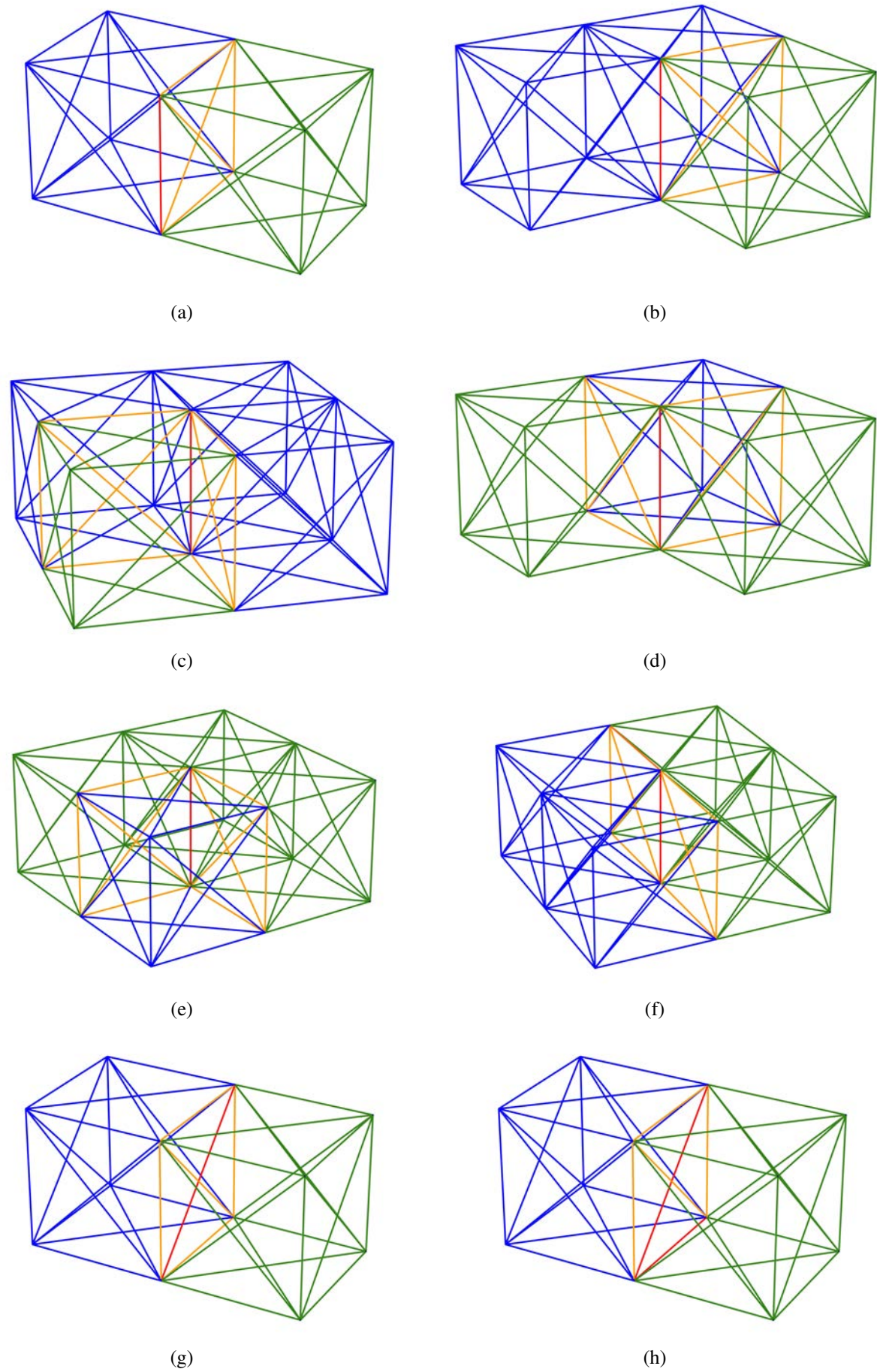


Figure A.3: The linear and angular springs which belong to two types of elastic elements.

A.2 The coarsening method

This is the second method proposed to calculate the acoustic properties of the Fontainebleau samples. The idea is to create smaller samples than the original one and to calculate them. The results for the original sample are obtained by extrapolation. As an example, a solid with different physical properties (A.1) is used and then compared to quartz by correction functions.

A.2.1 Coarsening of samples

Method

In order to make faster calculations, N_c is reduced by a factor 2 with respect to the real sample size. For this purpose, the coarsening method combines 8 elementary cubes which are neighbours into a new large elementary cube of size $2a$ as shown in Fig.A.4. The nature (solid or pore corresponding to 0 or 1) of the new large cube is chosen according to the majority rule.

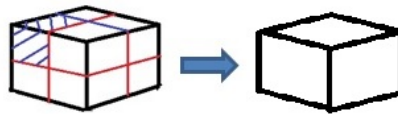


Figure A.4: The coarsening method.

The coarsened samples

The Fontainebleau samples are coarsened into $(240)^3$, $(120)^3$, and $(60)^3$ elementary cubes of size $a = 11.4 \mu m$, $22.8 \mu m$ and $45.6 \mu m$, respectively. The original and the coarsened samples FB22 are displayed in Fig.A.5. The calculations are done for the coarsened samples and the results for the original sample are obtained by extrapolation.

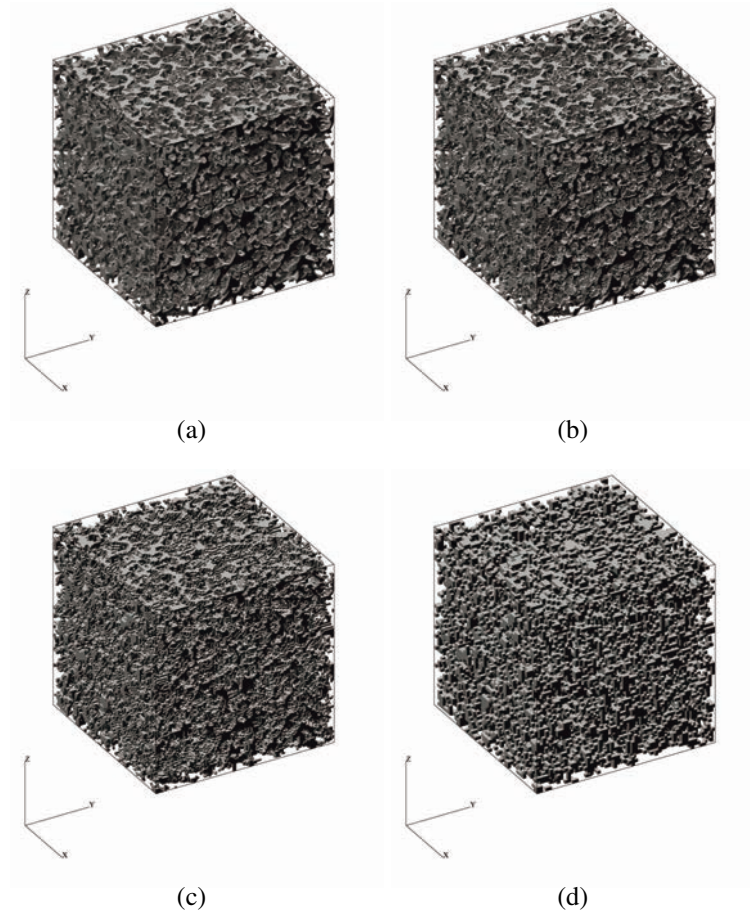


Figure A.5: The coarsened samples of FB22. (a) The original sample with $N_c=480$. (b) The sample with $N_c=240$. (c) The sample with $N_c=120$. (d) The sample with $N_c = 60$.

A.2.2 Numerical results

The input elastic properties of the solid used in simulations are the Young modulus $E_{s,nu}$ and the Poisson ratio $\nu_{s,nu}$ given by

$$E_s = 36GPa \quad \nu_s = 0.12 \quad (\text{A.1})$$

The coarsened samples FB22 are calculated first. The effective stiffness tensor of each sample is determined by 6 simulations with LSM. For the coarsened sample of size $60 \times 60 \times 60$, the computation time is about 2 days with a computer with 8 processors and the required memory is 0.352 Gb for each simulation. These quantities are about 8 times larger when N_c is doubled. The stiffness tensors and the acoustic velocities of these three coarsened samples are gathered and

compared in Table A.1.

$$\mathbf{C}_{60}^{(eff)} = \begin{pmatrix} 25.23 & 3.47 & 3.48 & 0 & 0 & 0 \\ 3.47 & 25.35 & 3.48 & 0 & 0 & 0 \\ 3.48 & 3.48 & 25.35 & 0 & 0 & 0 \\ 0 & 0 & 0 & 10.75 & 0 & 0 \\ 0 & 0 & 0 & 0 & 10.71 & 0 \\ 0 & 0 & 0 & 0 & 0 & 10.72 \end{pmatrix} \quad \mathbf{C}_{120}^{(eff)} = \begin{pmatrix} 21.98 & 3.29 & 3.31 & 0 & 0 & 0 \\ 3.29 & 22.01 & 3.31 & 0 & 0 & 0 \\ 3.31 & 3.31 & 22.11 & 0 & 0 & 0 \\ 0 & 0 & 0 & 9.35 & 0 & 0 \\ 0 & 0 & 0 & 0 & 9.31 & 0 \\ 0 & 0 & 0 & 0 & 0 & 9.34 \end{pmatrix}$$

$$\mathbf{C}_{240}^{(eff)} = \begin{pmatrix} 19.36 & 3.30 & 3.05 & 0 & 0 & 0 \\ 3.30 & 19.39 & 3.06 & 0 & 0 & 0 \\ 3.05 & 3.06 & 19.51 & 0 & 0 & 0 \\ 0 & 0 & 0 & 8.20 & 0 & 0 \\ 0 & 0 & 0 & 0 & 8.17 & 0 \\ 0 & 0 & 0 & 0 & 0 & 8.20 \end{pmatrix}$$

Size	x-axis		y-axis		z-axis		Errors	
	v_p^X (km/s)	v_s^X (km/s)	v_p^Y (km/s)	v_s^Y (km/s)	v_p^Z (km/s)	v_s^Z (km/s)	v_p %	v_s %
60 x 60 x 60	3.48	2.27	3.48	2.27	3.48	2.26	0.26	0.18
120 x 120 x 120	3.24	2.12	3.25	2.12	3.25	2.11	0.31	0.19
240 x 240 x 240	3.05	1.98	3.05	1.98	3.06	1.98	0.39	0.2

Table A.1: The effective stiffness tensors (GPa) and the acoustic velocities (km/s) along the three directions of the coarsened samples FB22 with $N_c = 60$, $N_c = 120$ and $N_c = 240$.

Extrapolation to the original size

The extrapolation of the larger samples is performed with linear approximation functions. The best fits and their correlation coefficient r are calculated. Then, the acoustic velocities in the original sample FB22 and the sample with an infinite discretization are also derived and given in Table A.2.

Velocities	linear function	r	$N_c = 480$	$N_c = \infty$
v_p^X	$33.4468/N_c + 2.9294$	0.9890	3.0	2.93
v_p^Y	$22.2093/N_c + 1.9602$	0.9882	3.0	2.93
v_p^Z	$33.9357/N_c + 2.9289$	0.9901	3.01	2.94
v_s^X	$22.1056/N_c + 1.9053$	0.9871	1.95	1.91
v_s^Y	$33.1982/N_c + 2.9419$	0.9891	1.95	1.91
v_s^Z	$22.2292/N_c + 1.9017$	0.9880	1.95	1.90

Table A.2: The best fits and their correlation coefficients for acoustic velocities in the sample FB22.

Accuracy of extrapolation function

In order to estimate the accuracy of this function, a simulation which calculates the compressional wave velocity along the x-direction of the original sample FB22 ($N_c = 480$) is performed. The simple stretching along the x-direction is simulated and yields C_{xxxx} . The result is equal to 18.3012 GPa. The compressional wave velocity along the x-direction is derived as $v_X^p = 2.96 \text{ km/s}$. Recall that the predicted value is $v_{prediction}^p = 3.00 \text{ km/s}$; therefore, the extrapolation method provides reliable results since the error is only about 1.3%.

The same procedure is repeated for the other samples FB18, FB13 and FB8. The acoustic velocities along the three directions in the original samples and the infinite discretization samples are given in Table A.3. As can be seen, the difference of the results between the three directions is very small (less than 1%); this shows that these samples can be considered as isotropic (as in Section 4.2).

Velocities (km/s)	Sample FB18		Sample FB13		Sample FB8	
	$N_c = 480$	$N_c = \infty$	$N_c = 480$	$N_c = \infty$	$N_c = 480$	$N_c = \infty$
v_p^X	3.10	3.05	3.32	3.27	3.50	3.48
v_p^Y	3.10	3.05	3.33	3.28	3.50	3.47
v_p^Z	3.10	3.05	3.33	3.28	3.50	3.47
v_s^X	2.02	1.98	2.17	2.14	2.29	2.27
v_s^Y	2.02	1.98	2.17	2.14	2.29	2.27
v_s^Z	2.02	1.98	2.17	2.14	2.29	2.27

Table A.3: Acoustic velocities in the samples FB18, FB13 and FB8 for the original size and the infinite discretization.

A.2.3 Correction of the solid properties

The input elastic properties of the solid ($E_{s,nu}$, $\nu_{s,nu}$) used in this method are given in (A.1). The values used in the direct simulations and in *Han* (1986) and *Arns* (1996) ($E_{s,H}$, $\nu_{s,H}$) for the quartz are given in (4.2). The corresponding Young modulus $E_{s,H}$ and the Poisson ratio $\nu_{s,H}$ are derived as

$$E_{s,H} = 94.5GPa \quad \nu_{s,H} = 0.0742 \quad (A.2)$$

Due to the difference between these input parameters, our simulations cannot be compared directly with the direct simulations (Section 4.3) or with *Han* (1986) and *Arns* (1996). If it is supposed that the Poisson ratio plays a minor role, three correction coefficients can be introduced

$$\eta_1 = \sqrt{\frac{E_{s,H}}{E_{s,nu}}} = 1.62; \quad \eta_2 = \frac{\nu_{s,H}}{\nu_{s,nu}} = 0.6183; \quad \eta_3 = \frac{K_{s,H}}{K_{s,nu}} = 2.3434 \quad (A.3)$$

The acoustic velocities were corrected by multiplying with η_1 and then compared with the direct simulation method in Table A.6 and with *Han* (1986) in Table 4.3. The results are summarized in Figure A.6. The macroscopic Poisson ratio is corrected by the factor η_2 , while the bulk modulus is multiplied by η_3 . The corrected results are compared with the experiments and *Arns'* results in Tables A.4 and A.5.

Sample	Porosity	$\nu_{m,nu}$	$\eta_2 \cdot \nu_{m,nu}$	$\nu_{m,A}$	Error	Direct simulations	Error
				<i>Arns</i> (1996)	%		%
FB8	0.08	0.12659	0.0783	0.0827	5.3	0.0872	5.3
FB13	0.129	0.1303	0.0806	0.0907	11.0	0.0961	16.1
FB18	0.177	0.13603	0.0841	0.1007	16.4	0.1034	18.6
FB22	0.21	0.1389	0.0859	0.1084	20.7	0.1089	21.1

Table A.4: The macroscopic Poisson ratio: comparison between the numerical macroscopic values $\eta_2 \nu_{m,nu}$ and Arns' results $\nu_{m,A}$ *Arns* (1996).

Sample	$\eta_3 \cdot K_{m,nu}$	IOS model	$K_{m,A}$	Error	Direct simulations	Error
		<i>Arns</i> (1996)	<i>Krief</i> (1990)	%		%
FB8	29.85	29.23	28.19	2.0	30.03	0.6
FB13	25.80	25.14	22.99	2.6	25.98	0.7
FB18	21.49	20.85	18.19	2.9	21.71	1.0
FB22	19.46	18.74	15.12	3.8	19.62	0.8

Table A.5: The macroscopic bulk modulus: comparison between the numerical, Arns results (IOS) and the empirical results (*Arns*, 1996; *Krief*, 1990).

Sample	Porosity	Celerities	Numerical v_0	$\eta_1 \cdot v_0$	Direct simulation (exact properties)	Error (%)
			(km/s)	(km/s)		
FB8	0.083	v_X^p	3.50	5.68	5.59	1.6
		v_X^s	2.29	3.7	3.74	1.1
FB13	0.129	v_X^p	3.32	5.37	5.28	1.7
		v_X^s	2.17	3.51	3.54	0.9
FB18	0.177	v_X^p	3.10	5.03	4.80	4.6
		v_X^s	2.02	3.27	3.20	2.1
FB22	0.21	v_X^p	3.0	4.85	4.76	1.9
		v_X^s	1.95	3.16	3.16	0

Table A.6: Comparison of the acoustic velocities in dry Fontainebleau samples between the two calculations ways.

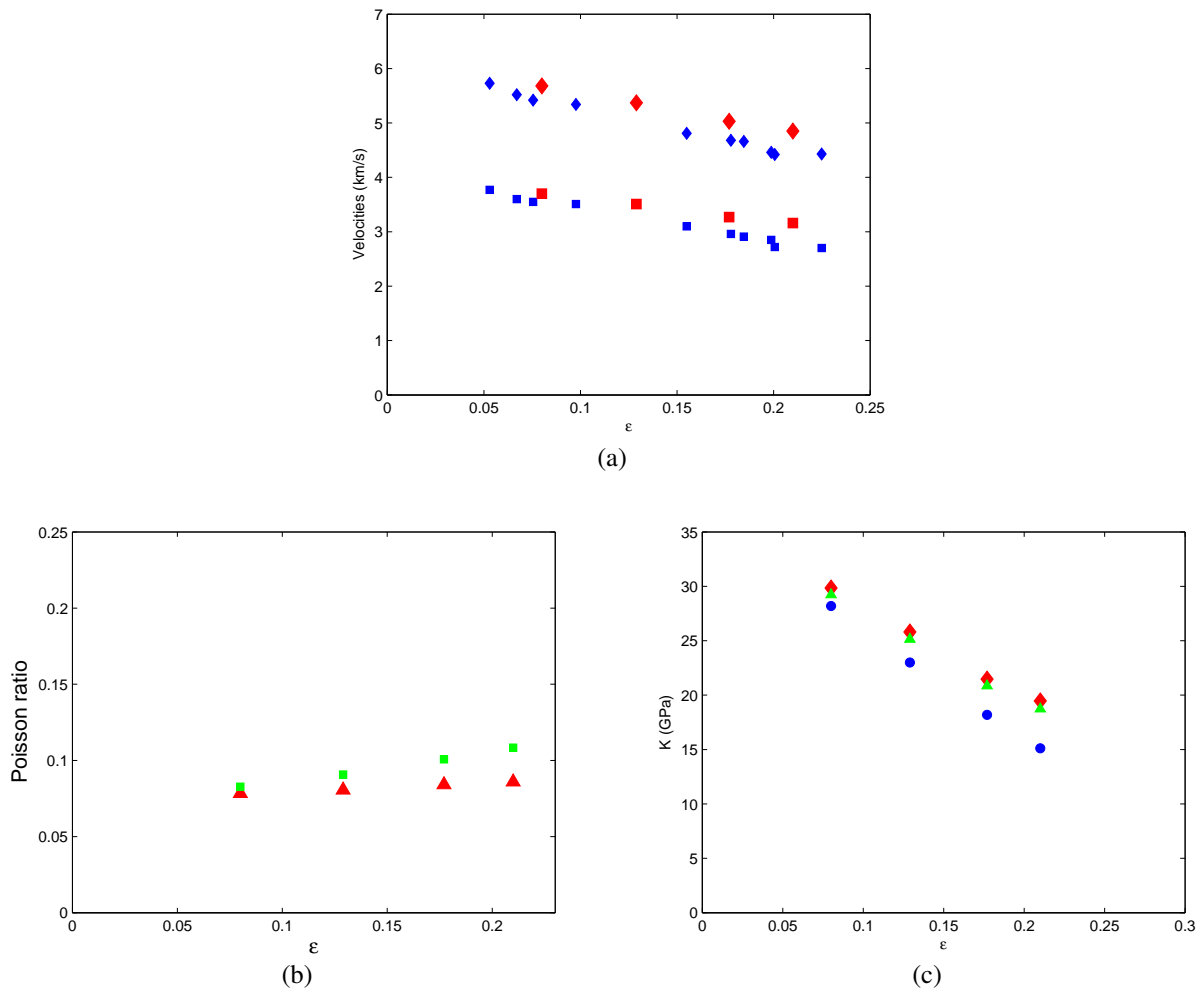


Figure A.6: Comparisons between the present simulation results and *Han* (1986), *Arns* (1996). (a) Acoustic velocities; (b) Macroscopic Poisson ratio; (c) Macroscopic bulk modulus. Data are for: numerical results (red), *Han* (1986) (blue) and *Arns* (1996) (green).

A.3 Acoustic velocities in saturated Fontainebleau samples.

ω	Original $N_{cx}=240$						Mirror $N_{cx}=480$					
	$C_f = 0$		$C_f = 4.6$		$C_f = 100$		$C_f = 0$		$C_f = 4.6$		$C_f = 100$	
	C_r	C_i	C_r	C_i	C_r	C_i	C_r	C_i	C_r	C_i	C_r	C_i
0.05	5.95	1.8e-11	4.754	9.4e-12	4.671	1.4e-11	5.95	1.9e-11	4.754	1.0e-11	4.671	1.5e-11
0.025	5.95	3.2e-11	4.754	1.7e-11	4.671	2.4e-11	5.95	3.4e-11	4.754	1.8e-11	4.671	2.6e-11
0.01	5.95	7.7e-11	4.754	4.0e-11	4.671	5.8e-11	5.95	7.9e-11	4.754	4.1e-11	4.671	6.0e-11
0.005	5.95	8.8e-11	4.754	4.6e-11	4.671	6.7e-11	5.95	9.6e-11	4.754	5.0e-11	4.671	7.3e-11
0.0025	5.95	9.2e-11	4.754	4.8e-11	4.671	7.0e-11	5.95	9.9e-11	4.754	5.1e-11	4.671	7.6e-11
0.001	5.95	6.8e-11	4.754	3.5e-11	4.671	5.2e-11	5.95	7.5e-11	4.754	3.9e-11	4.671	5.7e-11
0.0005	5.95	4.2e-11	4.754	2.2e-11	4.671	3.2e-11	5.95	4.7e-11	4.754	2.4e-11	4.671	3.6e-11
0.00025	5.95	2.3e-11	4.754	1.2e-11	4.671	1.7e-11	5.95	2.6e-11	4.754	1.3e-11	4.671	1.9e-11
0.0001	5.95	9.3e-12	4.754	4.8e-12	4.671	7.1e-12	5.95	1.1e-11	4.754	5.5e-12	4.671	8.0e-12
5e-05	5.95	4.7e-12	4.754	2.4e-12	4.671	3.6e-12	5.95	5.3e-12	4.754	2.7e-12	4.671	4.0e-12
2.5e-05	5.95	2.3e-12	4.754	1.2e-12	4.671	1.8e-12	5.95	2.6e-12	4.754	1.4e-12	4.671	2.0e-12

Table A.7: The fast compressional wave velocities in the original and mirror configurations of the coarsened sample FB22 ($N_c=240$) saturated by the three types of fluids.

ω	Original $N_{cx} = 240$						Mirror $N_{cx} = 480$					
	$C_f = 0$		$C_f = 4.6$		$C_f = 100$		$C_f = 0$		$C_f = 4.6$		$C_f = 100$	
	C_r	C_i	C_r	C_i	C_r	C_i	C_r	C_i	C_r	C_i	C_r	C_i
0.05	1.27e-04	5.38e-06	3.91e-05	1.66e-06	8.79e-06	3.72e-07	1.32e-04	5.49e-06	4.06e-05	1.69e-06	9.14e-06	3.80e-07
0.025	1.27e-04	9.52e-06	3.91e-05	2.93e-06	8.80e-06	6.58e-07	1.32e-04	9.68e-06	4.07e-05	2.98e-06	9.15e-06	6.69e-07
0.01	1.17e-04	2.47e-05	3.61e-05	7.59e-06	8.12e-06	1.71e-06	1.23e-04	2.41e-05	3.79e-05	7.41e-06	8.53e-06	1.67e-06
0.005	1.09e-04	3.07e-05	3.35e-05	9.44e-06	7.54e-06	2.12e-06	1.14e-04	3.17e-05	3.51e-05	9.74e-06	7.90e-06	2.19e-06
0.0025	9.28e-05	3.74e-05	2.85e-05	1.15e-05	6.42e-06	2.59e-06	9.76e-05	3.85e-05	3.00e-05	1.18e-05	6.75e-06	2.66e-06
0.001	6.53e-05	3.93e-05	2.01e-05	1.21e-05	4.51e-06	2.72e-06	6.92e-05	4.09e-05	2.13e-05	1.26e-05	4.79e-06	2.83e-06
0.0005	4.60e-05	3.45e-05	1.42e-05	1.06e-05	3.18e-06	2.38e-06	4.90e-05	3.62e-05	1.51e-05	1.11e-05	3.39e-06	2.50e-06
0.00025	3.16e-05	2.71e-05	9.72e-06	8.34e-06	2.19e-06	1.88e-06	3.37e-05	2.87e-05	1.04e-05	8.82e-06	2.33e-06	1.98e-06
0.0001	1.94e-05	1.82e-05	5.95e-06	5.59e-06	1.34e-06	1.26e-06	2.06e-05	1.93e-05	6.35e-06	5.94e-06	1.43e-06	1.34e-06
5e-05	1.35e-05	1.31e-05	4.15e-06	4.02e-06	9.34e-07	9.05e-07	1.44e-05	1.39e-05	4.42e-06	4.28e-06	9.95e-07	9.62e-07
2.5e-05	9.48e-06	9.33e-06	2.92e-06	2.87e-06	6.56e-07	6.45e-07	1.01e-05	9.92e-06	3.10e-06	3.05e-06	6.98e-07	6.86e-07

Table A.8: The slow compressional wave velocities of the coarsened sample FB22 ($N_c = 240$) saturated by the three types of fluids.

ω	Original $N_{cx} = 240$						Mirror $N_{cx} = 480$					
	$C_f = 0$		$C_f = 4.6$		$C_f = 100$		$C_f = 0$		$C_f = 4.6$		$C_f = 100$	
	C_r	C_i	C_r	C_i	C_r	C_i	C_r	C_i	C_r	C_i	C_r	C_i
0.05	3.105	9.3e-12	3.105	9.3e-12	3.105	9.3e-12	3.105	9.9e-12	3.105	9.9e-12	3.105	9.9e-12
0.025	3.105	1.7e-11	3.105	1.7e-11	3.105	1.7e-11	3.105	1.7e-11	3.105	1.7e-11	3.105	1.7e-11
0.01	3.105	4.0e-11	3.105	4.0e-11	3.105	4.0e-11	3.105	4.1e-11	3.105	4.1e-11	3.105	4.1e-11
0.005	3.105	4.6e-11	3.105	4.6e-11	3.105	4.6e-11	3.105	4.9e-11	3.105	4.9e-11	3.105	4.9e-11
0.0025	3.105	4.7e-11	3.105	4.7e-11	3.105	4.7e-11	3.105	5.1e-11	3.105	5.1e-11	3.105	5.1e-11
0.001	3.105	3.5e-11	3.105	3.5e-11	3.105	3.5e-11	3.105	3.9e-11	3.105	3.9e-11	3.105	3.9e-11
0.0005	3.105	2.2e-11	3.105	2.2e-11	3.105	2.2e-11	3.105	2.4e-11	3.105	2.4e-11	3.105	2.4e-11
0.00025	3.105	1.2e-11	3.105	1.2e-11	3.105	1.2e-11	3.105	1.3e-11	3.105	1.3e-11	3.105	1.3e-11
0.0001	3.105	4.8e-12	3.105	4.8e-12	3.105	4.8e-12	3.105	5.4e-12	3.105	5.4e-12	3.105	5.4e-12
5e-05	3.105	2.4e-12	3.105	2.4e-12	3.105	2.4e-12	3.105	2.7e-12	3.105	2.7e-12	3.105	2.7e-12
2.5e-05	3.105	1.2e-12	3.105	1.2e-12	3.105	1.2e-12	3.105	1.4e-12	3.105	1.4e-12	3.105	1.4e-12

Table A.9: The shear wave velocities in the original and mirror configurations of the coarsened sample FB22 ($N_c = 240$) saturated by the three types of fluids.

ω	Original $N_{cx} = 480$						Mirror $N_{cx} = 960$					
	$C_f = 0$		$C_f = 4.6$		$C_f = 100$		$C_f = 0$		$C_f = 4.6$		$C_f = 100$	
	C_r	C_i	C_r	C_i	C_r	C_i	C_r	C_i	C_r	C_i	C_r	C_i
0.05	5.78	1.1e-11	4.657	1.1e-11	4.543	1.7e-11	5.78	7.6e-12	4.657	7.5e-12	4.543	1.2e-11
0.025	5.78	1.1e-11	4.657	1.0e-11	4.543	1.7e-11	5.78	1.1e-11	4.657	1.1e-11	4.543	1.7e-11
0.01	5.78	4.0e-11	4.657	3.9e-11	4.543	6.3e-11	5.78	4.1e-11	4.657	4.0e-11	4.543	6.4e-11
0.005	5.78	3.9e-11	4.657	3.8e-11	4.543	6.0e-11	5.78	3.9e-11	4.657	3.8e-11	4.543	6.1e-11
0.0025	5.78	4.7e-11	4.657	4.6e-11	4.543	7.4e-11	5.78	5.0e-11	4.657	4.9e-11	4.543	7.7e-11
0.001	5.78	5.6e-11	4.657	5.5e-11	4.543	8.7e-11	5.78	5.9e-11	4.657	5.8e-11	4.543	9.3e-11
0.0005	5.78	5.2e-11	4.657	5.1e-11	4.543	8.2e-11	5.78	5.7e-11	4.657	5.6e-11	4.543	8.8e-11
0.00025	5.78	4.0e-11	4.657	3.9e-11	4.543	6.2e-11	5.78	4.4e-11	4.657	4.3e-11	4.543	6.9e-11
0.0001	5.78	2.1e-11	4.657	2.0e-11	4.543	3.2e-11	5.78	2.3e-11	4.657	2.3e-11	4.543	3.6e-11
5e-05	5.78	1.1e-11	4.657	1.1e-11	4.543	1.7e-11	5.78	1.2e-11	4.657	1.2e-11	4.543	1.9e-11
2.5e-05	5.78	5.5e-12	4.657	5.4e-12	4.543	8.6e-12	5.78	6.3e-12	4.657	6.2e-12	4.543	9.8e-12

Table A.10: The fast compressional wave velocities in the original and mirror configurations of the coarsened sample FB22 ($N_c = 480$) saturated by the three types of fluids.

ω	Original $N_{cx} = 480$						Mirror $N_{cx} = 960$					
	$C_f = 0$		$C_f = 4.6$		$C_f = 100$		$C_f = 0$		$C_f = 4.6$		$C_f = 100$	
	C_r	C_i	C_r	C_i	C_r	C_i	C_r	C_i	C_r	C_i	C_r	C_i
0.05	1.26e-04	4.67e-06	4.58e-05	1.70e-06	1.05e-05	3.90e-07	1.31e-04	3.18e-06	4.76e-05	1.16e-06	1.09e-05	2.66e-07
0.025	1.27e-04	4.55e-06	4.64e-05	1.66e-06	1.06e-05	3.81e-07	1.32e-04	4.53e-06	4.81e-05	1.65e-06	1.10e-05	3.78e-07
0.01	1.20e-04	1.84e-05	4.36e-05	6.69e-06	1.00e-05	1.54e-06	1.24e-04	1.79e-05	4.52e-05	6.53e-06	1.04e-05	1.50e-06
0.005	1.19e-04	1.78e-05	4.33e-05	6.47e-06	9.93e-06	1.49e-06	1.24e-04	1.72e-05	4.52e-05	6.26e-06	1.04e-05	1.44e-06
0.0025	1.13e-04	2.30e-05	4.10e-05	8.36e-06	9.41e-06	1.92e-06	1.18e-04	2.31e-05	4.28e-05	8.41e-06	9.83e-06	1.93e-06
0.001	9.67e-05	3.15e-05	3.52e-05	1.15e-05	8.08e-06	2.64e-06	1.01e-04	3.20e-05	3.69e-05	1.17e-05	8.48e-06	2.68e-06
0.0005	7.94e-05	3.60e-05	2.89e-05	1.31e-05	6.64e-06	3.01e-06	8.39e-05	3.69e-05	3.06e-05	1.35e-05	7.02e-06	3.09e-06
0.00025	6.01e-05	3.62e-05	2.19e-05	1.32e-05	5.03e-06	3.03e-06	6.40e-05	3.76e-05	2.33e-05	1.37e-05	5.35e-06	3.14e-06
0.0001	3.78e-05	2.97e-05	1.38e-05	1.08e-05	3.16e-06	2.48e-06	4.04e-05	3.13e-05	1.47e-05	1.14e-05	3.38e-06	2.62e-06
5e-05	2.59e-05	2.29e-05	9.45e-06	8.33e-06	2.17e-06	1.91e-06	2.78e-05	2.43e-05	1.01e-05	8.85e-06	2.32e-06	2.03e-06
2.5e-05	1.79e-05	1.68e-05	6.53e-06	6.12e-06	1.50e-06	1.41e-06	1.92e-05	1.79e-05	6.99e-06	6.53e-06	1.60e-06	1.50e-06

Table A.11: The slow compressional wave velocities of the coarsened sample FB22 ($N_c = 480$) saturated by the three types of fluids.

ω	Original $N_{cx} = 480$						Mirror $N_{cx} = 960$					
	$C_f = 0$		$C_f = 4.6$		$C_f = 100$		$C_f = 0$		$C_f = 4.6$		$C_f = 100$	
	C_r	C_i	C_r	C_i	C_r	C_i	C_r	C_i	C_r	C_i	C_r	C_i
0.05	3.011	1.1e-11	3.011	1.1e-11	3.011	1.1e-11	3.011	8.0e-12	3.011	8.0e-12	3.011	8.0e-12
0.025	3.011	1.1e-11	3.011	1.1e-11	3.011	1.1e-11	3.011	1.2e-11	3.011	1.2e-11	3.011	1.2e-11
0.01	3.011	4.3e-11	3.011	4.3e-11	3.011	4.3e-11	3.011	4.3e-11	3.011	4.3e-11	3.011	4.3e-11
0.005	3.011	4.1e-11	3.011	4.1e-11	3.011	4.1e-11	3.011	4.1e-11	3.011	4.1e-11	3.011	4.1e-11
0.0025	3.011	5.0e-11	3.011	5.0e-11	3.011	5.0e-11	3.011	5.3e-11	3.011	5.3e-11	3.011	5.3e-11
0.001	3.011	5.9e-11	3.011	5.9e-11	3.011	5.9e-11	3.011	6.3e-11	3.011	6.3e-11	3.011	6.3e-11
0.0005	3.011	5.5e-11	3.011	5.5e-11	3.011	5.5e-11	3.011	6.0e-11	3.011	6.0e-11	3.011	6.0e-11
0.00025	3.011	4.2e-11	3.011	4.2e-11	3.011	4.2e-11	3.011	4.7e-11	3.011	4.7e-11	3.011	4.7e-11
0.0001	3.011	2.2e-11	3.011	2.2e-11	3.011	2.2e-11	3.011	2.5e-11	3.011	2.5e-11	3.011	2.5e-11
5e-05	3.011	1.1e-11	3.011	1.1e-11	3.011	1.1e-11	3.011	1.3e-11	3.011	1.3e-11	3.011	1.3e-11
2.5e-05	3.011	5.8e-12	3.011	5.8e-12	3.011	5.8e-12	3.011	6.7e-12	3.011	6.7e-12	3.011	6.7e-12

Table A.12: The shear wave velocities in the original and mirror configurations of the coarsened sample FB22 ($N_c = 480$) saturated by the three types of fluids.

ω	Original $N_{cx} = 120$						Mirror $N_{cx} = 240$					
	$C_f = 0$		$C_f = 4.6$		$C_f = 100$		$C_f = 0$		$C_f = 4.6$		$C_f = 100$	
	C_r	C_i	C_r	C_i	C_r	C_i	C_r	C_i	C_r	C_i	C_r	C_i
0.05	6.08	1.3e-11	5.152	6.2e-12	5.102	8.2e-12	6.08	1.4e-11	5.152	6.7e-12	5.102	9.0e-12
0.025	6.08	2.2e-11	5.152	1.1e-11	5.102	1.4e-11	6.08	2.5e-11	5.152	1.2e-11	5.102	1.6e-11
0.01	6.08	5.0e-11	5.152	2.4e-11	5.102	3.2e-11	6.08	5.4e-11	5.152	2.6e-11	5.102	3.5e-11
0.005	6.08	4.3e-11	5.152	2.1e-11	5.102	2.8e-11	6.08	4.8e-11	5.152	2.3e-11	5.102	3.1e-11
0.0025	6.08	3.0e-11	5.152	1.5e-11	5.102	2.0e-11	6.08	3.5e-11	5.152	1.7e-11	5.102	2.3e-11
0.001	6.08	1.4e-11	5.152	7.0e-12	5.102	9.4e-12	6.08	1.7e-11	5.152	8.1e-12	5.102	1.1e-11
0.0005	6.08	7.4e-12	5.152	3.6e-12	5.102	4.8e-12	6.08	8.6e-12	5.152	4.2e-12	5.102	5.6e-12
0.00025	6.08	3.7e-12	5.152	1.8e-12	5.102	2.4e-12	6.08	4.3e-12	5.152	2.1e-12	5.102	2.8e-12
0.0001	6.08	1.5e-12	5.152	7.3e-13	5.102	9.7e-13	6.08	1.7e-12	5.152	8.5e-13	5.102	1.1e-12
5e-05	6.08	7.5e-13	5.152	3.6e-13	5.102	4.9e-13	6.08	8.7e-13	5.152	4.3e-13	5.102	5.7e-13
2.5e-05	6.08	3.7e-13	5.152	1.8e-13	5.102	2.4e-13	6.08	4.4e-13	5.152	2.1e-13	5.102	2.8e-13

Table A.13: The fast compressional wave velocities in the original and mirror configurations of the coarsened sample FB18 ($N_{cx} = 120$) saturated by the three types of fluids: incompressible fluid ($C_f = 0$), low-compressible ($C_f = 4.6$, water) and high-compressible ($C_f = 100$).

ω	Original $N_{cx} = 120$						Mirror $N_{cx} = 240$					
	$C_f = 0$		$C_f = 4.6$		$C_f = 100$		$C_f = 0$		$C_f = 4.6$		$C_f = 100$	
	C_r	C_i	C_r	C_i	C_r	C_i	C_r	C_i	C_r	C_i	C_r	C_i
0.05	9.20e-05	7.06e-06	2.40e-05	1.84e-06	5.31e-06	4.08e-07	9.87e-05	7.19e-06	2.57e-05	1.87e-06	5.70e-06	4.15e-07
0.025	9.20e-05	1.24e-05	2.40e-05	3.22e-06	5.32e-06	7.14e-07	9.81e-05	1.29e-05	2.56e-05	3.36e-06	5.67e-06	7.44e-07
0.01	7.99e-05	3.20e-05	2.08e-05	8.34e-06	4.62e-06	1.85e-06	8.48e-05	3.25e-05	2.21e-05	8.47e-06	4.90e-06	1.88e-06
0.005	6.54e-05	3.38e-05	1.70e-05	8.81e-06	3.78e-06	1.95e-06	7.05e-05	3.50e-05	1.84e-05	9.12e-06	4.07e-06	2.02e-06
0.0025	4.84e-05	3.24e-05	1.26e-05	8.43e-06	2.79e-06	1.87e-06	5.23e-05	3.43e-05	1.36e-05	8.93e-06	3.02e-06	1.98e-06
0.001	2.97e-05	2.49e-05	7.73e-06	6.48e-06	1.71e-06	1.44e-06	3.21e-05	2.67e-05	8.36e-06	6.95e-06	1.85e-06	1.54e-06
0.0005	2.04e-05	1.86e-05	5.31e-06	4.86e-06	1.18e-06	1.08e-06	2.20e-05	2.01e-05	5.74e-06	5.23e-06	1.27e-06	1.16e-06
0.00025	1.42e-05	1.35e-05	3.69e-06	3.52e-06	8.17e-07	7.82e-07	1.53e-05	1.46e-05	3.98e-06	3.80e-06	8.83e-07	8.43e-07
0.0001	8.84e-06	8.68e-06	2.30e-06	2.26e-06	5.11e-07	5.02e-07	9.55e-06	9.37e-06	2.49e-06	2.44e-06	5.51e-07	5.41e-07
5e-05	6.22e-06	6.17e-06	1.62e-06	1.61e-06	3.60e-07	3.56e-07	6.72e-06	6.66e-06	1.75e-06	1.73e-06	3.88e-07	3.84e-07
2.5e-05	4.39e-06	4.37e-06	1.14e-06	1.14e-06	2.54e-07	2.53e-07	4.74e-06	4.72e-06	1.23e-06	1.23e-06	2.74e-07	2.73e-07

Table A.14: The slow compressional wave velocities of the coarsened sample FB18 ($N_{cx} = 120$) saturated by the three types of fluids.

ω	Original $N_{cx} = 120$						Mirror $N_{cx} = 240$					
	$C_f = 0$		$C_f = 4.6$		$C_f = 100$		$C_f = 0$		$C_f = 4.6$		$C_f = 100$	
	C_r	C_i	C_r	C_i	C_r	C_i	C_r	C_i	C_r	C_i	C_r	C_i
0.05	3.414	5.6e-12	3.414	5.6e-12	3.414	5.6e-12	3.414	6.1e-12	3.414	6.1e-12	3.414	6.1e-12
0.025	3.414	9.8e-12	3.414	9.8e-12	3.414	9.8e-12	3.414	1.1e-11	3.414	1.1e-11	3.414	1.1e-11
0.01	3.414	2.2e-11	3.414	2.2e-11	3.414	2.2e-11	3.414	2.4e-11	3.414	2.4e-11	3.414	2.4e-11
0.005	3.414	1.9e-11	3.414	1.9e-11	3.414	1.9e-11	3.414	2.1e-11	3.414	2.1e-11	3.414	2.1e-11
0.0025	3.414	1.3e-11	3.414	1.3e-11	3.414	1.3e-11	3.414	1.5e-11	3.414	1.5e-11	3.414	1.5e-11
0.001	3.414	6.4e-12	3.414	6.4e-12	3.414	6.4e-12	3.414	7.4e-12	3.414	7.4e-12	3.414	7.4e-12
0.0005	3.414	3.3e-12	3.414	3.3e-12	3.414	3.3e-12	3.414	3.8e-12	3.414	3.8e-12	3.414	3.8e-12
0.00025	3.414	1.7e-12	3.414	1.7e-12	3.414	1.7e-12	3.414	1.9e-12	3.414	1.9e-12	3.414	1.9e-12
0.0001	3.414	6.8e-13	3.414	6.8e-13	3.414	6.8e-13	3.414	7.7e-13	3.414	7.7e-13	3.414	7.7e-13
5e-05	3.414	3.4e-13	3.414	3.4e-13	3.414	3.4e-13	3.414	3.9e-13	3.414	3.9e-13	3.414	3.9e-13
2.5e-05	3.414	1.7e-13	3.414	1.7e-13	3.414	1.7e-13	3.414	2.0e-13	3.414	2.0e-13	3.414	2.0e-13

Table A.15: The shear wave velocities in the original and mirror configurations of the coarsened sample FB18 ($N_{cx} = 120$) saturated by the three types of fluids.

ω	Original $N_{cx} = 240$						Mirror $N_{cx} = 480$					
	$C_f = 0$		$C_f = 4.6$		$C_f = 100$		$C_f = 0$		$C_f = 4.6$		$C_f = 100$	
	C_r	C_i	C_r	C_i	C_r	C_i	C_r	C_i	C_r	C_i	C_r	C_i
0.05	5.90	2.0e-11	4.921	1.2e-11	4.850	1.7e-11	5.90	1.3e-11	4.921	7.8e-12	4.850	1.1e-11
0.025	5.90	2.1e-11	4.921	1.2e-11	4.850	1.8e-11	5.90	2.3e-11	4.921	1.3e-11	4.850	1.9e-11
0.01	5.90	5.9e-11	4.921	3.5e-11	4.850	5.0e-11	5.90	6.2e-11	4.921	3.7e-11	4.850	5.3e-11
0.005	5.90	6.3e-11	4.921	3.7e-11	4.850	5.4e-11	5.90	6.6e-11	4.921	3.9e-11	4.850	5.7e-11
0.0025	5.90	6.3e-11	4.921	3.7e-11	4.850	5.4e-11	5.90	7.0e-11	4.921	4.1e-11	4.850	6.0e-11
0.001	5.90	4.8e-11	4.921	2.8e-11	4.850	4.1e-11	5.90	5.5e-11	4.921	3.2e-11	4.850	4.7e-11
0.0005	5.90	3.0e-11	4.921	1.8e-11	4.850	2.6e-11	5.90	3.5e-11	4.921	2.1e-11	4.850	3.0e-11
0.00025	5.90	1.6e-11	4.921	9.8e-12	4.850	1.4e-11	5.90	1.9e-11	4.921	1.1e-11	4.850	1.7e-11
0.0001	5.90	6.8e-12	4.921	4.0e-12	4.850	5.8e-12	5.90	7.9e-12	4.921	4.7e-12	4.850	6.8e-12
5e-05	5.90	3.4e-12	4.921	2.0e-12	4.850	2.9e-12	5.90	4.0e-12	4.921	2.4e-12	4.850	3.4e-12
2.5e-05	5.90	1.7e-12	4.921	1.0e-12	4.850	1.5e-12	5.90	2.0e-12	4.921	1.2e-12	4.850	1.7e-12

Table A.16: The fast compressional wave velocities in the original and mirror configurations of the coarsened sample FB18 ($N_c = 240$) saturated by the three types of fluids.

ω	Original $N_{cx} = 240$						Mirror $N_{cx} = 480$					
	$C_f = 0$		$C_f = 4.6$		$C_f = 100$		$C_f = 0$		$C_f = 4.6$		$C_f = 100$	
	C_r	C_i	C_r	C_i	C_r	C_i	C_r	C_i	C_r	C_i	C_r	C_i
0.05	1.18e-04	8.70e-06	3.60e-05	2.66e-06	8.08e-06	5.98e-07	1.27e-04	5.24e-06	3.88e-05	1.60e-06	8.73e-06	3.60e-07
0.025	1.21e-04	8.76e-06	3.71e-05	2.68e-06	8.34e-06	6.02e-07	1.28e-04	8.92e-06	3.92e-05	2.73e-06	8.82e-06	6.13e-07
0.01	1.12e-04	2.65e-05	3.43e-05	8.11e-06	7.70e-06	1.82e-06	1.19e-04	2.63e-05	3.65e-05	8.05e-06	8.20e-06	1.81e-06
0.005	1.04e-04	3.04e-05	3.19e-05	9.29e-06	7.18e-06	2.09e-06	1.11e-04	3.03e-05	3.39e-05	9.27e-06	7.63e-06	2.08e-06
0.0025	8.99e-05	3.55e-05	2.75e-05	1.09e-05	6.18e-06	2.44e-06	9.65e-05	3.65e-05	2.95e-05	1.12e-05	6.63e-06	2.51e-06
0.001	6.43e-05	3.78e-05	1.97e-05	1.16e-05	4.42e-06	2.60e-06	6.95e-05	3.99e-05	2.13e-05	1.22e-05	4.78e-06	2.74e-06
0.0005	4.56e-05	3.36e-05	1.39e-05	1.03e-05	3.13e-06	2.31e-06	4.95e-05	3.59e-05	1.51e-05	1.10e-05	3.40e-06	2.46e-06
0.00025	3.13e-05	2.66e-05	9.58e-06	8.15e-06	2.15e-06	1.83e-06	3.40e-05	2.87e-05	1.04e-05	8.77e-06	2.34e-06	1.97e-06
0.0001	1.92e-05	1.79e-05	5.86e-06	5.48e-06	1.32e-06	1.23e-06	2.08e-05	1.94e-05	6.35e-06	5.92e-06	1.43e-06	1.33e-06
5e-05	1.34e-05	1.29e-05	4.08e-06	3.95e-06	9.17e-07	8.88e-07	1.45e-05	1.40e-05	4.42e-06	4.27e-06	9.94e-07	9.60e-07
2.5e-05	9.37e-06	9.21e-06	2.86e-06	2.82e-06	6.44e-07	6.33e-07	1.01e-05	9.97e-06	3.10e-06	3.05e-06	6.97e-07	6.85e-07

Table A.17: The slow compressional wave velocities of the coarsened sample FB18 ($N_c = 240$) saturated by the three types of fluids.

ω	Original $N_{cx} = 240$						Mirror $N_{cx} = 480$					
	$C_f = 0$		$C_f = 4.6$		$C_f = 100$		$C_f = 0$		$C_f = 4.6$		$C_f = 100$	
	C_r	C_i	C_r	C_i	C_r	C_i	C_r	C_i	C_r	C_i	C_r	C_i
0.05	3.236	1.2e-11	3.236	1.2e-11	3.236	1.2e-11	3.236	7.7e-12	3.236	7.7e-12	3.236	7.7e-12
0.025	3.236	1.2e-11	3.236	1.2e-11	3.236	1.2e-11	3.236	1.3e-11	3.236	1.3e-11	3.236	1.3e-11
0.01	3.236	3.4e-11	3.236	3.4e-11	3.236	3.4e-11	3.236	3.6e-11	3.236	3.6e-11	3.236	3.6e-11
0.005	3.236	3.7e-11	3.236	3.7e-11	3.236	3.7e-11	3.236	3.9e-11	3.236	3.9e-11	3.236	3.9e-11
0.0025	3.236	3.7e-11	3.236	3.7e-11	3.236	3.7e-11	3.236	4.1e-11	3.236	4.1e-11	3.236	4.1e-11
0.001	3.236	2.8e-11	3.236	2.8e-11	3.236	2.8e-11	3.236	3.2e-11	3.236	3.2e-11	3.236	3.2e-11
0.0005	3.236	1.8e-11	3.236	1.8e-11	3.236	1.8e-11	3.236	2.1e-11	3.236	2.1e-11	3.236	2.1e-11
0.00025	3.236	9.6e-12	3.236	9.6e-12	3.236	9.6e-12	3.236	1.1e-11	3.236	1.1e-11	3.236	1.1e-11
0.0001	3.236	4.0e-12	3.236	4.0e-12	3.236	4.0e-12	3.236	4.6e-12	3.236	4.6e-12	3.236	4.6e-12
5e-05	3.236	2.0e-12	3.236	2.0e-12	3.236	2.0e-12	3.236	2.3e-12	3.236	2.3e-12	3.236	2.3e-12
2.5e-05	3.236	1.0e-12	3.236	1.0e-12	3.236	1.0e-12	3.236	1.2e-12	3.236	1.2e-12	3.236	1.2e-12

Table A.18: The shear wave velocities in the original and mirror configurations of the coarsened sample FB18 ($N_c = 240$) saturated by the three types of fluids.

ω	Original $N_{cx} = 480$						Mirror $N_{cx} = 960$					
	$C_f = 0$		$C_f = 4.6$		$C_f = 100$		$C_f = 0$		$C_f = 4.6$		$C_f = 100$	
	C_r	C_i	C_r	C_i	C_r	C_i	C_r	C_i	C_r	C_i	C_r	C_i
0.05	5.92	7.0e-12	4.875	8.5e-12	4.750	1.4e-11	5.92	8.5e-12	4.875	1.0e-11	4.750	1.7e-11
0.025	5.92	6.2e-12	4.875	7.6e-12	4.750	1.2e-11	5.92	6.4e-12	4.875	7.9e-12	4.750	1.3e-11
0.01	5.92	3.6e-11	4.875	4.4e-11	4.750	7.2e-11	5.92	3.1e-11	4.875	3.8e-11	4.750	6.3e-11
0.005	5.92	2.6e-11	4.875	3.1e-11	4.750	5.1e-11	5.92	2.6e-11	4.875	3.1e-11	4.750	5.2e-11
0.0025	5.92	2.8e-11	4.875	3.4e-11	4.750	5.7e-11	5.92	2.9e-11	4.875	3.6e-11	4.750	5.9e-11
0.001	5.92	3.2e-11	4.875	4.0e-11	4.750	6.5e-11	5.92	3.5e-11	4.875	4.3e-11	4.750	7.1e-11
0.0005	5.92	3.1e-11	4.875	3.8e-11	4.750	6.3e-11	5.92	3.5e-11	4.875	4.3e-11	4.750	7.0e-11
0.00025	5.92	2.5e-11	4.875	3.0e-11	4.750	5.0e-11	5.92	2.8e-11	4.875	3.4e-11	4.750	5.6e-11
0.0001	5.92	1.3e-11	4.875	1.6e-11	4.750	2.6e-11	5.92	1.5e-11	4.875	1.9e-11	4.750	3.1e-11
5e-05	5.92	7.0e-12	4.875	8.5e-12	4.750	1.4e-11	5.92	8.1e-12	4.875	1.0e-11	4.750	1.6e-11
2.5e-05	5.92	3.5e-12	4.875	4.3e-12	4.750	7.1e-12	5.92	4.2e-12	4.875	5.1e-12	4.750	8.4e-12

Table A.19: The fast compressional wave velocities in the original and mirror configurations of the coarsened sample FB18 ($N_c = 480$) saturated by the three types of fluids.

ω	Original $N_{cx} = 480$						Mirror $N_{cx} = 960$					
	$C_f = 0$		$C_f = 4.6$		$C_f = 100$		$C_f = 0$		$C_f = 4.6$		$C_f = 100$	
	C_r	C_i	C_r	C_i	C_r	C_i	C_r	C_i	C_r	C_i	C_r	C_i
0.05	1.14e-04	4.42e-06	4.39e-05	1.70e-06	1.02e-05	3.94e-07	1.16e-04	5.26e-06	4.47e-05	2.03e-06	1.04e-05	4.69e-07
0.025	1.11e-04	4.04e-06	4.27e-05	1.55e-06	9.88e-06	3.60e-07	1.17e-04	3.94e-06	4.52e-05	1.52e-06	1.05e-05	3.52e-07
0.01	1.08e-04	2.39e-05	4.17e-05	9.19e-06	9.66e-06	2.13e-06	1.13e-04	1.99e-05	4.37e-05	7.65e-06	1.01e-05	1.77e-06
0.005	1.05e-04	1.75e-05	4.06e-05	6.74e-06	9.40e-06	1.56e-06	1.10e-04	1.68e-05	4.25e-05	6.46e-06	9.84e-06	1.50e-06
0.0025	9.90e-05	2.05e-05	3.81e-05	7.90e-06	8.83e-06	1.83e-06	1.05e-04	2.00e-05	4.05e-05	7.69e-06	9.38e-06	1.78e-06
0.001	8.67e-05	2.70e-05	3.34e-05	1.04e-05	7.73e-06	2.41e-06	9.23e-05	2.77e-05	3.56e-05	1.07e-05	8.23e-06	2.47e-06
0.0005	7.21e-05	3.13e-05	2.78e-05	1.21e-05	6.43e-06	2.79e-06	7.73e-05	3.25e-05	2.98e-05	1.25e-05	6.89e-06	2.89e-06
0.00025	5.53e-05	3.21e-05	2.13e-05	1.24e-05	4.93e-06	2.86e-06	5.97e-05	3.38e-05	2.30e-05	1.30e-05	5.33e-06	3.02e-06
0.0001	3.49e-05	2.69e-05	1.35e-05	1.04e-05	3.12e-06	2.40e-06	3.80e-05	2.88e-05	1.46e-05	1.11e-05	3.38e-06	2.57e-06
5e-05	2.40e-05	2.09e-05	9.24e-06	8.06e-06	2.14e-06	1.87e-06	2.61e-05	2.26e-05	1.00e-05	8.69e-06	2.32e-06	2.01e-06
2.5e-05	1.65e-05	1.54e-05	6.37e-06	5.95e-06	1.48e-06	1.38e-06	1.80e-05	1.67e-05	6.92e-06	6.43e-06	1.60e-06	1.49e-06

Table A.20: The slow compressional wave velocities of the coarsened sample FB18 ($N_c = 240$) saturated by the three types of fluids.

ω	Original $N_{cx} = 480$						Mirror $N_{cx} = 960$					
	$C_f = 0$		$C_f = 4.6$		$C_f = 100$		$C_f = 0$		$C_f = 4.6$		$C_f = 100$	
	C_r	C_i	C_r	C_i	C_r	C_i	C_r	C_i	C_r	C_i	C_r	C_i
0.05	3.163	9.6e-12	3.163	9.6e-12	3.163	9.6e-12	3.163	1.2e-11	3.163	1.2e-11	3.163	1.2e-11
0.025	3.163	8.5e-12	3.163	8.5e-12	3.163	8.5e-12	3.163	8.8e-12	3.163	8.8e-12	3.163	8.8e-12
0.01	3.163	4.9e-11	3.163	4.9e-11	3.163	4.9e-11	3.163	4.3e-11	3.163	4.3e-11	3.163	4.3e-11
0.005	3.163	3.5e-11	3.163	3.5e-11	3.163	3.5e-11	3.163	3.5e-11	3.163	3.5e-11	3.163	3.5e-11
0.0025	3.163	3.9e-11	3.163	3.9e-11	3.163	3.9e-11	3.163	4.0e-11	3.163	4.0e-11	3.163	4.0e-11
0.001	3.163	4.5e-11	3.163	4.5e-11	3.163	4.5e-11	3.163	4.9e-11	3.163	4.9e-11	3.163	4.9e-11
0.0005	3.163	4.3e-11	3.163	4.3e-11	3.163	4.3e-11	3.163	4.8e-11	3.163	4.8e-11	3.163	4.8e-11
0.00025	3.163	3.4e-11	3.163	3.4e-11	3.163	3.4e-11	3.163	3.9e-11	3.163	3.9e-11	3.163	3.9e-11
0.0001	3.163	1.8e-11	3.163	1.8e-11	3.163	1.8e-11	3.163	2.1e-11	3.163	2.1e-11	3.163	2.1e-11
5e-05	3.163	9.6e-12	3.163	9.6e-12	3.163	9.6e-12	3.163	1.1e-11	3.163	1.1e-11	3.163	1.1e-11
2.5e-05	3.163	4.9e-12	3.163	4.9e-12	3.163	4.9e-12	3.163	5.7e-12	3.163	5.7e-12	3.163	5.7e-12

Table A.21: The shear wave velocities in the original and mirror configurations of the coarsened sample FB18 ($N_c = 480$) saturated by the three types of fluids.

ω	Original $N_{cx} = 240$						Mirror $N_{cx} = 480$					
	$C_f = 0$		$C_f = 4.6$		$C_f = 100$		$C_f = 0$		$C_f = 4.6$		$C_f = 100$	
	C_r	C_i	C_r	C_i	C_r	C_i	C_r	C_i	C_r	C_i	C_r	C_i
0.05	5.93	1.3e-11	5.271	8.3e-12	5.226	1.1e-11	5.93	8.3e-12	5.271	5.5e-12	5.226	7.5e-12
0.025	5.93	9.2e-12	5.271	6.1e-12	5.226	8.3e-12	5.93	1.0e-11	5.271	6.8e-12	5.226	9.3e-12
0.01	5.93	3.7e-11	5.271	2.4e-11	5.226	3.4e-11	5.93	3.8e-11	5.271	2.5e-11	5.226	3.5e-11
0.005	5.93	2.7e-11	5.271	1.8e-11	5.226	2.5e-11	5.93	3.0e-11	5.271	2.0e-11	5.226	2.7e-11
0.0025	5.93	2.1e-11	5.271	1.4e-11	5.226	1.9e-11	5.93	2.4e-11	5.271	1.6e-11	5.226	2.2e-11
0.001	5.93	1.2e-11	5.271	7.7e-12	5.226	1.1e-11	5.93	1.4e-11	5.271	9.4e-12	5.226	1.3e-11
0.0005	5.93	6.3e-12	5.271	4.2e-12	5.226	5.8e-12	5.93	7.8e-12	5.271	5.2e-12	5.226	7.1e-12
0.00025	5.93	3.2e-12	5.271	2.1e-12	5.226	2.9e-12	5.93	4.0e-12	5.271	2.7e-12	5.226	3.7e-12
0.0001	5.93	1.3e-12	5.271	8.6e-13	5.226	1.2e-12	5.93	1.6e-12	5.271	1.1e-12	5.226	1.5e-12
5e-05	5.93	6.5e-13	5.271	4.3e-13	5.226	5.9e-13	5.93	8.1e-13	5.271	5.4e-13	5.226	7.4e-13
2.5e-05	5.93	3.3e-13	5.271	2.2e-13	5.226	3.0e-13	5.93	4.1e-13	5.271	2.7e-13	5.226	3.7e-13

Table A.22: The fast compressional wave velocities in the original and mirror configurations of the coarsened sample FB13 ($N_c = 240$) saturated by the three types of fluids.

ω	Original $N_{cx} = 240$						Mirror $N_{cx} = 480$					
	$C_f = 0$		$C_f = 4.6$		$C_f = 100$		$C_f = 0$		$C_f = 4.6$		$C_f = 100$	
	C_r	C_i	C_r	C_i	C_r	C_i	C_r	C_i	C_r	C_i	C_r	C_i
0.05	8.26e-05	1.27e-05	2.33e-05	3.59e-06	5.20e-06	8.02e-07	9.20e-05	7.55e-06	2.60e-05	2.13e-06	5.79e-06	4.75e-07
0.025	8.48e-05	9.06e-06	2.39e-05	2.56e-06	5.34e-06	5.70e-07	9.32e-05	9.22e-06	2.63e-05	2.60e-06	5.87e-06	5.80e-07
0.01	8.12e-05	3.81e-05	2.29e-05	1.07e-05	5.11e-06	2.40e-06	8.56e-05	3.71e-05	2.41e-05	1.05e-05	5.39e-06	2.34e-06
0.005	6.86e-05	3.30e-05	1.94e-05	9.30e-06	4.32e-06	2.07e-06	7.55e-05	3.29e-05	2.13e-05	9.29e-06	4.76e-06	2.07e-06
0.0025	5.52e-05	3.19e-05	1.56e-05	9.00e-06	3.48e-06	2.01e-06	6.13e-05	3.33e-05	1.73e-05	9.40e-06	3.86e-06	2.10e-06
0.001	3.60e-05	2.71e-05	1.01e-05	7.65e-06	2.26e-06	1.71e-06	4.03e-05	2.94e-05	1.14e-05	8.30e-06	2.54e-06	1.85e-06
0.0005	2.48e-05	2.13e-05	7.00e-06	6.02e-06	1.56e-06	1.34e-06	2.78e-05	2.35e-05	7.84e-06	6.63e-06	1.75e-06	1.48e-06
0.00025	1.71e-05	1.59e-05	4.83e-06	4.47e-06	1.08e-06	9.98e-07	1.91e-05	1.76e-05	5.40e-06	4.96e-06	1.20e-06	1.11e-06
0.0001	1.06e-05	1.03e-05	3.00e-06	2.90e-06	6.68e-07	6.48e-07	1.18e-05	1.14e-05	3.34e-06	3.23e-06	7.46e-07	7.20e-07
5e-05	7.45e-06	7.34e-06	2.10e-06	2.07e-06	4.69e-07	4.62e-07	8.31e-06	8.17e-06	2.34e-06	2.30e-06	5.23e-07	5.14e-07
2.5e-05	5.25e-06	5.21e-06	1.48e-06	1.47e-06	3.31e-07	3.28e-07	5.85e-06	5.80e-06	1.65e-06	1.64e-06	3.68e-07	3.65e-07

Table A.23: The slow compressional wave velocities of the coarsened sample FB13 ($N_c = 240$) saturated by the three types of fluids.

ω	Original $N_{cx} = 240$						Mirror $N_{cx} = 480$					
	$C_f = 0$		$C_f = 4.6$		$C_f = 100$		$C_f = 0$		$C_f = 4.6$		$C_f = 100$	
	C_r	C_i	C_r	C_i	C_r	C_i	C_r	C_i	C_r	C_i	C_r	C_i
0.05	3.505	7.8e-12	3.505	7.8e-12	3.505	7.8e-12	3.505	5.1e-12	3.505	5.1e-12	3.505	5.1e-12
0.025	3.505	5.7e-12	3.505	5.7e-12	3.505	5.7e-12	3.505	6.4e-12	3.505	6.4e-12	3.505	6.4e-12
0.01	3.505	2.3e-11	3.505	2.3e-11	3.505	2.3e-11	3.505	2.4e-11	3.505	2.4e-11	3.505	2.4e-11
0.005	3.505	1.7e-11	3.505	1.7e-11	3.505	1.7e-11	3.505	1.8e-11	3.505	1.8e-11	3.505	1.8e-11
0.0025	3.505	1.3e-11	3.505	1.3e-11	3.505	1.3e-11	3.505	1.5e-11	3.505	1.5e-11	3.505	1.5e-11
0.001	3.505	7.2e-12	3.505	7.2e-12	3.505	7.2e-12	3.505	8.8e-12	3.505	8.8e-12	3.505	8.8e-12
0.0005	3.505	3.9e-12	3.505	3.9e-12	3.505	3.9e-12	3.505	4.8e-12	3.505	4.8e-12	3.505	4.8e-12
0.00025	3.505	2.0e-12	3.505	2.0e-12	3.505	2.0e-12	3.505	2.5e-12	3.505	2.5e-12	3.505	2.5e-12
0.0001	3.505	8.1e-13	3.505	8.1e-13	3.505	8.1e-13	3.505	1.0e-12	3.505	1.0e-12	3.505	1.0e-12
5e-05	3.505	4.0e-13	3.505	4.0e-13	3.505	4.0e-13	3.505	5.0e-13	3.505	5.0e-13	3.505	5.0e-13
2.5e-05	3.505	2.0e-13	3.505	2.0e-13	3.505	2.0e-13	3.505	2.5e-13	3.505	2.5e-13	3.505	2.5e-13

Table A.24: The shear wave velocities in the original and mirror configurations of the coarsened sample FB13 ($N_c = 240$) saturated by the three types of fluids.

ω	Original $N_{cx} = 480$						Mirror $N_{cx} = 960$					
	$C_f = 0$		$C_f = 4.6$		$C_f = 100$		$C_f = 0$		$C_f = 4.6$		$C_f = 100$	
	C_r	C_i	C_r	C_i	C_r	C_i	C_r	C_i	C_r	C_i	C_r	C_i
0.05	5.95	1.3e-11	5.233	2.0e-11	5.146	3.2e-11	5.95	3.3e-12	5.233	5.4e-12	5.146	8.5e-12
0.025	5.95	4.6e-12	5.233	7.5e-12	5.146	1.2e-11	5.95	3.9e-12	5.233	6.3e-12	5.146	9.9e-12
0.01	5.95	2.1e-11	5.233	3.3e-11	5.146	5.2e-11	5.95	2.2e-11	5.233	3.6e-11	5.146	5.5e-11
0.005	5.95	1.6e-11	5.233	2.5e-11	5.146	3.9e-11	5.95	1.5e-11	5.233	2.4e-11	5.146	3.7e-11
0.0025	5.95	1.2e-11	5.233	2.0e-11	5.146	3.1e-11	5.95	1.3e-11	5.233	2.1e-11	5.146	3.3e-11
0.001	5.95	1.1e-11	5.233	1.8e-11	5.146	2.8e-11	5.95	1.3e-11	5.233	2.1e-11	5.146	3.2e-11
0.0005	5.95	8.8e-12	5.233	1.4e-11	5.146	2.2e-11	5.95	1.1e-11	5.233	1.7e-11	5.146	2.7e-11
0.00025	5.95	5.7e-12	5.233	9.2e-12	5.146	1.4e-11	5.95	6.9e-12	5.233	1.1e-11	5.146	1.7e-11
0.0001	5.95	2.5e-12	5.233	4.1e-12	5.146	6.4e-12	5.95	3.1e-12	5.233	5.1e-12	5.146	7.9e-12
5e-05	5.95	1.3e-12	5.233	2.1e-12	5.146	3.3e-12	5.95	1.6e-12	5.233	2.6e-12	5.146	4.0e-12
2.5e-05	5.95	6.5e-13	5.233	1.0e-12	5.146	1.6e-12	5.95	8.0e-13	5.233	1.3e-12	5.146	2.0e-12

Table A.25: The fast compressional wave velocities in the original and mirror configurations of the coarsened sample FB13 ($N_c = 480$) saturated by the three types of fluids.

ω	Original $N_{cx} = 480$						Mirror $N_{cx} = 960$					
	$C_f = 0$		$C_f = 4.6$		$C_f = 100$		$C_f = 0$		$C_f = 4.6$		$C_f = 100$	
	C_r	C_i	C_r	C_i	C_r	C_i	C_r	C_i	C_r	C_i	C_r	C_i
0.05	8.45e-05	1.94e-05	3.12e-05	7.15e-06	7.17e-06	1.64e-06	5.09e-05	8.58e-06	1.88e-05	3.17e-06	4.32e-06	7.28e-07
0.025	8.57e-05	7.08e-06	3.16e-05	2.61e-06	7.27e-06	6.01e-07	5.20e-05	9.84e-06	1.92e-05	3.63e-06	4.41e-06	8.35e-07
0.01	8.52e-05	3.14e-05	3.15e-05	1.16e-05	7.23e-06	2.67e-06	8.86e-05	3.23e-05	3.27e-05	1.19e-05	7.52e-06	2.74e-06
0.005	7.79e-05	2.60e-05	2.88e-05	9.60e-06	6.62e-06	2.21e-06	8.25e-05	2.30e-05	3.05e-05	8.48e-06	7.00e-06	1.95e-06
0.0025	7.04e-05	2.26e-05	2.60e-05	8.35e-06	5.97e-06	1.92e-06	7.70e-05	2.23e-05	2.84e-05	8.23e-06	6.54e-06	1.89e-06
0.001	5.75e-05	2.50e-05	2.12e-05	9.23e-06	4.88e-06	2.12e-06	6.35e-05	2.62e-05	2.35e-05	9.66e-06	5.39e-06	2.22e-06
0.0005	4.47e-05	2.57e-05	1.65e-05	9.49e-06	3.79e-06	2.18e-06	4.97e-05	2.76e-05	1.83e-05	1.02e-05	4.22e-06	2.34e-06
0.00025	3.19e-05	2.32e-05	1.18e-05	8.55e-06	2.71e-06	1.97e-06	3.57e-05	2.53e-05	1.32e-05	9.33e-06	3.03e-06	2.15e-06
0.0001	1.95e-05	1.70e-05	7.18e-06	6.26e-06	1.65e-06	1.44e-06	2.18e-05	1.88e-05	8.04e-06	6.92e-06	1.85e-06	1.59e-06
5e-05	1.34e-05	1.25e-05	4.95e-06	4.62e-06	1.14e-06	1.06e-06	1.50e-05	1.39e-05	5.54e-06	5.13e-06	1.27e-06	1.18e-06
2.5e-05	9.35e-06	9.03e-06	3.45e-06	3.33e-06	7.93e-07	7.66e-07	1.04e-05	1.01e-05	3.85e-06	3.71e-06	8.86e-07	8.53e-07

Table A.26: The slow compressional wave velocities of the coarsened sample FB13 ($N_c = 480$) saturated by the three types of fluids.

ω	Original $N_{cx} = 480$						Mirror $N_{cx} = 960$					
	$C_f = 0$		$C_f = 4.6$		$C_f = 100$		$C_f = 0$		$C_f = 4.6$		$C_f = 100$	
	C_r	C_i	C_r	C_i	C_r	C_i	C_r	C_i	C_r	C_i	C_r	C_i
0.05	3.445	2.2e-11	3.445	2.2e-11	3.445	2.2e-11	3.445	5.8e-12	3.445	5.8e-12	3.445	5.8e-12
0.025	3.445	8.0e-12	3.445	8.0e-12	3.445	8.0e-12	3.445	6.8e-12	3.445	6.8e-12	3.445	6.8e-12
0.01	3.445	3.5e-11	3.445	3.5e-11	3.445	3.5e-11	3.445	3.8e-11	3.445	3.8e-11	3.445	3.8e-11
0.005	3.445	2.7e-11	3.445	2.7e-11	3.445	2.7e-11	3.445	2.5e-11	3.445	2.5e-11	3.445	2.5e-11
0.0025	3.445	2.1e-11	3.445	2.1e-11	3.445	2.1e-11	3.445	2.3e-11	3.445	2.3e-11	3.445	2.3e-11
0.001	3.445	1.9e-11	3.445	1.9e-11	3.445	1.9e-11	3.445	2.2e-11	3.445	2.2e-11	3.445	2.2e-11
0.0005	3.445	1.5e-11	3.445	1.5e-11	3.445	1.5e-11	3.445	1.8e-11	3.445	1.8e-11	3.445	1.8e-11
0.00025	3.445	9.8e-12	3.445	9.8e-12	3.445	9.8e-12	3.445	1.2e-11	3.445	1.2e-11	3.445	1.2e-11
0.0001	3.445	4.4e-12	3.445	4.4e-12	3.445	4.4e-12	3.445	5.4e-12	3.445	5.4e-12	3.445	5.4e-12
5e-05	3.445	2.2e-12	3.445	2.2e-12	3.445	2.2e-12	3.445	2.8e-12	3.445	2.8e-12	3.445	2.8e-12
2.5e-05	3.445	1.1e-12	3.445	1.1e-12	3.445	1.1e-12	3.445	1.4e-12	3.445	1.4e-12	3.445	1.4e-12

Table A.27: The shear wave velocities in the original and mirror configurations of the coarsened sample FB13 ($N_c = 480$) saturated by the three types of fluids.

A.4 Acoustic waves in saturated STATOIL samples

ω	Original $N_{cx} = 150$						Mirror $N_{cx} = 300$					
	$C_f = 0$		$C_f = 4.6$		$C_f = 100$		$C_f = 0$		$C_f = 4.6$		$C_f = 100$	
	C_r	C_i	C_r	C_i	C_r	C_i	C_r	C_i	C_r	C_i	C_r	C_i
0.05	15.32	6.2e-10	4.452	1.6e-11	4.353	2.3e-11	15.32	6.5e-10	4.452	1.7e-11	4.353	2.4e-11
0.025	15.32	1.1e-09	4.452	2.9e-11	4.353	4.2e-11	15.32	1.2e-09	4.452	3.0e-11	4.353	4.4e-11
0.01	15.32	2.1e-09	4.452	5.4e-11	4.353	7.8e-11	15.32	2.2e-09	4.452	5.6e-11	4.353	8.1e-11
0.005	15.32	2.2e-09	4.452	5.6e-11	4.353	8.1e-11	15.32	2.3e-09	4.452	5.9e-11	4.353	8.5e-11
0.0025	15.32	1.6e-09	4.452	4.1e-11	4.353	6.0e-11	15.32	1.7e-09	4.452	4.5e-11	4.353	6.5e-11
0.001	15.32	7.8e-10	4.452	2.0e-11	4.353	2.9e-11	15.32	8.5e-10	4.452	2.2e-11	4.353	3.2e-11
0.0005	15.32	4.0e-10	4.452	1.0e-11	4.353	1.5e-11	15.32	4.4e-10	4.452	1.1e-11	4.353	1.6e-11
0.00025	15.32	2.0e-10	4.452	5.2e-12	4.353	7.5e-12	15.32	2.2e-10	4.452	5.7e-12	4.353	8.2e-12
0.0001	15.32	8.1e-11	4.452	2.1e-12	4.353	3.0e-12	15.32	8.9e-11	4.452	2.3e-12	4.353	3.3e-12
5e-05	15.32	4.1e-11	4.452	1.0e-12	4.353	1.5e-12	15.32	4.5e-11	4.452	1.1e-12	4.353	1.7e-12
2.5e-05	15.32	2.0e-11	4.452	5.2e-13	4.353	7.5e-13	15.32	2.2e-11	4.452	5.7e-13	4.353	8.3e-13

Table A.28: The fast compressional wave velocities in the original and mirror configurations of the coarsened sample X7 ($N_{cx} = 150$) saturated by the three types of fluids: incompressible fluid ($C_f = 0$), low-compressible ($C_f = 4.6$, water in pressure of 1b) and high-compressible ($C_f = 100$).

ω	Original $N_{cx} = 150$						Mirror $N_{cx} = 300$					
	$C_f = 0$		$C_f = 4.6$		$C_f = 100$		$C_f = 0$		$C_f = 4.6$		$C_f = 100$	
	C_r	C_i	C_r	C_i	C_r	C_i	C_r	C_i	C_r	C_i	C_r	C_i
0.05	1.50e-04	1.04e-05	3.35e-05	2.32e-06	7.36e-06	5.10e-07	1.56e-04	1.05e-05	3.47e-05	2.34e-06	7.63e-06	5.14e-07
0.025	1.48e-04	1.91e-05	3.29e-05	4.26e-06	7.24e-06	9.35e-07	1.53e-04	1.93e-05	3.41e-05	4.31e-06	7.48e-06	9.48e-07
0.01	1.31e-04	4.01e-05	2.93e-05	8.94e-06	6.44e-06	1.96e-06	1.36e-04	4.00e-05	3.03e-05	8.93e-06	6.65e-06	1.96e-06
0.005	1.08e-04	5.02e-05	2.41e-05	1.12e-05	5.30e-06	2.46e-06	1.13e-04	5.08e-05	2.52e-05	1.13e-05	5.53e-06	2.49e-06
0.0025	7.95e-05	5.07e-05	1.77e-05	1.13e-05	3.90e-06	2.49e-06	8.34e-05	5.23e-05	1.86e-05	1.17e-05	4.09e-06	2.56e-06
0.001	4.86e-05	4.00e-05	1.08e-05	8.91e-06	2.38e-06	1.96e-06	5.10e-05	4.16e-05	1.14e-05	9.28e-06	2.50e-06	2.04e-06
0.0005	3.33e-05	3.01e-05	7.42e-06	6.72e-06	1.63e-06	1.48e-06	3.49e-05	3.15e-05	7.79e-06	7.02e-06	1.71e-06	1.54e-06
0.00025	2.31e-05	2.19e-05	5.14e-06	4.89e-06	1.13e-06	1.08e-06	2.42e-05	2.30e-05	5.39e-06	5.12e-06	1.19e-06	1.13e-06
0.0001	1.44e-05	1.41e-05	3.21e-06	3.15e-06	7.05e-07	6.91e-07	1.51e-05	1.48e-05	3.36e-06	3.29e-06	7.39e-07	7.24e-07
5e-05	1.01e-05	1.00e-05	2.26e-06	2.24e-06	4.96e-07	4.91e-07	1.06e-05	1.05e-05	2.37e-06	2.34e-06	5.20e-07	5.15e-07
2.5e-05	7.14e-06	7.10e-06	1.59e-06	1.58e-06	3.50e-07	3.48e-07	7.48e-06	7.44e-06	1.67e-06	1.66e-06	3.67e-07	3.65e-07

Table A.29: The slow compressional wave velocities of the coarsened sample X7 ($N_{cx} = 150$) saturated by the three types of fluids.

ω	Original $N_{cx} = 150$						Mirror $N_{cx} = 300$					
	$C_f = 0$		$C_f = 4.6$		$C_f = 100$		$C_f = 0$		$C_f = 4.6$		$C_f = 100$	
	C_r	C_i	C_r	C_i	C_r	C_i	C_r	C_i	C_r	C_i	C_r	C_i
0.05	2.857	1.5e-11	2.857	1.5e-11	2.857	1.5e-11	2.857	1.6e-11	2.857	1.6e-11	2.857	1.6e-11
0.025	2.857	2.8e-11	2.857	2.8e-11	2.857	2.8e-11	2.857	2.9e-11	2.857	2.9e-11	2.857	2.9e-11
0.01	2.857	5.2e-11	2.857	5.2e-11	2.857	5.2e-11	2.857	5.4e-11	2.857	5.4e-11	2.857	5.4e-11
0.005	2.857	5.4e-11	2.857	5.4e-11	2.857	5.4e-11	2.857	5.7e-11	2.857	5.7e-11	2.857	5.7e-11
0.0025	2.857	4.0e-11	2.857	4.0e-11	2.857	4.0e-11	2.857	4.3e-11	2.857	4.3e-11	2.857	4.3e-11
0.001	2.857	1.9e-11	2.857	1.9e-11	2.857	1.9e-11	2.857	2.1e-11	2.857	2.1e-11	2.857	2.1e-11
0.0005	2.857	1.0e-11	2.857	1.0e-11	2.857	1.0e-11	2.857	1.1e-11	2.857	1.1e-11	2.857	1.1e-11
0.00025	2.857	5.0e-12	2.857	5.0e-12	2.857	5.0e-12	2.857	5.5e-12	2.857	5.5e-12	2.857	5.5e-12
0.0001	2.857	2.0e-12	2.857	2.0e-12	2.857	2.0e-12	2.857	2.2e-12	2.857	2.2e-12	2.857	2.2e-12
5e-05	2.857	1.0e-12	2.857	1.0e-12	2.857	1.0e-12	2.857	1.1e-12	2.857	1.1e-12	2.857	1.1e-12
2.5e-05	2.857	5.0e-13	2.857	5.0e-13	2.857	5.0e-13	2.857	5.5e-13	2.857	5.5e-13	2.857	5.5e-13

Table A.30: The shear wave velocities in the original and mirror configurations of the coarsened sample X7 ($N_{cx} = 150$) saturated by th three types of fluids.

ω	Original $N_{cx} = 300$						Mirror $N_{cx} = 600$					
	$C_f = 0$		$C_f = 4.6$		$C_f = 100$		$C_f = 0$		$C_f = 4.6$		$C_f = 100$	
	C_r	C_i	C_r	C_i	C_r	C_i	C_r	C_i	C_r	C_i	C_r	C_i
0.05	15.32	6.2e-10	4.452	1.6e-11	4.353	2.3e-11	15.32	6.5e-10	4.452	1.7e-11	4.353	2.4e-11
0.05	11.49	5.8e-10	4.138	2.2e-11	4.003	3.8e-11	11.49	3.4e-10	4.138	1.3e-11	4.003	2.2e-11
0.025	11.49	6.0e-10	4.138	2.3e-11	4.003	3.8e-11	11.49	6.2e-10	4.138	2.4e-11	4.003	4.0e-11
0.01	11.49	1.3e-09	4.138	5.0e-11	4.003	8.4e-11	11.49	1.3e-09	4.138	5.0e-11	4.003	8.4e-11
0.005	11.49	1.6e-09	4.138	6.2e-11	4.003	1.0e-10	11.49	1.6e-09	4.138	6.3e-11	4.003	1.1e-10
0.0025	11.49	1.6e-09	4.138	6.2e-11	4.003	1.0e-10	11.49	1.7e-09	4.138	6.5e-11	4.003	1.1e-10
0.001	11.49	1.1e-09	4.138	4.3e-11	4.003	7.2e-11	11.49	1.2e-09	4.138	4.6e-11	4.003	7.7e-11
0.0005	11.49	6.6e-10	4.138	2.5e-11	4.003	4.2e-11	11.49	7.2e-10	4.138	2.7e-11	4.003	4.6e-11
0.00025	11.49	3.5e-10	4.138	1.3e-11	4.003	2.2e-11	11.49	3.8e-10	4.138	1.4e-11	4.003	2.4e-11
0.0001	11.49	1.4e-10	4.138	5.4e-12	4.003	9.1e-12	11.49	1.5e-10	4.138	5.9e-12	4.003	9.9e-12
5e-05	11.49	7.1e-11	4.138	2.7e-12	4.003	4.6e-12	11.49	7.8e-11	4.138	3.0e-12	4.003	5.0e-12
2.5e-05	11.49	3.6e-11	4.138	1.4e-12	4.003	2.3e-12	11.49	3.9e-11	4.138	1.5e-12	4.003	2.5e-12

Table A.31: The fast compressional wave velocities in the original and mirror configurations of the coarsened sample X7 ($N_{cx} = 300$) saturated by the three types of fluids: incompressible fluid ($C_f = 0$), low-compressible ($C_f = 4.6$, water) and high-compressible ($C_f = 100$).

ω	Original $N_{cx} = 300$						Mirror $N_{cx} = 600$					
	$C_f = 0$		$C_f = 4.6$		$C_f = 100$		$C_f = 0$		$C_f = 4.6$		$C_f = 100$	
	C_r	C_i	C_r	C_i	C_r	C_i	C_r	C_i	C_r	C_i	C_r	C_i
0.05	1.56e-04	1.22e-05	4.31e-05	3.37e-06	9.60e-06	7.50e-07	1.61e-04	6.86e-06	4.45e-05	1.90e-06	9.92e-06	4.22e-07
0.025	1.56e-04	1.25e-05	4.31e-05	3.44e-06	9.60e-06	7.67e-07	1.60e-04	1.26e-05	4.42e-05	3.47e-06	9.85e-06	7.73e-07
0.01	1.46e-04	2.91e-05	4.04e-05	8.03e-06	8.99e-06	1.79e-06	1.49e-04	2.84e-05	4.13e-05	7.85e-06	9.19e-06	1.75e-06
0.005	1.33e-04	3.97e-05	3.68e-05	1.10e-05	8.19e-06	2.44e-06	1.37e-04	3.92e-05	3.78e-05	1.08e-05	8.41e-06	2.41e-06
0.0025	1.11e-04	4.79e-05	3.05e-05	1.32e-05	6.80e-06	2.95e-06	1.15e-04	4.83e-05	3.16e-05	1.33e-05	7.05e-06	2.97e-06
0.001	7.54e-05	4.84e-05	2.08e-05	1.34e-05	4.64e-06	2.98e-06	7.86e-05	4.96e-05	2.17e-05	1.37e-05	4.84e-06	3.05e-06
0.0005	5.24e-05	4.11e-05	1.45e-05	1.13e-05	3.23e-06	2.53e-06	5.48e-05	4.25e-05	1.51e-05	1.17e-05	3.37e-06	2.61e-06
0.00025	3.59e-05	3.17e-05	9.92e-06	8.75e-06	2.21e-06	1.95e-06	3.75e-05	3.29e-05	1.04e-05	9.08e-06	2.31e-06	2.02e-06
0.0001	2.21e-05	2.10e-05	6.10e-06	5.79e-06	1.36e-06	1.29e-06	2.30e-05	2.18e-05	6.36e-06	6.03e-06	1.42e-06	1.34e-06
5e-05	1.54e-05	1.50e-05	4.26e-06	4.15e-06	9.49e-07	9.25e-07	1.61e-05	1.57e-05	4.45e-06	4.33e-06	9.90e-07	9.64e-07
2.5e-05	1.08e-05	1.07e-05	3.00e-06	2.96e-06	6.67e-07	6.59e-07	1.13e-05	1.12e-05	3.12e-06	3.08e-06	6.96e-07	6.87e-07

Table A.32: The slow compressional wave velocities of the coarsened sample X7 ($N_{cx} = 300$) saturated by the three types of fluids.

ω	Original $N_{cx} = 300$						Mirror $N_{cx} = 600$					
	$C_f = 0$		$C_f = 4.6$		$C_f = 100$		$C_f = 0$		$C_f = 4.6$		$C_f = 100$	
	C_r	C_i	C_r	C_i	C_r	C_i	C_r	C_i	C_r	C_i	C_r	C_i
0.05	2.611	2.5e-11	2.611	2.5e-11	2.611	2.5e-11	2.611	1.5e-11	2.611	1.5e-11	2.611	1.5e-11
0.025	2.611	2.6e-11	2.611	2.6e-11	2.611	2.6e-11	2.611	2.7e-11	2.611	2.7e-11	2.611	2.7e-11
0.01	2.611	5.6e-11	2.611	5.6e-11	2.611	5.6e-11	2.611	5.6e-11	2.611	5.6e-11	2.611	5.6e-11
0.005	2.611	7.0e-11	2.611	7.0e-11	2.611	7.0e-11	2.611	7.1e-11	2.611	7.1e-11	2.611	7.1e-11
0.0025	2.611	7.0e-11	2.611	7.0e-11	2.611	7.0e-11	2.611	7.3e-11	2.611	7.3e-11	2.611	7.3e-11
0.001	2.611	4.8e-11	2.611	4.8e-11	2.611	4.8e-11	2.611	5.1e-11	2.611	5.1e-11	2.611	5.1e-11
0.0005	2.611	2.8e-11	2.611	2.8e-11	2.611	2.8e-11	2.611	3.1e-11	2.611	3.1e-11	2.611	3.1e-11
0.00025	2.611	1.5e-11	2.611	1.5e-11	2.611	1.5e-11	2.611	1.6e-11	2.611	1.6e-11	2.611	1.6e-11
0.0001	2.611	6.1e-12	2.611	6.1e-12	2.611	6.1e-12	2.611	6.6e-12	2.611	6.6e-12	2.611	6.6e-12
5e-05	2.611	3.1e-12	2.611	3.1e-12	2.611	3.1e-12	2.611	3.3e-12	2.611	3.3e-12	2.611	3.3e-12
2.5e-05	2.611	1.5e-12	2.611	1.5e-12	2.611	1.5e-12	2.611	1.7e-12	2.611	1.7e-12	2.611	1.7e-12

Table A.33: The shear wave velocities in the original and mirror configurations of the coarsened sample X7 ($N_{cx} = 300$) saturated by the three types of fluids.

ω	Fast compressional velocity						Shear wave velocity					
	$C_f = 0$		$C_f = 4.6$		$C_f = 100$		$C_f = 0$		$C_f = 4.6$		$C_f = 100$	
	C_r	C_i	C_r	C_i	C_r	C_i	C_r	C_i	C_r	C_i	C_r	C_i
0.05	9.844	1.7e-10	3.955	7.9e-12	3.792	1.5e-11	2.465	1.0e-11	2.465	1.0e-11	2.465	1.0e-11
0.025	9.844	2.9e-10	3.955	1.4e-11	3.792	2.6e-11	2.465	1.8e-11	2.465	1.8e-11	2.465	1.8e-11
0.01	9.844	8.3e-10	3.955	3.9e-11	3.792	7.4e-11	2.465	5.0e-11	2.465	5.0e-11	2.465	5.0e-11
0.005	9.844	9.5e-10	3.955	4.4e-11	3.792	8.5e-11	2.465	5.7e-11	2.465	5.7e-11	2.465	5.7e-11
0.0025	9.844	1.2e-09	3.955	5.6e-11	3.792	1.1e-10	2.465	7.2e-11	2.465	7.2e-11	2.465	7.2e-11
0.001	9.844	1.3e-09	3.955	5.9e-11	3.792	1.1e-10	2.465	7.6e-11	2.465	7.6e-11	2.465	7.6e-11
0.0005	9.844	1.1e-09	3.955	5.0e-11	3.792	9.6e-11	2.465	6.4e-11	2.465	6.4e-11	2.465	6.4e-11
0.00025	9.844	7.3e-10	3.955	3.4e-11	3.792	6.5e-11	2.465	4.4e-11	2.465	4.4e-11	2.465	4.4e-11
0.0001	9.844	3.4e-10	3.955	1.6e-11	3.792	3.0e-11	2.465	2.0e-11	2.465	2.0e-11	2.465	2.0e-11
5e-05	9.844	1.7e-10	3.955	8.1e-12	3.792	1.6e-11	2.465	1.0e-11	2.465	1.0e-11	2.465	1.0e-11
2.5e-05	9.844	8.8e-11	3.955	4.1e-12	3.792	7.8e-12	2.465	5.3e-12	2.465	5.3e-12	2.465	5.3e-12

Table A.34: The fast compressional and shear wave velocities in the original configuration of the coarsened sample X7 ($N_{cr} = 600$) saturated by the three types of fluids.

ω	Original $N_{cx} = 150$						Mirror $N_{cx} = 300$					
	$C_f = 0$		$C_f = 4.6$		$C_f = 100$		$C_f = 0$		$C_f = 4.6$		$C_f = 100$	
	C_r	C_i	C_r	C_i	C_r	C_i	C_r	C_i	C_r	C_i	C_r	C_i
0.05	9.37	3.6e-10	4.943	9.9e-12	4.879	1.4e-11	9.37	4.8e-10	4.943	1.3e-11	4.879	1.9e-11
0.025	9.37	2.2e-10	4.943	6.1e-12	4.879	8.7e-12	9.37	3.2e-10	4.943	8.8e-12	4.879	1.2e-11
0.01	9.37	3.6e-10	4.943	1.0e-11	4.879	1.4e-11	9.37	8.8e-10	4.943	2.5e-11	4.879	3.5e-11
0.005	9.37	6.3e-10	4.943	1.8e-11	4.879	2.5e-11	9.37	7.2e-10	4.943	2.0e-11	4.879	2.8e-11
0.0025	9.37	3.7e-10	4.943	1.0e-11	4.879	1.5e-11	9.37	5.1e-10	4.943	1.4e-11	4.879	2.0e-11
0.001	9.37	1.7e-10	4.943	4.7e-12	4.879	6.7e-12	9.37	2.5e-10	4.943	6.8e-12	4.879	9.7e-12
0.0005	9.37	8.7e-11	4.943	2.4e-12	4.879	3.5e-12	9.37	1.3e-10	4.943	3.5e-12	4.879	5.0e-12
0.00025	9.37	4.4e-11	4.943	1.2e-12	4.879	1.7e-12	9.37	6.4e-11	4.943	1.8e-12	4.879	2.5e-12
0.0001	9.37	1.8e-11	4.943	4.9e-13	4.879	7.0e-13	9.37	2.6e-11	4.943	7.2e-13	4.879	1.0e-12
5e-05	9.37	8.9e-12	4.943	2.5e-13	4.879	3.5e-13	9.37	1.3e-11	4.943	3.6e-13	4.879	5.1e-13
2.5e-05	9.37	4.4e-12	4.943	1.2e-13	4.879	1.7e-13	9.37	6.5e-12	4.943	1.8e-13	4.879	2.5e-13

Table A.35: The fast compressional wave velocities in the original and mirror configurations of the coarsened sample Y5 ($N_{cx} = 150$) saturated by the three types of fluids: incompressible fluid ($C_f = 0$), low-compressible ($C_f = 4.6$, water) and high-compressible ($C_f = 100$).

ω	Original $N_{cx} = 150$						Mirror $N_{cx} = 300$					
	$C_f = 0$		$C_f = 4.6$		$C_f = 100$		$C_f = 0$		$C_f = 4.6$		$C_f = 100$	
	C_r	C_i	C_r	C_i	C_r	C_i	C_r	C_i	C_r	C_i	C_r	C_i
0.05	9.32e-05	2.18e-05	1.81e-05	4.22e-06	3.94e-06	9.22e-07	1.07e-04	2.54e-05	2.07e-05	4.92e-06	4.53e-06	1.07e-06
0.025	9.15e-05	1.37e-05	1.77e-05	2.65e-06	3.87e-06	5.79e-07	1.11e-04	1.62e-05	2.14e-05	3.14e-06	4.68e-06	6.87e-07
0.01	8.78e-05	2.36e-05	1.70e-05	4.57e-06	3.72e-06	9.98e-07	9.35e-05	5.35e-05	1.81e-05	1.04e-05	3.96e-06	2.26e-06
0.005	7.08e-05	5.05e-05	1.37e-05	9.78e-06	3.00e-06	2.14e-06	8.64e-05	4.72e-05	1.68e-05	9.14e-06	3.66e-06	2.00e-06
0.0025	5.22e-05	4.03e-05	1.01e-05	7.81e-06	2.21e-06	1.71e-06	6.53e-05	4.42e-05	1.27e-05	8.56e-06	2.77e-06	1.87e-06
0.001	3.32e-05	2.89e-05	6.44e-06	5.60e-06	1.41e-06	1.22e-06	4.09e-05	3.40e-05	7.92e-06	6.60e-06	1.73e-06	1.44e-06
0.0005	2.31e-05	2.15e-05	4.48e-06	4.16e-06	9.79e-07	9.09e-07	2.82e-05	2.56e-05	5.46e-06	4.97e-06	1.19e-06	1.09e-06
0.00025	1.61e-05	1.55e-05	3.13e-06	3.01e-06	6.83e-07	6.58e-07	1.96e-05	1.87e-05	3.79e-06	3.61e-06	8.28e-07	7.90e-07
0.0001	1.01e-05	9.95e-06	1.96e-06	1.93e-06	4.28e-07	4.21e-07	1.22e-05	1.20e-05	2.37e-06	2.32e-06	5.17e-07	5.07e-07
5e-05	7.12e-06	7.07e-06	1.38e-06	1.37e-06	3.01e-07	2.99e-07	8.60e-06	8.52e-06	1.67e-06	1.65e-06	3.64e-07	3.61e-07
2.5e-05	5.03e-06	5.01e-06	9.74e-07	9.70e-07	2.13e-07	2.12e-07	6.07e-06	6.04e-06	1.18e-06	1.17e-06	2.57e-07	2.56e-07

Table A.36: The slow compressional wave velocities of the coarsened sample Y5 ($N_{cx} = 150$) saturated by the three types of fluids.

ω	Original $N_{cx} = 150$						Mirror $N_{cx} = 300$					
	$C_f = 0$		$C_f = 4.6$		$C_f = 100$		$C_f = 0$		$C_f = 4.6$		$C_f = 100$	
	C_r	C_i	C_r	C_i	C_r	C_i	C_r	C_i	C_r	C_i	C_r	C_i
0.05	3.185	9.6e-12	3.184	9.4e-12	3.184	9.4e-12	3.185	1.3e-11	3.184	1.3e-11	3.184	1.3e-11
0.025	3.185	5.9e-12	3.184	5.8e-12	3.184	5.8e-12	3.185	8.5e-12	3.184	8.3e-12	3.184	8.3e-12
0.01	3.185	9.8e-12	3.184	9.6e-12	3.184	9.5e-12	3.185	2.4e-11	3.184	2.3e-11	3.184	2.3e-11
0.005	3.185	1.7e-11	3.184	1.6e-11	3.184	1.6e-11	3.185	1.9e-11	3.184	1.9e-11	3.184	1.9e-11
0.0025	3.185	9.9e-12	3.184	9.7e-12	3.184	9.7e-12	3.185	1.4e-11	3.184	1.3e-11	3.184	1.3e-11
0.001	3.185	4.5e-12	3.184	4.4e-12	3.184	4.4e-12	3.185	6.6e-12	3.184	6.4e-12	3.184	6.4e-12
0.0005	3.185	2.3e-12	3.184	2.3e-12	3.184	2.3e-12	3.185	3.4e-12	3.184	3.3e-12	3.184	3.3e-12
0.00025	3.185	1.2e-12	3.184	1.2e-12	3.184	1.2e-12	3.185	1.7e-12	3.184	1.7e-12	3.184	1.7e-12
0.0001	3.185	4.8e-13	3.184	4.6e-13	3.184	4.6e-13	3.185	6.9e-13	3.184	6.8e-13	3.184	6.8e-13
5e-05	3.185	2.4e-13	3.184	2.3e-13	3.184	2.3e-13	3.185	3.5e-13	3.184	3.4e-13	3.184	3.4e-13
2.5e-05	3.185	1.2e-13	3.184	1.2e-13	3.184	1.2e-13	3.185	1.7e-13	3.184	1.7e-13	3.184	1.7e-13

Table A.37: The shear wave velocities in the original and mirror configurations of the coarsened sample Y5 ($N_{cx} = 150$) saturated by the three types of fluids.

ω	Original $N_{cx} = 300$						Mirror $N_{cx} = 600$					
	$C_f = 0$		$C_f = 4.6$		$C_f = 100$		$C_f = 0$		$C_f = 4.6$		$C_f = 100$	
	C_r	C_i	C_r	C_i	C_r	C_i	C_r	C_i	C_r	C_i	C_r	C_i
0.05	15.32	6.2e-10	4.452	1.6e-11	4.353	2.3e-11	15.32	6.5e-10	4.452	1.7e-11	4.353	2.4e-11
0.05	8.13	4.2e-10	4.794	1.9e-11	4.713	2.9e-11	8.13	2.2e-10	4.794	1.0e-11	4.713	1.5e-11
0.025	8.13	5.8e-10	4.794	2.6e-11	4.713	4.0e-11	8.13	1.8e-10	4.794	7.9e-12	4.713	1.2e-11
0.01	8.13	9.4e-10	4.794	4.2e-11	4.713	6.4e-11	8.13	1.1e-09	4.794	5.0e-11	4.713	7.7e-11
0.005	8.13	6.4e-10	4.794	2.9e-11	4.713	4.4e-11	8.13	5.8e-10	4.794	2.6e-11	4.713	4.0e-11
0.0025	8.13	4.6e-10	4.794	2.1e-11	4.713	3.2e-11	8.13	5.0e-10	4.794	2.2e-11	4.713	3.4e-11
0.001	8.13	2.5e-10	4.794	1.1e-11	4.713	1.7e-11	8.13	3.4e-10	4.794	1.5e-11	4.713	2.3e-11
0.0005	8.13	1.4e-10	4.794	6.4e-12	4.713	9.8e-12	8.13	2.1e-10	4.794	9.5e-12	4.713	1.4e-11
0.00025	8.13	7.6e-11	4.794	3.4e-12	4.713	5.2e-12	8.13	1.2e-10	4.794	5.2e-12	4.713	7.9e-12
0.0001	8.13	3.1e-11	4.794	1.4e-12	4.713	2.1e-12	8.13	4.7e-11	4.794	2.1e-12	4.713	3.2e-12
5e-05	8.13	1.6e-11	4.794	7.0e-13	4.713	1.1e-12	8.13	2.4e-11	4.794	1.1e-12	4.713	1.6e-12
2.5e-05	8.13	7.8e-12	4.794	3.5e-13	4.713	5.3e-13	8.13	1.2e-11	4.794	5.3e-13	4.713	8.2e-13

Table A.38: The fast compressional wave velocities in the original and mirror configurations of the coarsened sample Y5 ($N_{cx} = 300$) saturated by the three types of fluids: incompressible fluid ($C_f = 0$), low-compressible ($C_f = 4.6$, water) and high-compressible ($C_f = 100$).

ω	Original $N_{cx} = 300$						Mirror $N_{cx} = 600$					
	$C_f = 0$		$C_f = 4.6$		$C_f = 100$		$C_f = 0$		$C_f = 4.6$		$C_f = 100$	
	C_r	C_i	C_r	C_i	C_r	C_i	C_r	C_i	C_r	C_i	C_r	C_i
0.05	1.15e-04	2.70e-05	2.65e-05	6.23e-06	5.84e-06	1.37e-06	1.14e-04	1.46e-05	2.63e-05	3.36e-06	5.79e-06	7.40e-07
0.025	1.13e-04	3.84e-05	2.59e-05	8.85e-06	5.71e-06	1.95e-06	1.19e-04	1.12e-05	2.73e-05	2.58e-06	6.02e-06	5.67e-07
0.01	1.08e-04	6.51e-05	2.48e-05	1.50e-05	5.46e-06	3.30e-06	1.09e-04	7.69e-05	2.50e-05	1.77e-05	5.51e-06	3.90e-06
0.005	9.61e-05	4.96e-05	2.21e-05	1.14e-05	4.88e-06	2.52e-06	9.98e-05	4.34e-05	2.30e-05	1.00e-05	5.07e-06	2.21e-06
0.0025	7.53e-05	4.56e-05	1.74e-05	1.05e-05	3.82e-06	2.32e-06	8.85e-05	4.19e-05	2.04e-05	9.66e-06	4.49e-06	2.13e-06
0.001	5.05e-05	3.64e-05	1.16e-05	8.40e-06	2.56e-06	1.85e-06	6.41e-05	3.98e-05	1.48e-05	9.18e-06	3.26e-06	2.02e-06
0.0005	3.62e-05	2.94e-05	8.35e-06	6.78e-06	1.84e-06	1.49e-06	4.58e-05	3.45e-05	1.06e-05	7.95e-06	2.32e-06	1.75e-06
0.00025	2.52e-05	2.25e-05	5.81e-06	5.18e-06	1.28e-06	1.14e-06	3.16e-05	2.72e-05	7.29e-06	6.26e-06	1.61e-06	1.38e-06
0.0001	1.56e-05	1.49e-05	3.59e-06	3.43e-06	7.91e-07	7.55e-07	1.94e-05	1.82e-05	4.47e-06	4.20e-06	9.85e-07	9.25e-07
5e-05	1.09e-05	1.07e-05	2.52e-06	2.46e-06	5.54e-07	5.41e-07	1.35e-05	1.31e-05	3.12e-06	3.02e-06	6.87e-07	6.66e-07
2.5e-05	7.67e-06	7.58e-06	1.77e-06	1.75e-06	3.89e-07	3.85e-07	9.50e-06	9.35e-06	2.19e-06	2.16e-06	4.82e-07	4.75e-07

Table A.39: The slow compressional wave velocities of the coarsened sample Y5 ($N_{cx} = 300$) saturated by the three types of fluids.

ω	Original $N_{cx} = 300$						Mirror $N_{cx} = 600$					
	$C_f = 0$		$C_f = 4.6$		$C_f = 100$		$C_f = 0$		$C_f = 4.6$		$C_f = 100$	
	C_r	C_i	C_r	C_i	C_r	C_i	C_r	C_i	C_r	C_i	C_r	C_i
0.05	3.062	1.9e-11	3.061	1.9e-11	3.061	1.9e-11	3.062	1.0e-11	3.061	1.0e-11	3.061	1.0e-11
0.025	3.062	2.7e-11	3.061	2.6e-11	3.061	2.6e-11	3.062	8.2e-12	3.061	8.1e-12	3.061	8.1e-12
0.01	3.062	4.4e-11	3.061	4.3e-11	3.061	4.3e-11	3.062	5.2e-11	3.061	5.1e-11	3.061	5.1e-11
0.005	3.062	3.0e-11	3.061	2.9e-11	3.061	2.9e-11	3.062	2.7e-11	3.061	2.6e-11	3.061	2.6e-11
0.0025	3.062	2.1e-11	3.061	2.1e-11	3.061	2.1e-11	3.062	2.3e-11	3.061	2.3e-11	3.061	2.3e-11
0.001	3.062	1.1e-11	3.061	1.1e-11	3.061	1.1e-11	3.062	1.6e-11	3.061	1.6e-11	3.061	1.6e-11
0.0005	3.062	6.6e-12	3.061	6.5e-12	3.061	6.5e-12	3.062	9.8e-12	3.061	9.6e-12	3.061	9.6e-12
0.00025	3.062	3.5e-12	3.061	3.4e-12	3.061	3.4e-12	3.062	5.3e-12	3.061	5.2e-12	3.061	5.2e-12
0.0001	3.062	1.4e-12	3.061	1.4e-12	3.061	1.4e-12	3.062	2.2e-12	3.061	2.2e-12	3.061	2.2e-12
5e-05	3.062	7.2e-13	3.061	7.1e-13	3.061	7.1e-13	3.062	1.1e-12	3.061	1.1e-12	3.061	1.1e-12
2.5e-05	3.062	3.6e-13	3.061	3.5e-13	3.061	3.5e-13	3.062	5.5e-13	3.061	5.4e-13	3.061	5.4e-13

Table A.40: The shear wave velocities in the original and mirror configurations of the coarsened sample Y5 ($N_{cx} = 300$) saturated by the three types of fluids.

ω	Fast compressional velocity						Shear wave velocity					
	$C_f = 0$		$C_f = 4.6$		$C_f = 100$		$C_f = 0$		$C_f = 4.6$		$C_f = 100$	
	C_r	C_i	C_r	C_i	C_r	C_i	C_r	C_i	C_r	C_i	C_r	C_i
0.05	7.397	4.1e-10	4.717	2.7e-11	4.625	4.3e-11	2.999	2.9e-11	2.998	2.9e-11	2.998	2.9e-11
0.025	7.397	6.4e-10	4.717	4.2e-11	4.625	6.7e-11	2.999	4.6e-11	2.998	4.5e-11	2.998	4.5e-11
0.01	7.397	1.2e-09	4.717	8.1e-11	4.625	1.3e-10	2.999	8.8e-11	2.998	8.6e-11	2.998	8.6e-11
0.005	7.397	5.8e-10	4.717	3.8e-11	4.625	6.1e-11	2.999	4.2e-11	2.998	4.1e-11	2.998	4.1e-11
0.0025	7.397	4.5e-10	4.717	3.0e-11	4.625	4.7e-11	2.999	3.2e-11	2.998	3.1e-11	2.998	3.1e-11
0.001	7.397	3.1e-10	4.717	2.0e-11	4.625	3.2e-11	2.999	2.2e-11	2.998	2.2e-11	2.998	2.2e-11
0.0005	7.397	2.0e-10	4.717	1.3e-11	4.625	2.2e-11	2.999	1.5e-11	2.998	1.4e-11	2.998	1.4e-11
0.00025	7.397	1.4e-10	4.717	9.0e-12	4.625	1.4e-11	2.999	9.7e-12	2.998	9.5e-12	2.998	9.5e-12
0.0001	7.397	6.5e-11	4.717	4.2e-12	4.625	6.8e-12	2.999	4.6e-12	2.998	4.5e-12	2.998	4.5e-12
5e-05	7.397	3.4e-11	4.717	2.2e-12	4.625	3.5e-12	2.999	2.4e-12	2.998	2.3e-12	2.998	2.3e-12
2.5e-05	7.397	1.7e-11	4.717	1.1e-12	4.625	1.8e-12	2.999	1.2e-12	2.998	1.2e-12	2.998	1.2e-12

Table A.41: The fast compressional and shear wave velocities in the original configuration of the coarsened sample Y5 ($N_{cr} = 600$) saturated by the three types of fluids.